Geodätisch-geophysikalische Arbeiten in der Schweiz

(Fortsetzung der Publikationsreihe
«Astronomisch-geodätische Arbeiten in der Schweiz»)

herausgegeben von der

Schweizerischen Geodätischen Kommission
(Organ der Akademie der Naturwissenschaften Schweiz)

Vierundachtzigster Band
Volume 84

Water Vapor Tomography using Global Navigation Satellite Systems

Donat Perler

2012

Adresse der Schweizerischen Geodätischen Kommission:

Institut für Geodäsie und Photogrammetrie
Eidg. Technische Hochschule Zürich
ETH Zürich
8093 Zürich
Switzerland

Internet: http://www.sgc.ethz.ch

ISBN 978-3-908440-30-7

Redaktion des 84. Bandes:
Dr. D. Perler, J. Müller-Gantenbein, A.Geiger
Druck: Print-Atelier ADAG, Zürich

VORWORT

Die geodätischen Wissenschaften haben in der letzten Dekade zunehmende Bedeutung im Kontext der Atmosphärenforschung erlangt. Die Installation von kontinuierlich arbeitenden und dicht verteilten GNSS-Stationsnetzen ermöglicht die Anwendung tomographischer Lösungsansätze zur Bestimmung der Wasserdampfverteilung in der Atmosphäre an Hand von GNSS Messungen. Allerdings sind für den Praxis nahen Einsatz der GNSS-Tomographie neben theoretischen auch methodische Entwicklungen nötig. Es ist wichtig, dass sowohl meteorologische Kenntnisse als auch mathematisches und computertechnisches Wissen zusammengeführt werden, um ein greifbares Resultat erreichen zu können.

Die tomographische Methode wurde weiter verbessert: Zum Einen durch die räumlich variable Modellierung der Refraktion innerhalb einer Digitalisationszelle, zum Anderen durch die Berücksichtigung der zeitlichen Variation des Wasserdampfgehaltes mittels Filteransätzen (Kalman-Filter). Dies wird real-time Berechnungen und deren Einbindung in die neueste Generation der in Entwicklung begriffenen Assimilationsverfahren ermöglichen. Die Validierung der neuen Algorithmen und Verfahren erfolgte anhand von Simulationen und von realen Daten.

Eine grosse Stärke der neu entwickelten Software liegt in der Möglichkeit der kompletten Simulation von Messdaten und Resultaten. Damit können Methodentests aber auch a priori Untersuchungen zu verschiedenen Netzkonfigurationen und Satellitenkonstellationen durchgeführt werden. Die Untersuchungen haben gezeigt, dass alleine durch den Einsatz eines weiteren Satellitensystems (Galileo) die Genauigkeit um etwa 10 Prozent verbessert wird. Ein dreimal dichteres Messnetz würde demgegenüber eine Verbesserung von zehn bis zwanzig Prozent bringen.

Die Arbeiten reihen sich ein in die GNSS Meteorologie Aktivitäten des Institutes für Geodäsie und Photogrammmetrie der ETH Zürich und der Schweizerischen Geodätischen Kommission (SGK). Wir danken dem Verfasser, Herrn Dr. Perler, für den wertvollen Beitrag zur Geodäsie. Der MeteoSchweiz danken wir für die aktive Unterstützung, insbesondere wären derartige Studien nicht möglich ohne deren qualitativ hochwertigen meteorologischen Daten. Ebenso danken wir dem Bundesamt für Umwelt (BAFU, UTF 186.16.06, « GANUWE ») für die Projektfinanzierung. Der SCNAT danken wir für die Übernahme der Druckkosten.

Prof. Dr. M. Rothacher
Institut für Geodäsie und Photogrammetrie
ETH Zürich

Prof. Dr. A. Geiger
ETH Zürich
Präsident der SGK

PREFACE

Durant cette dernière décennie, les sciences géodésiques n'ont cessé de gagner de l'importance dans la recherche sur l'atmosphère. L'installation dense de stations GNSS permanentes donne la possibilité d'envisager la détermination de la distribution spatio-temporelle de la vapeur d'eau dans l'atmosphère, par tomographie, grâce à l'observation des signaux GNSS. Cependant, la réalisation pratique d'un système de tomographie GNSS nécessite des développements tant théoriques que méthodologiques. Afin de pouvoir obtenir des résultats tangibles, il est indispensable de pouvoir marier de solides connaissances en météorologie avec des compétences en mathématiques et en informatique.

La méthode de tomographie a été principalement améliorée grâce à, d'une part, la modélisation de la variabilité spatiale de la réfraction à l'intérieur d'une cellule de discrétisation, et d'autre part, grâce à la prise en compte de la variation temporelle de la vapeur d'eau, intégrée dans un filtre de Kalman. Ceci permet d'envisager des calculs en temps-réel ainsi qu'une intégration dans les nouvelles générations de processus d'assimilation. La validation des nouveaux algorithmes a été réalisée avec succès, à l'aide de données réelles et simulées.

Un des atouts majeurs du nouveau logiciel est de pouvoir faire des simulations de tout le processus, depuis les mesures jusqu'aux résultats. Celles-ci permettent de tester différentes méthodes ainsi que de réaliser des analyses a priori de diverses configurations de réseaux dont les observations sont issues de constellations satellitaires multiples. Ces recherches ont pu démontrer que l'introduction du système de navigation Galileo va augmenter la précision du système d'environ dix pour cent. De plus, un réseau de récepteurs trois fois plus dense pourrait améliorer la précision de dix à vingt pour cent.

Ces travaux s'inscrivent dans le cadre des activités de météorologie GNSS de l'institut de Géodésie et Photogrammétrie de l'ETH Zürich et de la Commission Géodésique Suisse (CGS). Nous remercions son auteur, Monsieur Dr. Perler , pour sa contribution de très haute qualité à la géodésie. Nous remercions également MétéoSuisse pour son soutien actif, et la mise à disposition de leurs données météorologiques de très hautes qualités sans lesquelles de telles études ne seraient pas envisageables. Au même titre, nous remercions l'office fédéral de l'environnement (OFEV, UTF 186.16.06, « GANUWE ») pour le financement de ce projet.

La Commission Géodésique Suisse (CGS) est reconnaissante envers l'Académie Suisse des Sciences Naturelles (SCNAT) pour avoir pris à sa charge les coûts d'impression du présent manuscrit.

Prof. Dr. M. Rothacher
Institut de Géodésie et Photogrammétrie
ETH Zürich

Prof. Dr. A. Geiger
ETH Zürich
Président de la CGS

FOREWORD

During the last decade, the importance of geodetic sciences in atmospheric research has significantly increased. Newly installed, continuously running, and densely distributed GNSS receivers provide observations that enable the application of tomographic approaches for the determination of water vapour concentration in the atmosphere. However, for the practical application of GNSS tomography, theoretical as well as methodological developments are necessary. In order to get a concrete result, it is important that both meteorological knowledge and computational expertise are combined.

The tomographic methodology has been further improved, on the one hand by modelling the spatially varying refraction inside each digitalisation cell, on the other hand by considering the temporal variation of water vapour concentration using Kálmán filters. This allows real-time calculations that can be integrated in the latest assimilation processes. The new algorithms have been validated with simulations made on the basis of real data.

Its option to entirely simulate observations and results is a major strength of the newly developed software. With this, methods can easily be tested, and a-priori studies for different network configurations and satellite constellations can be carried out. Such studies have shown that an additional satellite system, Galileo, can improve the accuracy by ten percent. A densification of the observation network by a factor of three would improve the tomography up to twenty percent.

The presented work is part of a series of activities in GNSS meteorology at the Institute of Geodesy and Photogrammetry at ETH Zürich and by the Swiss Geodetic Commission. Thanks go to the author, Dr Donat Perler, for his valuable contribution to geodesy and meteorology, to Meteo Swiss for their active support, particularly for their high-quality meteorological data, to the Federal Office for the Environment (FOEN, UTF 186.16.06, « GANUWE ») for funding the project, and the Swiss Academy of Sciences for covering the printing costs of this volume.

Prof. Dr. M. Rothacher
Institute of Geodesy and Photogrammetry
ETH Zurich

Prof. Dr. A. Geiger
ETH Zurich
President of SGC

Abstract

Water vapor plays an important role in the atmosphere. It is involved in many atmospheric processes and is a major contributor to the atmospheric energy budget and as such is a key quantity in numerical weather prediction (NWP) models. In recent years, NWP models gain in importance in hazard mitigation. But to provide precise quantitative forecasts, especially with respect to precipitation, we need accurate knowledge of the water vapor distribution in the atmosphere. Ground-based Global Navigation Satellite System (GNSS) tomography is a technique which can provide highly resolved and accurate water vapor profiles in space and time.

The main objective of this thesis is to develop new tomographic algorithms which fulfill the requirements to assimilate refractivity measurements derived from GNSS into NWP models. A new tomography software called AWATOS 2 has been implemented. It is an assimilation system for point and integrated refractivity measurements. The tomographic model in AWATOS 2 is formulated as a Kalman filter and different voxel parameterizations are provided. The new trilinear and spline-based parameterizations allow a more accurate representation of the refractivity field without considerably increasing the number of unknowns. Advantages of these new parameterizations are a) more accurate results, b) point observations need not to be interpolated to the voxel centers and c) the tomographic solutions are at least C^0-continuous in space. The stochastic prediction model implemented in AWATOS 2 relies on in-situ measurements and NWP model data. The prediction model is evaluated and adjusted with respect to data from the high-resolution NWP model COSMO-2 and from balloon soundings in Europe. In addition, AWATOS 2 provides a sophisticated simulation framework to carry out synthetic tests based on simple refractivity fields and on NWP model data.

The algorithms of AWATOS 2 are assessed with synthetic tests and with real data in a long-term study using one year of data. The synthetic tests have confirmed the theoretical properties of the model such as a bias-free solution in case of bias-free input data, fast convergence rates, and the capability to resolve vertical structures in the wet refractivity field. In the long-term study, a root-mean-square (RMS) error of 3.0 ppm (0.4 $\mathrm{g\,m^{-3}}$ absolute humidity) is achieved with respect to the NWP model COSMO-7. The investigations have shown that the newly introduced voxel parameterizations lead to significantly more accurate results than the classical constant parameterization. The improvements are about 15% with respect to balloon soundings and 5% with respect to NWP analysis data. The performance of the trilinear and spline-based parameterizations are similar.

Further investigations have revealed the importance of a bias correction model. A newly developed bias correction model has decreased the RMS error with respect to the NWP model analysis from 4.9 ppm (0.7 $\mathrm{g\,m^{-3}}$) to 3.0 ppm (0.4 $\mathrm{g\,m^{-3}}$) using the spline parameterization. For the other parameterizations, the improvements are significantly smaller. The systematic differences corrected here are mainly caused by a) systematic differences between GPS tropospheric path delays and the NWP model data and b) by discretization errors. Another error source is related to the departure of the NWP model's topography from the true one which can amount to several hundred meters in alpine areas. Investigations have shown that processes near the Earth's surface have a strong impact on the wet refractivity. Therefore, differences between the true topography and that of the NWP model can cause substantial errors. This topic has to be addressed if GNSS observations are assimilated into NWP models in complex terrain.

Considerable progress has been made in the field of low-cost GNSS receivers in recent years

allowing to build dense networks at low costs. Furthermore, the existing GNSSs are improved and new ones are being launched. These developments offer new possibilities in GNSS tomography. With error analyses, the potential of such improvements for GNSS tomography have been investigated. The use of GPS together with Galileo has the potential to improve the formal accuracy of the GNSS tomography by 10-15% compared to a GPS-only solution. In Switzerland, equipping the SwissMetNet with GNSS receivers would increase the number of GNSS stations from 31 to 91. This would improve the formal accuracy of the tomographic solution by about 20-25%. The investigations have shown that the improvements obtained by a more dense network and additional GNSSs are cumulative. Placing the stations on different altitudes and choosing locations with good satellite visibility are important to achieve accurate results and should be considered in the design of GNSS networks.

All investigations have demonstrated that accurate 4D distributions of the wet refractivity in the troposphere can be estimated with GNSS tomography. The work has also revealed the possibilities and limitations of GNSS tomography in view of the assimilation into NWP models and proposes solution strategies to overcome the limitations.

Zusammenfassung

Wasserdampf spielt eine wichtige Rolle in der Atmosphäre. Er ist in vielen atmosphärischen Prozessen involviert und beeinflusst stark den Energiehaushalt der Atmosphäre. Als solcher ist er eine der wichtigsten meteorologischen Grössen in den numerischen Wettervorhersagemodellen. In den letzten Jahren wurden Wettermodelle zu einem wichtigen Bestandteil in der Vorhersage und Beurteilung von Unwetter. Um jedoch präzise Vorhersagen über beispielsweise die Niederschlagsmenge machen zu können, bedarf es genauer Kenntnisse über die Verteilung des Wasserdampfes in der Atmosphäre. Wasserdampf-Tomografie mittels globaler Positionierungssysteme (GNSS) ist eine Methode, die zeitlich und räumlich hoch aufgelöste Wasserdampffelder mit hoher Genauigkeit zur Verfügung stellen kann.

Das Hauptziel dieser Arbeit ist die Entwicklung neuer Tomografie-Algorithmen, welche die Anforderungen zur Assimilation von Feuchtrefraktivitäten in numerische Wettermodelle erfüllen. Zu diesem Zweck ist eine neue Tomografie-Software namens AWATOS 2 entwickelt worden. Die Software ist ein System zum Assimilieren von beliebigen Punkt- und Integralmessungen, die auf der Refraktivität basieren. AWATOS 2 basiert auf einem Kalman-Filter und bietet verschiedene Parameterisierungen des Wasserdampffeldes an. Die Parameterisierung mittels trilinearen Funktionen und kubischen Spline Funktionen erlauben eine genauere Wiedergabe des Wasserdampffeldes, ohne die Anzahl der zu schätzenden Parameter wesentlich zu erhöhen. Die Vorteile dieser neuen Parameterisierungen sind a) genauere Resultate, b) Punktmessungen müssen nicht mehr auf das Voxelzentrum interpoliert werden und c) die tomografische Lösung ist in jedem Fall C^0-kontinuierlich im Raum. Das in AWATOS 2 implementierte stochastische Vorhersagemodell basiert auf Erkenntnissen aus in-situ Beobachtungen (Bodenstationen und Ballonsondierungen) und Wettermodell-Daten. AWATOS 2 bietet ausserdem viele Simulationsmöglichkeiten an, um synthetische Tests basierend auf generischen Wasserdampffeldern und Wettermodell-Daten durchzuführen.

Die in AWATOS 2 verwendeten Modelle wurden in synthetischen Tests und in einer Langzeitstudie von einem Jahr Dauer mit realen Daten getestet. Die synthetischen Tests haben die theoretischen Eigenschaften der Modelle bestätigt. Insbesondere wurden die Eigenschaften, dass die Tomografie-Lösung keine systematischen Fehler aufweist, insofern auch die Messungen keine aufweisen, bestätigt, wie auch die schnelle Konvergenzrate und das Auflösungsvermögen von vertikalen Strukturen im Refraktivitätsfeld. In der Langzeitstudie wurde eine Genauigkeit (mittlere quadratische Abweichung) von 3.0 ppm (0.4 $\mathrm{g\,m^{-3}}$ absolute Feuchte) bezüglich des Wettermodells COSMO-7 erreicht. Die Untersuchungen haben gezeigt, dass die neuen Parameterisierungen im Vergleich zur Parameterisierung mit konstanten Voxelrefraktivitäten zu signifikant genaueren Resultaten führen. Die Verbesserungen betragen 15% im Vergleich mit Ballonsondierungen und 5% im Vergleich mit Wettermodelldaten. Zwischen den Genauigkeiten, die mit den beiden neuen Parameterisierungen erreicht werden, gibt es kaum Unterschiede.

Weitergehende Untersuchen haben die Bedeutung eines Modells für die Korrektur von systematischen Fehler deutlich gemacht. Ein in dieser Arbeit entwickeltes Modell verkleinert den Fehler (mittlere quadratische Abweichung) der Tomografie gegenüber dem Wettermodell von 4.9 ppm (0.7 $\mathrm{g\,m^{-3}}$) auf 3.0 ppm (0.4 $\mathrm{g\,m^{-3}}$) bei Verwendung von der auf kubischen Spline basierenden Parameterisierung. Die Verbesserungen bei den anderen Parameterisierungen sind signifikant kleiner. Die systematischen Differenzen beruhen vorwiegend a) auf systematischen Differenzen zwischen dem numerischen Wettermodell und den troposphärischen Weglängenverzögerungen aus GPS Messungen und b) auf Diskretisierungsfehler. Eine andere Fehlerquelle ist die Abweichung der Mo-

dellorographie des Wettermodells von der realen Topographie. Diese Abweichung kann in alpinen Regionen bis zu mehreren hundert Meter betragen. Untersuchungen haben gezeigt, dass Prozesse in der Nähe der Erdoberfläche grossen Einfluss auf die Feuchtrefraktivität haben. Dadurch können sich grosse Unterschiede zwischen Wettermodell und Tomographielösung an Stellen im Feuchtrefraktivitätsfeld ergeben, wo sich die Topografie des Wettermodells stark von der Wirklichkeit unterscheidet. Diese Erkenntnis sollte bei der Assimilation von GNSS Daten in numerische Wettermodelle in Gebieten mit komplexer Topografie beachtet werden.

Beachtenswerte Fortschritte wurden im Bereich von günstigen GNSS-Empfängern in den letzten Jahren gemacht. Diese erlauben mit geringen Kosten dichte Empfängernetze aufzubauen. Andererseits wurden existierende globale Positionierungssysteme technisch verbessert und neue sind im Aufbau. Diese Entwicklungen eröffnen neue Möglichkeiten für die Wasserdampf-Tomografie. Mittels Fehleranalysen wurde das Potential dieser Entwicklungen für die Wasserdampf-Tomografie abgeschätzt. Die formale Genauigkeit der Tomografie kann durch die Verwendung von Galileo als zusätzliches Satellitensystem zu GPS um 10-15% verbessert werden. Würde man das SwissMetNet mit GNSS-Empfänger ausrüsten, würde dies die Anzahl der Stationen in der Schweiz von 31 auf 91 erhöhen und die formale Genauigkeit der Tomografie um 20-25% verbessern. Die Untersuchungen haben auch gezeigt, dass die Genauigkeitsgewinne durch zusätzliche Satellitensysteme und dichtere Netze kumulativ sind. Zudem hat sich gezeigt, dass die Platzierung der Empfänger an Orten, die gut über die Höhe verteilt sind und die eine gute Sichtbarkeit der Satelliten aufweisen, wichtig ist, um genaue Ergebnisse mit der Wasserdampf-Tomografie erzielen zu können. Dies sollte beim Planen neuer Netze beachtet werden.

Alle Untersuchungen haben gezeigt, dass genaue vierdimensionale Verteilungen der Feuchtrefraktivität in der Troposphäre mittels Wasserdampf-Tomografie geschätzt werden können. Die Arbeit hat auch die Möglichkeiten und Grenzen der Wasserdampf-Tomografie in Hinblick auf die Assimilation der Feuchtrefraktivität in numerische Wettermodelle aufgezeigt. Zudem wurden Lösungsstrategien vorgeschlagen, wie die Limitierungen überwunden werden können.

Acknowledgments

I would like to thank Dr. Daniel Leuenberger and the Swiss Federal Office of Meteorology and Climatology for providing meteorological data, and Dr. Elmar Brockmann (Swiss Federal Office of Topography) for providing and processing the GPS data. I appreciate Dr. Marc Troller's introduction into GNSS tomography, Fabian Hurter for the interesting and fruitful discussions and the proofreading of this manuscript, Dr. Dominique Ruffieux (co-examiner) and Prof. M. Rothacher (co-examiner) for the helpful and valuable comments and reviews, and Prof. A. Geiger (doctoral adviser) for the insightful discussions. Tanks to the co-workers at the Geodesy and Geodynamics Lab at ETH Zurich for the good time I spent with you and a big thank you to my girlfriend Andrea Beck for having been so patient and for the moral support. This work was financially supported by the Swiss Federal Office of Environment (FOEN).

Donat Perler, Zurich, January 2012

Contents

Abbreviations

AGNES	Automatic GNSS Network for Switzerland
ART	Algebraic Reconstruction Technique
AWATOS	Atmospheric Water Vapor Tomography Software
COSMO	Consortium for Small-scale Modeling
DDD	Double Difference Delay
EOF	Empirical Orthogonal Functions
GNSS	Global Navigation Satellite System
GPS	Global Positioning System (United States)
IGS	International GNSS Service
LIDAR	Light Detection and Ranging
LSQ	Least Squares
NWP	Numerical Weather Prediction
NCAR	National Center for Atmospheric Research
NCEP	National Center for Environmental Prediction
PCA	Principle Component Analysis
PPP	Precise Point Positioning
SPD	Slant Path Delay
SMN	SwissMetNet
ZPD	Zenith Path Delay

List of Symbols

x, y, z	Cartesian coordinates
ϕ, λ, h	Latitude, longitude, height
ϑ	Zenith angle
R	Radius
$\Delta\varrho$	Total path delay
$\Delta\varrho_{\text{tot}}$	Total tropospheric path delay
$\Delta\varrho_{\text{dry}}$	Dry tropospheric path delay
$\Delta\varrho_{\text{wet}}$	Wet tropospheric path delay
N	(Wet) refractivity
P	Pressure
P_{dry}	Partial pressure of dry air
P_{wet}	Partial water vapor pressure
P^*_{wet}	Saturated water vapor pressure
γ	Lapse rate
RH	Relative humidity
T	Temperature
R_L	Gas constant for dry air
μ	Expected value
σ^2	Variance
ω	Angular velocity
f, λ, τ	Frequency, wavelength, and period
π	≈3.14150
θ	Phase shift
t	Time
X_t	Stochastic process
W_t	Brownian motion

$\mathbf{x}$	State vector
$\mathbf{P}$	Covariance matrix of the state vector
$\mathbf{A}, \mathbf{H}$	Design/observation matrix
$\mathbf{F}$	Propagation matrix
$\mathbf{C}$	Covariance matrix

Chapter 1

Introduction

1.1 Significance of tropospheric water vapor measurements

Water vapor is involved in many processes in the atmosphere. It is a potent greenhouse gas and an important chemical reactant. In addition, water vapor is one of the most important terms in the atmospheric energy budget as a considerable amount of latent heat is released and absorbed during the condensation and evaporation processes. These make water vapor a key quantity in the modeling of the atmosphere (Jacobson 2005). To validate and to initialize such models, appropriate observations of water vapor in the atmosphere are needed (Jacob et al. 2007; Buzzi 2008; Clark 2009). Global Navigation Satellite System tomography is a promising technique to provide such 4D distributions of water vapor in the troposphere. Better Numerical Weather Prediction (NWP) forecasts would also be of economic value and for hazard mitigation.

Several studies have been carried out to investigate the economical value of meteorological services including NWP. They have revealed that a cost/benefit ratio of about 1:5 is achieved in industrialized countries considering national meteorological services (Anaman et al. 1995; Lazo and Chestnut 2002; Leiviäkangas et al. 2008). For instance, the costs for meteorological operations and research in the U.S. in 2007 was about 5.1 billion U.S. dollars in total and the estimated economical value 31.5 billion U.S. dollars (Lazo et al. 2009). The sectors of economy which benefit from these services are mainly agriculture, construction, the energy sector, insurance, telecommunication, transport, logistics and water availability (Frei 2010).

Urban growth and the advancing settlement of rural areas increase the vulnerability to natural hazards (Clark 2002). It is therefore of utmost interest to better understand the impact of global climate change on natural hazards and to improve hazard mitigation (Pilon 2005). Recent studies have been carried out to investigate the extent and the occurrence of natural hazards such as floods and landslides with highly resolved climate simulations (see for example Dankers et al. 2009). Rockel and Woth 2007 expect an increase of up to 20% in the frequency of extreme wind events for the period 2071-2100 compared to 1961-1990. For Switzerland, a study carried out by Ecoplan/Sigmaplan in 2007 revealed that the expected average economic damage due to climate change will rise to 1 billion Swiss francs per year for the period 2005-2100. As a result of this, several warning systems based on NWP models have been implemented for natural hazard mitigation in recent years (e.g. Zappa et al. 2008 and Falconer et al. 2009). GNSS tomography can help to improve the reliability of such warning systems by providing accurate information about the 4D distribution of the water vapor in the troposphere.

1.2 A short review of the research in GNSS tomography

GNSS tomography is a technique providing water vapor content with high spatial and temporal resolution. Most tomography software packages operate on the basis of slant path delays. These delays are usually estimated with Precise Point Positioning (PPP) (Flores et al. 2000; Hirahara

2000). The wet refractivity field is then computed using a *Kalman filter*. LSQ estimation was used by Champollion et al. 2005. Instead of PPP, they process the raw GPS data in double difference mode and reconstruct the slant path delays by mapping the zenith path delays. Nilsson and Gradinarsky 2005 estimate the wet refractivity field directly from GPS data. They also use the Kalman filter approach. Another algorithm to reconstruct the wet refractivity field is the *Algebraic Reconstruction Technique* (ART), which is successfully applied by Bender et al. 2011. A more complete review of the research in the field of water vapor tomography can be found in Lutz 2009 and Perler et al. 2010.

The Least Squares (LSQ) approach to estimate the 3D wet refractivity field based on tropospheric double difference delays is used in the tomography software AWATOS. The software has been successfully applied to several campaigns (Kruse 2001; Troller et al. 2002; Troller 2004; Troller et al. 2005; Troller et al. 2006). In the scope of this thesis, AWATOS was rewritten and extended. The increased performance allowed the error analyses presented in Chapter 7. The new version of AWATOS supports tropospheric gradients and enhanced statistical models (see Section 3). The software was used in the investigations presented in Lutz 2009 and Lutz et al. 2010. In the following, the main results of the campaigns carried out with AWATOS are summarized (Perler et al. 2010):

- Troller 2004 and Troller et al. 2006 conclude that additional observations and appropriate constraints are necessary to strengthen the tomographic equation system. As additional observations, they introduce a priori information derived from several sources such as ground-based meteorological sensors, balloon soundings and NWP models. In their papers, they also investigate the use of intervoxel constraints and state that the constraints can be problematic in cases where they smooth out rapid refractivity changes and inversions.

- The campaign described in Lutz 2009 was used to investigate questions concerning high-resolution tomography in the context of hazard mitigation. The campaign took place in the Swiss Alps and included 30 GPS receivers covering an area of 50 km by 50 km. The campaign comprised two parts (July 2005 and October 2005). Each part had a duration of 2 weeks. The investigations revealed that better results are obtainted with highly resolved grids. He proposed a horizontal resolution similar to the mean inter-station distance (3 km) and 43 layers. Comparisons with balloon soundings showed a good agreement of 7.1 ppm RMS in July and 3.0 ppm RMS in October.

- Near real-time processing is considered in the work published in Lutz 2009. To process Global Navigation Satellite System (GNSS) phase observations, highly accurate satellite orbits are needed. Such orbit data are provided by the *International GNSS Service* (IGS) (Dow et al. 2009). Several data products with different accuracies and latencies are offered. Lutz 2009 has investigated these products in view of their usability for near real-time tomography. He showed that *ultra-rapid orbits* fulfill the trade off between accuracy and availability best.

- Investigations of high-resolution tomography in mountainous regions have shown that better results can be achieved by refining the vertical discretization (Lutz 2009). However, higher resolution increases the computational costs and the influence of intervoxel constraints on the results. The latter may introduce unintentional artifacts.

Based on these results, the tomography software AWATOS 2 has been developed within this thesis. AWATOS 2 is a completely new software and has the ability to assimilate any kind of refractivity measurement formulated as point or integral observation. It introduces two new voxel parameterizations and uses the Kalman filter approach. The parameterization of voxels is a technique that reduces the effects of discretization and negligibly increases the computational costs. Moreover, the interpolation of in-situ measurements to voxel central points becomes obsolete with parameterization (Perler et al. 2011). AWATOS 2 provides, in addition, sophisticated simulation capabilities of point and integral observations. All the investigations presented in Chapters 8 and 9 are based on AWATOS 2.

1.3 Objectives and structure of the thesis

This thesis investigates ground-based GNSS tomography and its results in view of the assimilation into NWP models. The investigations focus on the determination and the modeling of the 4D distribution of wet refractivity in the troposphere. The main objectives are

- to develop an assimilation system for refractivity observations. Integral and point measurements have to be supported. In particular, the system should incorporate different observations from GNSSs such as double difference delays and zenith path delays.
- to implement a simulation toolbox for investigating properties of the models implemented in the tomography software. This toolbox should help answering questions about the tomographic capability to resolve vertical structures in the troposphere. In addition, the impact of technical improvements such as a denser receiver network and new GNSSs on the accuracy of the tomographic solution shall be investigated.
- to determine the statistical properties of the wet refractivity field. Based on these investigations, a prediction model for a tomographic assimilation software shall be developed and its parameter settings specified.
- to evaluate the assimilation software within a long-term study using real data. The tomographic solutions shall be validated with independent observations such as balloon soundings and a NWP model.

In Chapter 2, the governing equations and models for GNSS processing are described and the relationship between path delay, refractivity and meteorological quantities are explained. They show how GNSS raw observations are related to the water vapor content in the atmosphere. Chapter 3 introduces the GNSS tomography and describes the algorithms and models implemented in AWATOS 2. The simulation capabilities of AWATOS 2 are also specified in this chapter. In addition, software packages used for preprocessing GNSS and meteorological data are shortly introduced.

Chapter 4 describes data sets and their availability. Based on these data sets, statistical investigations of the wet refractivity distribution in the troposphere are performed in Chapter 5. The results of these investigations are used to develop appropriate tomographic models and to specify the model parameters. Moreover, the discretization error is quantified for the grid resolution used in the tomographic reconstruction. This shows the accuracy which can theoretically be achieved with the given grid resolution and voxel parameterization.

In Chapter 6, balloon sounding data used for evaluating the tomographic solutions are compared to GNSS-based tropospheric delays which serve as input data into the tomographic processing. The findings of this chapter will help to interpret the results obtained by GNSS tomography.

In Chapter 7, the impact of technical improvements, such as additional GNSSs and denser receiver networks, on the accuracy of the tomographic solution is investigated. Furthermore, the problem of network design is discussed, in particular the essential properties for the selection of the receiver locations.

The results of synthetic tests investigating the resolvability and convergence properties of AWATOS 2 are presented in Chapter 8. The investigations allow to specify how and how quickly the tomographic algorithms react to changes of the wet refractivity distribution in the troposphere. These results will have an impact on how the tomographic results could be assimilated in NWP models. Furthermore, the investigations of the resolvability will illustrate how accurate the tomographic algorithms can reconstruct spatial perturbations in the wet refractivity field and which kind of measurements complements ground-based GNSS observations best.

In Chapter 9, the evaluation of a long-term study using GPS double difference data of more than one year is described and discussed. The accuracy of the different voxel parameterizations with respect to balloon soundings and NWP analyses is quantified. Regional and seasonal differences are investigated as well as the accuracy at different height levels. The impact of the topography, artifacts of the NWP model and measurement issues of balloon soundings on the accuracy is

discussed and, the implication of that, the need for a bias correction model. Such a model is introduced and validated in this chapter.

Concluding remarks and an outlook for further research are given in Chapters 10 and 11.

Chapter 2

Introduction to the propagation of radio waves in the atmosphere

GNSS observations are influenced by the composition and the physical conditions of the atmosphere. This relationship enables to extract information on meteorological quantities from GNSS observations. In this chapter, this relationship is explained. The governing equations and tropospheric models used in GNSS processing are given. This chapter provides the theoretical basis for algorithms used in GNSS tomography.

2.1 Propagation of radio waves in the atmosphere

GNSS satellites transmit signals on carrier frequencies in the L band (1-2 GHz). The atmosphere considerably influences propagation of radio waves within this frequency range on the way from the emitting satellite to the receiver located on the Earth's surface. The propagation velocity of the waves is, thereby, affected by the propagation medium (Leick 1989). In vacuum, the speed is equal to the speed of light c (Melbourne et al. 1983)

$$c \;=\; 2.99792458 \cdot 10^8 \mathrm{ms}^{-1} \tag{2.1}$$

The propagation velocity in other media may be different and can be characterized by the refractive index

$$n \;=\; \frac{c}{v} \tag{2.2}$$

with the propagation velocity v within a certain material or medium.

Positioning with GNSS is based on light travel times. The light travel time Δt is the time differences between signal emission t_r and reception t_p. It is also related to the refractive index

$$\Delta t \;=\; t_p \;-\; t_r \;=\; \int_{t_r}^{t_p} \mathrm{d}t \;=\; \int_S \frac{1}{\mathrm{v}(s)}\,\mathrm{d}s \;=\; \frac{1}{c}\int_S \mathrm{n}(s)\,\mathrm{d}s \tag{2.3}$$

with the ray path S. In the processing of GNSS signals, these time differences are mapped to Euclidean distances (geometrical path). The difference between the effective light travel time and the light travel time without atmosphere is called *path delay* and is denoted by $\Delta\varrho$.

$$\Delta\varrho \;=\; \int_S \mathrm{n}(s)\,\mathrm{d}s \;-\; \int_{S_0} \mathrm{d}s \tag{2.4}$$

$$= \int_S \Big(\mathrm{n}(s) \;-\; 1\Big)\,\mathrm{d}s \;+\; \underbrace{\int_S \mathrm{d}s \;-\; \int_{S_0} \mathrm{d}s}_{\text{refraction}} \tag{2.5}$$

with the geometric path S_0.

The path delay $\Delta\varrho$ can be further split into a direct effect caused by the slower propagation of the ray and geometric path elongation due to ray bending. In the troposphere, largest bending effect are observed at low elevation angles. Bending effects are usually neglected for elevations above 10° (Mendes 1999). Thus, Equation 2.5 can be simplified to

$$\Delta\varrho \;=\; \int_S \Big(\mathrm{n}(s) \,-\, 1\Big)\,\mathrm{d}s \;=\; 10^{-6} \int_S \mathrm{N}(s)\,\mathrm{d}s \tag{2.6}$$

where the refractivity N is defined as

$$N = 10^6\,(n \,-\, 1). \tag{2.7}$$

In the ionosphere, microwaves are dispersively propagated. Dispersion means that signals with different frequencies are propagated at different velocities. This fact can be used to widely eliminate the ionospheric effects by combining several frequencies. GNSS satellites, therefore, transmit on two or more frequencies.

Contrary, the troposphere is non-dispersive for radio waves and the propagation velocity only depends on the composition of the medium (Seeber 2003). Refractivity is determined by meteorological quantities. This relationship is described by an empirical formula developed by Essen and Froome 1951. In the last decades, several authors improved the parameters of this formula (Smith and Weintraub 1953; Tatarskii 1971; Thayer 1974; Hill et al. 1982; Hartmann and Leitinger 1984; Bevis et al. 1994; Rüeger 2002). In this thesis, the parameters of the best-average formula proposed by Rüeger 2002 is used:

$$N \;=\; \underbrace{k_1 \frac{P_{\mathrm{dry}}}{T}}_{N_{\mathrm{dry}}} + \underbrace{k_2 \frac{P_{\mathrm{wet}}}{T} \;+\; k_3 \frac{P_{\mathrm{wet}}}{T^2}}_{N_{\mathrm{wet}}} \tag{2.8}$$

with

$$\begin{aligned} k_1 &= 77.6890\,\mathrm{K\,hPa^{-1}} \\ k_2 &= 71.2952\,\mathrm{K\,hPa^{-1}} \\ k_3 &= 375463\,\mathrm{K^2\,hPa^{-1}} \end{aligned}$$

where $P_{\mathrm{dry}} = (P_{\mathrm{tot}} - P_{\mathrm{wet}})$ is the partial dry air pressure in [hPa], P_{wet} the partial water vapor pressure in [hPa], and T the temperature in [K]. The single terms of Equation 2.8 reflect the composition of the atmosphere. The first term is associated with dry air and the remaining two with water vapor. This subdivision is made for the tropospheric path delay $\Delta\varrho_{\mathrm{tot}}$, too.

$$\Delta\varrho_{\mathrm{tot}} \;=\; \underbrace{10^{-6} \int_S \mathrm{N}_{\mathrm{dry}}(s)\,\mathrm{d}s}_{\text{dry part}} \;+\; \underbrace{10^{-6} \int_S \mathrm{N}_{\mathrm{wet}}(s)\,\mathrm{d}s}_{\text{wet part}} \tag{2.9}$$

2.2 Modeling the path delay

2.2.1 Mapping functions

Path delays are often referred to as *slant path delay* (SPD). For comparing and modeling purposes, slant path delays are mapped to the direction of the zenith (see Fig 2.1). Such a delay is called *zenith path delay* (ZPD) $\Delta\varrho_{\mathrm{tot},0}$.

$$\Delta\varrho_{\mathrm{tot}} \;=\; \mathrm{m}(\vartheta)\,\Delta\varrho_{\mathrm{tot},0} \tag{2.10}$$

where $\mathrm{m}(\vartheta)$ is the mapping function depending on zenith angle ϑ. A simple mapping function is

$$\mathrm{m}(\vartheta) \;=\; \frac{1}{\cos(\vartheta)} \tag{2.11}$$

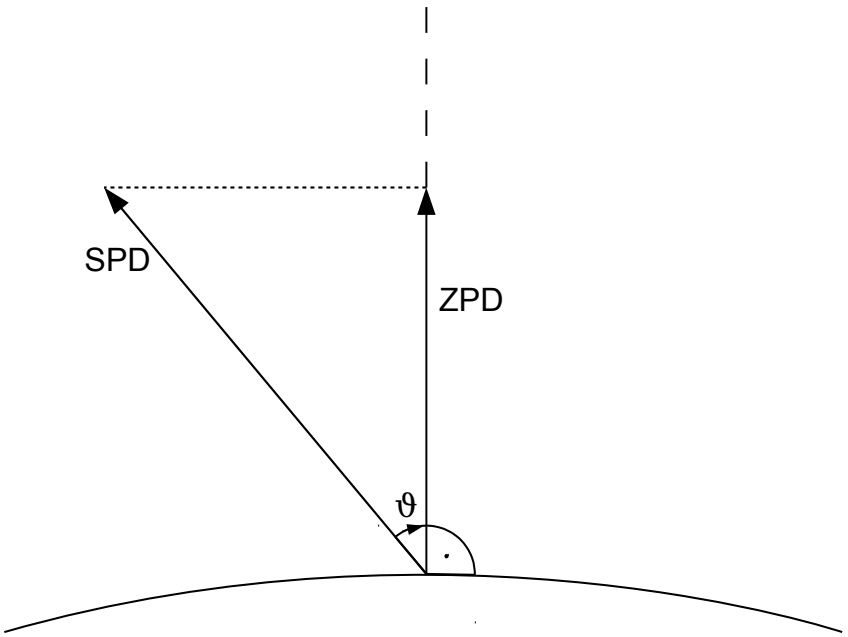

Figure 2.1: Mapping of a *slant path delay* (SPD) onto the zenith. The resulting vector is called *zenith path delay* (ZPD). The angle between the slant path vector and the zenith path vector is denoted by the zenith angle ϑ.

More sophisticated mapping functions take the curvature of the Earth's surface and atmospheric layering into account. Due to the different vertical distribution of the components of the atmosphere, separate functions for dry air and water vapor are introduced. In this thesis, Niell's mapping functions are used (Niell 1996). The mapping functions depend on the zenith angle ϑ, latitude ϕ, height h of the site above sea level, and time t. The function is for both parts

$$\mathrm{m}(\vartheta,\phi,h,t) \;=\; \frac{1+\frac{a}{1+\frac{b}{1+c}}}{\cos(\vartheta)+\frac{a}{\cos(\vartheta)+\frac{b}{\cos(\vartheta)+c}}} + h\,\Delta\mathrm{m}(\vartheta). \tag{2.12}$$

However, they differ in the parameters a, b, c and $\Delta\mathrm{m}(\vartheta)$. For the hydrostatic mapping function, the parameters a, b, and c are determined by the following formula, respectively.

$$\mathrm{a}(\phi,t) \;=\; \mathrm{a}_{\mathrm{avg}}(\phi) \;-\; \mathrm{a}_{\mathrm{amp}}(\phi)\,\cos\left(\frac{2\,\pi}{\tau}\,(t\;-\;t_0)\right) \tag{2.13}$$

$$\begin{aligned} \mathrm{a}_{\mathrm{avg}}(\phi): &\quad \text{linearly interpolated from tabulated values}\\ \mathrm{a}_{\mathrm{amp}}(\phi): &\quad \text{linearly interpolated from tabulated values}\\ t_0: &\quad \text{phase shift of 28 days}\\ \tau: &\quad \text{period of 365.25 days} \end{aligned}$$

The height correction term for the hydrostatic mapping function is

$$\Delta\mathrm{m}(\vartheta) \;=\; \frac{1}{\cos(\vartheta)} \;-\; \frac{1+\frac{a_{\mathrm{ht}}}{1+\frac{b_{\mathrm{ht}}}{1+c_{\mathrm{ht}}}}}{\cos(\vartheta)+\frac{a}{\cos(\vartheta)+\frac{b}{\cos(\vartheta)+c}}} \tag{2.14}$$

with tabulated values a_{ht}, b_{ht}, and c_{ht}. For the wet mapping function, the parameters a, b, and c are constants and the height correction term $\Delta\mathrm{m}(\vartheta)$ is 0. A comparison with other mapping functions can be found in Ifadis 2000.

2.2.2 Saastamoinen's formula

Often, no meteorological quantities required to compute the refractivity are available along the whole ray path. Therefore, models are developed to estimated the path delay from meteorological quantities on the ground. A widely used model is the one derived by Saastamoinen 1972; Saastamoinen 1973a; Saastamoinen 1973c; Saastamoinen 1973b. The model depends on the pressure P in [hPa], the temperature T in [K], and the partial water vapor pressure P_{wet} in [hPa]. Originally, Saastamoinen has used parameters published by Essen and Froome 1951. In this study, the parameters presented in (Rüeger 2002) are applied to Saastamoinen's formula. This leads to

$$\Delta\varrho_{\text{tot,Saas}} = \frac{k_1}{\cos(\vartheta)} \left(P + \left(\frac{k_2}{T} + k_3 \right) P_{\text{wet}} - B \tan^2(\vartheta) \right) + \delta_R. \tag{2.15}$$

with

$$\begin{aligned} k_1 &= 0.002279\,\text{m}\,\text{hPa}^{-1} \\ k_2 &= 1153\,\text{K} \\ k_3 &= 0.074 \end{aligned}$$

The term $B \tan^2(\vartheta)$ is a correction term modeling the effects of the curvature of the atmospheric layers. The factor B depends on the station height. Values for different heights are tabulated in Saastamoinen 1972. The term δ_R is a range correction. It depends on the zenith angle and the station height. The values are listed in Hofmann-Wellenhof et al. 2001.

To compute the dry delay, the partial water vapor pressure P_{wet} is usually set to zero in Equation 2.15. According to Troller 2004, this practice results only in partially accurate solutions. He presented another partitioning between dry and wet path delay. In this work, Troller's formula is used but applying the parameters presented in Rüeger 2002.

$$\Delta\varrho_{\text{dry,Saas}} = \frac{k_1}{\cos(\vartheta)} \left(P - k_3' P_{\text{wet}} - B \tan^2(\vartheta) \right) + \delta_R \tag{2.16}$$

$$\Delta\varrho_{\text{wet,Saas}} = \frac{k_1}{\cos(\vartheta)} \left(\frac{k_2}{T} + k_3'' \right) P_{\text{wet}} \tag{2.17}$$

with

$$\begin{aligned} k_1 &= 0.002279\,\text{m}\,\text{hPa}^{-1} \\ k_2 &= 1153\,\text{K} \\ k_3' &= 0.155500 \\ k_3'' &= 0.229425 \end{aligned}$$

Chapter 3

GNSS tomography with the software package AWATOS 2

The 4D distribution of the wet refractivity in the troposphere can be estimated with the tomographic technique from GNSS observations. This chapter introduces the tomographic technique and describes the models and algorithms implemented in AWATOS 2 (Atmospheric Water Vapor Tomography Software). The chapter also includes a description of the simulation capabilities of AWATOS 2. The tomography software AWATOS 2 uses tropospheric delays which are estimated with the help of software packages not developed within this thesis. The models and functionality of the software is summarized in a separate subsection about the preprocessing of the tropospheric delays.

3.1 Overview of AWATOS 2

AWATOS 2 is a software to estimate the atmospheric refractivity field from different types of measurements for assimilation into numerical weather prediction models. Integral measurements, such as GNSS double difference delays and slant path delays, are supported as well as point measurements. To reconstruct the field, an underdetermined inverse problem has to be solved. The algorithms are optimized to solve such underdetermined problems by using regularization techniques. AWATOS 2 also allows it to simulate integral and point observations from predefined functions and from data fields provided by NWP models.

The software is based on the Kalman filter approach. This allows to compute the time-evolving 3D refractivity field and its covariances. The accuracies of the estimated refractivities can be considered in the assimilation in numerical weather prediction models to control their impact on prognostical variables. Another advantage of the Kalman filter approach is that measurements are successively processed. There is no need to collected the observations and process them in e.g. hourly batches. Thus, solutions considering the newest data are instantly available.

The 3D refractivity field is discretized into volumetric pixels called *voxels*. Due to this discretization, not all details of the refractivity field can be represented anymore. The results are so called *discretization errors*. A possibility to reduce this error is to increase the resolution of the grid. Refining the grid, however, increases the number of unknowns in the reconstruction of that field and, hence, further increases the underdetermination of the inverse problem. In the tomographic reconstruction, this increase in the number of unknowns might be problematic as the regularization of the problem becomes more important and may then cause artificial effects in the reconstructed field. Another way to reduce the discretization error is the use of sophisticated parameterization of the voxels. An appropriate parameterization can reduce the discretization error without increasing the number unknowns. The software provides 3 different voxel parameterizations. Besides the classical parameterization of the voxels representing the refractivity as a constant within the voxel, trilinear and an hybrid parameterization using cubic spline functions in combination with

bilinear parameterization have been implemented. These parameterizations will be explained in more details in Section 3.3.

The software packages AWATOS 2 supports different kinds of measurements and observations. They are grouped in a) integral measurements, b) point measurements, c) pseudo-observations. Figure 3.1 gives an overview of supported observations and the groups, to which they are assigned.

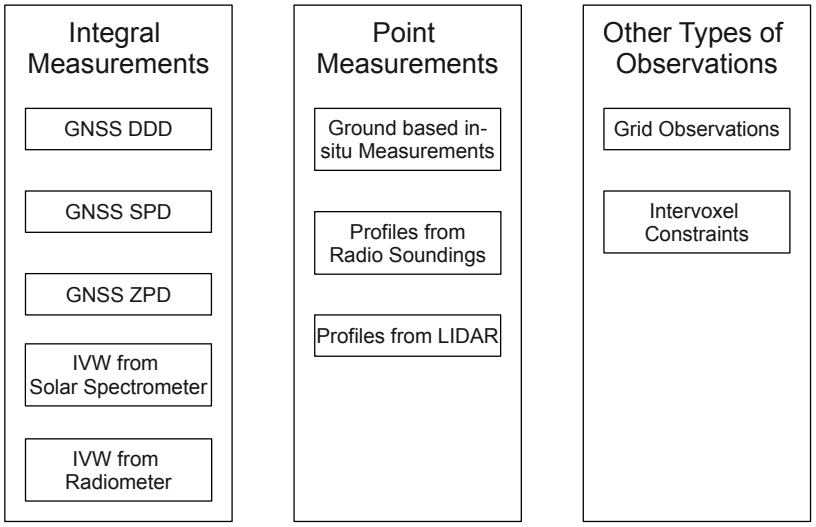

Figure 3.1: Measurement types supported by AWATOS 2.

Integral measurements: The implementation of AWATOS 2 focuses on the support of GNSS tropospheric delays. Zenith path delays (GNSS ZPD), GNSS slant path delays (GNSS SPD), and GNSS double difference delays (GNSS DDD) are supported. Other integral measurements can also be included as long as their path delays are related to the material properties in the same way as the GNSS signals (see Section 2.1).

Point measurements: In-situ wet refractivity observations are usually computed from temperature and from humidity measurements using Equation 2.8. Such observations are often carried out at ground or by radio soundings. In the recent years, optical remote sensing techniques have been developed providing temperature and humidity observations. Such systems are called *Light Detection and Ranging* (LIDAR).

Pseudo-observations: In the tomographic reconstruction, additional observations are usually introduced. Spatial smoothing pseudo-observation referred to as *intervoxel constraints* in literature, are used to stabilize the tomographic reconstruction. Besides these pseudo-observations, boundary values and a priori values are set. The boundary values and the a priori values are subsumed under the umbrella term *grid observations*.

3.2 Preprocessing of GNSS double difference delays

Computing a wet refractivity field from GNSS data is a procedure involving several steps. Figure 3.2 gives an overview of this process. In a first step, the tropospheric zenith path delays and station coordinates are estimated with the GPS processing software Bernese 5.0 (Dach et al. 2007). These two parameters in combination with residuals are used by the tomography software AWATOS 2. If the humidity in the troposphere is of interest, the part of the delay related to dry air has to

be eliminated. The dry delay can accurately be estimated from the partial pressure of dry air at the receiver station using Saastamoinen's model (see Section 2.2.2). For stations, which are not equipped with meteorological sensors providing these measurements, the quantities are interpolated using the collocation software COMEDIE (Eckert et al. 1992a; Eckert et al. 1992b; Geiger and Cocard 1992; Kruse 2001; Troller et al. 2002). Finally, the (wet) delays in combination with the station coordinates, satellite orbits and residuals are used by AWATOS 2 to compute a time-evolving 3D (wet) refractivity field. The details of the GPS raw data processing with Bernese 5.0, the interpolation of the meteorological observations with COMEDIE, the elimination of the dry part, and the construction of double difference delays are described in the subsequent subsections.

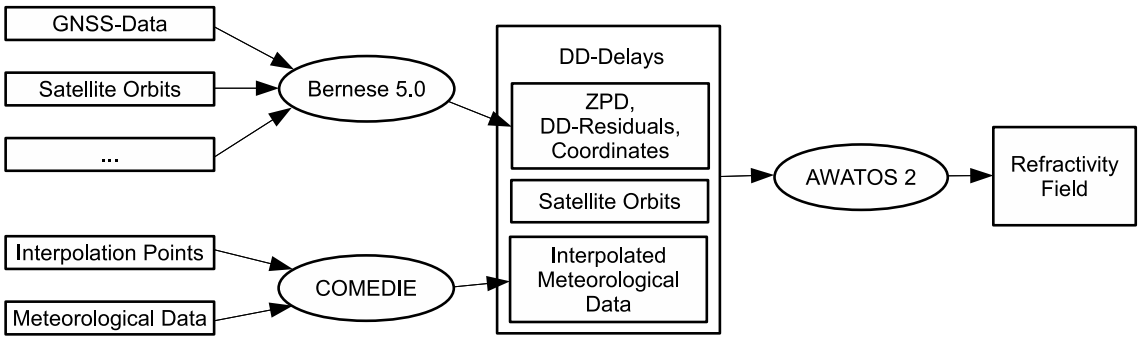

Figure 3.2: Overview of the processing of GNSS data.

3.2.1 GPS data processing with Bernese 5.0

The processing of GPS observations can be done in different ways. The choice of the processing method, thereby, depends on the capabilities of the receivers and on the accuracy requirements. One way is to process the codes modulated on the carrier (code pseudoranges). However, this is a rather inaccurate technique. A more accurate way is to process the phase pseudoranges. The phase pseudorange ψ is a phase measurement of the carrier in cycles.

GNSS satellites emit signals on two or more frequencies. For instance, current GPS satellites send on the two frequencies listed in Table 3.1. The most recent GPS satellite generation provides signals emitted on a third frequency (1176.45 MHz). With this extension, there are as many frequency available on GPS as on Galileo.

Table 3.1: Carrier frequencies used by GPS satellites (Dach et al. 2007).

	Frequency f_i	**Wavelength** λ_i
Carrier 1	1575.42 MHz	19.0 cm
Carrier 2	1227.60 MHz	24.4 cm

A geodetic GPS receiver usually provides phase pseudoranges for both frequencies. The observation equation is as followed (Dach et al. 2007):

$$L^r_{1,p} = \lambda_1 \psi^r_{1,p} = \varrho^r_p + c\,\delta_p - c\,\delta^r - I^r_p + \Delta\varrho^r_{\mathrm{tot},p} + \lambda_1\, n^r_{1,p} \tag{3.1a}$$

$$L^r_{2,p} = \lambda_2 \psi^r_{2,p} = \varrho^r_p + c\,\delta_p - c\,\delta^r - \frac{f_1^2}{f_2^2} I^r_p + \Delta\varrho^r_{\mathrm{tot},p} + \lambda_2\, n^r_{2,p} \tag{3.1b}$$

where

$\psi^r_{F,p}$: Phase measurement in cycles of the signal emitted by satellite r recorded from receiver p at frequency F

ϱ^r_p : Geometrical distance between satellite r and receiver p

δ^r, δ_p : Clock error of satellite r and receiver p, respectively

I^r_p : Ionospheric refraction at frequency f_1 between satellite r and receiver p

$\Delta\varrho^r_{\mathrm{tot},p}$: Tropospheric refraction between satellite r and receiver p

$n^r_{F,p}$: Initial phase ambiguity ($n^r_{F,p} \in \mathbb{N}$)

f_F : Frequency of carrier F

λ_F : Wavelength of carrier F

c : Speed of light in vacuum

In Equation 3.1, the frequency-dependent ionospheric effect is linearly approximated using the property that the effect is roughly proportional to $1/f^2$. With the linear combination

$$L_3 = \frac{1}{f_1^2 - f_2^2}(f_1^2 L_1 - f_2^2 L_2), \tag{3.2}$$

the linear part of the ionospheric effect is eliminated. The satellite and receiver clock errors can be mostly eliminated by building differences. The definition of a double difference is

$$L^{r,s}_{F,p,q} = \left(L^r_{F,p} - L^r_{F,q}\right) - \left(L^s_{F,p} - L^s_{F,q}\right) \tag{3.3}$$

with observations between satellites r and s and receivers p and q.

Combining Equations 3.1-3.2 leads to

$$L_{3,p,q} = \varrho^{r,s}_{k,q} + \Delta\varrho^{r,s}_{\mathrm{tot},k,q} + \frac{1}{f_1^2 - f_2^2}\left(f_1^2\,\lambda_1\, n^{r,s}_{1,p,q} - f_2^2\,\lambda_2\, n^{r,s}_{2,p,q}\right) \tag{3.4}$$

where the double difference notation from Equation 3.3 is used for the symbols $\varrho^{r,s}_{k,q}$, $\Delta\varrho^{r,s}_{k,q}$, $n^{r,s}_{1,p,q}$, and $n^{r,s}_{2,p,q}$.

As the tropospheric effect $\Delta\varrho_{\mathrm{tot}}$ is of major interest in GNSS tomography, a closer look is taken at this parameter. The Bernese GPS processing software offers several approaches to model the tropospheric delay. All provided models split the delay in an a priori and in a correction part:

$$\Delta\varrho^r_{\mathrm{tot},p} = \Delta\varrho^r_{\mathrm{apr},p} + \Delta\varrho^r_{\mathrm{cor},p} \tag{3.5}$$

In this thesis, the dry part of the Saastamoinen model (see Section 2.2.2) is used as a priori model for the zenith path delay. The values for the input parameters of the model are derived from a standard atmosphere (ISO 2533:1975 1975). Contrary to the original mapping function used in the model, Niell's hydrostatic mapping function is applied (see Section 2.2.1).

The correction term in the tropospheric delay (Equation 3.5) is modeled by estimating the tropospheric zenith path delay for each receiver.

$$\Delta\varrho^r_{p,\mathrm{cor}} = \mathrm{m}_{\mathrm{wet}}(\vartheta^r_p)\,\Delta\varrho_{\mathrm{cor},0,p} \tag{3.6}$$

with mapping function m_{wet} presented by Niell (see Section 2.2.1) for the wet path delays, zenith angle ϑ_p^r between receiver p and satellite r and tropospheric zenith path delay $\Delta\varrho_{cor,0,p}$. The Bernese software also provides estimations of tropospheric gradients. Lutz 2009 has shown that gradient estimation has no significant influence on the accuracy of tomographic results. Therefore, no gradients are estimated.

3.2.2 Interpolation of meteorological quantities with COMEDIE

Collocation technique

There are GNSS stations, which are not equipped with any meteorological sensor. For such stations, the meteorological observations are interpolated from measurements in the neighborhood. Such an interpolation technique is the collocation method (Moritz 1973).

The collocation method comprises a deterministic and a stochastic model and subdivides the measurement into a) a deterministic part (f(∘)), b) a stochastic signal part s, and c) a noise part (n).

$$b \;=\; \mathrm{f}(\mathbf{x},\mathbf{y}) \;+\; s \;+\; n \tag{3.7}$$

The deterministic model is usually a function $\mathrm{f}(\mathbf{x},\mathbf{y})$ depending on the location $\mathbf{x}$ of the observation b and on an internal parameter set $\mathbf{y}$. The stochastic model takes the part of the measurement not considered by the deterministic model into account and split it into the signal (colored noise) and the (white) noise part.

The partitioning into signal and noise is done by splitting the covariance matrix of the observations into a correlated (signal) and in an uncorrelated part (white noise). The covariance matrix for the signal part is denoted by $\mathbf{C}_{ss}$ and for the noise part by $\mathbf{C}_{nn}$. The latter is usually a diagonal matrix representing white noise.

The internal parameters $\mathbf{y}$ of the deterministic model are estimated by weighted LSQ from the measurements $\mathbf{b}$. The following expression is minimized:

$$\min_{\mathbf{y}}(\mathbf{b} \;-\; \mathbf{A}\mathbf{y})^T \left(\mathbf{C}_{ss} \;+\; \mathbf{C}_{nn}\right)^{-1} (\mathbf{b} \;-\; \mathbf{A}\mathbf{y}) \tag{3.8}$$

where $\mathbf{A}$ is the design matrix of the deterministic model depending on the positions of the measurements. Thereby, the deterministic model is linearized in the input parameters The residual vector $\mathbf{r} = \mathbf{b} - \mathbf{A}\mathbf{y}$ is then split into a signal $\mathbf{s}$ and a white noise $\mathbf{n}$:

$$\mathbf{s} \;= \mathbf{C}_{ss} \left(\mathbf{C}_{ss} \;+\; \mathbf{C}_{nn}\right)^{-1} \mathbf{r} \tag{3.9a}$$

$$\mathbf{n} \;= \mathbf{C}_{nn} (\mathbf{C}_{ss} \;+\; \mathbf{C}_{nn})^{-1} \mathbf{r} \tag{3.9b}$$

The estimated value b' at some location $\mathbf{x}$ is composed of the contribution of the deterministic part $\mathrm{f}(\mathbf{x},\hat{\mathbf{y}})$ and of the stochastic part s' where $\hat{\mathbf{y}}$ denotes the previously estimated internal parameter set of the deterministic model. A covariance matrix $\mathbf{C}_{s's}$ is used in the stochastic part. The matrix describes the covariances between the signal at the interpolation locations and the observations.

$$b' \;= \mathrm{f}(\mathbf{x},\hat{\mathbf{y}}) \;+\; s' \tag{3.10a}$$

$$s' \;= \mathbf{C}_{s's} (\mathbf{C}_{ss} \;+\; \mathbf{C}_{nn})^{-1} \mathbf{r} \tag{3.10b}$$

COMEDIE

The software package COMEDIE (Collocation of Meteorological Data for Interpolation and Estimation of Tropospheric Path Delays) was developed by Eckert et al. 1992a; Eckert et al. 1992b. The deterministic models were improved by Hirter 1998; Troller 2004. A detailed description of the software can be found in Troller et al. 2002. The software package provides methods for the interpolation of pressure P, temperature T, and partial water vapor pressure P_{wet} in 4 dimensions.

Deterministic models

The deterministic model for the pressure is

$$\mathrm{P}(x,y,z,t) = \Big(P_0 + a_P(x-x_0) + b_P(y-y_0) + c_P(t-t_0)\Big)\ \exp\left(-\frac{z-z_0}{H_P}\right) \tag{3.11}$$

$\mathrm{P}(x,y,z,t)$:	Pressure at location (x,y,z) at time t
x_0, y_0, z_0, t_0 :	Reference coordinates and reference time
P_0 :	Pressure at the reference point (x_0, y_0, z_0)
a_P, b_P, c_P :	Coefficients of the horizontal and temporal gradients
H_P :	Scale height

The reference horizontal coordinates x_0 and y_0 and the reference time t_0 are the mean values of all measurement locations and times. The vertical reference height is set to 0 m. The parameters a_P, b_P, c_P, P_0, and H_P are fitted.

There are two deterministic models for the temperature; one for the troposphere and one for the lower stratosphere. The model for the troposphere assumes a linear change of the temperature with height. Contrary, the model for the lower stratosphere assumes no change of the temperature with height (see Figure 3.3).

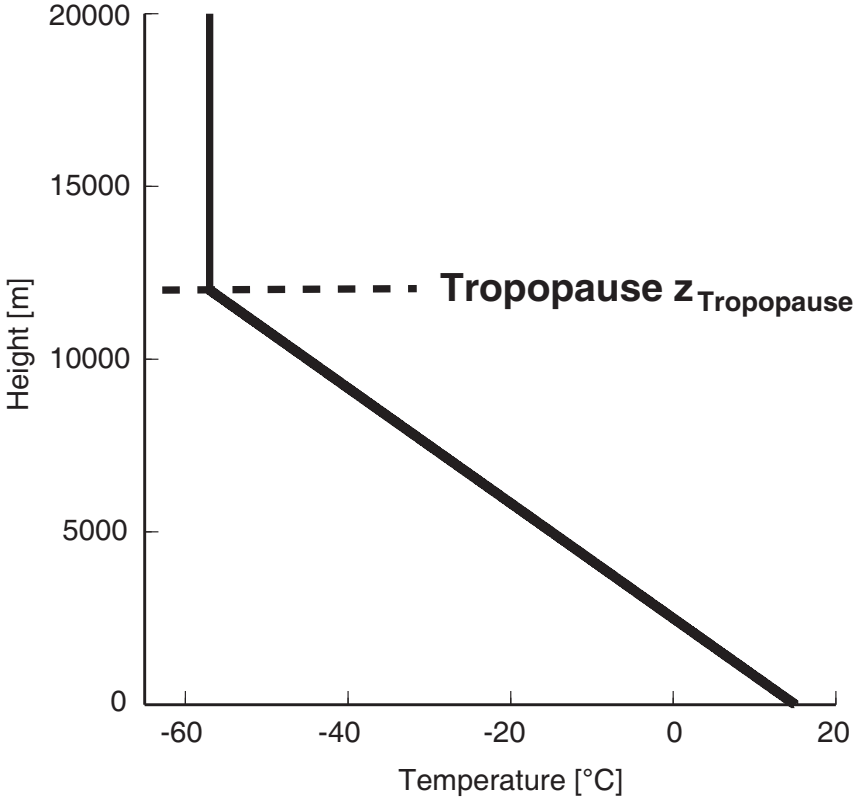

Figure 3.3: Deterministic models of the collocation for the troposphere and for the lower stratosphere. In the model for the troposphere, the temperature decreases linearly with the height. On the other hand, the temperature stays constant with height in the model of the stratosphere. (Source: Troller 2004)

If a sufficient number of measurements is available above the tropopause, the two deterministic

models are combined using a weighting function

$$\mathrm{S}(z - z_{\mathrm{Tropopause}}) \;=\; \frac{1}{\pi}\left(\arctan(z \;-\; z_{\mathrm{Tropopause}})\right) \;+\; 0.5 \tag{3.12}$$

with $z_{\mathrm{Tropopause}} = 11$ km. The combined deterministic model for the temperature is

$$\begin{aligned}\mathrm{T}(x,y,z,t) = a_T(x-x_0) + b_T(y-y_0) + c_T(t-t_0) + \gamma(z-z_0) + \\ (T_0 + \gamma z)\big(1 - \mathrm{S}(z - z_{\mathrm{Tropopause}})\big) + T_1\,\mathrm{S}(z - z_{\mathrm{Tropopause}})\end{aligned} \tag{3.13}$$

$\mathrm{T}(x,y,z,t)$: Temperature at location (x,y,z) at time t
x_0, y_0, z_0, t_0 : Reference coordinates and reference time
T_0 : Temperature at the reference point (x_0, y_0, z_0) at time t_0
T_1 : Temperature in the stratosphere along the vertical profile at (x_0, y_0)
a_T, b_T, c_T : Coefficients of the horizontal and temporal gradients
γ : Temperature laps rate

If there are not enough measurements available in the stratosphere, only the model for the troposphere is fitted.

$$\mathrm{T}(x,y,z,t) = T_0 + a_T(x-x_0) + b_T(y-y_0) + c_T(t-t_0) + \gamma(z-z_0) \tag{3.14}$$

The reference coordinates and the reference time is determined in the same way as in the pressure model. The parameters a_T, b_T, c_T, T_0, T_1, and γ are estimated.

The model for estimating the partial water vapor pressure has the same characteristics as the model for the pressure.

$$\mathrm{P}_{\mathrm{wet}}(x,y,z,t) = \Big(P_{\mathrm{wet},0} + a_{\mathrm{wet}}(x-x_0) + b_{\mathrm{wet}}(y-y_0) + c_{\mathrm{wet}}(t-t_0)\Big)\,\exp\left(-\frac{z-z_0}{H_{\mathrm{wet}}}\right) \tag{3.15}$$

$\mathrm{P}(x,y,z,t)$: Partial water vapor pressure at location (x,y,z) at time t
x_0, y_0, z_0, t_0 : Reference coordinates and reference time
$P_{\mathrm{wet},0}$: Pressure at the reference point (x_0, y_0, z_0) at time t_0
$a_{\mathrm{wet}}, b_{\mathrm{wet}}, c_{\mathrm{wet}}$: Coefficients of the horizontal and temporal gradients
H_{wet} : Scale height

Again, the reference coordinates and the reference time are the same as in the previous models. The fitted parameters are $a_{\mathrm{wet}}, b_{\mathrm{wet}}, c_{\mathrm{wet}}, P_{\mathrm{wet},0}$, and H_{wet}.

Stochastic model

The covariance matrices $\mathbf{C}_{ss}$ and $\mathbf{C}_{s's}$ are determined by a covariance function depending on the spatial and temporal distance between two locations. The covariance function $\Phi_{i,j}$ proposed by Wehrli 1986 and extended by Troller 2004 with a height-dependent damping factor is used in the COMEDIE software package for the three meteorological parameters.

$$\Phi_{i,j} = \frac{\sigma_0^2}{1 + \left(\left(\frac{x_i - x_j}{\Delta x_0}\right)^2 + \left(\frac{y_i - y_j}{\Delta y_0}\right)^2 + \left(\frac{z_i - z_j}{\Delta z_0}\right)^2 + \left(\frac{t_i - t_j}{\Delta t_0}\right)^2\right)\exp\left(-\frac{z_i + z_j}{2z_s}\right)} \tag{3.16}$$

σ_0^2 : A priori variance of the signal
z_s : Scaling height
x_i, y_i, z_i, t_i : Coordinates and time of the observation i
x_j, y_j, z_j, t_j : Coordinates and time of the observation j
$\Delta x_0, \Delta y_0, \Delta z_0, \Delta t_0$: Correlation length of the individual components

The parameters for the stochastic model are different for the three meteorological quantities. They are listed in Table 3.2.

The correlation matrix $\mathbf{C}_{nn}$ of the noise has non-zero elements only on the diagonal that is uncorrelated noise. The noise of the pressure and partial water vapor pressure measurements is set to 0.5 hPa. For the temperature measurements, a noise of 0.5 K is assumed.

Table 3.2: Parameters of the stochastic model of the collocation used for interpolating pressure, temperature, and partial water vapor pressure.

	σ_0 [hPa] or [°K]	Δx_0 [km]	Δy_0 [km]	Δz_0 [km]	Δt_0 [h]	z_s [km]	noise [hPa] or [K]
P	0.5	200	200	1	6	3	0.5
T	0.7	200	200	1	6	3	0.5
$\mathbf{P_{wet}}$	0.6	50	50	0.2	2	4	0.5

3.2.3 Elimination of the dry part in GNSS double difference observations

We have seen how zenith path delays at the GNSS stations are estimated by the Bernese GPS processing software and how the meteorological quantities are interpolated at the GNSS stations, where no meteorological sensors are mounted. From these quantities, double difference delays are computed by the following algorithm:

1. Compute the isotropic part of the total slant path delay $\widetilde{\Delta\varrho}^{r}_{\mathrm{tot},p}$ between satellite r and station p:

$$\widetilde{\Delta\varrho}^{r}_{\mathrm{tot},p} = \widetilde{\Delta\varrho}_{\mathrm{apr},0,p} \cdot \mathrm{m}_{\mathrm{apr}}(\vartheta^r_p) + \widetilde{\Delta\varrho}_{\mathrm{cor},0,p} \cdot \mathrm{m}_{\mathrm{cor}}(\vartheta^r_p)$$

   where the zenith path delays $\widetilde{\Delta\varrho}_{\mathrm{apr},0,p}$ and $\widetilde{\Delta\varrho}_{\mathrm{cor},0,p}$ at station p are estimated by the Bernese GPS Software using mapping functions $\mathrm{m}_{\mathrm{apr}}(\vartheta^r_p)$ and $\mathrm{m}_{\mathrm{cor}}(\vartheta^r_p)$ with zenith angle ϑ^r_p at station p to satellite r. The tilde denotes the isotropic delays.

2. Eliminate the dry part of the slant path delay by applying a modified version of Saastamoinen's formula $\Delta\varrho_{\mathrm{dry,Saas}}(P_{\mathrm{dry},p}, \vartheta^r_p, h_p)$ (see Equation 2.16). For this step, partial pressure of dry air $P_{\mathrm{dry},p}$ at the receiver station p, and station altitude h_p are needed. For GNSS stations which are not equipped with meteorological sensors, the missing data are interpolated by the collocation approach (see Section 3.2.2). The isotropic part of the wet slant path delay is computed by

$$\widetilde{\Delta\varrho}^{r}_{\mathrm{wet},p} \;=\; \widetilde{\Delta\varrho}^{r}_{\mathrm{tot},p} \;-\; \Delta\varrho_{\mathrm{dry,Saas}}(P_{\mathrm{dry},p}, \vartheta^r_p, h_p).$$

3. Build the isotropic double differences of the wet path delays from the isotropic wet slant path delays using Equation

$$\widetilde{\Delta\varrho}^{rs}_{\mathrm{wet},pq} \;=\; \left(\widetilde{\Delta\varrho}^{r}_{\mathrm{wet},q} \;-\; \widetilde{\Delta\varrho}^{r}_{\mathrm{wet},p}\right) \;-\; \left(\widetilde{\Delta\varrho}^{s}_{\mathrm{wet},q} \;-\; \widetilde{\Delta\varrho}^{s}_{\mathrm{wet},p}\right) \tag{3.17}$$

4. Add the double difference residuals $\Delta\varrho^{rs}_{\mathrm{res},pq}$ from the processing with Bernese GPS Software. As in Flores et al. 2000; Gradinarsky and Jarlemark 2004; Troller et al. 2006, we assume that the residuals are dominated by the effect of the non-isotropic distribution of the wet refractivity.

$$\Delta\varrho^{rs}_{\mathrm{wet},pq} \;=\; \widetilde{\Delta\varrho}^{rs}_{\mathrm{wet},pq} \;+\; \Delta\varrho^{rs}_{\mathrm{res},pq} \tag{3.18}$$

3.3 Discretization of the refractivity field and parameterization

The wet refractivity field is discretized with a rectilinear grid whose edges are parallel to the axes longitude λ, latitude ϕ and height h with reference to the WGS84 ellipsoid. AWATOS 2 provides 3 different parameterizations of the grid cells. These are a) constant, b) trilinear, and c) spline/bilinear parameterizations. In the follow subsections, their exact definitions will be given.

Constant parameterization

This parameterization is the simplest one and is widely used in GNSS tomography (e.g. Flores et al. 2001; Troller et al. 2002; Champollion et al. 2005; Lutz 2009). The field is assumed constant within a voxel and the refractivity in the voxel is modeled with a single parameter (see Figure 3.4a)). Thus, the number of unknowns is the same as the number of voxels.

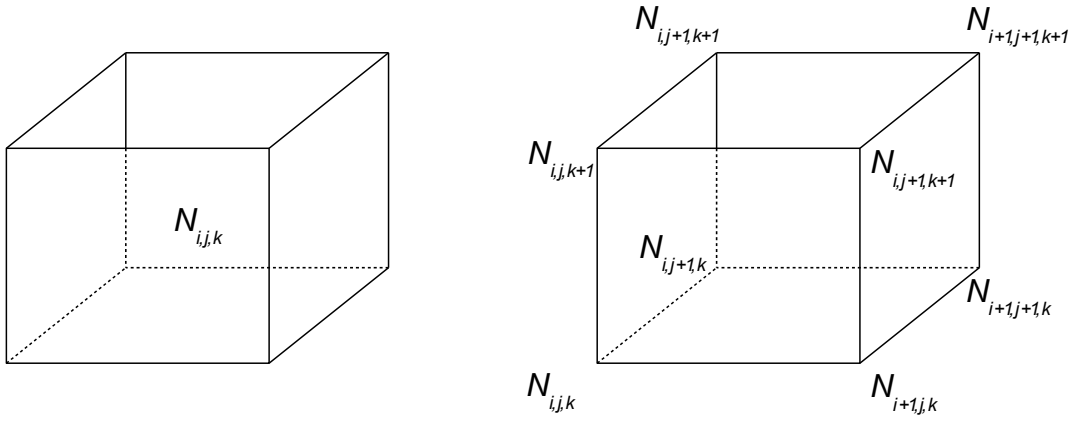

(a) Constant Parameterization

(b) Complex Parameterization

Figure 3.4: Parameterization of a voxel. a) The classical way to parameterize a voxel. The refractivity within a voxel is assumed constant and is modeled by one parameter per voxel. b) In the case of trilinear and spline/bilinear parameterization, the field is described by a weighted sum of refractivities at the vertices of the grid.

Trilinear parameterization

In the trilinear parameterization, the refractivity at the point (λ, ϕ, h) is determined by a weighted sum of the 8 refractivity values at the corners of the voxel in which the point is located (see Figure 3.4b)). The refractivity within a voxel is defined by the following interpolation function:

$$\mathrm{N}(\lambda, \phi, h) = \boldsymbol{\omega}^T \mathbf{N}_{voxel,i,j,k} \tag{3.19}$$

$$\boldsymbol{\omega} = \begin{bmatrix} \frac{\lambda_{i+1}-\lambda}{\lambda_{i+1}-\lambda_i} \frac{\phi_{j+1}-\phi}{\phi_{j+1}-\phi_j} \frac{h_{k+1}-h}{h_{k+1}-h_k} \\ \frac{\lambda-\lambda_i}{\lambda_{i+1}-\lambda_i} \frac{\phi_{j+1}-\phi}{\phi_{j+1}-\phi_j} \frac{h_{k+1}-h}{h_{k+1}-h_k} \\ \vdots \\ \frac{\lambda-\lambda_i}{\lambda_{i+1}-\lambda_i} \frac{\phi-\phi_j}{\phi_{j+1}-\phi_j} \frac{h-h_k}{h_{k+1}-h_k} \end{bmatrix} \tag{3.20}$$

$$\mathbf{N}_{voxel,i,j,k} = \begin{bmatrix} N_{i,j,k} \\ N_{i+1,j,k} \\ \vdots \\ N_{i+1,j+1,k+1} \end{bmatrix} \tag{3.21}$$

In contrast to the constant parameterization, the estimated parameters represent the refractivity at specified points. As a consequence of that, there are slightly more parameters to estimate: $(n_\lambda + 1)\,(n_\phi + 1)\,(n_h + 1)$ instead of $n_\lambda\, n_\phi\, n_h$ where n_λ is the number of voxels in longitudinal, n_ϕ in latitudinal, and n_h in the vertical direction, respectively. In contrast to the constant parameterization, the trilinear parameterization is C^0-continuous in space.

Spline/bilinear parameterization

This approach uses two different techniques of parameterization. In the horizontal directions, the bilinear form is used and, in the vertical one, natural spline functions. This leads to a representation which is C^0-continuous in latitudinal and longitudinal directions and C^1 along the vertical.

The bilinear interpolation works in the same way as the trilinear interpolation except that the bilinear one acts only in two dimensions. The refractivity at any point inside the voxel can be expressed by a weighted sum of the 4 refractivity values $N_{i,j}$, $N_{i,j+1}$, $N_{i+1,j}$ and $N_{i+1,j+1}$ lying all at the same height on the vertical edges of the voxel (see Figure 3.5).

$$\mathrm{N}(\lambda, \phi) = \mathbf{\Omega}^T \mathbf{N}_{\mathrm{plane},i,j} \tag{3.22}$$

with

$$\mathbf{\Omega} = \begin{bmatrix} \frac{\lambda_{i+1}-\lambda}{\lambda_{i+1}-\lambda_i} & \frac{\phi_{j+1}-\phi}{\phi_{j+1}-\phi_j} \\ \frac{\lambda-\lambda_i}{\lambda_{i+1}-\lambda_i} & \frac{\phi_{j+1}-\phi}{\phi_{j+1}-\phi_j} \\ \frac{\lambda_{i+1}-\lambda}{\lambda_{i+1}-\lambda_i} & \frac{\phi-\phi_j}{\phi_{j+1}-\phi_j} \\ \frac{\lambda-\lambda_i}{\lambda_{i+1}-\lambda_i} & \frac{\phi-\phi_j}{\phi_{j+1}-\phi_j} \end{bmatrix}$$

$$\mathbf{N}_{\mathrm{plane},i,j} = \begin{bmatrix} N_{i,j} \\ N_{i,j+1} \\ N_{i+1,j} \\ N_{i+1,j+1} \end{bmatrix}$$

The refractivity along a vertical profile is described by natural spline functions (Schwarz 1997). These functions have the following properties:

- The function is based on k sampling points located at the grid vertices on the corresponding vertical profile. For the profile i, j the height of the nodes are denoted by $h_{i,j,1}$, $h_{i,j,2}, \ldots, h_{i,j,n_k}$. As they are equal for different profiles, the indices i and j of the profiles are omitted.
- The refractivity between two nodes is determined by a cubical polynomial, which is denoted by

  $$\mathrm{N_k}(h) = a_k(h - h_k)^3 + b_k(h - h_k)^2 + c_k(h - h_k) + d_k \tag{3.23}$$

  with

  $$a_k = \frac{1}{6dh_k}(\mathrm{N}''_{k+1} - \mathrm{N}''_k) \tag{3.24a}$$

  $$b_k = \frac{1}{2}\mathrm{N}''_k \tag{3.24b}$$

  $$c_k = \frac{1}{dh_k}(\mathrm{N}_{k+1} - \mathrm{N}_k) - \frac{dh_k}{6}(\mathrm{N}''_{k+1} + 2\mathrm{N}''_k) \tag{3.24c}$$

  $$d_k = \mathrm{N}_k \tag{3.24d}$$

  where $dh_k = h_{k+1} - h_k$ is the thickness of the k-th layer. The N_k and N''_k are the refractivity and its second derivative at the node located at height h_k, respectively.
- The resulting spline function has the refractivity N_k at the node with height h_k. Furthermore, it is at least one time continuously differentiable at the inner nodes and 4 times between the nodes.

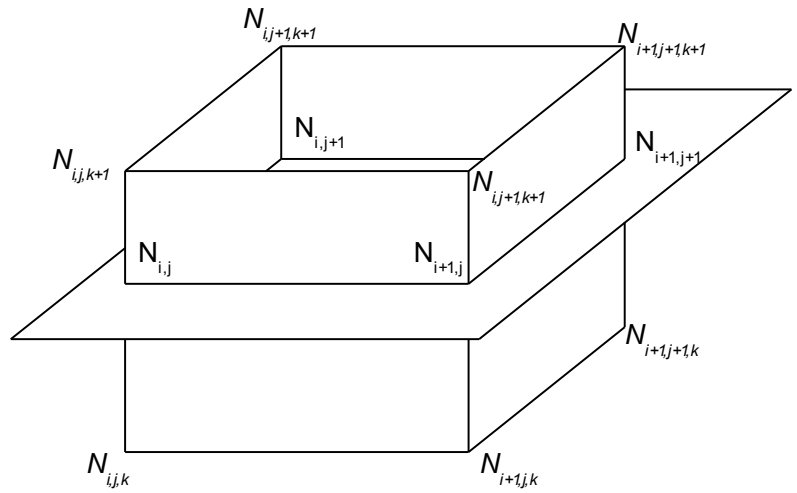

Figure 3.5: Bilinear/spline parameterization. Each point in the voxel can be described by the refractivity and its second derivative at the 8 corners of the voxel. For instance, the refractivity at the points $N_{i,j}$, $N_{i,j+1}$, $N_{i+1,j}$ and $N_{i+1,j+1}$ lying all on the same height level as the point of interest can be described by cubical spline functions along vertical profiles. Having the refractivity at these points, the refractivity at the point of interest can be described in bilinear form from these 4 refractivities.

The Equations 3.23 and 3.24a-e can also be expressed as a weighted sum of refractivities and its derivatives. The Equation 3.23 becomes for $h \in [h_k; h_{k+1}]$

$$\mathrm{N}(h) = \boldsymbol{\omega}^T \begin{bmatrix} \mathrm{N}_k \\ \mathrm{N}_{k+1} \\ \mathrm{N}''_k \\ \mathrm{N}''_{k+1} \end{bmatrix} \tag{3.25}$$

with

$$\boldsymbol{\omega} = \begin{bmatrix} 1 - \frac{h-h_k}{dh_k} \\ \frac{h-h_k}{dh_k} \\ \frac{(h-h_k)^2}{2} - \frac{dh_k(h-h_k)}{3} - \frac{(h-h_k)^3}{6dh_k} \\ \frac{(h-h_k)^3}{6dh_k} - \frac{dh_k(h-h_k)}{6} \end{bmatrix}.$$

In a next step, the second derivative will be expressed in terms of the refractivity at the nodes. This can be done by solving the following system of equations where vectors $\mathbf{N}$ and $\mathbf{N}''$ contain the refractivity and its second derivatives with respect to the parameter h at the n_k nodes, respectively.

$$\mathbf{C}\mathbf{N}'' = -\mathbf{D}\mathbf{N} \tag{3.26}$$

with

$$\mathbf{C} = \begin{bmatrix} 1 & 0 & \cdots & \cdots & \cdots & \cdots & 0 \\ dh_1 & c_1 & dh_2 & 0 & \cdots & \cdots & 0 \\ 0 & dh_2 & c_2 & dh_3 & 0 & \cdots & 0 \\ \vdots & \ddots & \ddots & \ddots & \ddots & \ddots & \vdots \\ 0 & \cdots & 0 & dh_{n_k-3} & c_{n_k-3} & dh_{n_k-2} & 0 \\ 0 & \cdots & \cdots & 0 & dh_{n_k-2} & c_{n_k-2} & dh_{n_k-1} \\ 0 & \cdots & \cdots & \cdots & \cdots & 0 & 1 \end{bmatrix}$$

$$\mathbf{D} = \begin{bmatrix} 0 & \cdots & \cdots & \cdots & \cdots & \cdots & 0 \\ \frac{6}{dh_1} & d_1 & \frac{6}{dh_2} & 0 & \cdots & \cdots & 0 \\ 0 & \frac{6}{dh_2} & d_2 & \frac{6}{dh_3} & 0 & \cdots & 0 \\ \vdots & \ddots & \ddots & \ddots & \ddots & \ddots & \vdots \\ 0 & \cdots & 0 & \frac{6}{dh_{n_k-3}} & d_{n_k-3} & \frac{6}{dh_{n_k-2}} & 0 \\ 0 & \cdots & \cdots & 0 & \frac{6}{dh_{n_k-2}} & d_{n_k-2} & \frac{6}{dh_{n_k-1}} \\ 0 & \cdots & \cdots & \cdots & \cdots & \cdots & 0 \end{bmatrix}$$

where $c_k = 2(dh_k + dh_{k+1})$ and $d_k = -\frac{6}{dh_k} - \frac{6}{dh_{k+1}}$. As natural splines are used, the second derivatives N_1'' and N_{n_k}'' are set to zero. This is indicated by the first and last row in matrix $\mathbf{D}$. With the equation system 3.26, the second derivatives can be pre-eliminated and, thus, the field of the second derivatives do not have to be stored. As the refractivities and its second derivatives of all nodes on the vertical profile are involved in the pre-elimination step, the weight vector $\boldsymbol{\omega}$ in Equation. 3.25 has to be adapted. The adapted version is denoted by $\tilde{\boldsymbol{\omega}}$. This leads to the following equation.

$$\mathrm{N}(h) = \tilde{\boldsymbol{\omega}}^T \begin{bmatrix} \mathbf{I} \\ -\mathbf{C}^{-1}\mathbf{D} \end{bmatrix} \mathbf{N} \tag{3.27}$$

with

$$\tilde{\omega}_k = \begin{cases} \omega_1 & \text{if } h_k \le h < h_{k+1}, \\ \omega_2 & \text{if } h_{k-1} \le h < h_k, \\ 0 & \text{else.} \end{cases}$$

$$\tilde{\omega}_{n_k+k} = \begin{cases} \omega_3 & \text{if } h_k \le h < h_{k+1}, \\ \omega_4 & \text{if } h_{k-1} \le h < h_k, \\ 0 & \text{else.} \end{cases}$$

for $k = 1 \ldots n_k$. Since $\mathbf{C}$ and $\mathbf{D}$ are the same for any (λ_i, ϕ_j) and the grid geometry does not change over time, the matrix $-\mathbf{C}^{-1}\mathbf{D}$ has to be computed only ones.

Finally, the bilinear and the spline part have to be combined. A point at (λ, ϕ, h) can be parameterized in two ways leading to the same result. In both cases, Equations 3.22 and 3.27 are used.

- In a first step, all refractivities on the 4 adjoining profiles are bilinearly mapped onto the vertical profile at (λ, ϕ). From these refractivities, the refractivity at the point (λ, ϕ, h) is

then computed using the spline parameterization.

$$\mathrm{N}(\lambda,\phi,h) = \tilde{\boldsymbol{\omega}}^T \begin{bmatrix} \mathbf{I} \\ -\mathbf{C}^{-1}\mathbf{D} \end{bmatrix} \begin{bmatrix} \boldsymbol{\Omega}^T & 0 & \cdots & 0 \\ 0 & \boldsymbol{\Omega}^T & \ddots & \vdots \\ \vdots & \ddots & \ddots & 0 \\ 0 & \cdots & 0 & \boldsymbol{\Omega}^T \end{bmatrix} \begin{bmatrix} \mathbf{N}_{\mathrm{plane},i,j,1} \\ \mathbf{N}_{\mathrm{plane},i,j,2} \\ \cdots \\ \mathbf{N}_{\mathrm{plane},i,j,n_k} \end{bmatrix} \tag{3.28}$$

where $\mathbf{N}_{\mathrm{plane},i,j,k}$ is a vector containing the refractivities at the points (λ_i, ϕ_j, h_k), $(\lambda_i, \phi_{j+1}, h_k)$, $(\lambda_{i+1}, \phi_j, h_k)$, and $(\lambda_{i+1}, \phi_{j+1}, h_k)$.

- Contrary to the previous approach (see Equation 3.28), the refractivity on the height h is computed at first using the spline interpolation. This is done along the 4 vertical profiles adjoining the coordinate (λ, ϕ). In a second step, the refractivity at the point (λ, ϕ, h) is bilinearly interpolated from these 4 refractivities:

$$\mathrm{N}(\lambda,\phi,h) = \boldsymbol{\Omega}^T \begin{bmatrix} \tilde{\boldsymbol{\omega}}^T & 0 & 0 & 0 \\ 0 & \tilde{\boldsymbol{\omega}}^T & 0 & 0 \\ 0 & 0 & \tilde{\boldsymbol{\omega}}^T & 0 \\ 0 & 0 & 0 & \tilde{\boldsymbol{\omega}}^T \end{bmatrix} \mathbf{T} \begin{bmatrix} \mathbf{N}_{i,j} \\ \mathbf{N}_{i,j+1} \\ \mathbf{N}_{i+1,j} \\ \mathbf{N}_{i+1,j+1} \end{bmatrix} \tag{3.29}$$

with

$$\mathbf{T} = \begin{bmatrix} \mathbf{I} & 0 & 0 & 0 \\ -\mathbf{C}^{-1}\mathbf{D} & 0 & 0 & 0 \\ 0 & \mathbf{I} & 0 & 0 \\ 0 & -\mathbf{C}^{-1}\mathbf{D} & 0 & 0 \\ 0 & 0 & \mathbf{I} & 0 \\ 0 & 0 & -\mathbf{C}^{-1}\mathbf{D} & 0 \\ 0 & 0 & 0 & \mathbf{I} \\ 0 & 0 & 0 & -\mathbf{C}^{-1}\mathbf{D} \end{bmatrix}$$

and $\mathbf{N}_{i,j}$ a vector containing the refractivities along the vertical profile located at (λ_i, ϕ_j).

3.4 Modeling the refractivity field with the Kalman filter approach

The refractivity field in the troposphere is a time-evolving field. Its behavior in space and time can be modeled. However, such models can represent the field only to a certain extent. To take this limitation into account, a model considering uncertainty is implemented in AWATOS 2. The wet refractivity is modeled by a simple stochastic differential equation system. This allows to describe the temporal behavior of the refractivity field and its probability density function.

Measurements, such as GNSS double difference delays and in-situ observations, represent the state of the refractivity field over time. As they are available over a longer period, they can be seen as time series. Due to measurement inaccuracies and modeling errors, such as the conversion from meteorological quantities to refractivity, measured values differ from the true value. AWATOS 2 models this inaccuracy by describing each measurement as random variable with a certain probability distribution.

The time-evolving model of the refractivity field and the measurements are combined in AWATOS 2 using the Kalman filter approach (Gelb 1974; Øksendal 2010). The model of the refractivity field is called *prediction model*. As the measurements represent the refractivity at certain time points, the discrete-time Kalman filter is used. The state of the refractivity field is predicted with the prediction model to the time where the next measurements are available. In the *update step*, the predicted state is combined with the measurements and the most probable state is estimated. In the following, the notation of the Kalman filter is introduced.

3.4.1 Definition of the Kalman filter

The discrete-time Kalman filter with prediction step from time t_{m-1} to t_m is defined by

$$\hat{\mathbf{x}}_{m|m-1} = \mathbf{F}_m \hat{\mathbf{x}}_{m-1|m-1} \tag{3.30}$$

$$\mathbf{P}_{m|m-1} = \mathbf{F}_m \mathbf{P}_{m-1|m-1} \mathbf{F}_m^T + \mathbf{Q}_m \tag{3.31}$$

and the update step by

$$\hat{\mathbf{x}}_{m|m} = \hat{\mathbf{x}}_{m|m-1} + \mathbf{K}_m \left(\mathbf{z}_m - \mathbf{H}_m \hat{\mathbf{x}}_{m|m-1}\right) \tag{3.32}$$

$$\mathbf{P}_{m|m} = \left(\mathbf{I} - \mathbf{K}_m \mathbf{H}_m\right) \mathbf{P}_{m|m-1} \tag{3.33}$$

with the Kalman gain

$$\mathbf{K}_m = \mathbf{P}_{m|m-1}\mathbf{H}_m^T(\mathbf{H}_m\mathbf{P}_{m|m-1}\mathbf{H}_m^T + \mathbf{R}_m)^{-1} \tag{3.34}$$

where $\hat{\mathbf{x}}_{m-1|m-1} \in \mathbb{R}^n$ represents the estimated refractivity field at time t_{m-1} described by n parameters, and $\mathbf{P}_{m-1|m-1} \in \mathbb{R}^{n\times n}$ its covariance matrix. The matrix $\mathbf{F}_m \in \mathbb{R}^{n\times n}$ propagates the field one time step forward and $\mathbf{Q}_m \in \mathbb{R}^{n\times n}$ reflects the uncertainty of the propagation. In the update step, the predicted state $\hat{\mathbf{x}}_{m|m-1} \in \mathbb{R}^n$ is mapped by the observation matrix $\mathbf{H}_m \in \mathbb{R}^{k\times n}$ into the k-dimensional space of the observations. The observation vector is denoted $\mathbf{z}_m \in \mathbb{R}^k$ and its covariance matrix by $\mathbf{R}_m \in \mathbb{R}^{k\times k}$.

3.4.2 Prediction model

The time-evolving refractivity field is modeled by a Gaussian random walk. The motivation to use the random walk model is its simplicity and the high sample rate of the observations compared to temporal scale on which synoptic processes evolve. The stochastic differential equation (SDE) of the random walk model is

$$dX_t = \mathbf{B}\, dW_t \tag{3.35}$$

where X is the n-dimensional multivariate random variable describing the refractivity field with respect to time t, $\mathbf{B}$ a $n \times n$ matrix and W_t a vector of uncorrelated standard Brownian motions. The matrix $\mathbf{B}$ is defined by

$$\mathbf{B} = \mathbf{G}\mathbf{K}^{\frac{1}{2}} \tag{3.36}$$

with

$$G_{i,j} = \begin{cases} s_0 \exp\left(-\frac{h_i}{2\,h_0}\right) & \text{if } i = j, \\ 0 & \text{if } i \neq j \end{cases} \tag{3.37}$$

and

$$K_{i,j} = \exp\left(-\sqrt{\left(\frac{h_i - h_j}{dh_0}\right)^2 + \left(\frac{\mathrm{dist}_{i,j}}{l_0}\right)^2}\right) \tag{3.38}$$

where h_i is the height of the i-th voxel and $\mathrm{dist}_{i,j}$ the horizontal distance between the i-th and j-*th* voxel. The symbols s_0, h_0, dh_0, and l_0 are model parameters. In Section 5.4, they are fitted to refractivities computed from the analyses of a numerical weather prediction model. Note that $\mathbf{K}^{\frac{1}{2}}$ can be computed by $\mathbf{V}\,\mathbf{\Lambda}^{1/2}\,\mathbf{V}^T$ where $\mathbf{V}$ is the matrix of eigenvectors of $\mathbf{K}$ and $\mathbf{\Lambda}^{1/2}$is a diagonal matrix with the square roots of $\mathbf{K}$'s eigenvalues.

The expected value $\mathbf{x} = \mathrm{E}[X_t]$ and the second moment $\mathbf{P} = \mathrm{E}[X_t^2]$ of the random walk (see Equation 3.35) can be expressed by two ordinary differential equations (Øksendal 2010):

$$\frac{\mathrm{d}\mathbf{x}}{\mathrm{d}t} = 0 \tag{3.39}$$

$$\frac{\mathrm{d}\mathbf{P}}{\mathrm{d}t} = \mathbf{B}\,\mathbf{B}^T \tag{3.40}$$

Integrating them from time t_{m-1} to t_m leads to the Kalman filter formulation stated in Equations 3.30 and 3.31 with

$$\mathbf{F}_m \;=\; \mathbf{I} \tag{3.41}$$

$$\mathbf{Q}_m \;=\; (t_m \;-\; t_{m-1})\,\mathbf{B}\,\mathbf{B}^T \;=\; (t_m \;-\; t_{m-1})\,\mathbf{G}\,\mathbf{K}\,\mathbf{G}^T \tag{3.42}$$

3.4.3 Observation model

The observation matrix $\mathbf{H}_m$ and the covariance matrix $\mathbf{R}_m$ of the observations are defined for different measurement types in this section. They are used in the update step of the Kalman filter (see Equations 3.32 and 3.33). For the observation types *point measurements* and *integral measurements*, the observation equations are given in respect of the different parameterizations. Further, several pseudo-observations are defined.

Integral observations

Integral measurements, such as GNSS slant delays and GNSS zenith path delays, are expressed as line integrals (see Equation 2.9). The ray path is modeled by a straight line neglecting any bending effects. The line integral is subdivided into sections where the section boundaries coincide with the voxel boundaries (see Figure 3.6). The intersection points between the ray and the voxel faces are determined by a ray-tracing algorithm (see Appendix A). Discretizing Equation 2.9 in this way leads to

$$\Delta\varrho_{\text{wet}} \;=\; 10^{-6} \int_S \mathrm{N}_{\text{wet}}(s)\,\mathrm{d}s \;=\; 10^{-6} \sum_{l=1}^{n_s} \int_{S_l} \mathrm{N}_{\text{wet}}(s)\,\mathrm{d}s \tag{3.43}$$

where n_s is the number of sections and S_l the l-th section.

The observation equations of integral measurements for the constant, the trilinear, and the spline/bilinear parameterizations are:

Constant parameterization: The integral along the section S_l in the voxel with index (i, j, k) can be analytically solved because the refractivity is modeled constant within the voxel

$$\int_{S_l} \mathrm{N}_{\text{wet}}(s)\,\mathrm{d}s \;=\; N_{i,j,k} \int_{S_l} \mathrm{d}s \;=\; N_{i,j,k}\,\Delta s_l \tag{3.44}$$

where $N_{i,j,k}$ is the refractivity in voxel (i, j, k) and Δs_l the geometric length of the l-th section. Substituting Equation 3.44 in Equation. 3.43 leads to

$$\Delta\varrho_{\text{wet}} \;=\; \sum_{l=1}^{n_s} \Delta s_l\, N_{\pi(l)} \tag{3.45}$$

where $\pi(l)$ maps the section index l to the corresponding voxel index (i, j, k).

Trilinear and spline/bilinear parameterization: Contrary to the constant parameterization, the integral along the section S_l cannot be expressed analytically in ellipsoidal coordinated with trilinear or with spline/bilinear parameterization. The reason for this is that there exits no closed form of the transformation from the geocentric Cartesian to the ellipsoidal coordinates. Therefore, a numerical integration scheme is used. Boole's rule is used for integration, which belongs to the Newton-Cotes quadrature family (see Appendix B). Newton-Cotes quadrature rules approximate an integral with a weighted sum with $n_m + 1$ summands per section (n_m is the number of subsections). In our case, the summands are refractivity values at nodes, which are located along the ray path. The refractivities at the nodes are determined by Equation 3.19 for the trilinear parameterization and by Equation 3.29 for the spline/bilinear parameterization. In this way, GNSS delays can be written as a weighted sum of refractivities at grid nodes. The weights are determined by the integral weights and by one of the

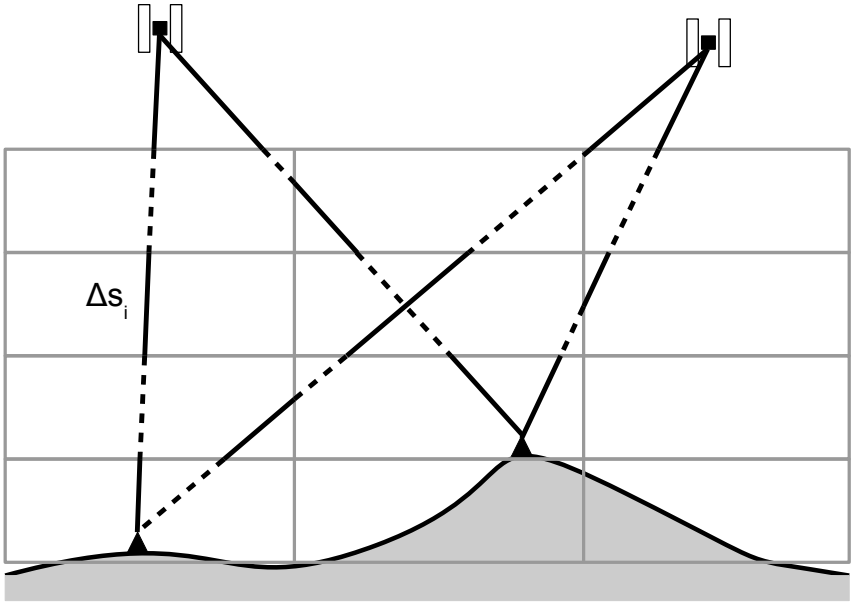

Figure 3.6: Principle of GNSS tomography. Satellites emit signals and devices at ground receive these signals. The receivers are represented by black triangles and the signal by the solid/dashed black lines. In GNSS tomography, the atmosphere is discretized, here indicated by the grid line (gray lines). According to this discretization, the signal path is subdivided (indicated by Δs_i). This corresponds to the discretization of the integral in Equation 2.5. Combining many rays, the refractivity in the grid boxes can be estimated from the slant path delays.

interpolation formulas. The observation equation for integral measurements is then defined by

$$\Delta\varrho_{\text{wet}} = \sum_{l=1}^{n_s} \int_{S_l} \mathrm{N}_{\text{wet}} \mathrm{d}s \tag{3.46}$$

with

$$\begin{aligned}\int_{S_l} \mathrm{N}_{\text{wet}}(s)\mathrm{d}s = \frac{2\,\delta s}{45}\Bigg(7\big(\mathrm{N}(s_{l,0}) + \mathrm{N}(s_{l,4n_m})\big) + 32\big(\mathrm{N}(s_{l,1}) + \mathrm{N}(s_{l,3})\big) + \\ 12\mathrm{N}(s_{l,2}) + \sum_{m=1}^{n_m-1}\Big(14\mathrm{N}(s_{l,4m}) + 32\big(\mathrm{N}(s_{l,4m+1}) + \\ \mathrm{N}(s_{l,4m+3})\big) + 12\mathrm{N}(s_{l,4m+2})\Big)\Bigg)\end{aligned}$$

where the integration step width $\delta s = \frac{\Delta s_l}{4n_m}$ and $\mathrm{N}(s_{l,i})$ is the refractivity at the i-th node in the l-th section.

GNSS double difference delays are treated the same way as GNSS slant path delays. The observation equation of a double difference delay is constructed from the 4 observation equations of the involved slant path delays. As the observation equations of slant path delays are linear, double differences of them stay linear and can be directly considered in the Kalman filter's update step.

The matrix $\mathbf{R}_m$ describes the covariances of the measurements at time t_m. GNSS path delays are expected to be independent from each other. An additive Gaussian measurement error is assumed with zero mean and predetermined variance. The variance is predetermined for delays in zenith direction and increases by $1/\cos^2(\vartheta)$ with decreasing zenith angle ϑ. It follows that for zenith path delay and slant delay observations, the covariance matrix $\mathbf{R}_m$ has non-zero elements only on the diagonal. For GNSS double difference observations, the convariance matrix $\mathbf{R}_m$ also shows non-zero off-diagonal elements. GNSS double difference delays with common slant delays are correlated. This correlation is considered in the stochastic model and is the reason for non-zero off-diagonal elements.

Point observations

The observation equation of point measurements has the form

$$N = \mathrm{N}(\lambda, \phi, h) \tag{3.47}$$

where N is the observation and $\mathrm{N}(\lambda, \phi, h)$ is defined by the voxel parameterization. For the constant parameterization, $\mathrm{N}(\lambda, \phi, h)$ is equal to the refractivity parameter $N_{i,j,k}$ of the voxel (i, j, k), in which the refractivity is measured. For the trilinear and for the spline/bilinear parameterization, $\mathrm{N}(\lambda, \phi, h)$ is substituted by Equation 3.19 for the trilinear parameterization and by Equation 3.29 for the spline/bilinear parameterization.

Pseudo-observations

There are two different types of intervoxel constraints implemented in AWATOS 2. The constraints are introduced in the tomographic reconstruction as pseudo-observations.

Neighborhood averaging constraints: This kind of constraints have been introduced by Troller 2004. For each voxel or grid point, an observation equation is put. The refractivity of the voxel or grid point is, thereby, equal to the weighted sum of the 6 refractivities of the surrounding voxels or nodes. The weights depend on the distance between the voxel middle points or on the distance between the nodes, respectively (see Wehrli 1986). For the voxel or node with index (i, j, k), the observation equation is

$$\begin{bmatrix} \frac{\Phi_{i,j,k-1}}{\Phi_{\mathrm{sum}}} \\ \frac{\Phi_{i,j-1,k}}{\Phi_{\mathrm{sum}}} \\ \frac{\Phi_{i-1,j,k}}{\Phi_{\mathrm{sum}}} \\ \frac{\Phi_{i+1,j,k}}{\Phi_{\mathrm{sum}}} \\ \frac{\Phi_{i,j+1,k}}{\Phi_{\mathrm{sum}}} \\ \frac{\Phi_{i,j,k+1}}{\Phi_{\mathrm{sum}}} \\ -1 \end{bmatrix}^T \begin{bmatrix} N_{i,j,k-1} \\ N_{i,j-1,k} \\ N_{i-1,j,k} \\ N_{i+1,j,k} \\ N_{i,j+1,k} \\ N_{i,j,k+1} \\ N_{i,j,k} \end{bmatrix} = 0 \tag{3.48}$$

with weight functions

$$\Phi_{i,j,k-1} = \frac{1}{1 + \left(\frac{\lambda_{i,j,k}-\lambda_{i,j,k-1}}{\Delta\lambda}\right)^2 + \left(\frac{\phi_{i,j,k}-\phi_{i,j,k-1}}{\Delta\phi}\right)^2 + \left(\frac{h_{i,j,k}-h_{i,j,k-1}}{\Delta h}\right)^2}$$
$$\Phi_{i,j-1,k} = \frac{1}{1 + \left(\frac{\lambda_{i,j,k}-\lambda_{i,j-1,k}}{\Delta\lambda}\right)^2 + \left(\frac{\phi_{i,j,k}-\phi_{i,j-1,k}}{\Delta\phi}\right)^2 + \left(\frac{h_{i,j-1,k}-h_{i,j,k}}{\Delta h}\right)^2}$$
$$\Phi_{i-1,j,k} = \frac{1}{1 + \left(\frac{\lambda_{i,j,k}-\lambda_{i-1,j,k}}{\Delta\lambda}\right)^2 + \left(\frac{\phi_{i,j,k}-\phi_{i-1,j,k}}{\Delta\phi}\right)^2 + \left(\frac{h_{i,j,k}-h_{i-1,j,k}}{\Delta h}\right)^2}$$
$$\Phi_{i+1,j,k} = \frac{1}{1 + \left(\frac{\lambda_{i,j,k}-\lambda_{i+1,j,k}}{\Delta\lambda}\right)^2 + \left(\frac{\phi_{i,j,k}-\phi_{i+1,j,k}}{\Delta\phi}\right)^2 + \left(\frac{h_{i,j,k}-h_{i+1,j,k}}{\Delta h}\right)^2}$$
$$\Phi_{i,j+1,k} = \frac{1}{1 + \left(\frac{\lambda_{i,j,k}-\lambda_{i,j+1,k}}{\Delta\lambda}\right)^2 + \left(\frac{\phi_{i,j,k}-\phi_{i,j+1,k}}{\Delta\phi}\right)^2 + \left(\frac{h_{i,j,k}-h_{i,j+1,k}}{\Delta h}\right)^2}$$
$$\Phi_{i,j,k+1} = \frac{1}{1 + \left(\frac{\lambda_{i,j,k}-\lambda_{i,j,k+1}}{\Delta\lambda}\right)^2 + \left(\frac{\phi_{i,j,k}-\phi_{i,j,k+1}}{\Delta\phi}\right)^2 + \left(\frac{h_{i,j,k}-h_{i,j,k+1}}{\Delta h}\right)^2},$$

and

$$\Phi_{\text{sum}} = \Phi_{i,j,k-1} + \Phi_{i,j-1,k} + \Phi_{i-1,j,k} + \Phi_{i+1,j,k} + \Phi_{i,j+1,k} + \Phi_{i,j,k+1}.$$

The scaling lengths $\Delta\lambda$, $\Delta\phi$, and Δh are normalizing the 3 dimensions and allow to adjust their influence.

Spatial gradient constraints: In AWATOS 2, it is possible to individually constrain the single spatial derivatives of the refractivity field. They have the same form for all parameterizations. The horizontal derivatives are set to zero whereas the vertical derivative is equal to the derivative of the exponential model $N_0 \exp(-\frac{h}{h_s})$ with refractivity N_0 on the reference ellipsoid and the scaling height h_s. This leads to the following 3 pseudo-observation equations.

$$N_{i+1,j,k} - N_{i,j,k} = 0 \tag{3.49a}$$
$$N_{i,j+1,k} - N_{i,j,k} = 0 \tag{3.49b}$$
$$N_{i,j,k+1} - N_{i,j,k} = N_0\left(\exp\left(-\frac{h_{k+1}}{h_s}\right) - \exp\left(-\frac{h_k}{h_s}\right)\right) \tag{3.49c}$$

The pseudo-observations belonging to one of these constraint types are independent among each other. For each type, a weight can be specified. The reciprocal of this weight is then used in the covariance matrix R_m. As no correlations between pseudo-observations are considered, there are no non-zero off-diagonal elements for pseudo-observations.

3.5 Simulation capabilities in AWATOS 2

Synthetic tests are helpful for testing new algorithms and for investigating the behavior of different configurations on specific atmospheric processes. Such synthetic tests comprise of two parts: a) simulation of the observations (forward modeling) and b) the tomographic reconstruction of the refractivity field (backward modeling). In this section, the simulation of different observations is described. AWATOS 2 supports to simulate different point and integral measurements from predefined refractivity fields. Such fields can be described by functions or can be derived from data of numerical weather prediction models.

3.5.1 Predefined refractivity fields

Predefined functions

Two predefined functions are implemented in AWATOS 2. The first one is an exponential function depending on the height. It accurately models the average refractivity along a vertical profile (see Figure 5.4a)). The model is extended to support horizontal and temporal variations.

$$\mathrm{N}(t,\lambda,\phi,h) \;=\; N_0\,\mathrm{f}_{\mathrm{time}}(t)\,\mathrm{f}_{\mathrm{space}}(\lambda,\phi,h)\,\exp\left(-\frac{h}{h_f}\right) \tag{3.50}$$

with

$$\begin{aligned}\mathrm{f}_{\mathrm{time}}(t) \;&=\; 1 \,+\, a\,\sin(\omega\,t \,+\, \theta)\\ \mathrm{f}_{\mathrm{space}}(\lambda,\phi,h) \;&=\; 1 \,+\, b\,\exp\left(-\frac{1}{2}\left(\left(\frac{\lambda-\lambda_0}{\lambda_s}\right)^2+\left(\frac{\phi-\phi_0}{\phi_s}\right)^2+\left(\frac{h-h_0}{h_s}\right)^2\right)\right)\end{aligned}$$

where N_0 denotes the refractivity on the reference ellipsoid, h_f the scaling height of the base function, a the amplitude of the temporal perturbation, ω the angular rate, θ the phase shift, b the size of the spatial perturbation, (λ_0, ϕ_0, h_0) the point where the spatial perturbation is maximal, and λ_s, ϕ_s and h_s the scaling longitude, latitude and height for the spatial perturbation, respectively.

The second function describes a vertical perturbation. Atmospheric inversions are an example of such perturbations and are commonly observed in the Swiss Plateau during winter (Wanner 1979). It is, therefore, of importance to assess the capability to properly reconstruct such patterns. The perturbation function is defined as

$$\mathrm{N}(\lambda,\phi,h) = \begin{cases} N_0 & \text{if } h \in [h_{\mathrm{lower}}, h_{\mathrm{upper}}] \\ 0 & \text{else} \end{cases} \tag{3.51}$$

where N_0 is the perturbation.

Refractivity fields derived from data of numerical weather prediction models

AWATOS 2 is capable to derive time-evolving (wet) refractivity fields from data of numerical weather prediction models such as COSMO-7 and COMSO-2 (Doms and Schättler 2002). Using Equation 2.8, the (wet) refractivity at the grid nodes is computed from the pressure, temperature and humidity fields. Between grid nodes, the refractivity is trilinearly interpolated (see Equation 3.19). As a 3D refractivity field represents the atmosphere at a certain time, the refractivities in between two consecutive 3D fields are linearly interpolated.

3.5.2 Simulated observations

Integral observations, such as GNSS double difference delays, slant path delays and zenith path delays, can be simulated. Besides integral observations, the simulation of in-situ measurements is supported, too.

Integral measurements

Ray paths are modeled as straight lines between the emitting satellites and the receivers. The visibility of satellites from a receiver station can be restricted by a cutoff angle or by defining the horizon around that station. For instance, the horizon can be calculated from a digital elevation model. Numerical integration is used to compute the delay along the ray path. Boole's quadrature rule is used (see Appendix B). Integration limits are at the receiver and either at the top of the atmospheric grid or at a given height level. AWATOS 2 provides the possibility to add measurement errors to the delays. The error is modeled by a Gaussian distribution where the measurement bias is specified by expectation value μ and the measurement noise by the variance σ^2. Measurement

errors are modeled without correlation among each other. For slant path delays, the error is multiplied by the mapping function $1/\cos(\vartheta)$, where ϑ is the zenith angle of the slant path delay.

$$\Delta\tilde{\varrho} = \Delta\varrho + \frac{1}{\cos(\vartheta)}\varepsilon \tag{3.52}$$

with

$$\varepsilon \sim \mathcal{N}(\mu, \sigma^2)$$

where $\Delta\varrho$ is the exact delay and $\Delta\tilde{\varrho}$ the perturbed delay.

GNSS double difference observations are simulated by combining 4 slant path delay observations. There are different possibilities how double difference observations can be built. A possibility is to specify a spanning tree, where the vertices represent the receiver stations. The edges represent the baselines. Slant path delays which belong to two stations of a common baseline are combined to double difference observations. In AWATOS 2, the spanning tree is determined by computing a minimum spanning tree in respect of a cost function from a complete graph. The minimum spanning tree is calculated with Kruskal's algorithm (Matoušek and Nešetřil 1998). Three cost functions are supported:

Maximum common observations: For each edge, the number of common slant path delays is computed. The cost function is the negative number of common slant path delays.

Minimum distance: The ellipsoidal distance between two stations is used as cost function.

Maximum distance: The negative ellipsoidal distance between two stations is used as cost function.

Measurement bias and measurement noise are added on the slant path delay level. The same measurement error model as for slant path delays is used (see Equation 3.52).

Point measurements

In-situ measurements are simulated by point observations. They represents the refractivity at a given point. A measurement error can be added.

$$\tilde{N} \;=\; \mathrm{N}(\lambda, \phi, h) \;+\; \varepsilon \tag{3.53}$$

with

$$\varepsilon \sim \mathcal{N}(\mu, \sigma^2)$$

where $\tilde{N}$ is the perturbed refractivity, $\mathrm{N}(\lambda, \phi, h)$ the exact refractivity at point (λ, ϕ, h) derived from the give refractivity field, μ the measurement bias, and σ^2 the variance of the Gaussian measurement noise. The measurement noise of the point observations is uncorrelated among each other.

Chapter 4

Overview of the data sets

Data from different sources are used within this study. This chapter gives an overview of these data sets and shortly describes their sources, availability and main properties. Figure 4.1 illustrates the availability of the single data sets. Processed and prepared data from GPS observations are available for the year 2006. Meteorological measurements, such as balloon soundings and measurements from the synoptic measurement network SwissMetNet, are available for a period of 2 years beginning in 2006. In addition, data from NWPs are provided from the Swiss Federal Office of Meteorology and Climatology for the years 2006 and 2007 (COSMO-7) and for 4 months in 2008 and 2009 (COSMO-2).

4.1 GPS data

The GPS data stems from more that 120 GPS permanent stations distributed over central Europe (see Figure 4.2). In the area indicated by the dark blue box, the network shows a high station density. This is the core area in which the tomographic processing is carried out. The mean shortest inter-station distance is about 30 km in this region. 31 of the stations in this area belong to the Automated GNSS NEtwork of Switzerland (AGNES) operated by the Swiss Federal Office of Topography (Ineichen et al. 2009). 50 stations located outside this area mainly belong to the EUREF permanent network (EPN). For details see Bruyninx and Roosbeek 2009. The processing of the GPS data is carried out by the Swiss Federal Office of Topography (Brockmann et al. 2006; Brockmann et al. 2007). Further details about the processing can be found in Section 3.2.

4.2 Balloon soundings

Balloon sounding measurements (TEMP upper air soundings) are available for 93 stations located in Europe (see Figure 4.3). The data set spans a period of 2 years starting in the year 2006 and comprises more than 112'000 measurement profiles. It includes measurements of pressure, temperature and relative humidity.

The only balloon sounding station located in the area of investigation is that in Payerne. During this time, a sounding device called *SRS-400* had been used (Richner 1999; Ruffieux and Joss 2003). Balloons are launched usually twice per day: One at midnight and one at noon with respect to UTC time. Occasionally, there are launches at 6 a.m. and 6 p.m. UTC. In total, there have been 1738 balloon launches in Payerne during these 2 years providing more than 78'000 observation triples (pressure, temperature, relative humidity). In the average, these are 44.974 triples per launch. The observations are non-uniformly distributed over the height (see Figure 4.4). The measurement density decreases with height. Below 906 m and above 12'931 m, no observations are available.

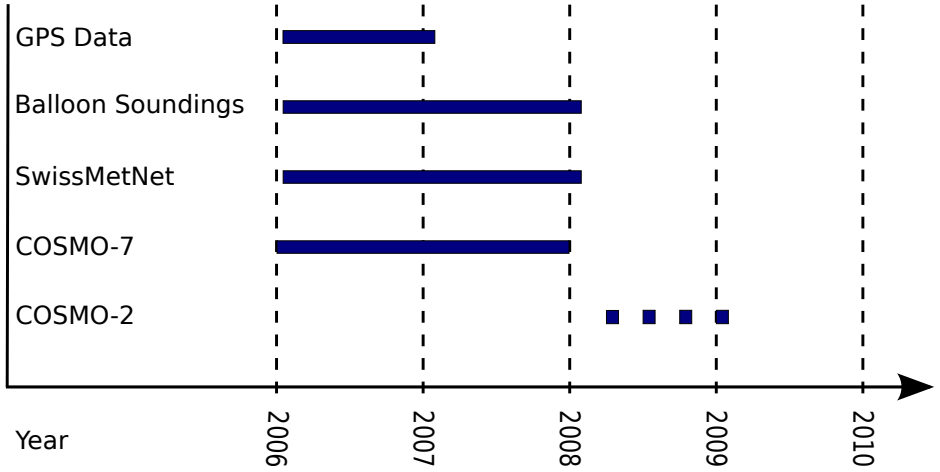

Figure 4.1: Availability of the data sets.

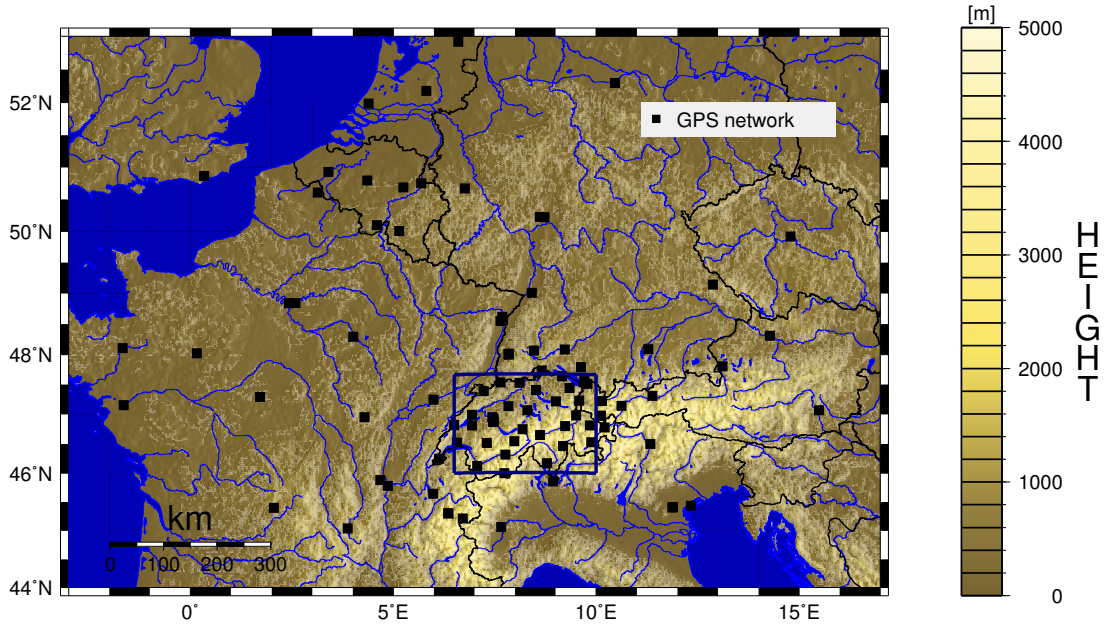

Figure 4.2: Locations of the GPS receiver stations used in the preprocessing carried out at the Swiss Federal Office of Topography (black squares). The area framed by the dark blue lines is the area in which the tomographic processing is investigated.

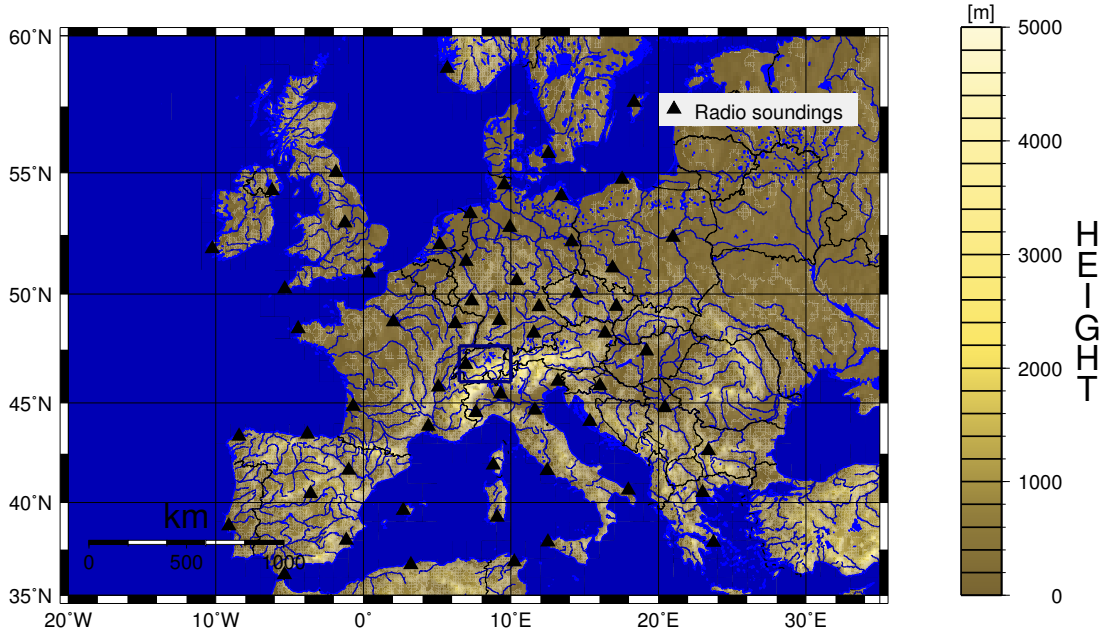

Figure 4.3: Locations of the balloon sounding stations (black triangles). The area framed by the dark blue lines is the area in which tomographic processing is investigated.

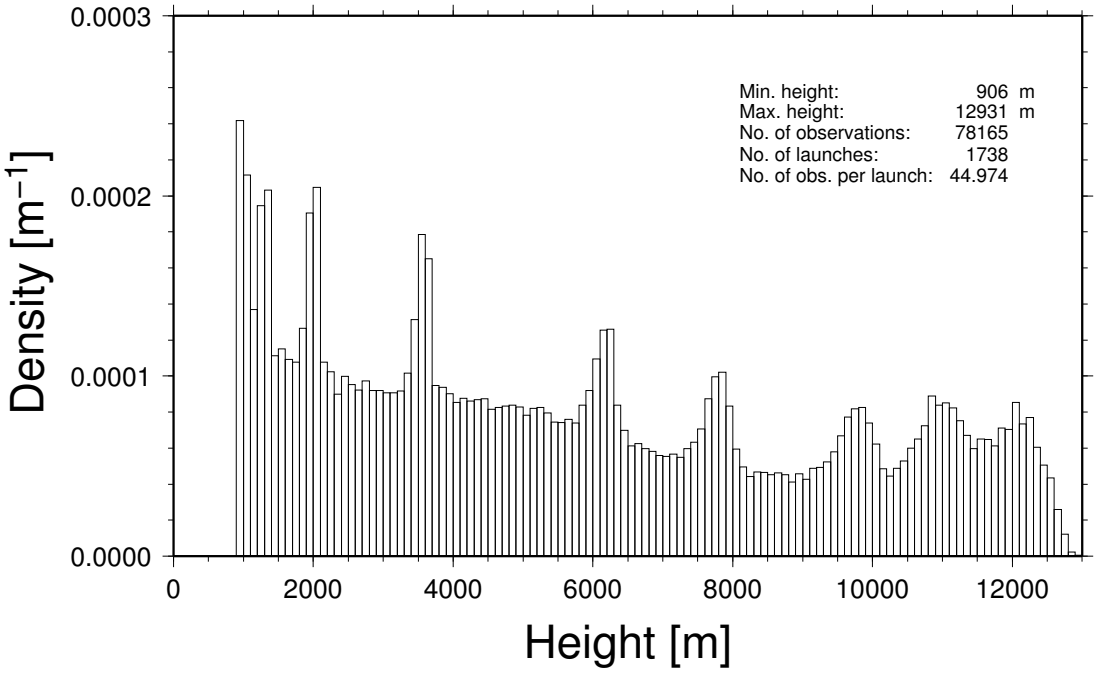

Figure 4.4: Vertical distribution of the balloon sounding measurements in Payerne.

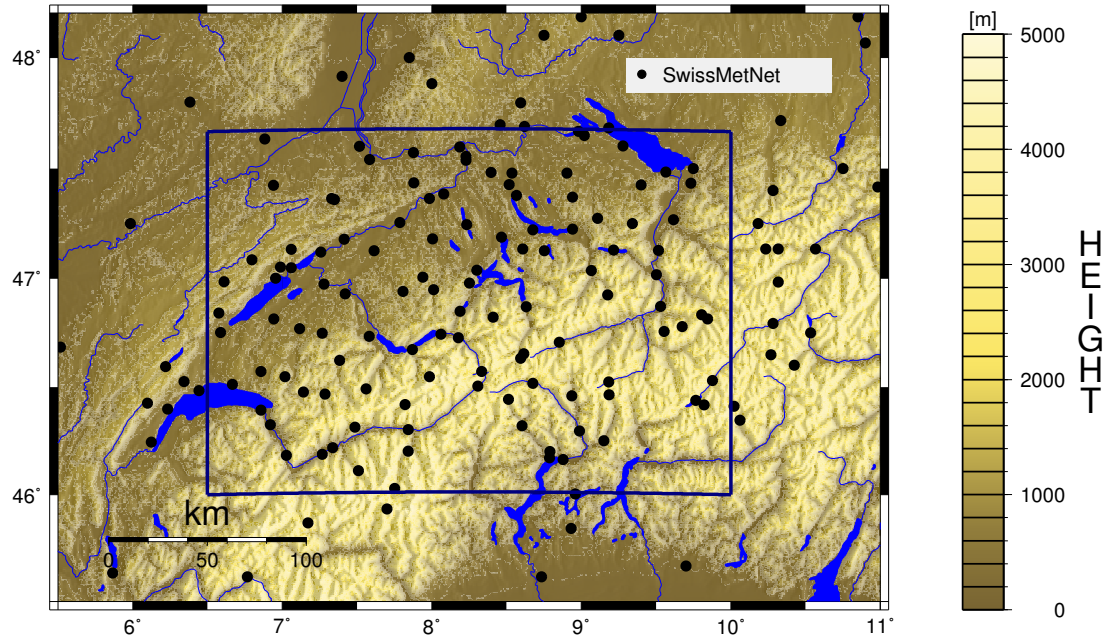

Figure 4.5: Stations of the synoptic measurement network SwissMetNet and stations located in adjoining countries (black circles). The area framed by the dark blue lines is the area in which the tomographic processing is investigated.

4.3 Synoptic network SwissMetNet

Ground-based meteorological measurements collected by 124 stations belonging to the SwissMetNet (formerly called ANETZ) and from stations in adjoining countries are provided by the Swiss Federal Office of Meteorology and Climatology (see Figure 4.5). The meteorological quantities pressure, temperature at 2 m above Earth's surface and relative humidity, wind guest, 10 minutes average wind velocity, and wind direction are used within this study. The data is sampled with a rate of 10 minutes (Suter et al. 2006).

4.4 Numerical weather prediction model COSMO

COSMO is a non-hydrostatic local NWP model developed by the COSMO consortium (Consortium of small scale modelling). The Swiss Federal Office of Meteorology and Climatology operates this model in two different setups: a) COSMO-7 and b) COSMO-2 (Doms and Schättler 2002; Buzzi 2008; Baldauf et al. 2011). The configurations mainly differ in their resolution (7 and 2 km horizontal resolution and 45 and 60 levels, respectively) and the lead time up to which forecasts are computed (72 and 24 h). The domains of the two configurations are shown in Figure 4.6. For the investigations in this study, data from the assimilation cycle (corresponding to lead time zero) are considered. The data is also referred to as analysis in this study.

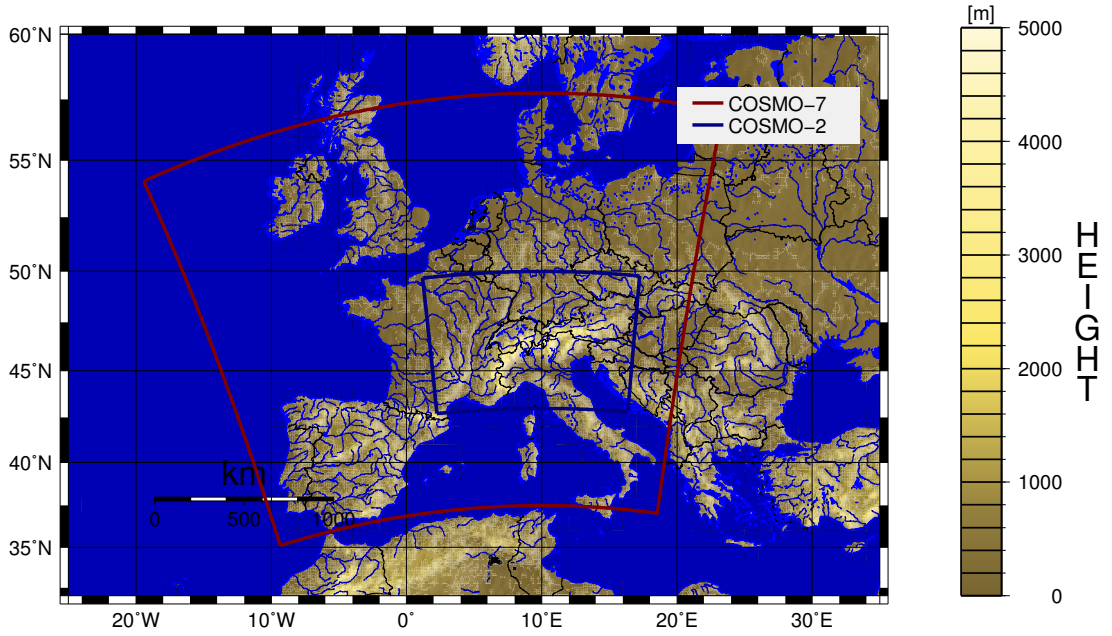

Figure 4.6: Domains of COSMO-7 (red box) and COSMO-2 (blue box).

Chapter 5

Description of the wet refractivity field

Several aspects of the wet refractivity field are considered in this chapter. In the first two sections of this chapter, the tempo-spatial distribution of the wet refractivity in the troposphere is investigated. Time series of wet refractivity at different regions and altitudes are analyzed to identify the main frequencies and the underlying processes. In addition, the vertical distribution of the wet refractivity is investigated. The goal of these investigations is a better understanding of the processes causing changes in the wet refractivity field and to deduce the main statistical characteristics. This knowledge enables us to better interpret the tomographic results presented in subsequent chapters and to assess the implemented models in AWATOS 2, especially the different intervoxel constraints.

The next two sections address the discretization error. The investigations are based on the data from the NWP COSMO-2 with a horizontal grid resolution of 2 km. The discretization error is calculated for the tomographic grid with a horizontal resolution of 37 km. This is the grid resolution used in the tomographic processing presented in subsequent chapters. The investigations will provide information on the tempo-spatial structure of the discretization error. This error will be split into a time invariant and in a time variant part. This splitting will help us to decide whether observations can be treated as bias free in view of the tomography model or if a bias correction is needed. On the other hand, the discretization error can be regarded as an accuracy limit for the tomographic solutions obtained with the given configuration. Comparing the actual error of the tomographic solution with the discretization error allows us to judge the performance of the tomographic algorithms.

In a last part of this chapter, the prediction model implemented AWATOS 2 is validated and parameters for this model specified. The configuration of subsequent tomographic investigations will be based on these numbers.

Several studies have been carried out to identify statistical properties of the wet refractivity field, such as temporal and spatial correlation lengths of the wet refractivity in the troposphere. Treuhaft and Lanyi 1987 have investigated the wet tropospheric effect on radio interferometric measurements. Their model is based on Kolmogorov turbulence theory and describes the correlation between slant wet delays. Nilsson and Gradinarsky 2005 have applied this model to microwave radiometry. The same techniques are used in GPS tomography to describe the covariance between the wet refractivity at different locations by Gradinarsky 2002 and Nilsson and Gradinarsky 2006.

In view of the horizontal grid spacing on the order of 15-50 km used in this work, it is debatable if turbulent theory yields a valuable approach. Looking at the time period of observed wind speed variations near the Earth's surface, we see a spectral gap between 30 minutes and 1 hour (see Figure 5.1). This gap is used to separate the synoptic scale from the turbulent scale (e.g. Stull 1999). Assuming that temporal fluctuations of wet refractivity are caused by spatial patterns which are advected by wind on the synoptic scale, the temporal scale can be transformed into a spatial scale. A common value for the mean horizontal wind in mid-latitude is 8 $\mathrm{m\,s^{-1}}$ (Treuhaft and Lanyi

1987). A temporal scale of 30 minutes then corresponds to a spatial scale of about 14 km. This can be seen as an upper bound for the turbulent scale. As the grid spacing used in our work is larger, statistical characteristics of the wet refractivity field are empirically estimated from observations on the synoptic scale.

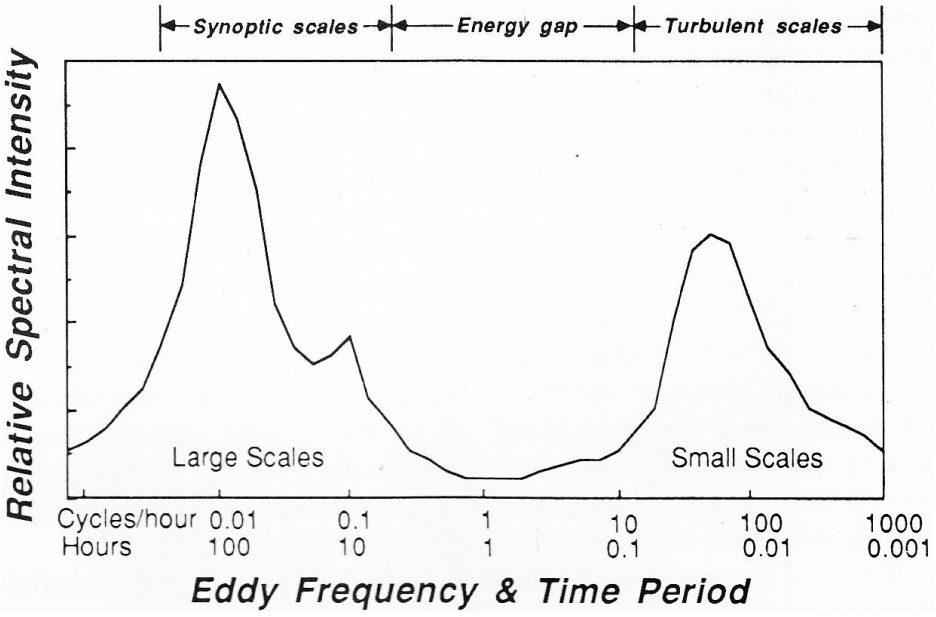

Figure 5.1: Schematic spectrum of wind speed near the ground (Stull 1999).

The following data types are taken into account for the investigations:

Balloon soundings: The vertical resolution of balloon soundings is suitable for investigating the vertical correlations and the most data points are representative for the free atmosphere. Neither horizontal nor temporal resolution is sufficient for horizontal cross-correlations and for autocorrelations, respectively.

Synoptic stations: The synoptic stations indeed feature a high temporal resolution. As they are located at the Earth's surface they might not be representative for the free atmosphere. Such stations are located in the planetary boundary layer in which wind regimes are different from that in the free atmosphere. Hence, we expect different statistical properties from the synoptic stations and the radiosondes.

Numerical weather prediction model data: As additional data sources, data from the numerical weather models COSMO-7 and COSMO-2 are considered.

5.1 Tempo-spatial variation of the wet refractivity field

The wet refractivity field is influenced by processes at different time scales. Figure 5.2 shows the time series of wet refractivity at the synoptic station in Payerne. In Figure 5.3a), the amplitude spectrum of these time series is plotted. A seasonal cycle is clearly visible with a maximum during summer. One can, therefore, estimated the seasonal cycle the following way

$$\mathrm{N}(t) \;=\; a\left(1 \;+\; b\,\cos\left(\frac{2\pi}{\tau}\,(t \;-\; \theta)\right)\right) \tag{5.1}$$

with wet refractivity N at time t, a period of 1 year denoted by τ and the unknown parameters a (mean), b (relative amplitude to the mean), and θ (phase shift). These parameters are estimated

from time series of several SwissMetNet stations. The resulting parameters a, b, and θ are plotted in Figure 5.4. In addition, the parameters at different height levels are estimated from time series based on balloon sounding data from Payerne. The spacing between two subsequent levels is 100 m.

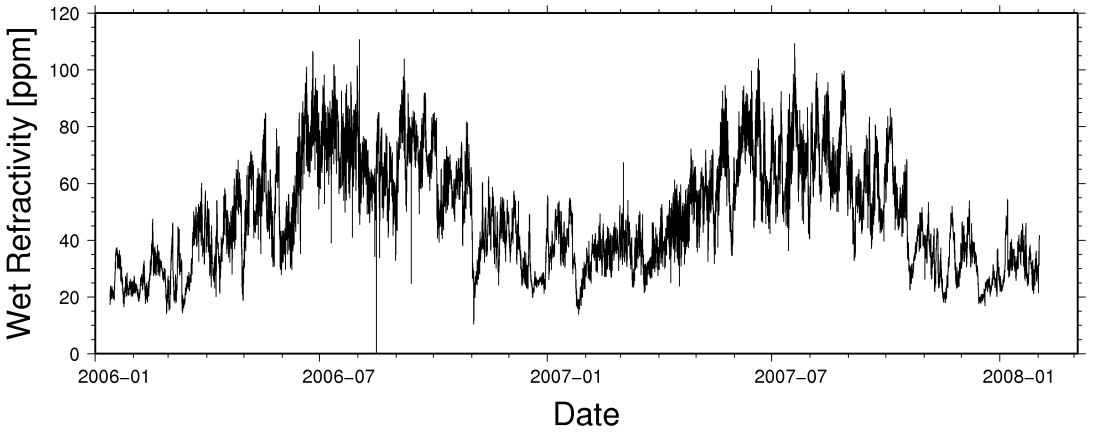

Figure 5.2: Time series of wet refractivity at the synoptic station in Payerne.

The largest mean wet refractivities are found in the lower troposphere. The maximum mean values measured by the considered synoptic stations are between 50 and 60 ppm. However, this strongly depends on the height at which the station is located. The higher the altitude the lower the refractivity. The decrease of the wet refractivity with height can be described by an exponential function as the water vapor pressure is the dominating quantity in the wet part of the refractivity approximation formula (see Equation 2.8) and as the partial water vapor pressure can be well approximated with an exponential function (Hann and Süring 1957).

At noon, there is no significant difference between the mean wet refractivity measured at synoptic stations and that observed by balloon soundings (see Figure 5.4a)). In contrast to that, the wet refractivity at synoptic stations is significantly smaller (up to 5-8 ppm smaller in layer between 1000-2000 m altitude) than that measured by balloon soundings at the same altitude at midnight (not shown in any of the figures).

The difference between the mean wet refractivities (parameter a) estimated for the synoptic stations and for the balloon soundings at the same height as the corresponding station is located are plotted in Figure 5.5a). The majority of the synoptic stations in inner alpine valleys has a smaller wet refractivity than the corresponding measurements above the balloon sounding station. This might be related to the fact that inner alpine valleys are dryer than areas at the foothills of the Alps as less precipitation occurs in inner alpine valleys due to the lee effect.

The synoptic stations in the foothills of the Alps and the synoptic stations in the Jura mountains show larger wet refractivity values than the balloon sounding measurements in the Swiss Plateau during the night (see Figure 5.5b)). The wet refractivity at the synoptic stations is for all stations lower than the values measured by balloon soundings. This suggests that evaporation and condensation processes are involved near the Earth's surface. During day time, evapotranspiration occurs near the Earth's surface and increases the wet refractivity. As a result of this, the wet refractivity measured near the Earth's surface tends to be larger than that in the (free) atmosphere at the same altitude. The opposite can be observed during night time. Near Earth's surface, water vapor is condensing and lowering the wet refractivity more than in the (free) atmosphere at the same height.

Figure 5.5b) shows the amplitude of the seasonal cycle for SwissMetNet stations (black dots) and for the balloon soundings in Payerne (black line). The amplitude of the seasonal cycle is about half the mean value of the wet refractivity and, according to the balloon sounding data, the relative amplitude is quite insensitive to height in the lowest 6 km of the atmosphere atmosphere. Looking at observations measured at the synoptic stations, a different height dependent behavior can be observed. The relative amplitude increases with height whereas the absolute amplitude is

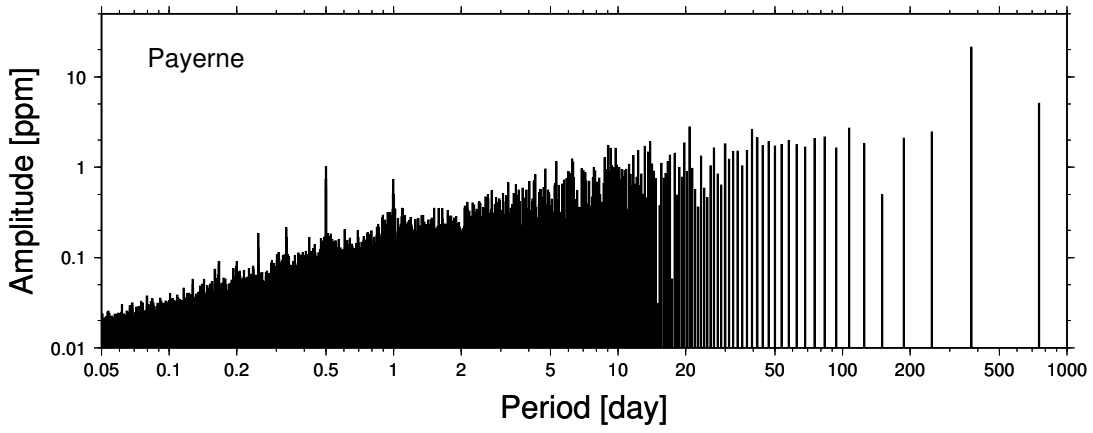

(a) Payerne

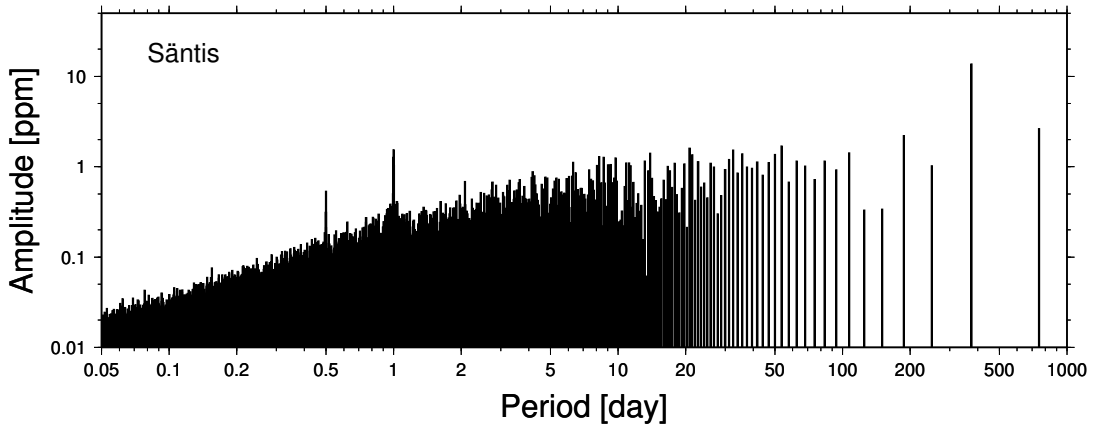

(b) Säntis

Figure 5.3: Amplitude spectra of wet refractivity measured at the synoptic stations a) Payerne located in the Swiss Plateau and b) Mount Säntis (2500 m above mean sea level).

independent of the station height. This shows that processes near the Earth's surface strongly influence the wet refractivity field in the layers where these effects are present. As the GNSS stations are located on the Earth's surface, GNSS observations cross these layers and, therefore, reflect this difference in wet refractivity. Regarding the impact on the result of GNSS tomography, this can lead to significant seasonal systematic errors if the tomographic grid is not fine enough to represent such atmospheric structures.

Figure 5.4c) shows when the seasonal cycle reaches its maximum. It occurs around the 24^{th} of July and does not vary considerably with height. The estimated phase shift is a few days smaller for the synoptic stations than for the balloon soundings.

Besides the seasonal cycle, fluctuations on the order of a few days to a few weeks are visible in the time series shown in Figure 5.2 and in its spectrum plotted in Figure 5.3a). These variations are mainly driven by effects of synoptic scale (Hogg et al. 1981; Ciotti et al. 1987), such as frontal passages. The spectrum at the synoptic station in Payerne has peaks at periods of half a day and one day. Small peaks are also visible for periods of 8 h (1/3 day) and 6 h (1/4 day) which might be a result of non-sinusoidal diurnal or semi-diurnal variations. Similar spectra are found for other stations in the Swiss Plateau.

Figure 5.6 shows the mean diurnal cycle of the wet refractivity measured at the synoptic station in Payerne in the period from the beginning of 2006 to the end of 2007. The semi-diurnal cycle is slightly visible, but the variations do not differ significantly from the daily mean. Large seasonal

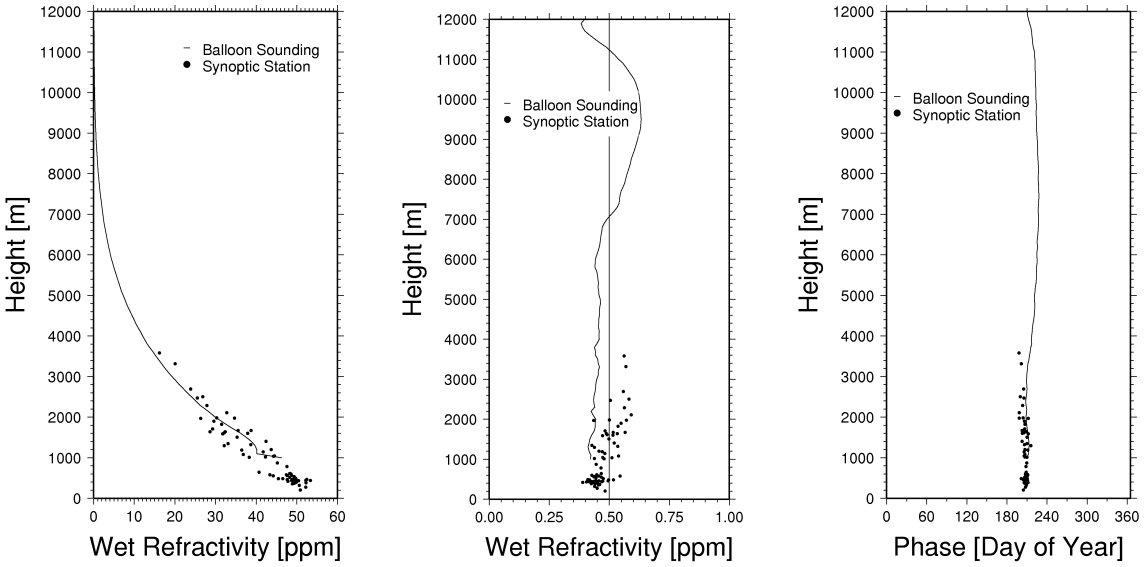

(a) Mean a (b) Relative amplitude b (c) Phase θ

Figure 5.4: These plots show a) the mean wet refractivity a, b) the relative seasonal amplitude of wet refractivity b, and c) the phase shift of the maximum θ. All parameters are estimated from synoptic stations at noon in Switzerland (dots) or from balloon soundings launched at Payerne (lines). The measurement period consists of 2 years of data.

and synoptical variations superimpose the diurnal signal. Analyzing the data from different seasons separately, the diurnal variations are significant in the summer half year. The variations account for about 6-8% of the daily mean, as shown in Figure 5.7a). During winter, no semi-diurnal cycle is visible, but, a small diurnal cycle with an amplitude of few percents of the daily mean is still recognizable.

As the wet refractivity is a compound quantity depending on meteorological quantities, such as partial water vapor pressure, temperature and horizontal wind speed, the diurnal cycle of these meteorological quantities are also investigated (see Figures 5.7b)-d)). Like the wet refractivity, the partial water vapor pressure also shows a semi-diurnal cycle. Contrary to that, the temperature and the horizontal wind do not. The relative variation during the day is also much smaller for the temperature than for the partial water vapor pressure. To quantify the impact of the diurnal temperature and partial water vapor variation on the wet refractivity, partial derivatives of Rüeger's wet refractivity formula (see Equation 2.8) are computed:

$$\frac{\partial N_{\text{wet}}}{\partial P_{\text{wet}}} = \frac{k_2}{T} + \frac{k_3}{T^2}, \tag{5.2}$$

$$\frac{\partial N_{\text{wet}}}{\partial T} = -k_2 \frac{P_{\text{wet}}}{T^2} - 2\,k_3 \frac{P_{\text{wet}}}{T^3}. \tag{5.3}$$

with

$$k_2 = 71.2952\,\text{K}\,\text{hPa}^{-1}$$
$$k_3 = 375463\,\text{K}^2\,\text{hPa}^{-1}$$

Assuming a partial water vapor pressure of 10 hPa and variation of ± 0.5 hPa, which is similar to that of the diurnal cycle in Payerne, results in a diurnal wet refractivity variation of ± 2.3 ppm. For a temperature of 293 K with a diurnal variation of ± 5.8 K, we get a variation of ∓ 1.8 ppm in wet refractivity. This shows that the impact of the diurnal partial water vapor cycle on the diurnal wet refractivity variation is about 20-25% larger than that of the diurnal temperature variation.

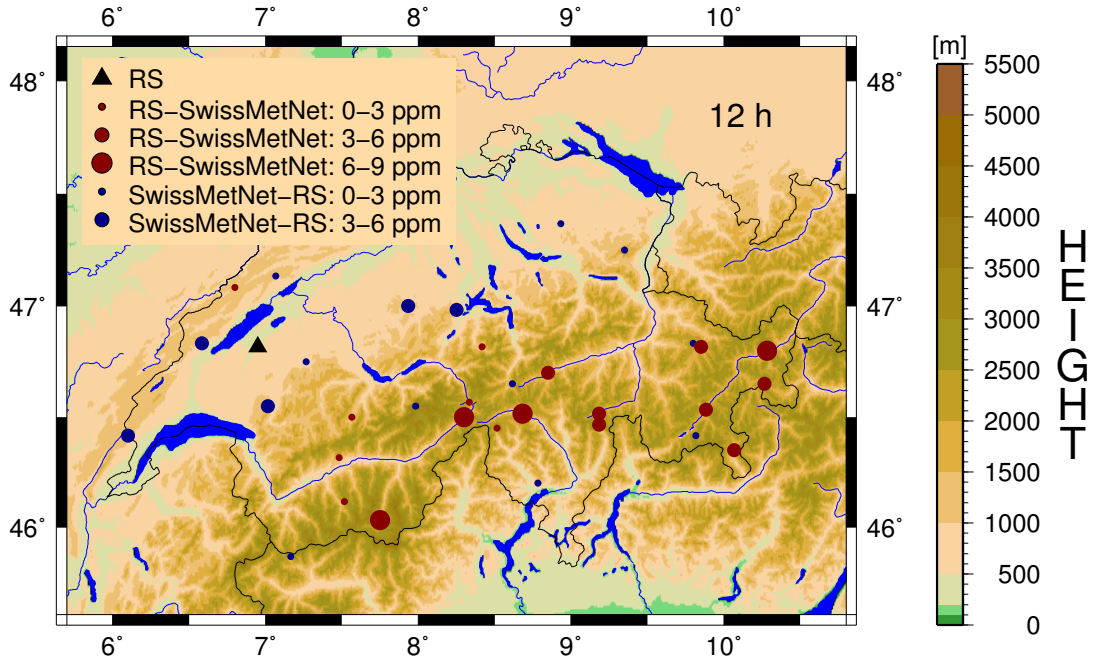

(a) Noon

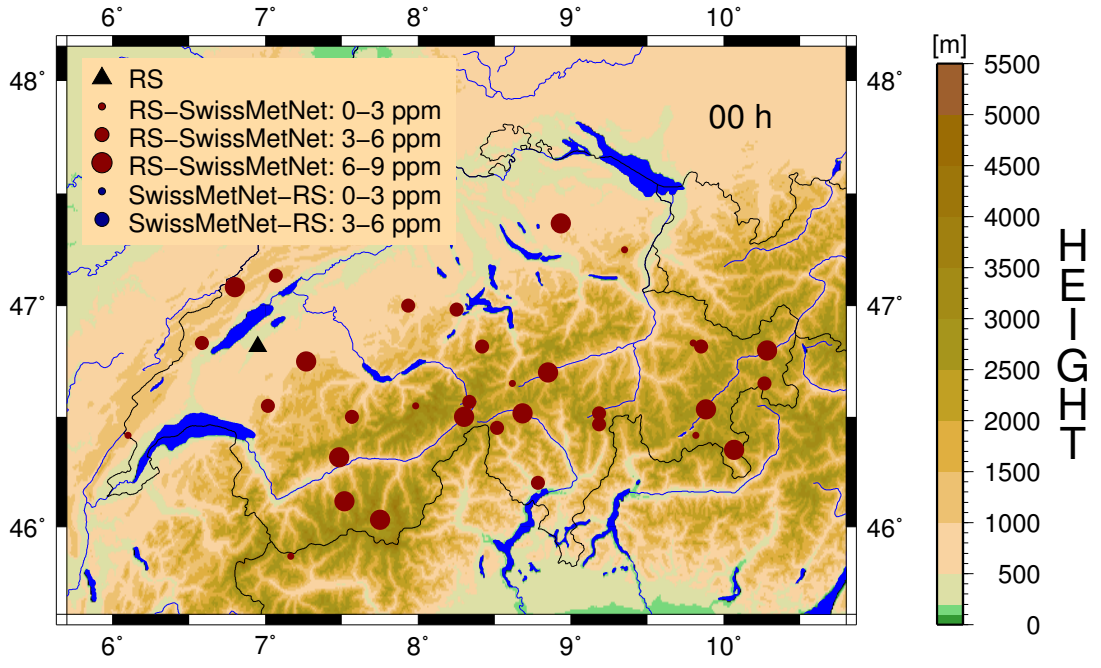

(b) Midnight

Figure 5.5: Difference of wet refractivity measured at the synoptic stations (SwissMetNet) and at the corresponding height observed by balloon soundings (RS) above Payerne. The values are averaged over a period of 2 years.

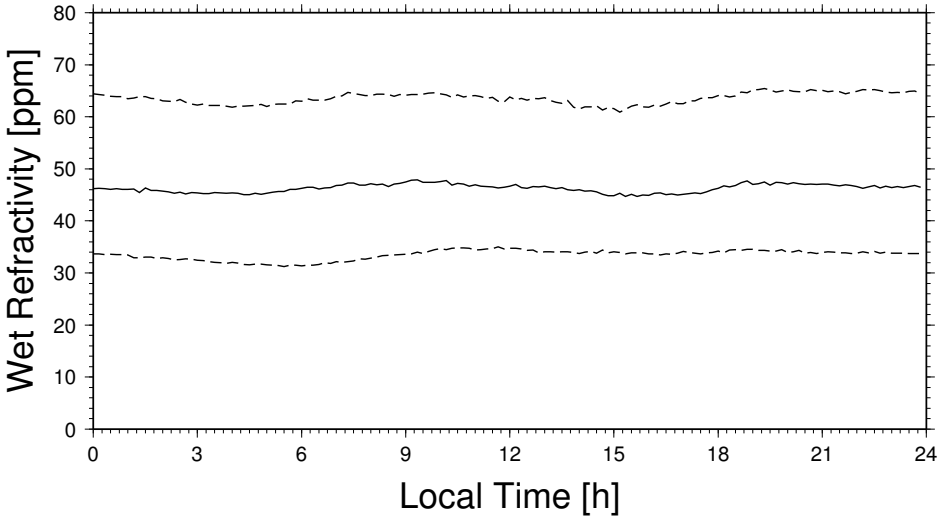

Figure 5.6: Diurnal variation of the wet refractivity at the synoptic station in Payerne. The data set spans 2 years. The solid line represents the median and the dashed lines the 25%-quantiles.

So far, temporal variation of the wet refractivity a few meters above the Earth's surface have been analyzed. In the following, we will discuss the question to which height above Earth's surface the diurnal cycle can be observed. Figures 5.8a) and c) show the diurnal variation of the wet refractivity and of the zenith total delay during July 2006. Both quantities show similar diurnal variations. Assuming that 1 ppm wet refractivity corresponds to 1 mm of zenith wet delay and that the diurnal wet refractivity variation linearly decreases with height, the variation would have to be observable up to 2 km above the Earth's surface in order to match the diurnal cycle of the zenith path delay. This indicates that during the summer, diurnal variations of wet refractivity are observable up to a few kilometers above Earth's surface in the investigated area.

The synoptic station in Payerne is located in the planetary boundary layer and is, therefore, affected by effects observed in this layer. How do the temporal variations look like above the planetary boundary layer? The synoptic station on the Mount Säntis is located at 2500 m above mean sea level and is assumed to be located in the free atmosphere most of the time (Livingstone 1997). Note that planetary boundary layer can reach stations at this height especially during summer (Collaud Coen et al. 2011). Figure 5.3b) shows the amplitude spectrum of the wet refractivity on Mount Säntis for periods of one hour to a few years. The time series of the station on Mount Säntis is also dominated by a seasonal cycle as seen for the station in Payerne (see Figure 5.3a)). The diurnal cycle has the second largest amplitude and this amplitude is even larger than those related to synoptic effects. Compared to the synoptic station in Payerne, the diurnal variation is much stronger on Mount Säntis whereas variations on the synoptic scale are of the same order of magnitude. These observations are remarkable with respect to the considerably lower wet refractivity typically measured at Mount Säntis (2500 m altitude and about 26 ppm wet refractivity) compared to that at Payerne (500 m altitude and about 50 ppm wet refractivity). These relatively larger amplitudes might be related to orographic effects and to thermal convection. Air motions driven by synoptic scale systems, such as frontal passages, but also by local wind systems, cause moist air to rise across mountain ridges. This leads to a rapid increase of the humidity on the mountain ridges. After the passage of such a system, the wind velocities decrease and the supply of moist air from lower layers reduces or even stops. Hence, the humidity decreases on the mountain ridges. As a result of this, larger amplitudes of humidity are measured on mountain ridges compared to stations located in the plains. A similar effect is caused by thermal convection. At sunrise, the air near the Earth's surface is heated and begins to rise on the mountain ridges. Compared to air on the mountain ridge, the lifted air is more moist. As a result of this, the humidity increases on the mountain ridges. In the late afternoon, the thermally driven wind decreases and subsidence

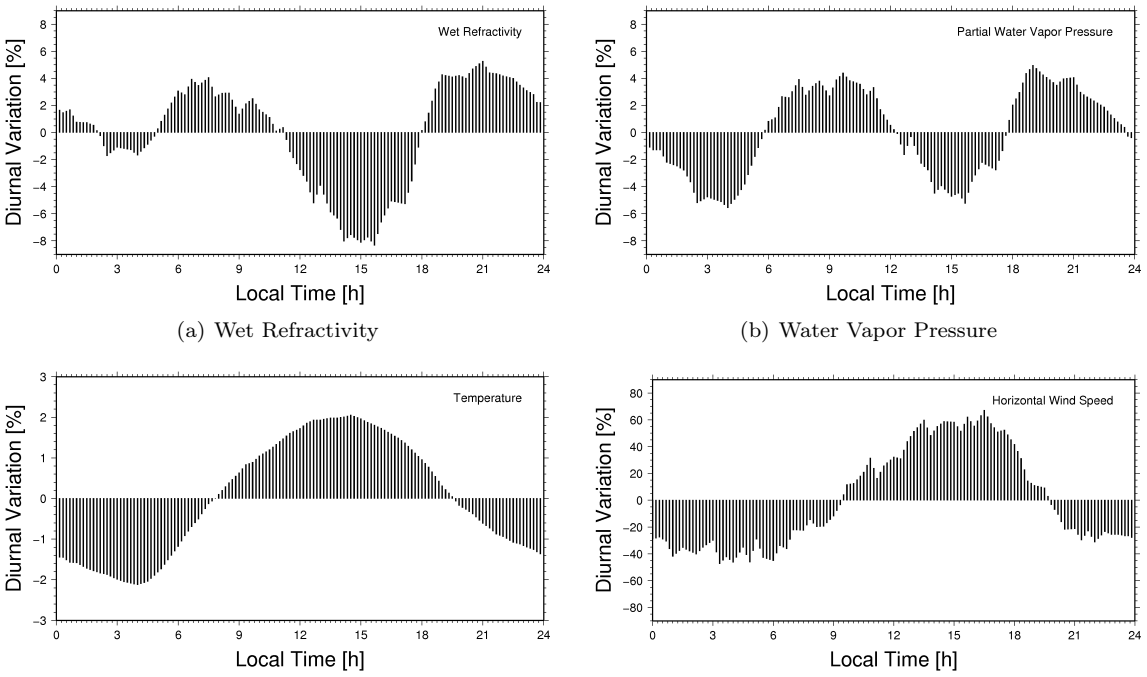

(a) Wet Refractivity

(b) Water Vapor Pressure

(c) Temperature

(d) Wind Speed

Figure 5.7: Mean diurnal variability as percentage of the diurnal mean value at the synoptic station in Payerne for July 2006: a) wet refractivity b) partial water vapor pressure c) temperature and d) wind speed.

increases. Hence, the humidity measured at the mountain ridges reduces. This leads to a diurnal amplitude larger than observed at stations located in the plains. Jungfraujoch is another station located on a mountain ridge on 3500 m altitude. This station shows a similar diurnal variation as the station on Mount Säntis. The semi-diurnal cycle is missing altogether (see Figure 5.8b)). This shows that the peaks of the higher harmonics in the spectrum are mainly related to the non-sinusoidal shape of the diurnal cycle for the stations showing the same wind regime as the stations Mount Säntis and Jungfraujoch. Further investigations on wet refractivity variations show that synoptic stations in the Swiss Plateau and in the inner alpine valleys mostly have a semi-diurnal and a diurnal cycle during the summer half year whereas stations at higher altitudes only show a diurnal cycle.

Zenith total delays estimated from GPS phase observations show similar diurnal variations as that of wet refractivity measured 2 m above the Earth's surface, especially during the summer half year. This suggests that diurnal variations observed in the zenith delays during the summer time are mainly driven by effects in the boundary layer. A comparison of two sites located at different altitudes is shown in Figures 5.8a)-d). Payerne is at about 500 m and Jungfraujoch at about 3500 m altitude. Although the zenith wet delay in Payerne is about 2-3 times larger than that at Jungfraujoch, the amplitude of the diurnal cycle at Jungfraujoch is as large as that at Payerne.

Figure 5.9a) shows the maximum amplitude of the mean diurnal variation of July 2008 computed from the analysis of the numerical weather model COSMO-2 at 2000 m altitude. The largest amplitudes are found where the Earth's surface approaches the 2000 m level (see Figure 5.9b)). The mean diurnal variation at the 2000 m level during the July 2008 is shown in Figures 5.10a)-h) for different day times (every 3 hours). Above mountains, the diurnal maximum is usually reached during the afternoon. Above the larger plains such as the Padan plain and above inner alpine valleys, the diurnal variation is counter-cyclic. The maximum is observed between the late evening and midnight, the minimum in the early afternoon.

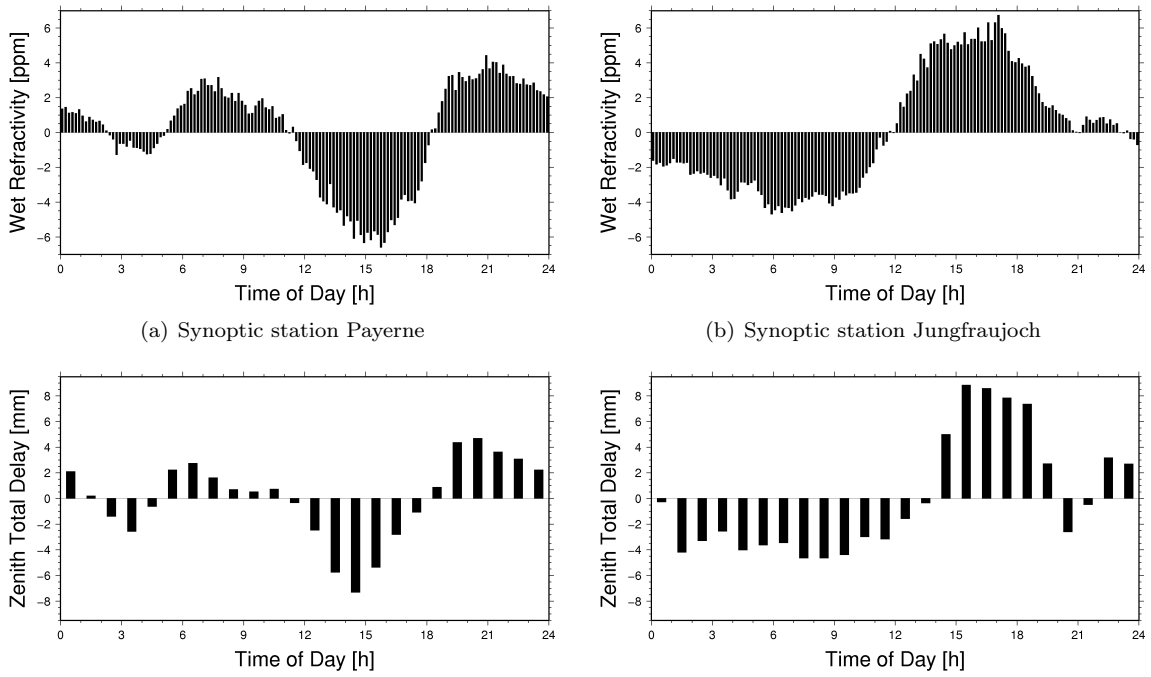

(a) Synoptic station Payerne

(b) Synoptic station Jungfraujoch

(c) GPS station Payerne

(d) GPS station Jungfraujoch

Figure 5.8: Comparison between wet refractivity measured 2 m above ground (a and b) and zenith total delays estimated from GPS phase observations (c and d) during July 2006. The ordinate shows derivation from daily mean. Payerne is located in the Swiss Plateau at 500 m altitude and Jungfraujoch is on a 3500 m high mountain station. Periods of wet refractivity variations between one hour and a few days are considered.

An hypothesis to explain why the wet refractivity is larger during the day than during the night near the Earth's surface is that evapotranspiration during the day increases the wet refractivity close to the Earth's surface and condensation processes lead to lower wet refractivities near the Earth's surface during the night. This effect explains why the wet refractivity is larger during the day than during the night near the Earth's surface, but it cannot explain the semi-diurnal cycle in the plains and inner alpine valleys. At least in valleys, local wind systems seem to play an important role. Solar radiation heats the air near the Earth's surface. As warm air is less dense than cold air, the warm air moves uphill the valleys and the valley faces (see Figure 5.11). This leads to subsidence of cold dry air in the middle of the valley and to an ascent of the wet warm air along the mountain ridges. The temporal change of the wet refractivity at the bottom of the valley, therefore, reflects the counteracting processes of the local increase of wet refractivity by evapotranspiration and the advection of the dry air. If the diurnal cycle of advection differs from that of evapotranspiration, i.e, if there is a phase difference between these two processes, we observe a kind of semi-diurnal cycle at the bottom of the valleys. On the other hand, wet air is advected during the day above mountain ridges. Thus, the time segment where wet air is advected coincides with that when evapotranspiration occurs. This may explain the observation that no semi-diurnal cycle is visible above mountain ridges.

5.2 Discretization Error

In tomographic reconstruction, the wet refractivity field is usually discretized. We use constantly parametrized voxels in this investigation. A horizontal grid resolution of the same order of magnitude as the mean inter-station distance is commonly chosen (Troller 2004; Lutz 2009; Bender et al.

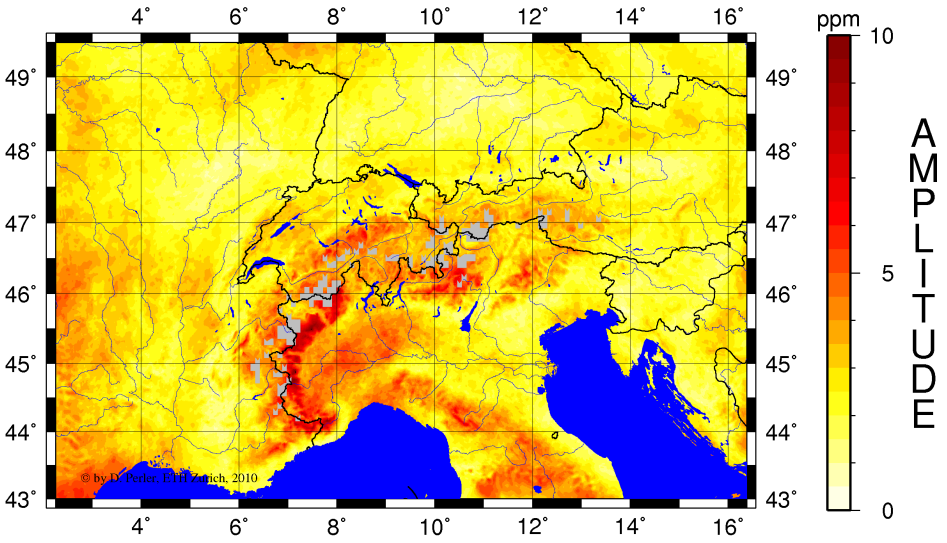

(a) Diurnal amplitude

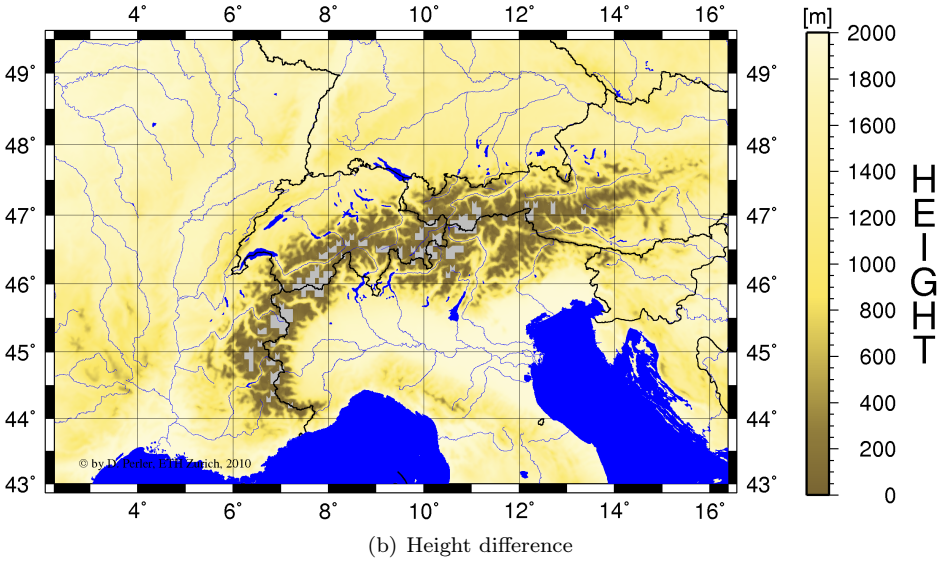

(b) Height difference

Figure 5.9: a) Mean diurnal amplitude of the wet refractivity at 2000 m altitude in July 2008 computed from the COSMO-2 numerical weather model. b) Height difference between the 2000 m level and the Earth's surface.

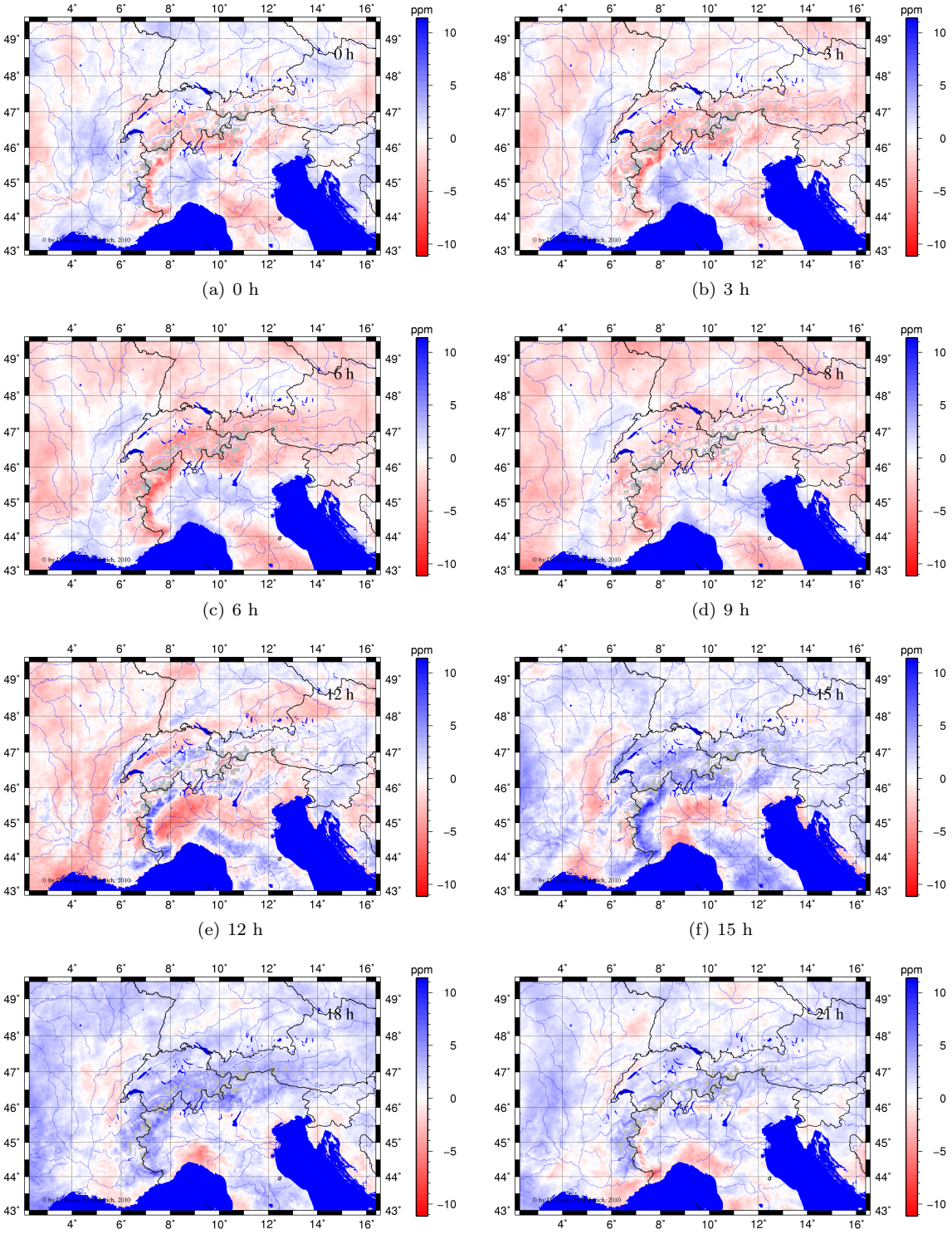

(a) 0 h (b) 3 h

(c) 6 h (d) 9 h

(e) 12 h (f) 15 h

(g) 18 h (h) 21 h

Figure 5.10: Deviation of wet refractivity from the daily mean at 2000 m altitude in July 2008 computed from the COSMO-2 numerical weather model. The figures show the differences every 3 hours in local time, respectively.

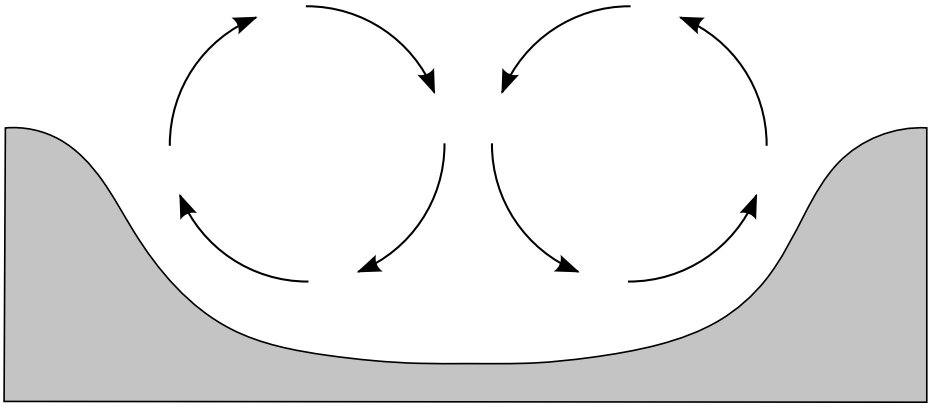

Figure 5.11: Cross section of a valley with schematic wind circulations during the afternoon (e.g. Stull 1999)

2009). The AGNES network, which is used in this work, has a mean inter-station distance of about 30 km. In our setup, a grid resolution of about 37 km is used. The vertical resolution decreases with height. The lowest layers are a few hundred meter and the top layer is about 4.5 km thick. For this resolution, we investigate spatial variations of the wet refractivity field on the subgrid-scale. The goals of the analyses are a) to determine the discretization error assuming a perfect tomography algorithm, and b) to estimate the systematic part of this error. This knowledge will help us to decide whether a bias correction is necessary and how it could look like. The analysis will give us also an estimation of the upper bound of the achievable accuracy.

Since the wet refractivity of the atmosphere is not exactly known, we use the analysis of the high-resolution weather model COSMO-2. It has a horizontal grid spacing of about 2 km and the temporal resolution is 1 hour. The variation of the refractivity of the subgrid-scale is computed for different day times (0 h UTC, 1 h UTC, ..., 23 h UTC) over a period of 1 month. Data of 4 months at different seasons (April 2008, July 2008, October 2008, and January 2009) are considered. The following algorithm is used:

1. Compute the mean voxel wet refractivity $\overline{N}_{j,k}$ from the weather model data $N_{i,k}$ for each voxel j at each time step k. The set $\mathcal{V}_j$ contains all indices i of the weather model grid points belonging to voxel j.

$$\overline{N}_{j,k} = \frac{1}{|\mathcal{V}_j|} \sum_{i \in \mathcal{V}_j} N_{i,k}$$

2. Calculate the residual at weather model grid point i in voxel j.

$$\Delta N_{i,k} = N_{i,k} - \overline{N}_{j,k}; \qquad \text{for } \forall i \in \mathcal{V}_j$$

3. Compute the bias and the standard deviation of the residuals at each grid point i of the weather model over time. The set containing the time indices is denoted by $\mathcal{T}$.

$$\overline{\Delta N}_i = \frac{1}{|\mathcal{T}|} \sum_{k \in \mathcal{T}} \Delta N_{i,k} \tag{5.4a}$$

$$\sigma_i = \sqrt{\frac{1}{|\mathcal{T}| - 1} \sum_{k \in \mathcal{T}} \left(\Delta N_{i,k} - \overline{\Delta N}_i \right)^2} \tag{5.4b}$$

Figure 5.12 shows the mean and standard deviation of the discretization error at different day times interpolated at the level 2000 m above mean sea level during July 2008. The bias within a grid box varies in the range of ±2 ppm during the night and ±5 ppm during the day. Generally, the range of observed biases is slightly larger in alpine regions than in flat areas, such as the Swiss Plateau. Especially during day time, topographic patterns can be recognized. A positive bias is often observed above mountain ridges. On the other hand, negative biases are found above larger valleys (e.g. Rhone valley or the upper Rhine valley) or near lakes (Lake Constance or Lake Neuchâchtel).

Looking at the standard deviation, large differences can be observed between the plots during night and early morning and those at noon and in the evening. During the night and early morning, the standard deviations are around 1-3 ppm and hardly vary within grid boxes. In contrast to this, large variations within grid boxes can be seen during day time. Standard deviations are in the range between 3-9 ppm and the largest ones are observed in the foothills of the Alps.

How does the discretization error change with height? To answer this question, we compute the bias and standard deviation of the discretization error in the same way as described in the previous paragraphs using equations 5.4a and 5.4b, respectively. However, we calculate the fields not only for the 2000 m level, but also for levels between 500 m and 5000 m in 100 m steps. For each level and field, the quartiles are computed from the values located within the grid. The quartiles at each level are plotted for the bias and for the standard deviation field as Box-Whisker plots in Figure 5.13a) and b), respectively. All calculations are based on COSMO-2 analyses data from July 2008.

Looking at Figure 5.13a), biases between ±12 ppm are observed. The range of observed biases is largest between 900 and 2100 m. The decrease of the bias range with the height above this layer is expected, as the wet refractivity decreases with height, too. Below this layer, the reason is not obvious. In the layers below 900 m, data is only partly available in alpine regions because Earth's surface is often above the top of these layers. As a result of this, alpine regions can less contributed to the range of the observed biases in these layers. This considerably influences the range of observed biases in these layers as the largest ranges are observed in such alpine regions.

The median varies only little and is seldom beyond ±1 ppm. Especially in the higher layers, oscillations of the median around zero are observed. They are related to the vertical grid discretization: As the refractivity within a voxel is assumed constant, the median of the bias is negative in the upper part of the voxel and positive in the lower part. It is also clearly visible how the wavelength of the oscillations increases with height. This increase corresponds to the increase of the voxel thickness with height. A similar effect is visible for the inter-quartile range (difference between the 75%- and 25%-quartile). They are clearly larger near the voxel boundaries than in the middle of the voxel.

Figure 5.13b) shows Box-Whisker plots for the standard deviation at different heights. The median varies between 2-5 ppm with the maximum at 1600 m above mean sea level. This is the same height as on which the largest range of the biases are observed (see Figure 5.13a)). The inter-quartile ranges (IQR) for the standard deviations are proportional to their medians and vary between 1-2 ppm. It is supposed that the decrease of the median and the IQR with height above 1600 m altitude is related to the decrease of wet refractivity with height and the increase below this altitude to planetary boundary layer effects.

In Figures 5.14a)-d), the histograms of the discretization error of 4 voxels at different heights are shown. They illustrate the distribution of the discretization errors. Normal distributions with the same mean value and standard deviation as the data are plotted as dashed lines. Comparing the 2 distributions indicates that the kurtosis of the sample distributions are different: The histograms are more peaked than the dashed lines representing the fitted normal distribution. Concerning skewness, the histograms are not skewed (a) and b)) or show only a very weak skewness (c) and d)).

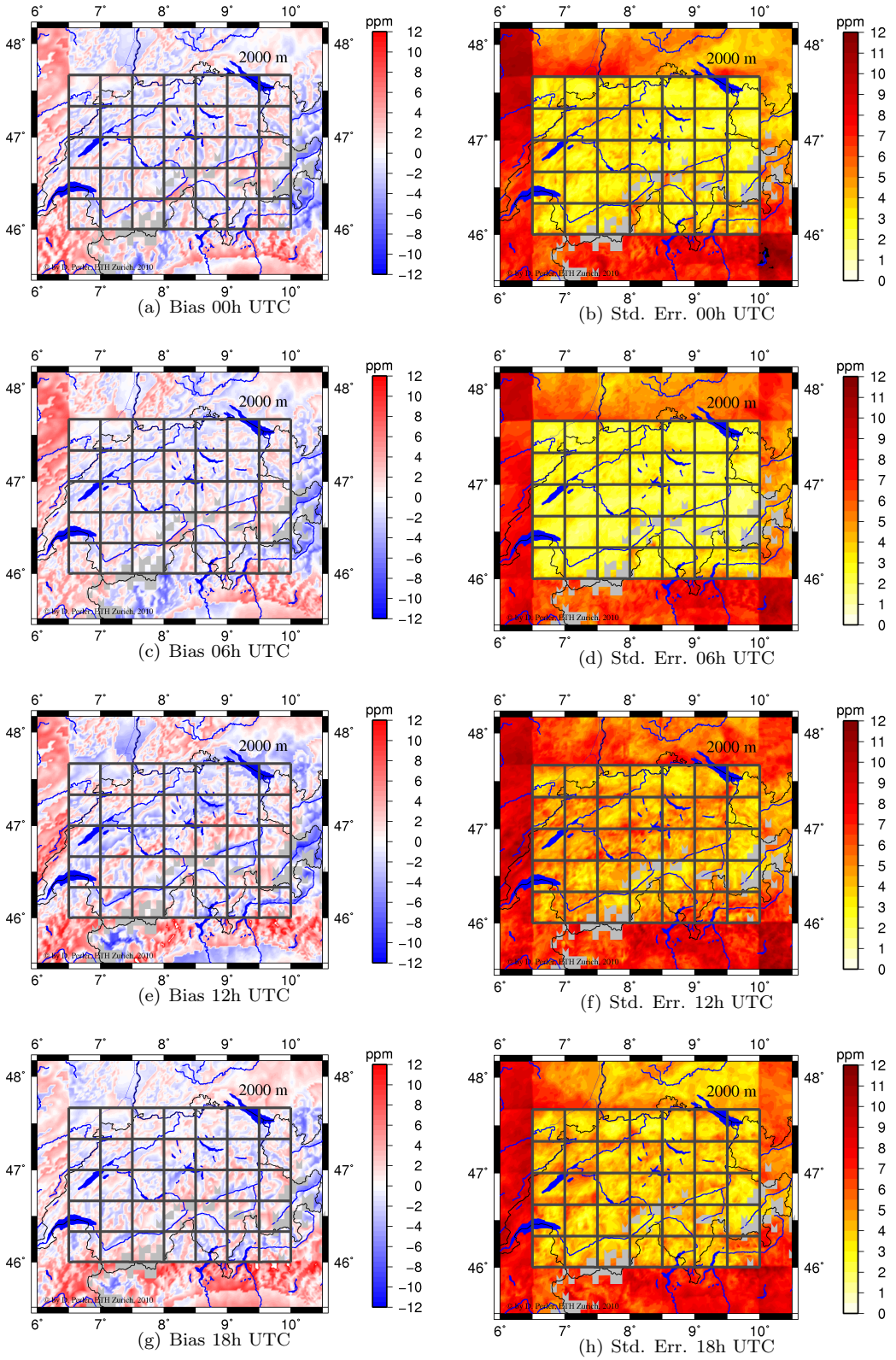

(a) Bias 00h UTC (b) Std. Err. 00h UTC

(c) Bias 06h UTC (d) Std. Err. 06h UTC

(e) Bias 12h UTC (f) Std. Err. 12h UTC

(g) Bias 18h UTC (h) Std. Err. 18h UTC

Figure 5.12: Discretization error of the wet refractivity field at the 2 km level during July 2008 using a grid of 37-38 km horizontal resolution.

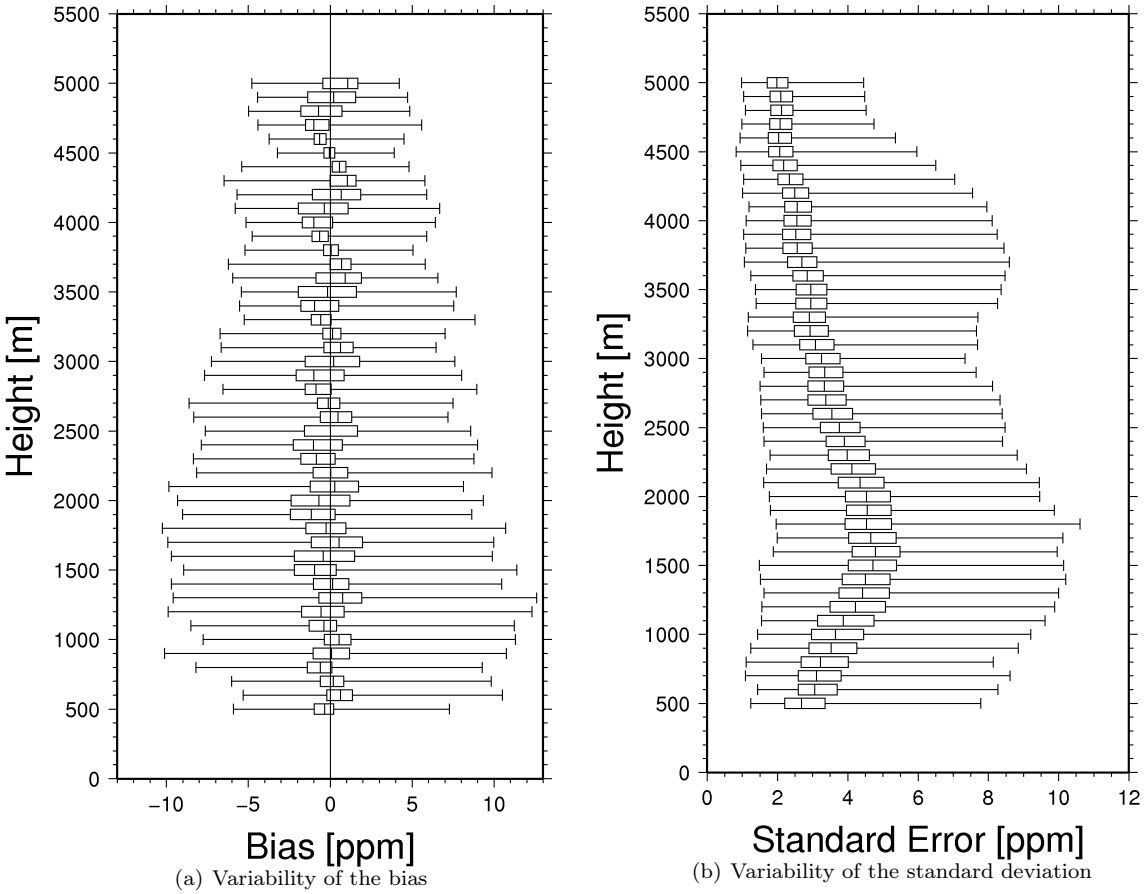

(a) Variability of the bias

(b) Variability of the standard deviation

Figure 5.13: Box-Whisker plot of the variability of the discretization error within the voxels (bias and the standard deviation) on different height levels during July 2008.

Figure 5.15 shows quantile-quantile plots of the discretization error for the same 4 voxels as in Figure 5.14. As already visible in the Figure 5.14, the distribution of the data and the fitted normal distribution mainly differs in the kurtosis. The Pearson's χ^2-test (Rice 1995) is carried out to check for normality. In all 4 cases, the test clearly rejects the hypothesis that the data is normally distributed.

In Figure 5.16 the bias and the standard deviation of the discretization error is plotted for different seasons at the 2000 m level at 12 h UTC. The largest biases can be observed during summer. The biases are significantly lower during the other months, especially during winter. In winter, usually they do not exceed 2 ppm. The spatial distribution is similar throughout the year. During summer, 75% of the biases are significantly different from zero (assuming normally distributed biases and a significance level of 5%). Although the biases are smaller during winter than during summer, 83% of them are significantly different from zero (spring: 80% and autumn: 77%). The standard deviations of the discretization error are shown in Figure 5.16b). During summer and winter, standard deviations of up to 9 ppm and up to 3 ppm are observed, respectively. Locations with a large bias do not necessarily show a large standard deviation.

5.3 Representation of the discretization error

The method of empirical orthogonal functions (EOF, see Appendix C) is used to find characteristic spatial patterns in the discretization error and how they evolve over time. In a further step, we will

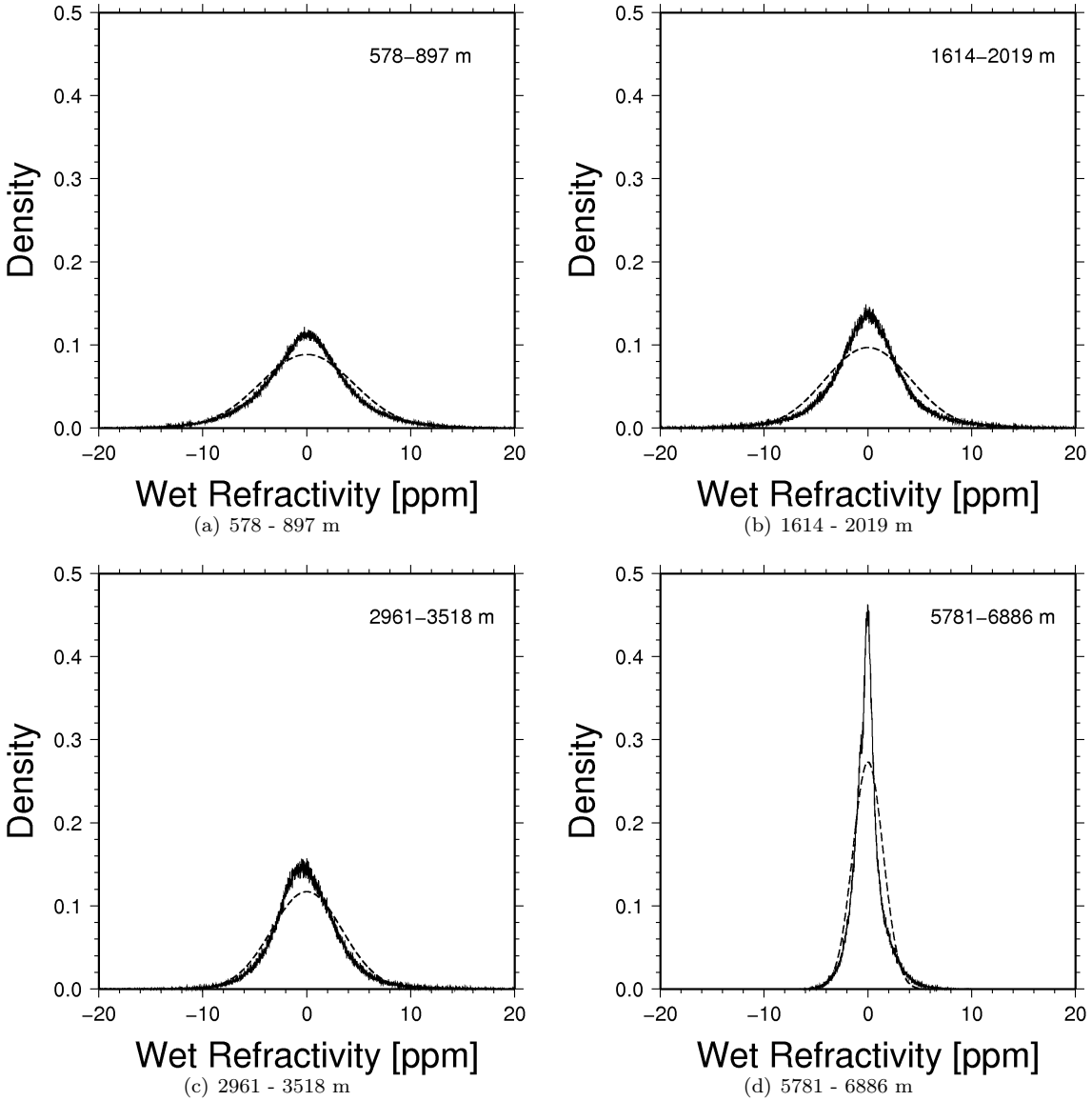

(a) 578 - 897 m

(b) 1614 - 2019 m

(c) 2961 - 3518 m

(d) 5781 - 6886 m

Figure 5.14: Histograms of the difference between voxel mean value and actual values in a voxel (thick lines) and fitted normal distributions (dashed lines).

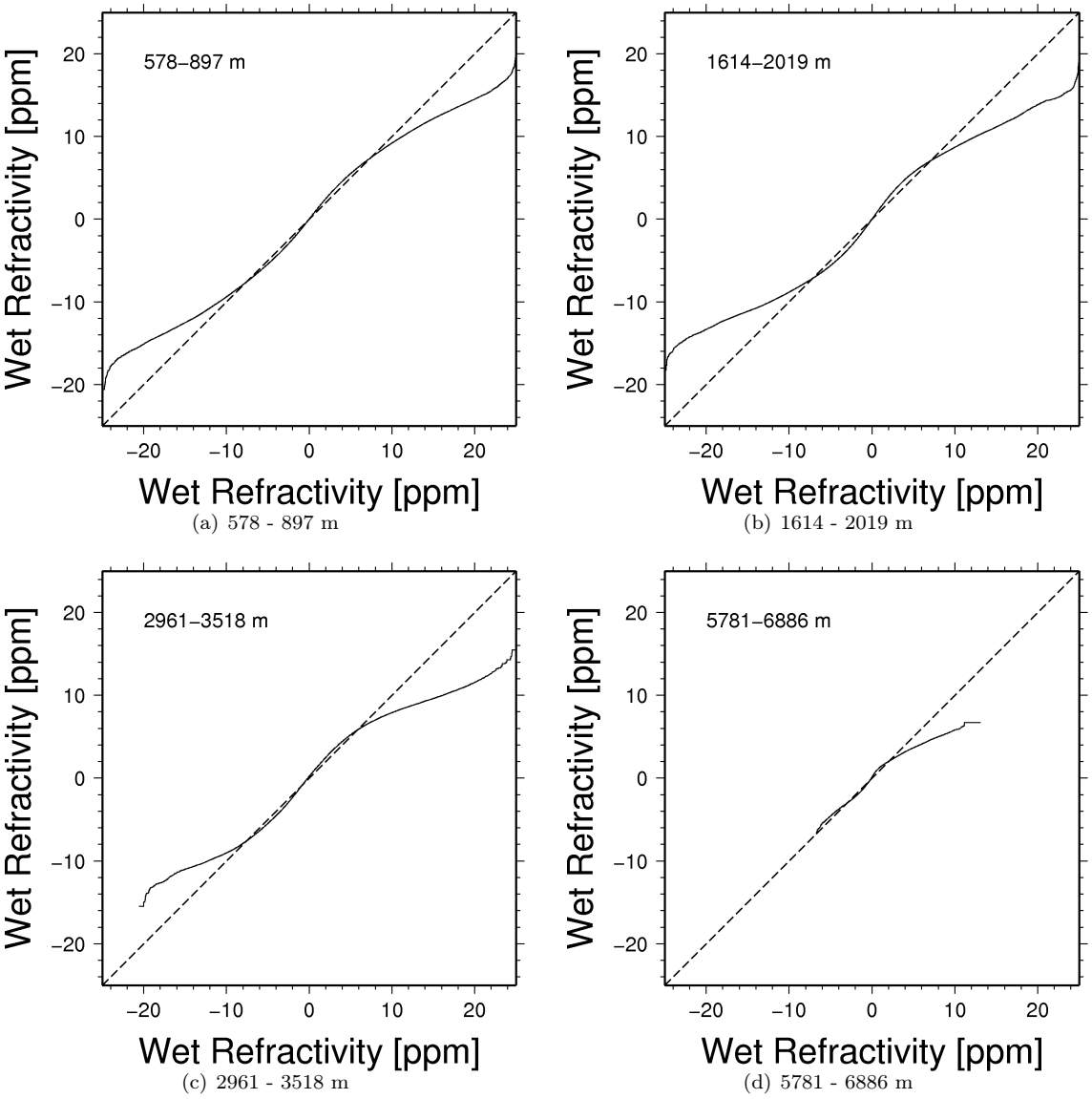

(a) 578 - 897 m

(b) 1614 - 2019 m

(c) 2961 - 3518 m

(d) 5781 - 6886 m

Figure 5.15: Quantile-quantile plots of the discretization error compared to fitted normal distributions.

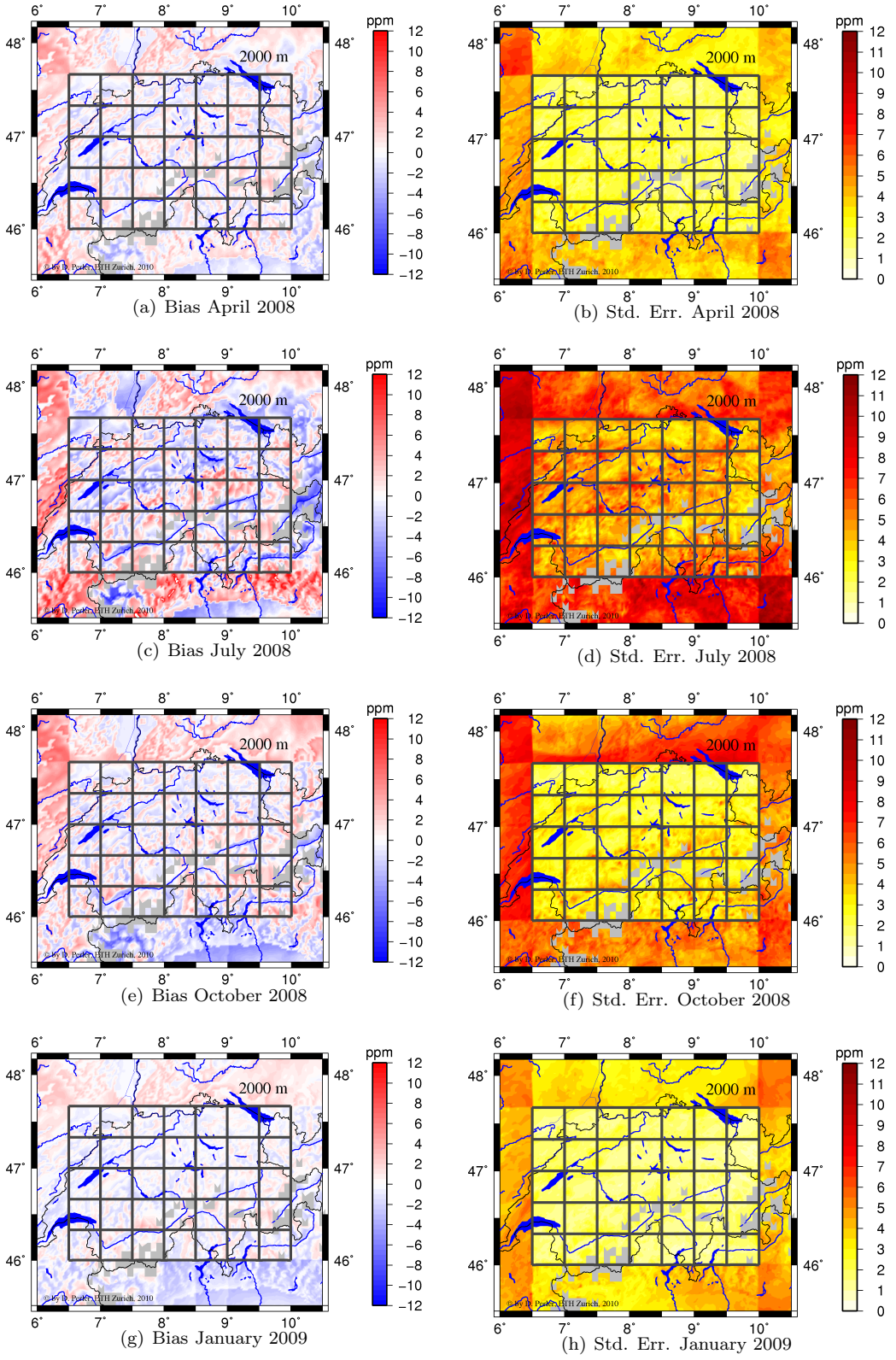

(a) Bias April 2008 (b) Std. Err. April 2008

(c) Bias July 2008 (d) Std. Err. July 2008

(e) Bias October 2008 (f) Std. Err. October 2008

(g) Bias January 2009 (h) Std. Err. January 2009

Figure 5.16: Discretization error of the wet refractivity field at the 2 km level during different seasons at 12h UTC using a grid of 37 km horizontal resolution (gray lines). The results are based on data from the NWP COSMO-2 with a horizontal grid resolution of 2 km.

compare the principle patterns with the topography, the gradients of the Earth's surface and the slope aspect. The results can be used to implement a bias correction model for any observations used in the tomography. As systematic local variations are already removed in the observations, the tomographic model would not have to take them into account. As a result of this, a coarser grid could be used in the tomographic processing. To get a wet refractivity field including these local variations, the correction model would have to be added on the tomographic result. Another application would be to use the main orthogonal functions in the tomographic processing. Instead of estimating the refractivity at the grid points, one estimates the factor of the main empirical orthogonal functions. A main advantage of this technique is that local effects can be taken into account with a relative small number of parameters.

The data set is the same as that used for the previous investigations. The EOF is computed for the discretization error using a grid with a horizontal resolution of about 38 km on the 2000 m level. We have restricted us to evaluate only an single level due to the high computational demands of EOF. To allow comparisons to previous investigations, the 2000 m level is investigated.

The months April, July, October 2008, and January 2009 are evaluated together. The time series has a length of 2928 hours and a sampling rate of 1 hour. At epoch, 8090 data points are available at the 2000 m level. Figure 5.17a) shows the mean value of the time series at each point of the 2000 m level. It looks similar to the bias computed for the month July 2008 (see Figure 5.16). This is expected as this month shows much larger biases than the other three months.

The time series of each point at the 2000 m level is reduced by its mean value. On this data, we compute the principle components and their variances (eigenvalues). The cumulative explanation of the variance can be computed from the eigenvalues.

$$s^2_{\text{total}} = \sum_{i=1}^{n} \lambda_i \tag{5.5a}$$

$$\alpha^2_{j,\text{total}} = \sum_{i=1}^{j} \frac{\lambda_i}{s^2_{\text{total}}} \tag{5.5b}$$

where λ_i denotes the i-th eigenvalue with $\lambda_i \geq \lambda_{i+1}$ and n the number of eigenvalues. The number of eigenvalues is equal to the smaller value of the length of the time series and of the number of time series. The total variance is denoted by s^2_{total} and the cumulative explanation by $\alpha^2_{j,\text{total}}$.

Figure 5.17b) shows the cumulative explanation of the principle components. To explain 80% of the total variance, the first 187 out of 2928 principle components are needed.

In Figures 5.18a), c), e), and g), the first 4 principle components are plotted. The first two factors seem to show patterns related to the topography. The inner Alpine valleys, the Jura Mountains and the Swiss Plateau are well recognizable. The discretization error is compared to several quantities, therefore, related to the topography. These are

- Height above mean sea level
- Angle of slope
- South-North component of the slope
- West-East component of the slope.

Looking at the correlation coefficients between the discretization errors and these quantities, no significant or only weak correlations are found. The first factor shows a weak correlation (0.244) with Earth's surface height and a weak negative correlation (-0.258) with the slope aspect in North-South direction. The second factor is also correlated with the slope aspect in North-South direction, but stronger with 0.338.

The third factor shows, especially in the Swiss Plateau, a North-West to South-East gradient within the grid boxes. Similar patterns are visible in the Alps in the forth factor. The forth factor also shows a weak correlation of 0.248 with the angle of slope.

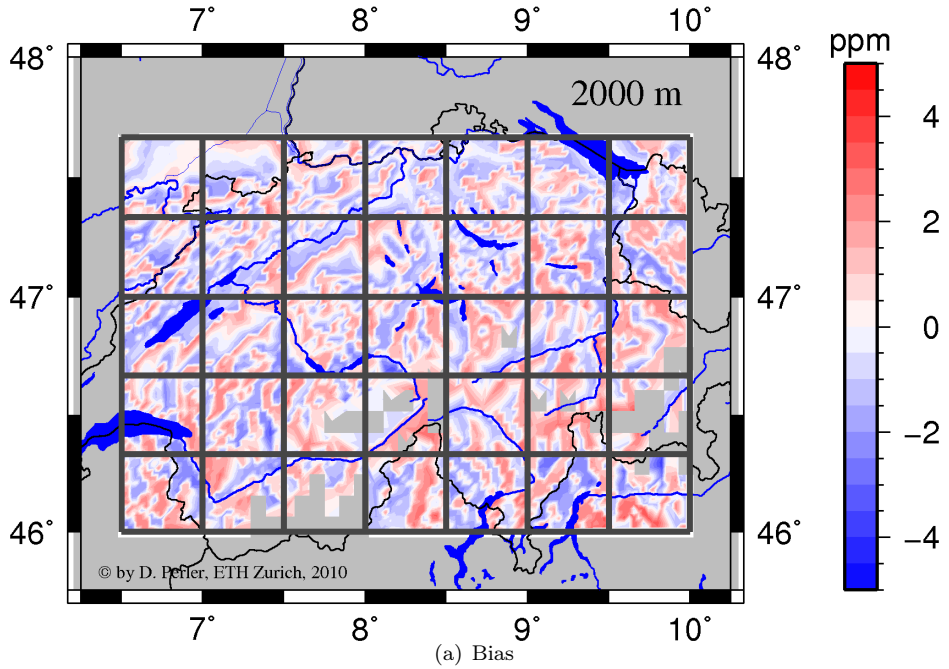

(a) Bias

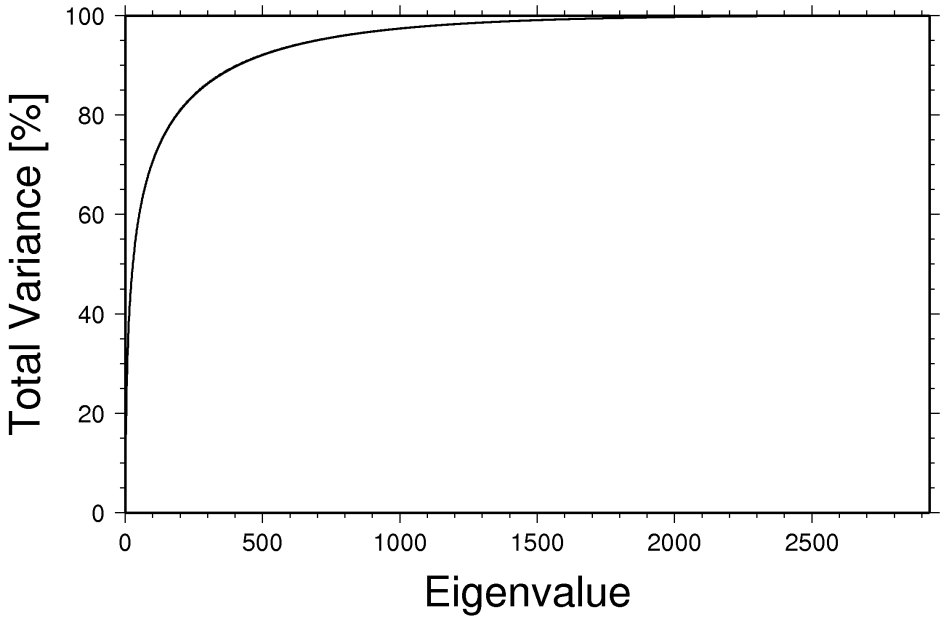

(b) Cumulative representation of the variance through factors

Figure 5.17: Discretization error caused by the discretization grid (dark gray lines) at an altitude of 2000 m. a) Bias of the discretization error computed for the months April, July, October in 2008, and January 2009 from the NWP model COSMO-2. Light gray shaded areas indicate regions with no data. b) Cumulative representation of the principal components of the discretization error.

Looking at the time series of the scores for these 4 factors, we can see that they show variations on the synoptic time scale. In addition, the first two factors have a weak seasonal cycle. In contrast to them, the third and fourth do not.

The correlation of the first two factors with the topography and the presence of a seasonal cycle are indicators for a relationship with solar effects. Therefore, a diurnal cycle is expected especially during summer. A Fourier analysis is carried out for the time series of the scores for summer and winter. The amplitude spectra are shown in Figure 5.19. In the summer, diurnal cycles are clearly visible for all 4 time series. The first two show an amplitude of 70 and 60 ppm, respectively. The amplitudes for the other two time series are smaller and below 40 ppm. During winter, the time series show only weak diurnal signals. These findings support the relationship between solar effects and the first few principle components of the discretization error.

The previous investigations have shown diurnal signals in the principle components of the discretization error. This is the motivation for a closer look at the diurnal cycle. For July 2008, the mean diurnal discretization error $\bar{e}_{\phi,\lambda,i}$ at position (ϕ, λ) at day time i is computed.

$$\bar{e}_{\phi,\lambda,i} = \frac{1}{\|\mathcal{E}_i\|} \sum_{e_{\phi,\lambda,t} \in \mathcal{E}_i} e_{\phi,\lambda,t} \tag{5.6}$$

with

$$\mathcal{E}_i = \{e_{\phi,\lambda,t} | \text{day time of } t = i\}$$

where $e_{\phi,\lambda,t}$ is the discretization error at point (ϕ, λ) at time t. The mean diurnal discretization error is computed hourly from wet refractivity values interpolated at the 2000 m level from COSMO-2 analyses.

For this diurnal discretization errors, the empirical orthogonal function are again computed. In Figure 5.20, the cumulative explanation of the variance for the principle components are plotted. The first component explains already more than 60% of the variance and the 4 first components more than 80%.

The first 4 principle components of the mean diurnal discretization error are shown in Figure 5.21. There are topographic patterns recognizable in the factors as observed in the factor previously computed from the discretization errors, but, the errors are again only weakly correlated with topographic quantities. Factor 1 and 3 show a weak correlation of 0.257 and 0.299 with the Earth's surface height, respectively. Factor 3 shows also a weak correlation of 0.239 with the angle of slope. For the other factors, no significant correlations are found with one of the quantities related to the topography.

In the left column of Figure 5.21, the time series of scores for these 4 factors are shown. The series for the first factor features a single oscillation with the maximum at noon. The second series reaches its maximum in the late afternoon (17h UTC). After 19 h UTC, the values quickly decrease until midnight. The decrease slows down during the night and ends at 11 h UTC. Comparing these diurnal variations with the diurnal variation of solar radiation and temperature, they are in good agreement. The first factor has the diurnal maximum at the same time as the solar radiation. The second factor has a similar diurnal variation as the temperature with the maximum occurring during the second part of the day. This agreement indicates a relationship between the first two factors and solar radiation.

5.4 Investigations of the process noise using a random walk model

So far, the spatial distribution, the discretization error and diurnal cycles of the wet refractivity field have been considered. In this section, the focus will be on the prediction error of the random walk model used in AWATOS 2 (see Section 3.4). Time series analyses are carried out with the goal to answer questions such as how the prediction error increases with lead time, whether the random walk is a suitable model to describe the time series and how the stochastic parameters of this model have to be set. The outcome of these investigations will be the basis to configure

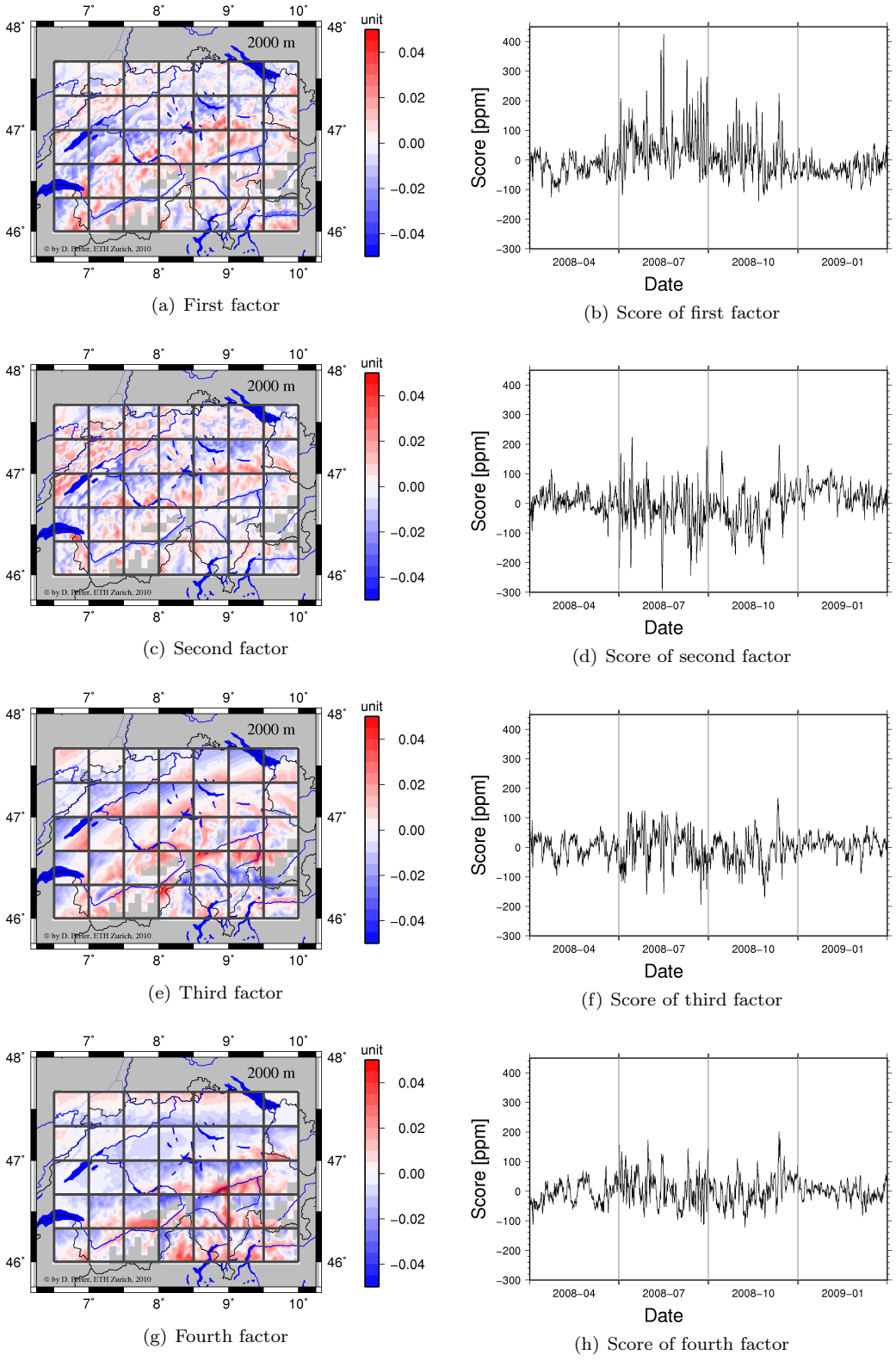

(a) First factor

(b) Score of first factor

(c) Second factor

(d) Score of second factor

(e) Third factor

(f) Score of third factor

(g) Fourth factor

(h) Score of fourth factor

Figure 5.18: Factors (left column) and their scores (right column) for the first 4 principle components of the wet refractivity discretization error at the 2000 m level. The data set consists of 4 months of data at different seasons from the numerical weather model COSMO-2 with a grid resolution of 2 km. The coarse grid (gray lines) has a grid spacing of 37 km.

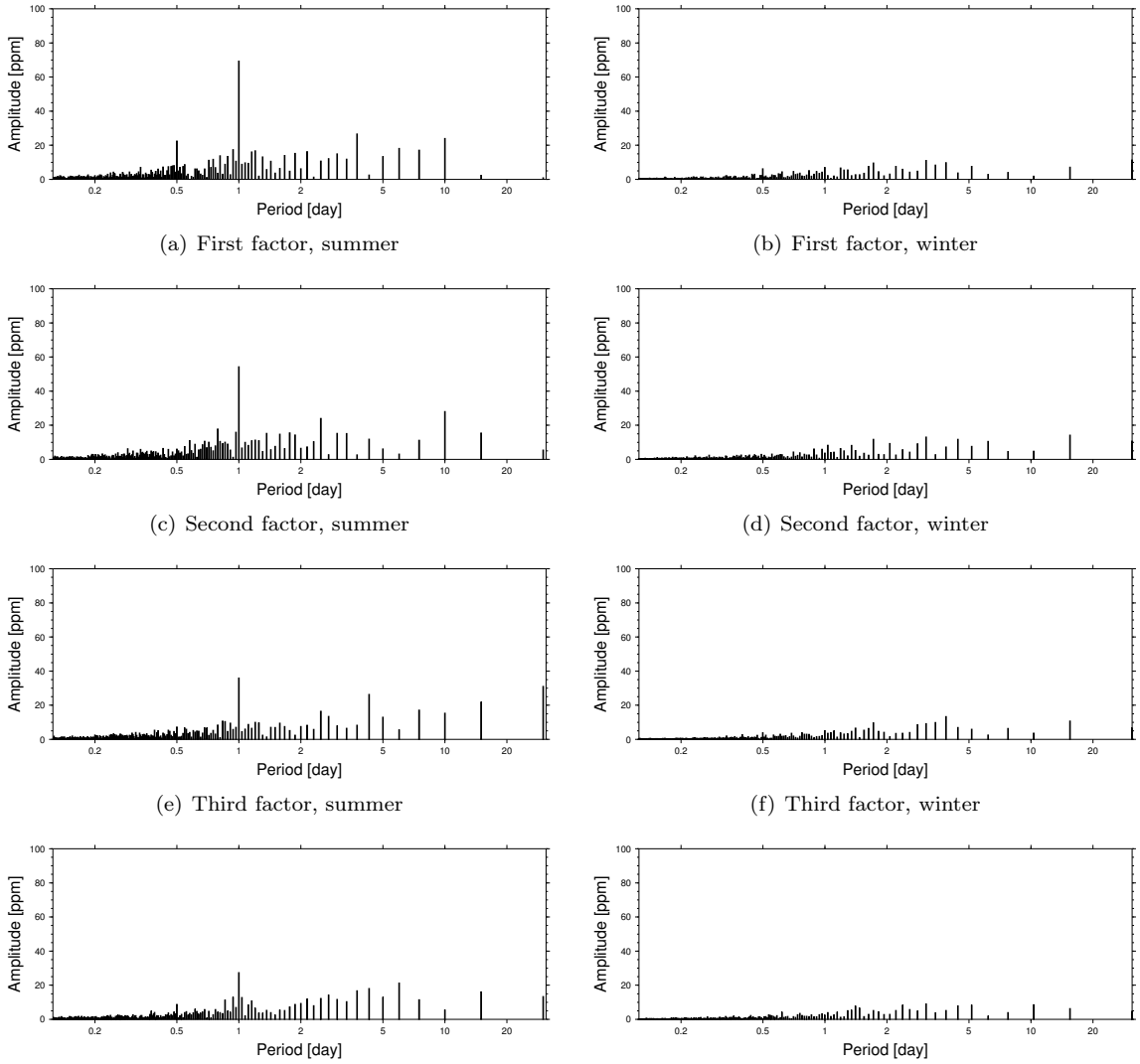

(a) First factor, summer

(b) First factor, winter

(c) Second factor, summer

(d) Second factor, winter

(e) Third factor, summer

(f) Third factor, winter

(g) Forth factor, summer

(h) Forth factor, winter

Figure 5.19: Amplitude spectra of the principle component's scores. The principle components are computed on the basis of the wet refractivity discretization error at the 2000 m level over Switzerland using data from the analysis of the numerical weather model COSMO-2. The data set consists of 4 months in years 2008 and 2009.

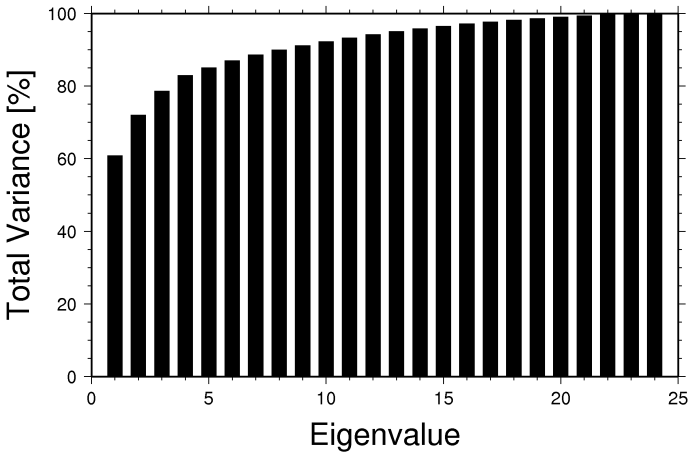

Figure 5.20: Cumulative explanation of the variance through factors for the diurnal discretization error of the wet refractivity field at the 2000 m level.

the Kalman filter, especially the propagation step, in AWATOS 2. The investigations are based on two time series: a) meteorological measurements from the synoptic network SwissMetNet in Switzerland and b) data from the numerical weather prediction model COSMO-7 (see Section 4).

5.4.1 Setup, models and methods

Data from the numerical weather prediction model COSMO-7 and from selected stations of the synoptic measurement network SwissMetNet will be used (see Section 4). The data sets span a period of 1 and 2 years, respectively. The data from synoptic stations have the advantage that they are available with a much higher sampling rate (10 minutes) than that derived from COSMO-7 (sampling rate of 1 hour). This is insofar of importance as the sampling rate of our GPS data is 30 seconds and to make any suggestion for the stochastic model parameters at this time scale requires data with a similar sampling rate. With the use of data from synoptic stations, one is much closer to this sampling rate than with NWP model data. Moreover, the data from the synoptic stations may represent the reality better as they do not suffer from modeling effects like the NWP model data. A drawback of the data from synoptic stations is that they are measured at Earth's surface and, therefore, may not be representative for the entire atmosphere. To counteract this point, stations exposed on mountain peaks and ridges are considered.

Both data sets provide the meteorological quantities pressure, temperature, and relative humidity. The wet refractivity is computed from these quantities using Equation 2.8. For the COSMO-7 data set, voxel averages are computed (see Section 5.2). Thus, the time series analysis is based on point observations for the SwissMetNet data set and on voxel averages for the COSMO-7 data set.

Statistical properties of the underlying process of the prediction model (see Section 3.4) and of the time series derived from the two data sets are compared among each other. The investigation is based on the increments

$$Y_t^{(n)} = X_t - X_{t-n} \tag{5.7}$$

where X_t denotes the stochastic process at a voxel or at a station at time t and n the lead time (difference between actual and forecast time). A path of the process Y_t will also be referred to as *integrated time series* in this subsection. The error of the prediction model is

$$\tilde{Y}_t^{(n)} = X_{t+n} - \mathrm{f}(X_t, n) = X_{t+n} - X_t = Y_{t-n}^{(n)} \tag{5.8}$$

where $\mathrm{f}(X_t, n)$ is the propagation model and n is the prediction lead time. The function $\mathrm{f}(X_t, n)$ is equal to X_t for the prediction model used in AWATOS 2 (see Section 3.4). One can see that the propagation error corresponds to the process $Y_t^{(n)}$. The prediction model is based on a stochastic differential equation (SDE). The statistical properties of this equation will be compared to those of

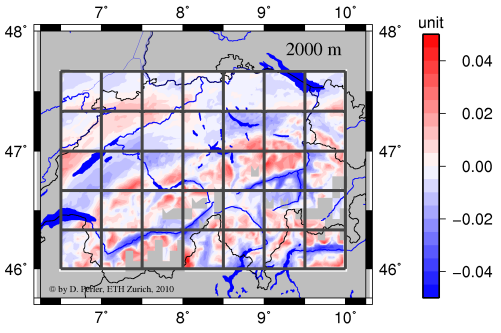

(a) First factor

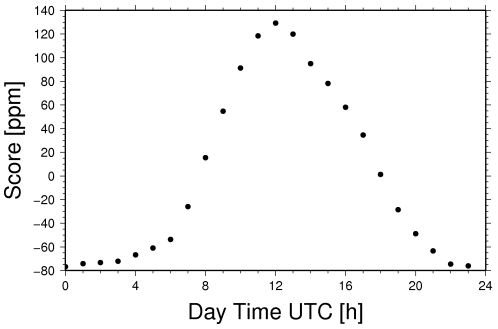

(b) Score of first factor

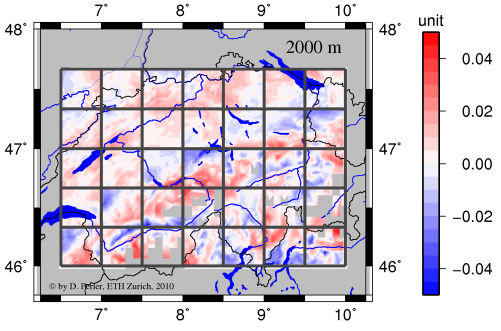

(c) Second factor

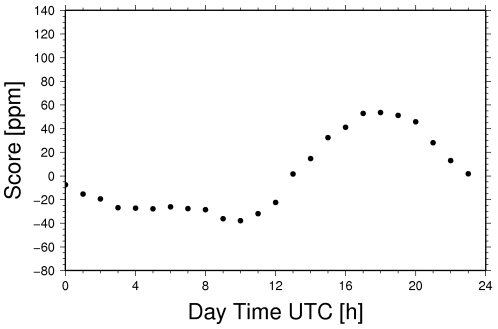

(d) Score of second factor

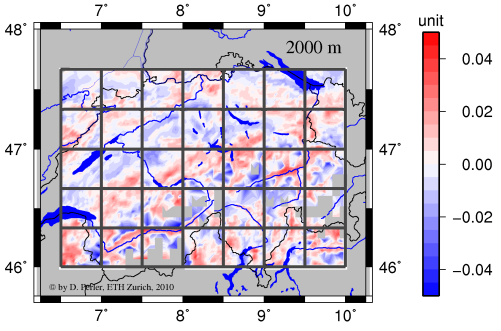

(e) Third factor

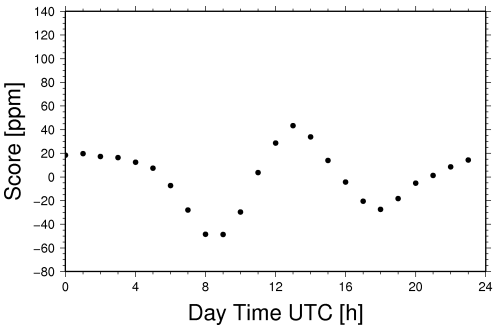

(f) Score of third factor

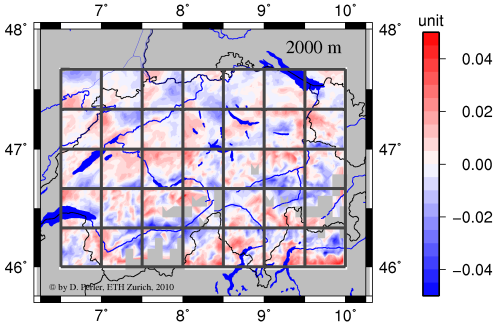

(g) Fourth factor

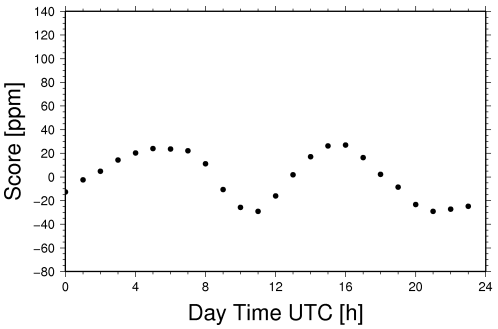

(h) Score of fourth factor

Figure 5.21: Factors (left column) and their scores (right column) for the first 4 principle components of the mean diurnal discretization error of the wet refractivity field. The data set consists of data from July 2008 from the NWP model COSMO-2 with a grid resolution of 2 km. The coarse grid (gray lines) has a grid spacing of 37 km.

the process $Y_t^{(n)}$. To be a suitable prediction model, the statistical properties of the SDE should be similar to those observed in $Y_t^{(n)}$. The SDE of the prediction model have the following theoretical properties:

1. Time increments are normally distributed.
2. The expectation value of the increments is zero.
3. Two non-overlapping increments are independent.
4. The variance of the increment increases proportionally to the time step n.
5. It is assumed that the covariances between the increments of two time series at different locations depend on the height difference and the distance between them (see Section 3.4).

For the two data sets, the computation of the increment's properties are subdivided into tasks. Each task will refer to one of these properties. Note that for all tasks, stationarity of the time series is assumed.

Distribution of the increments: The distribution of the increments are illustrated by histograms. For each SwissMetNet station and lag, a histogram is computed and the parameters *sample mean* and *sample variance* are estimated. The density function of the normal distribution corresponding to the estimated parameters is plotted in the same figure as the histogram. This allows to easily compare their shapes. In addition, quantile-quantile plots are generated with the estimated density function on the abscissa and with the histogram data on the ordinate (see Rice 1995). The first two properties are verified by this task.

Autocorrelation of the integrated time series: Autocorrelation functions are computed for each SwissMetNet station from the integrated time series. The autocorrelation function gives information about the correlation between values of a process at different epochs as a function of the time difference between two epochs. This time difference will also be referred to as *lag*. If the increments are independent of each other, the autocorrelation function is a Dirac delta function. Otherwise the function may show values significantly different from zero for non-zero lags. If the time series show no correlation in cases where the lag differs from zero, this indicates that the prediction model is a suitable model for the refractivity field with respect to property 3.

Variance of the increments in dependence of different lead times: The variance of the Y_t with respect to the lead time is computed for each SwissMetNet station and for each voxel. Assuming stationarity and ergodicity, the variance $\sigma^2(n)$ can be computed from the integrated time series with lead time n:

$$\sigma^2(n) = \mathrm{Var}(Y_{t-n}) = \frac{1}{|\mathcal{T}| - 1} \sum_{t \in \mathcal{T}} (x_t - x_{t-n})^2 \tag{5.9}$$

where $\mathcal{T}$ is the set of epochs and x_t a measured path of the process X_t. The lead-time-dependent variances computed from SwissMetNet data and from NWP model data are compared with each other. The impact of the height on the variance is investigated by comparing lead-time-dependent variances on different height levels. Therefore, the weighted mean of the variances is computed for each voxel layer:

$$\sigma^2_{L_h}(n) = \frac{1}{\sum_{i \in L_h} c_i} \sum_{i \in L_h} c_i \, \sigma_i^2(n) \tag{5.10}$$

where $\mathcal{L}_h$ is the set of voxel indices located in the layer at height $h = 0.5\,(h_{\mathrm{bottom}} + h_{\mathrm{top}})$, c_i the number of COSMO-7 grid points within the i-th voxel, and $\sigma_i^2(n)$ the variance of the prediction error in the i-th voxel at lead time n.

The prediction error of a time step in the Kalman filter is modeled by a lead-time-dependent and by a distance dependent part in AWATOS 2 (see Section 3.4). This subdivision is also applied in the investigations. For the lead-time-dependent part, the following model is investigated:

$$\sigma^2(n) = s^2 \left(1 \; - \exp\left(- \, n \, \frac{\Delta t}{\Delta t_0} \right) \right). \tag{5.11}$$

where s^2 denotes the reference variance, Δt the time difference between two epochs and Δt_0 the scaling time. The parameters Δt_0 and s^2 are fitted using non-linear LSQ adjustment at each station for the SwissMetNet data set and at each voxel for the COSMO-7 data set. Variances for lead times up to 167 hours are considered. For the COSMO-7 data set, the reference variance s^2 is modeled as a function of height. This is the same model as that used in the prediction model (see Equation 3.37):

$$\mathrm{s}^2(h) = s_0^2 \exp\left(- \frac{h}{h_0} \right) \tag{5.12}$$

where h_0 is the scaling height. The investigation of this task is intended to answer the question whether the lead-time-dependent part of the prediction model is a suitable model to describe the time evolution of the wet refractivity field in terms of property 4. If it does, the fitted parameters can be used to configure the prediction model.

Spatial correlation of the prediction error: In this task, the distance dependent part of the prediction model is analyzed. The correlations between the process $Y_{t,i}$ of the i-th voxel and the process $Y_{t,j}$ of the j-th voxel are computed for different lead times. The lead time, for which correlations are computed, ranges from 1 to 167 hours. Using this correlations, horizontal and vertical correlation lengths are estimated and the impact of the lead time on them is investigated. The horizontal and vertical correlation lengths l_0 and Δh_0, respectively, are computed by non-linear LSQ solving one of the following equations

$$\exp\left(- \sqrt{\frac{l}{l_0}} \right) = \rho \tag{5.13}$$

$$\exp\left(- \sqrt{\frac{\Delta h}{\Delta h_0}} \right) = \rho \tag{5.14}$$

where ρ denotes the correlation computed from two integrated time series at different grid points, and l and Δh the horizontal and vertical distance between the two voxels, respectively.

For each voxel layer and lead time, a correlation lengths is computed from all correlations of this layer. The correlation length, dependent on the lead time, will be analyzed for different voxel layers. For estimating the vertical correlation length, correlations of voxels located in the same voxel column are considered. The correlation length is estimated for each lead time. This will show if and how the correlations of the prediction error depend on the lead time. This investigation will provide data to quantify the parameters of the prediction model.

5.4.2 Results and discussion

Figure 5.22 shows histograms of wet refractivity increments with a lead time of 10 minutes for the synoptic stations a) Payerne and b) Mount Säntis. Both distributions are symmetric around zero. The expectation value is zero for both stations. This is also observed for all the other stations considered. A expectation value of zero is expected as a non-zero value would mean that the wet refractivity changes considering a longer period.

The shape of the two histograms differs around the expectation value. The probability density for Payerne smoothly decreases with increasing distance to the origin whereas there are two side peaks at ±0.2ppm for Mount Säntis. This difference might be related to the different surroundings

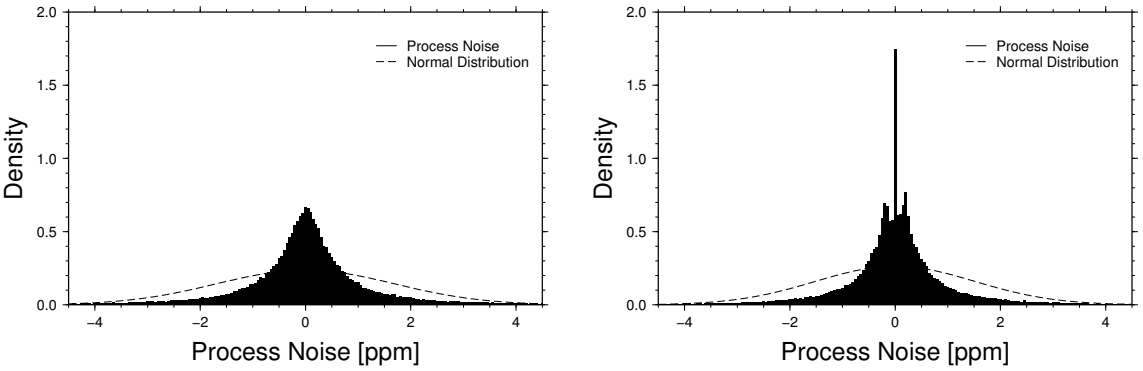

(a) Payerne (b) Mount Säntis

Figure 5.22: Histogram of the wet refractivity increments of a lead time of 10 minutes at the synoptic stations in a) Payerne and b) Mount Säntis. The dashed line represents the density function of the normal distribution with mean and variance equal to those of the wet refractivity increments.

at the stations. Payerne is located in the Swiss Plateau and Mount Säntis is a wind exposed peak at altitude of about 2500 m.

The density function of normal distribution with the same mean value and variance as those of the data are plotted as dashed line in Figure 5.22. The slopes of the faces are less steep for the density functions than for the sampling density. On the other hand, the sample density has a longer tail than the density function. This is also clearly visible in the quantile-quantile plots of Figure 5.23. This investigation has shown that the increments are not normally distributed. However, the sample distribution function and the theoretical distribution function of the prediction error show common properties. Both functions are symmetric around their mean value and both functions have a mean value of zero.

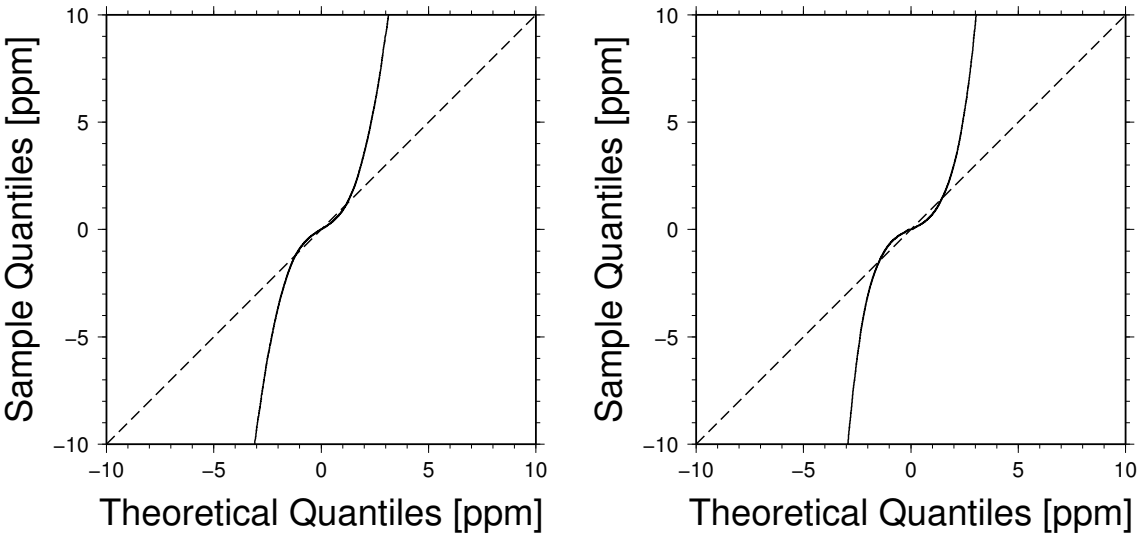

(a) Payerne (b) Mount Säntis

Figure 5.23: Quantile-quantile plot of the sample distribution derived from wet refractivity increments at the synoptic stations a) in Payerne and b) on Mount Säntis and the normal distribution with the same mean value and variance as the increments at the stations.

The autocorrelation functions of the wet refractivity increments of a lead time of 10 minutes are shown in Figures 5.24 for a) Payerne and b) Mount Säntis. The sample autocorrelation function is 1 at a lag of 0 and about -0.2 at a lag of 10 minutes for both stations. For larger lags, only non-significant to very weak correlations are observed. Similar autocorrelation functions are observed for the other synoptic stations. For the prediction error model, the autocorrelation function is a Dirac function as the prediction error of two non-overlapping increments are independent. Comparing this function to those from SwissMetNet stations show that the autocorrelation functions at the SwissMetNet stations can be well approximated by a Dirac function at this time scale.

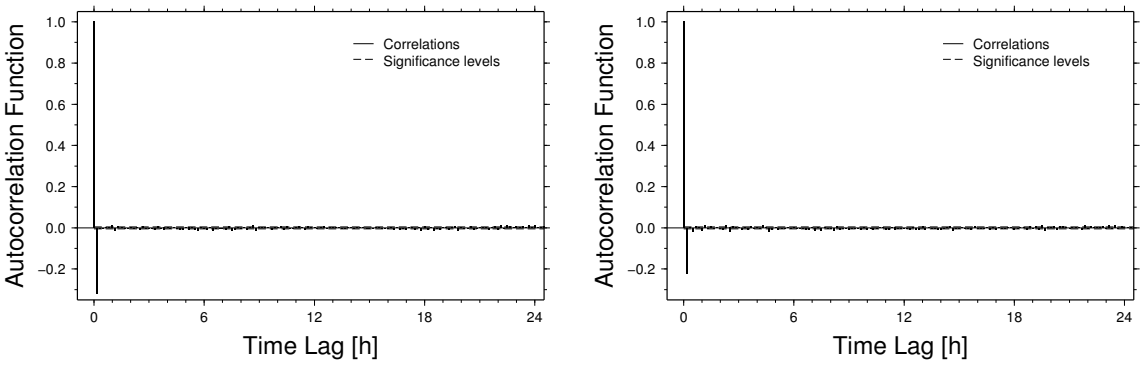

(a) Payerne (b) Mount Säntis

Figure 5.24: Autocorrelation function of wet refractivity increments for a lead time of 10 minutes at the synoptic station a) in Payerne and b) Mount Säntis. Dashed lines represent the significance levels (significance level $\alpha = 0.05$).

How does the prediction error change by increasing the lead time? The implemented prediction model has the property that the variance of the prediction error linearly increases with lead time. For the synoptic station in Payerne, the prediction error variance is computed from its measurements for different lead times. In Figure 5.25, the median (solid line) and the quartiles (dashed lines) of these variances are plotted in dependence of the lead time. The median shows a linear increase with a slop of about 6.5 ppm^2/h for lead times up to about 6 hours. Thereafter, the slope of the curve decreases and begins to oscillate with a period of 24 hours. This plot shows that the modeled prediction error well approximates the behavior of the observed prediction error for lead times between 10 minutes to 6 hours.

The variances of the prediction errors within a voxel layer are collected and the weighted mean value is computed from them for different lead times. These values are plotted in Figure 5.26 as a function of lead time. The curves are computed from data of the numerical weather prediction model COSMO-7. At all heights, the curves show a similar increase of the prediction error variance with lead time as those computed from data measured at SwissMetNet stations. The weighted mean variance linearly increases with lead time for lead times up to 6 hours. The slope varies between 4.9-7.5 ppm^2/h below 2500 m altitude. This shows that the variances of the prediction error of both data sets behave similar and that the prediction error model fits well for lead times up to 6 hours. For larger lead times, the slope of the curves decrease with lead time. If the lead time tends to infinity, each curve approaches an asymptote. The value of these asymptotes seems to depend on the height. Comparing the curves derived from the COSMO-7 data set with those from the SwissMetNet data set, we can see that the values of the asymptotes are of the same order of magnitude.

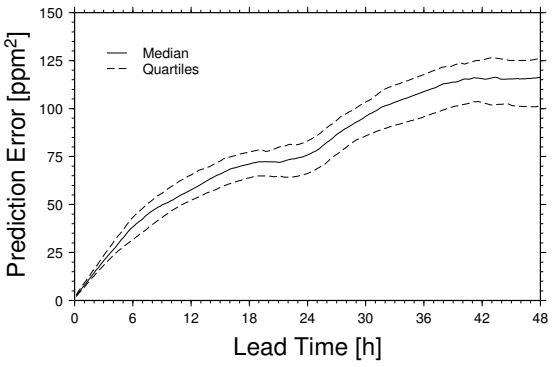

Figure 5.25: Median (solid line) and quartile (dashed lines) of the prediction error variance at the SwissMetNet station vs. lead time.

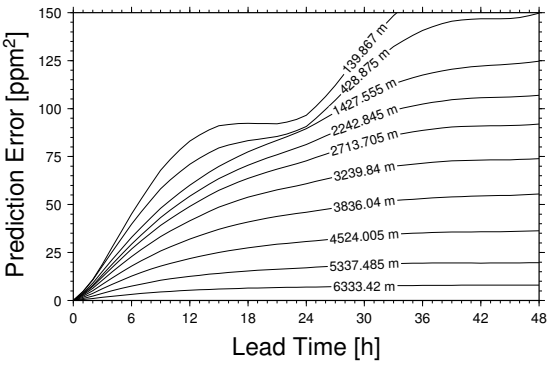

Figure 5.26: Weighted mean of the prediction error variance for different voxel layers vs. lead time. Each curve represents the prediction error variance for a voxel layer. The curves are labeled with the height of the layer ($\frac{1}{2}$ (height$_{\text{bottom}}$ + height$_{\text{top}}$)).

Near the Earth's surface, the prediction error also has a diurnal signal similar to that seen in the SwissMetNet data. The diurnal signal quickly vanishes with increasing height. This observation suggests that the signal is related to effects near the Earth's surface and, therefore, the decrease of the signal is rather connected with height above the Earth's surface than with height above the reference ellipsoid. In the middle and upper troposphere, the variance of the prediction error decreases with height.

For each SwissMetNet station and voxel, the model defined by Equation 5.11 is fitted. It describes the increase of the prediction error variance with the lead time. Weighted mean values are computed for the two model parameters. Each fitted parameter of an SwissMetNet station or of a voxel is weighted by the reciprocal of the parameter's formal variance. Such weighted mean values are computed for the SwissMetNet stations and for each voxel layer.

The scaling time Δt_0 indicates how quick the prediction error variance approaches the reference variance s^2 (asymptote). Comparing the estimated scaling time of the two data sets, the scaling time is significantly smaller for the SwissMetNet data set than for the COSMO-7 data set (see Table 5.1 and Table 5.2). The dashed line in Figure 5.27a) shows the mean value of all fitted scaling times on the basis of COSMO-7 data (see Equation 5.11). In the lower troposphere, the scaling time is up to twice as large as the mean scaling time. In the upper troposphere, the scaling time is smaller than in the lower troposphere.

Table 5.1: Fitted parameters of the model described by Equation 5.11 using SwissMetNet data.

Parameter	**Estimated value**	**Standard deviation**
Reference prediction variance s^2	116.0705 ppm^2	1.3124 ppm^2
Scaling time Δt_0	16.0556 h	0.3363 h

In Figure 5.26, we can see that each curve approaches an asymptote. The value of this asymptote is represented by the parameter s^2 (reference variance) in Equation 5.11. The reference variance is plotted for each voxel layer in Figure 5.27b) indicated by circles. The reference variance exponentially decreases with height and fits well with the model described by Equation 5.12 (dashed line). The estimated parameters are listed in Table 5.2. The fitted model with the parameters Δt_0 and s^2 can be used to configure the prediction model of AWATOS 2.

The spatial correlation of the prediction error is investigated using Equations 5.13 and 5.14. Figure 5.28 shows the horizontal correlation length l_0 as a function of the lead time and of height.

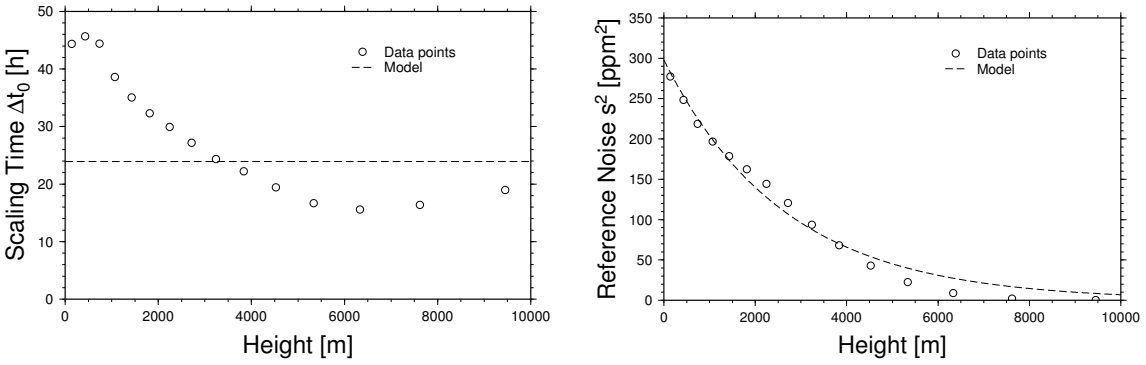

(a) Scaling time Δt_0

(b) Reference prediction variance s^2

Figure 5.27: Scaling time Δt_0 and reference variance s^2 of the prediction error variance (see Equation 5.11) at different heights (circles) and for the model extended by Equation 5.12 (dashed line). The plots are based on COSMO-7 data.

Table 5.2: Fitted parameters of the model described by Equations 5.11 and 5.12 using COSMO-7 data.

Parameter	**Estimated value**	**Standard deviation**
Reference prediction variance s_0^2	297.745 ppm^2	8.355 ppm^2
Scaling height h_0	2650.868 m	136.024 m
Scaling time Δt_0	23.901 h	2.258 h

Horizontal correlation lengths are shortest at about 1 km height. Below and above this altitude, the horizontal correlation length is longer. The question whether the altitude with the shortest horizontal correlation length is related to the planetary boundary layer height might be interesting to investigate.

In layers close to the Earth's surface, a signal with a period of 24 hours is visible. It quickly vanishes with increasing height above the Earth's surface. This indicates that this signal is related to surface effects. Independent of the height, the horizontal correlation lengths increase with lead time. This must be taken into account when the prediction model is configured, as the prediction model of the Kalman filter assumes constant correlation lengths with respect to the lead time.

Figure 5.29 shows the vertical correlation length with respect to the lead time. As observed for the horizontal correlation length, the vertical correlation length increases with lead time and, thus, is not constant. This has to be considered in the configuration of AWATOS 2. Nevertheless, the vertical and horizontal correlation lengths show only a small increase with lead times for lead time shorter than 3 hours.

5.5 Conclusions

In this chapter, the properties of the wet refractivity field in Switzerland have been investigated. On the one hand, the results of these investigations provide numbers to configure AWATOS 2, on the other hand, they show limitations concerning the tomographic processing and the accuracy of the tomographic results.

The main results of the tempo-spatial investigations are:

- The refractivity field in the troposphere is dominated by variations on the synoptical and seasonal time scale.
- Especially during summer, diurnal variations are visible in the lower troposphere. Two different patterns are often observed in data from synoptic stations: a) an oscillation with a period

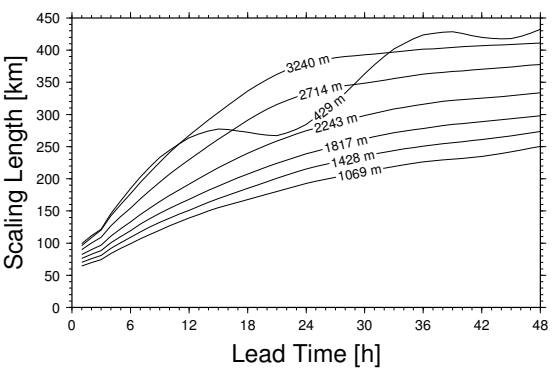

Figure 5.28: Horizontal correlation lengths of the prediction error for different lead times and layer heights. The correlations are computed from COSMO-7 data.

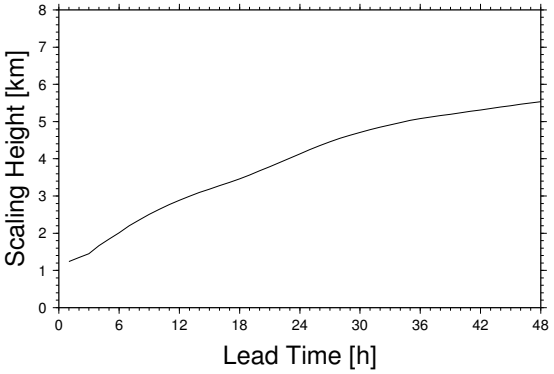

Figure 5.29: Vertical correlation lengths of the prediction error for different lead times. They are computed from COSMO-7 data.

of one day with a maximum in the late afternoon, and b) two oscillations with a period of half a day with maxima around 8 am and 8 pm local time. Amplitudes of oscillations with a period of 24 hours are computed from NWP model data. At 2000 m altitude, mean amplitudes up to 7 ppm (1.0 $\mathrm{g\,m^{-3}}$ absolute humidity) are observed during July 2008. Largest amplitudes are found near the Earth's surface. They decrease with the height above ground. During summer, diurnal variations are also visible in the zenith path delays estimated from GPS phase observations. They are proportional to the wet refractivity variations and show mean amplitudes of 6-8 mm during July 2008. Estimations have revealed that diurnal variations of the refractivity affecting the diurnal variation of zenith path delays are expected to be present up to a few kilometers above ground.

- The assumption that the atmosphere is horizontally layered does not hold in alpine regions. Mean wet refractivities measured on the same altitude but at different locations may differ significantly from each other. At midnight, the mean wet refractivity is smaller if measured near the Earth's surface at high-elevated stations than at the same height for balloon soundings in Payerne. At noon, the opposite is observed for stations in the Swiss planes and the foothills of the Alps. For stations located in the inner alpine valleys, similar differences as at midnight are observed.

- Near the Earth's surface, boundary layer effects and locality have a significant impact on the wet refractivity and on path delays. It is, therefore, expected that they are of importance for tomographic reconstruction of the atmosphere's refractivity field.

Investigations of the discretization error are carried out on a grid of about 37 km horizontal resolution in Central Europe. This is the same grid resolution which will be used for the tomographic construction. The results of these investigations can be summarized as follows:

- The discretization error mainly varies on the synoptic and seasonal time scale. Diurnal and semi-diurnal cycles are also visible, especially during summer. Significant monthly biases up 12 ppm (1.8 $\mathrm{g\,m^{-3}}$) are observed during summer. About 50% of the monthly biases are below $\pm$2ppm ($\pm$0.3 $\mathrm{g\,m^{-3}}$) in the lower troposphere in July 2008. The standard error is typically about 4 ppm (0.6 $\mathrm{g\,m^{-3}}$) considering data from July 2008. During winter, significant biases are also observed. They are significantly lower than those in summer and rarely exceed $\pm$2 ppm ($\pm$0.3 $\mathrm{g\,m^{-3}}$). The standard deviation is also smaller during winter and is about 1-3 ppm (0.1-0.4 $\mathrm{g\,m^{-3}}$). These numbers show the limits of the accuracy which can be reached with a grid resolution of 37 km and constantly parametrized voxels. For more accurate results, the grid resolution needs to be refined and a dedicated GNSS network must be

available. Another possibility would be a more precise prediction model, which exploits the high temporal resolution of GNSS measurements.

- Largest discretization errors occur at an altitude of 1600 m.
- The spatial variation of the discretization shows patterns similar to the topographic pattern. Investigations using the technique of empirical orthogonal functions have shown that the main principle components are weakly correlated with height above ground and surface exposition. The wet refractivity error described by main principle components is dominated by effects on the synoptic time scale but shows a diurnal or semi-diurnal cycle as well.
- The significant biases observed in these investigations show that observations cannot be treated as bias free in view of the tomographic model with the given grid resolution and constant parametrization. This suggests a bias correction on the observation level. The significant biases also show that a bias correction on the tomographic solution level has the potential to considerably improve the accuracy of the tomographic results.

In the last part of this chapter, the stochastic properties of the wet refractivity field are compared to the stochastic model proposed in Chapter 3. The investigations revealed that the stochastic model well represents the reality in terms of the requirements of the Kalman filter.

Chapter 6

Comparison of balloon sounding data and GNSS-derived zenith path delays

Many different measurements from various types of sensors are used as input into the tomographic reconstruction and for its validation. All these observations reflect the true atmosphere with a certain accuracy. To validate the performance of tomographic algorithms with such data, we need to distinguish between errors caused by deficiencies of the sensors and inaccuracies of the tomographic reconstruction technique. This is pointed out in this chapter. The main error sources of balloon sounding measurements and observations from synoptic stations are discussed in terms of their impact on the tomographic reconstruction and on the validation of tomographic results. In addition, differences between these two measurement types and path delays derived from GPS are investigated as well as the impact of inaccuracies in modeling dry delays by Saastamoinen's model on zenith wet delays.

6.1 Error budget of meteorological sensors

Data from radio soundings are mainly used for validating the outcome of tomographic reconstruction in this work. This validation is based on comparisons between wet refractivities estimated by the tomography software and in-situ measurements from radio soundings. According to Equation 2.8, the wet refractivity N_{wet} can be computed from the temperature T and partial water vapor pressure P_{wet}. Sensors mounted on radio sounds or at stations on ground provide observations of relative humidity RH or dew point temperature $T_{\text{dew point}}$. In combination with temperature measurements, the partial water vapor pressure can be computed.

$$P_{\text{wet}} = \frac{RH}{100}\,\mathrm{P}^*_{\text{wet}}(T) \tag{6.1}$$

$$P_{\text{wet}} = \mathrm{P}^*_{\text{wet}}(T_{\text{dew point}}) \tag{6.2}$$

where RH is the relative humidity in [%], T the temperature in Kelvin, and $\mathrm{P}^*_{\text{wet}}(T)$ the saturated water vapor pressure over water. Murray's approximation was used to compute the saturated water vapor pressure P^*_{wet} (Kraus 2004).

$$P^*_{\text{wet}} = k\,\exp\left(\frac{a\,(T - c)}{T - b}\right) \tag{6.3}$$

where

$$\begin{aligned} k &= 6.1078\,\text{hPa} \\ a &= 17.2693882 \\ b &= 35.86\,\text{K} \\ c &= 273.16\,\text{K} \end{aligned}$$

Table 6.1: Typical standard deviations of random errors for temperature and humidity measurements for radio soundings (Vaisala and RS80-A and RS92-SGP) and for ground-based measurements (Meteolabor VT36 and VTP37). For details see Meteolabor 2002, Meteolabor 2008, Miloshevich et al. 2001, and Bian et al. 2011.

Measurement type	**σ of temperature**	**σ of humidity**
Radio sounding	0.25 K	2% (1)
Ground-based measurement	0.2 K	0.25 K (2)

(1) relative humidity, (2) dew point temperature

The wet refractivity can be computed from temperature and humidity measurements. The impact of random errors in these measurements on the wet refractivity is estimated by the law of error propagation (Schönwiese 2000).

$$\mathbf{\Sigma}_{f,f} \;=\; \mathbf{J}\,\mathbf{\Sigma}_{x,x}\,\mathbf{J}^T \tag{6.4}$$

where $\mathbf{J}$ is the Jacobian matrix of the function $\mathrm{f}(x_1, \ldots, x_m) \in \mathbb{R}^n$ relating temperature and humidity to wet refractivity, n the number of dimensions of the function's image, and $\mathbf{\Sigma}_{x,x}$ the covariance matrix of the input values $x_1, \ldots, x_m$. The base observations (temperature and humidity) are assumed to be independent. Accordingly, the covariance matrix $\mathbf{\Sigma}$ is a diagonal matrix with the precisions σ^2 of the temperature and humidity sensor on the diagonal. The Jacobian $\mathbf{J}$ is computed from the Equations 2.8 and 6.1 for balloon soundings, and Equations 2.8 and 6.2 for ground-based stations. The resulting equations are non-linear and have, therefore, to be linearized.

Given the sensor precisions listed in Table 6.1, the wet refractivity error is estimated for different temperature and humidity values (see Figure 6.1a) and b)). In the case of balloon sounding measurements, the error in wet refractivity mainly depends on the temperature. The higher the temperature the larger the wet refractivity error. The wet refractivity error does usually not exceed 4 ppm standard error for temperatures below 30° C. In the case where humidity is provided by sensors measuring dew point temperature, the wet refractivity error is dominated by inaccuracies in the dew point measurement. The wet refractivity error increases with dew point temperature and is small than 2.5 ppm standard error for temperature below 30° C.

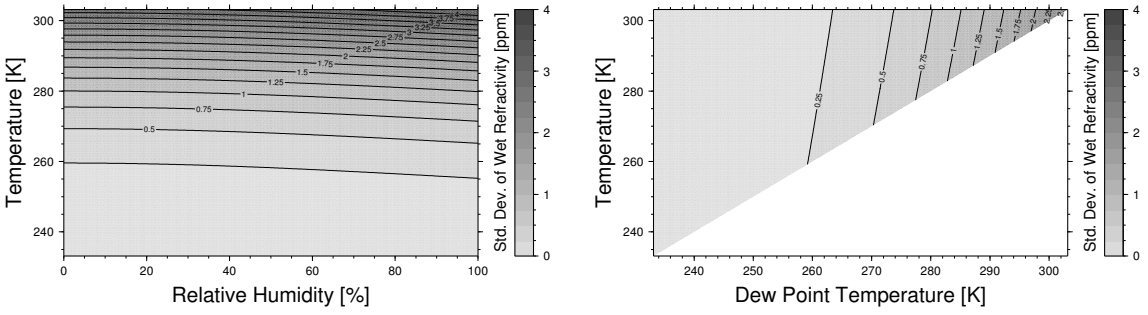

(a) Standard deviation of radio soundings in ppm wet refractivity units.

(b) Standard deviation of ground based observation in ppm wet refractivity unit.

Figure 6.1: Wet refractivity standard deviation caused by the temperature and humidity measurement inaccuracies for a) balloon soundings and b) for ground-based meteorological stations.

In the last decades, the observations from balloon sounding have been investigated in terms of systematic errors and accuracy. Miloshevich et al. 2001; Wang et al. 2002; Vömel et al. 2003; Fujiwara et al. 2003 have analyzed radio sounding equipment from different manufacturers and compared them among each other and to reference measurements from high-precision sensors. They found significant biases between the different sensors and the reference measurements. These biases are significantly larger than the precisions given by the manufacturers of the sounding devices

(WMO 2008). The main systematic errors are listed for temperature and humidity sensors mounted on balloon soundings. Note that the errors may considerably differ for different sensor types.

Temperature sensors:

Calibration: According to WMO 2008, most modern temperature sensors have only small sonde errors caused by calibration between the surface and 30 hPa.

Thermal lag: Temperature sensors have a certain response time on temperature changes. As the temperature of the atmosphere usually decreases with height, the sensor reports too warm temperatures. Typically, the reported temperatures are too high by about 0.1 K in the lower and 0.25 K in the upper troposphere. However, the vertical temperature gradients may exceed 4 K per 100 m in strong temperature inversions. So, the temperature error may be much larger than the values quoted above for short periods (WMO 2008).

Radiative heat exchange in the infrared: Heat exchange with the infrared background can generate significant errors at high altitudes. At pressures lower than 30 hPa, positive temperature errors larger than 0.5 K are found on flights, where air temperatures lower than -75°C were measured (WMO 2008).

Heating by solar radiation: At daytime, incident solar radiation causes heating errors up to 1 K. Software correction schemes are used to correct these errors. They feature an expected uncertainty of 20 % (WMO 2008) leading to a maximal uncertainty of the temperature measurements of 0.2 K.

Deposition of ice or water on the sensor: The deposition of water or ice on the temperature sensor leads to psychrometric cooling of the sensor during the ascent in an environment with relative humidity less than 100 %. Moreover, if the deposition of water or ice changes its aggregate state, latent heat is released or absorbed by the deposition and, accordingly, the temperature measured by the sensor is influenced (WMO 2008).

Humidity sensors:

Calibration: A variation of several percent in relative humidity is observed between humidity sensors from different batches (Nash et al. 1995) possibly as a consequence of faulty calibration procedures during manufacturing (WMO 2008).

Slow sensor response and sensor hysteresis: Systematic errors caused by the slow response of humidity sensors are only significant below -20°C for thin-film capacitors and carbon hygristors. Errors caused by hysteresis are limited to a few percent for most of the sensors (WMO 2008).

Differences between sensor temperature and true atmospheric temperature: The temperature and the humidity sensor have usually a different time response to changes in temperature and in humidity, respectively. This causes systematic errors if both measurements are used to compute quantities like dew point temperature or wet refractivity. This can lead to an error of -1.5% at 50% relative humidity. The error is even larger at lower temperatures. A decrease of 4-6% of relative humidity at temperatures between -10° and -30° C is caused by this kind of effect.

Wetting or icing in cloud: Wetting or icing in cloud increases the relative humidity by at least 10% on average (Nash et al. 1995). Under severe icing conditions, relative humidity values may be expected that are up to 30 percent too high (WMO 2008).

The measurements provided by the balloon soundings will be used to validate the output of the tomographic reconstruction. To draw correct conclusions from the validations, the influence of the systematic temperature and humidity measurement errors on the wet refractivity should be taken into account. Figures 6.2a)-f) show the influence of these errors on wet refractivity.

Systematic errors in the temperature measurements are usually below 0.5 K. Figure 6.2c) shows that the resulting error in wet refractivity is below 5 ppm for atmospheric condition found in Central Europe. However, errors caused by the thermal lag of temperature sensors may be larger than 0.5 K. As can be seen in Figure 6.2a), errors of this magnitude lead to errors up of to 10 ppm in wet refractivity.

Regarding the systematic errors in humidity measurements, they cause larger errors in wet refractivity than those of temperature measurements. Calibration errors and errors caused by the difference between sensor temperature and true atmospheric temperature amount to a few percents. A relative humidity error of 5 percent leads to an error below 10 ppm in wet refractivity. Wetting and icing in cloud may cause relative humidity errors in the order of 10%. Errors of this magnitude result in wet refractivity errors up to 15 ppm.

Another quantity of interest in validating tomographic output is the zenith wet path delay. The impact of measurement errors made by balloon soundings on the zenith path delay is investigated by (Haase et al. 2003). They observed biases up to 15 mm in the zenith total delay, mainly caused by the heating due to solar radiation.

In-situ measurements from synoptic stations and from balloon soundings are used to eliminate the dry part from the tropospheric delays estimated from GNSS observations by the Saastamoinen model and for validation of the tomographic results on the basis of an integrated quantity, such as zenith path delays, respectively. Their impact on zenith path delays is investigated in the subsequent paragraphs.

For the Saastamoinen model, the impact of temperature and relative humidity measurement errors on the zenith dry and wet delay is computed in the following way

$$\Delta_{\mathrm{error,T}} = \Delta\varrho_{\mathrm{Saas}}(P,\, T + \Delta T,\, RH) - \Delta\varrho_{\mathrm{Saas}}(P,T,RH) \tag{6.5}$$

$$\Delta_{\mathrm{error,RH}} = \Delta\varrho_{\mathrm{Saas}}(P,\, T,\, RH + \Delta RH) - \Delta\varrho_{\mathrm{Saas}}(P,T,RH) \tag{6.6}$$

where $\Delta\varrho_{\mathrm{Saas}}$ is the dry or the wet part of the modified Saastamoinen model (see Equation 2.16 and 2.17, respectively), P the pressure, T the temperature, RH the relative humidity, ΔT the systematic error of the temperature measurement, ΔRH the systematic error of the relative humidity measurement. In addition to the Saastamoinen model, Equation 6.1 is needed to compute the partial water vapor pressure from temperature and relative humidity.

For sounding-based measurements, it is assumed that the temperature or the relative humidity sensor reports values during the ascent which are all equally biased. Accordingly, a constant observation error is added for each measurement. For temperature and relative humidity measurement error, the resulting error in the zenith delay is then given by

$$\Delta_{\mathrm{error,T}} = 10^{-6} \int_{z_{\mathrm{bottom}}}^{z_{\mathrm{top}}} \mathrm{N}(P,\, T + \Delta T,\, RH) - \mathrm{N}(P,T,RH)\,\mathrm{d}z \tag{6.7}$$

$$\Delta_{\mathrm{error,RH}} = 10^{-6} \int_{z_{\mathrm{bottom}}}^{z_{\mathrm{top}}} \mathrm{N}(P,\, T,\, RH + \Delta RH) - \mathrm{N}(P,T,RH)\,\mathrm{d}z, \tag{6.8}$$

respectively, with pressure P, temperature T, and relative humidity RH. The function $\mathrm{N}(P,T,RH)$ denotes the dry or the wet refractivity. The refractivities can be estimated by Rüeger's formula (see Equation 2.8). As this formula requires the partial water vapor pressure, Equation 6.1 is used to convert relative humidity to partial water vapor pressure. The integration starts at mean sea level and stops at 25 km and 60 km altitude for zenith wet and dry delays, respectively.

The pressure, temperature and relative humidity values are based on an atmospheric model similar to that of the U.S. standard atmosphere (ISO 2533:1975 1975). This standard atmosphere divides the atmosphere into layers with different temperature gradients. The gradients are listed in Table 6.2. Given a temperature at the reference level, which is at mean sea level, a temperature profile can be computed from the tabulated gradients using the following relation:

$$\mathrm{T(z)} = T_0 + \gamma(z - z_0) \tag{6.9}$$

where γ is the lapse rate in [K/km], z the height above the lower boundary z_0 of the layer, both in [km], and T_0 the temperature at height z_0 in [K].

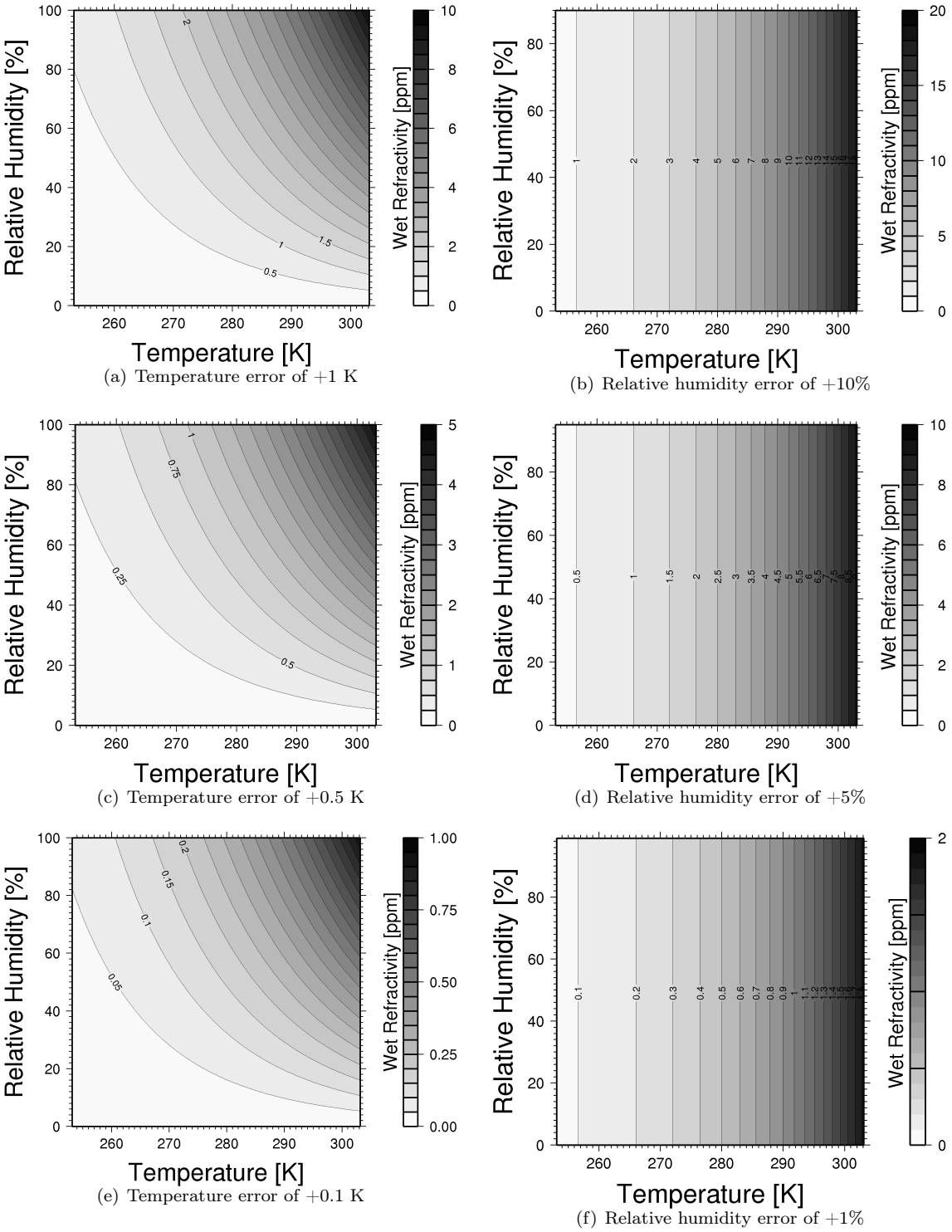

(a) Temperature error of +1 K

(b) Relative humidity error of +10%

(c) Temperature error of +0.5 K

(d) Relative humidity error of +5%

(e) Temperature error of +0.1 K

(f) Relative humidity error of +1%

Figure 6.2: Dependence of the wet refractivity error on different atmospheric conditions for different systematic measurement errors in temperature (first column) and in relative humidity (second column).

Table 6.2: Lapse rate for different atmospheric layers ranging from the *Lower* to upper *Upper* boundary (ISO 2533:1975 1975).

Lower [km]	**Upper [km]**	**Gradient [K/km]**
0	11	-6.5
11	20	0.0
20	32	1.0
32	47	2.8
47	51	0.0
51	71	-2.8

The pressure profile is computed by

$$P = P_0 \left(\frac{T_0 - \gamma (z - z_0)}{T_0} \right)^{\frac{g}{\gamma R}} \tag{6.10}$$

$$P = P_0 \exp \left(- \frac{g(z - z_0)}{RT} \right) \tag{6.11}$$

with

z : Height
P : Pressure
T : Temperature
z_0 : Lower boundary of the layer (reference level)
P_0 : Pressure at the reference level
T_0 : Temperature at the reference level
g : Gravitational acceleration (≈ 9.81 ms^{-1})
R : Gas constant of air (≈ 287 J kg^{-1})

Equation 6.10 is used in layers in which the lapse rate is zero. Otherwise, Equation 6.11 is applied. Along the whole profile, a constant relative humidity of 50% is assumed.

Figure 6.3 shows zenith path delay errors for different temperatures and temperature errors. Using the Saastamoinen model, a positive temperature measurement error has only little effect on the zenith dry delay. At a temperature of 30° C at mean sea level, a measurement error of 1°C leads to an error of about 0.3 mm in the zenith dry delay. If the temperature is below 30°C at mean sea level, the error is even smaller. Temperature measurement errors by balloon soundings have a much large impact on the zenith dry delay. The error in the zenith dry delay increases by 10 mm/K with the temperature error. The temperature and dry path delay errors are negatively correlated. In contrast to that, a sensor reporting too high temperatures results in a too large zenith wet delay. At a temperature of 0° C at mean sea level, a temperature error of 1° C leads to a zenith wet path delay error of 2.0 mm and 2.5 mm for the Saastamoinen model and for balloon soundings, respectively. The error is considerably larger at higher temperatures. At a temperature of 30° C at mean sea level, the errors increase to 6.5 mm and 9.5 mm, respectively.

Combining the dry and wet delay errors, we can estimate the zenith total delay error. For Saastamoinen's model, the zenith total delay error is about -6 mm for a temperature error of 1°C at 20°C at mean sea level and -2 mm at 0°C. The error for biased temperature measurements from balloon soundings is -2.5 mm and 8 mm for a positive temperature bias of 1°C at 20° and 0°C, respectively.

Besides temperature measurements, humidity measurements are needed to compute zenith path delays from meteorological observations. Figure 6.4 shows the impact of biased relative humidity

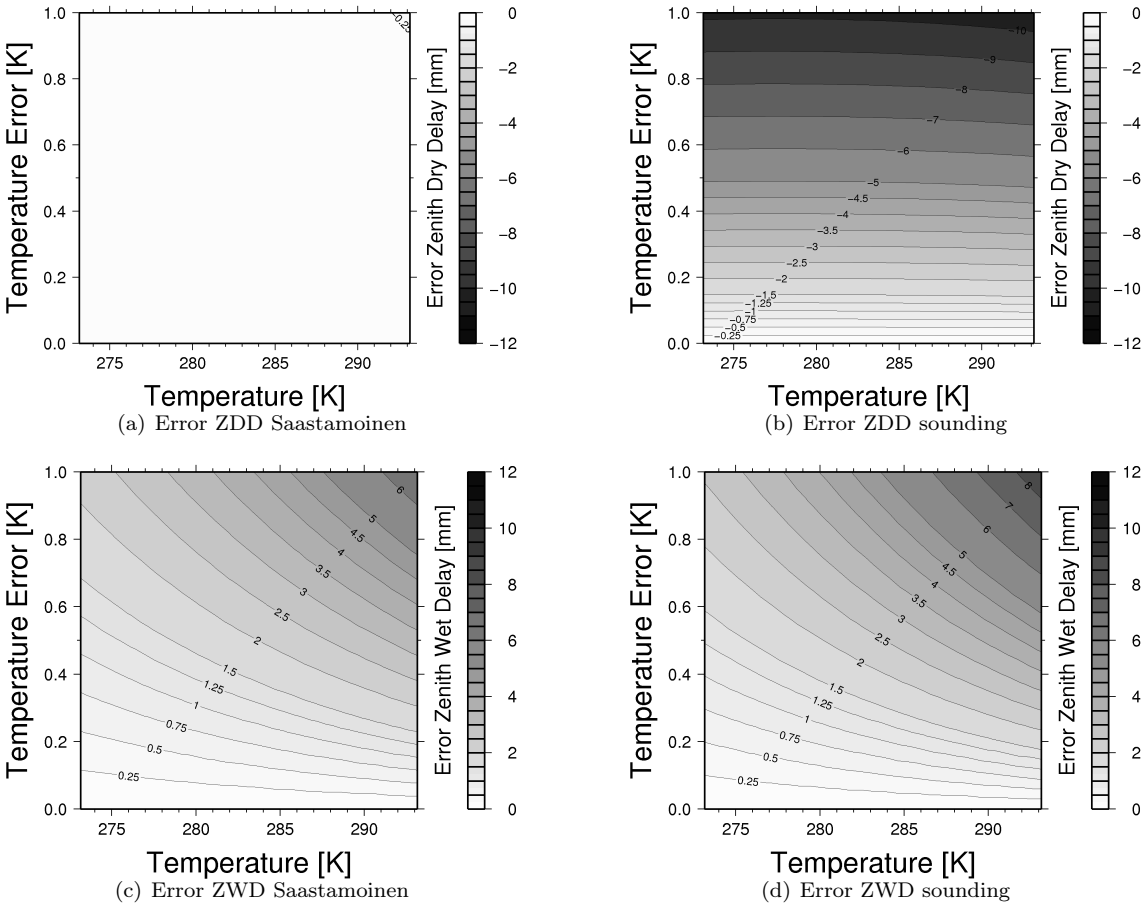

(a) Error ZDD Saastamoinen
(b) Error ZDD sounding
(c) Error ZWD Saastamoinen
(d) Error ZWD sounding

Figure 6.3: Errors in the zenith dry and wet delay caused by systematic errors in temperature measurements. In the first column, Saastamoinen's model is used to estimate the zenith dry delay (ZDD) and the zenith wet delay (ZWD) from meteorological measurement at the Earth surface. In the second column, the delay error is computed by integrating along a vertical profile through a model atmosphere. Thereby, a constant measurement error is assumed.

measurements (measured minus truth) on zenith dry and wet path delays at different temperatures. For the Saastamoinen model, a relative humidity of 10% larger than the truth results in a zenith dry delay error of less than one millimeter (-0.8 mm) for temperatures lower than 20° C at mean sea level. In contrast to this, the impact of biased humidity measurements on the dry path delay is much larger for delays computed from balloon sounding data. A sensor reporting relative humidity values which are 10% larger than the truth results in zenith dry delays which are 40 mm and 9 mm too short for temperatures of 20° C and of 0° C at mean sea level, respectively. For biased humidity measurements, the error in the zenith wet delay is 22 mm for the Saastamoinen model and 26 mm for balloon soundings at a temperature of 20° C at mean sea level and measured relative humidity values which are 10% larger than the truth. At a temperature of 0° C at mean sea level, the zenith wet delays are about 6-7 mm too large for both approaches.

For the Saastamoinen model, the impact of biased humidity measurements on zenith total delays is similar to that on zenith wet delays (see Figure 6.4c)) because the influence on the wet part of the zenith path delay is one order of magnitude larger than that on the dry part. For the zenith total delays derived from balloon soundings, measured relative humidities which are 10% larger than the truth lead to zenith total delays which are 14 mm shorter than the truth at temperature of 20° C at mean sea level. The error reduces with temperature and the zenith total delays are about 3 mm too short at freezing temperature at mean sea level.

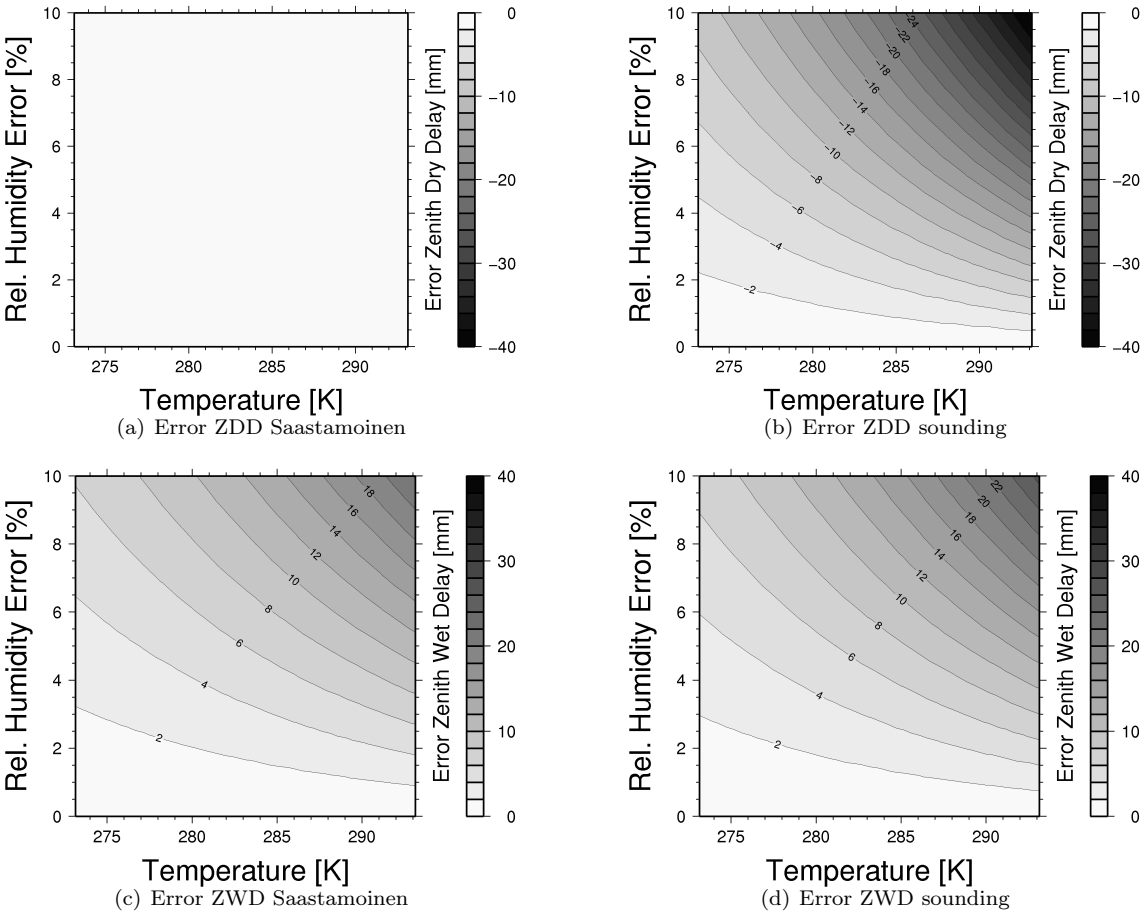

(a) Error ZDD Saastamoinen
(b) Error ZDD sounding
(c) Error ZWD Saastamoinen
(d) Error ZWD sounding

Figure 6.4: Error of the the zenith dry and wet delay caused by errors in the relative humidity measurements. In the first column, Saastamoinen's model is used to estimate the zenith dry delay (ZDD) and the zenith wet delay (ZWD) from meteorological measurements at the Earth's surface. In the second column, the delay error is computed by integrating along a vertical profile though a model atmosphere. Thereby, a constant measurement error is assumed.

6.2 Intercomparison between zenith path delays of different sources

In this section, zenith total, wet, and dry delays will be investigated in terms of systematic differences between time series derived from different sensors. Similar investigations have been subject of several studies in recent years (Elgered et al. 1997; Bevis et al. 1992; Rocken et al. 1993; Duan et al. 1996; Emardson et al. 1998; Tregoning et al. 1998). Haase et al. 2003 have compared zenith total delays and zenith wet delays derived from GPS, radio soundings, and numerical weather model for 51 stations in the Western Mediterranean. Guerova et al. 2003 investigated the accuracy of integrated water vapor at Payerne in Switzerland during the winter 2000/2001.

The investigations presented in this section are based on time series from different observations collected in Payerne: a) balloon soundings, b) ground-based meteorological measurements, and c) GPS phase observations. The time series spans a period of 2 years and has a sampling rate of 12 hours (observations at midnight and noon). The time series from different observation sources are compared in view of the following points:

Mean value: The mean values from different time series are tested on significant differences. This allows us to judge if significant differences exist already between the input data of the to-

mography (GPS derived data) and the validation data (balloon sounding data). Mean values are separately computed for observations at noon and midnight.

Day-night difference: The mean difference between observations at the noon and midnight is computed for each time series. If this difference varies from sensor to sensor, this is an indicator that the sensors are affected by different systematic measurement errors. A main goal is to figure out whether the systematic errors of balloon sounding observations listed in the previous section are significant in the zenith path delay.

Synoptic signal: After removing systematic errors, variations of the synoptic scale are extracted from each time series. The correlation coefficient between two time series and the variance for each time series are computed. These statistical measures are then compared with each others. With these measures, we can coarsely estimate the precision of the observations.

The investigations listed above are performed by fitting a simple model. The model estimates the mean value for the observations at noon and midnight. In addition, the seasonal variation is removed. This results in a band-pass filter where the postfit residuals contain variations on the synoptic scale and higher order harmonics of the seasonal cycle.

$$\Delta\varrho \;=\; \mu_{\mathrm{day}} \;+\; \Delta\mu\,\mathrm{f}_{\mathrm{night}}(t) \;+\; \mathrm{f}_{\mathrm{day}}(t)\,a_{\mathrm{day}}\,\sin\left(\frac{2\,\pi}{\tau}(t \;+\; \phi_{\mathrm{day}})\right) + \\ +\; \mathrm{f}_{\mathrm{night}}(t)\,a_{\mathrm{night}}\,\sin\left(\frac{2\,\pi}{\tau}(t \;+\; \phi_{\mathrm{night}})\right) \tag{6.12}$$

$\Delta\varrho$: Zenith path delay in meters

t : Time in days

$$f_{\mathrm{day}}(t) = \begin{cases} 1 & \text{at noon} \\ 0 & \text{at midnight} \end{cases}$$

$$f_{\mathrm{night}}(t) = \begin{cases} 0 & \text{at noon} \\ 1 & \text{at midnight} \end{cases}$$

μ_{day} : Mean value at noon

$\Delta\mu$: Offset between noon and midnight

a_{day} : Amplitude of the seasonal cycle at noon

a_{night} : Amplitude of the seasonal cycle at midnight

ϕ_{day} : Seasonal phase shift at noon

ϕ_{night} : Seasonal phase shift at midnight

τ : Seasonal period (365.25 days)

6.2.1 Zenith total delays

In this subsection, zenith total delays from radio sounding data and GPS phase observations are investigated. Figure 6.5 shows a time series of zenith total delays derived from balloon soundings. A seasonal variation is clearly visible. The mean value of the zenith total delays is 2.2857 m and the standard deviation 4.28 cm for the radio soundings. The mean value and the standard deviation of the zenith total delay computed from GPS phase observations are 2.2874 m and 4.68 cm, respectively.

Is there any significant bias between these two observations? We have, therefore, compute the differences between the two times series (ZTD GPS minus ZTD radio sounding). The mean value

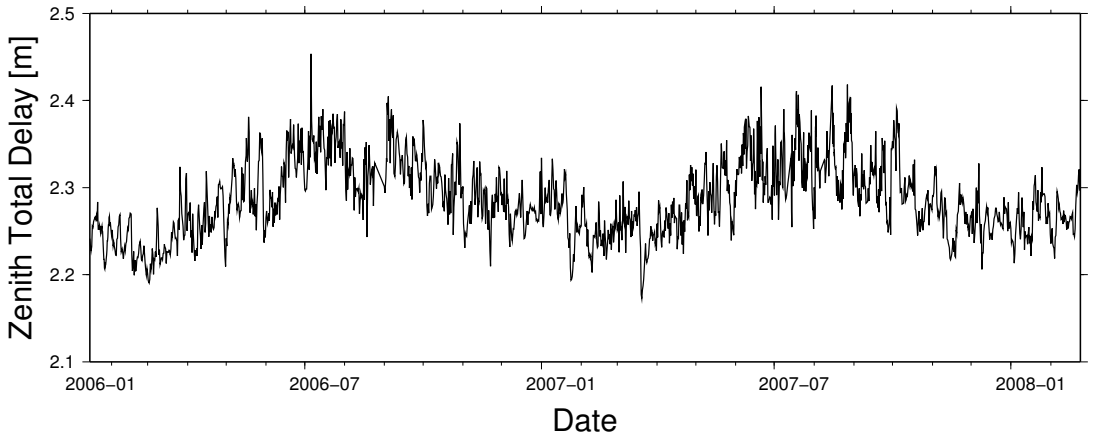

Figure 6.5: Time series of zenith total delays computed from radio soundings at the station in Payerne.

and the standard deviation of the differences are 1.7 mm and 12.3 mm, respectively. The mean value is significantly different from zero meaning that there is a bias between the zenith total delays derived from GPS and those from balloon soundings. A seasonal cycle is still recognizable in the time series (see Figure 6.6), but with a lower amplitude than in the series shown in Figure 6.5. This shows that the bias between the two observation types varies with time and suggests a seasonal bias corrections.

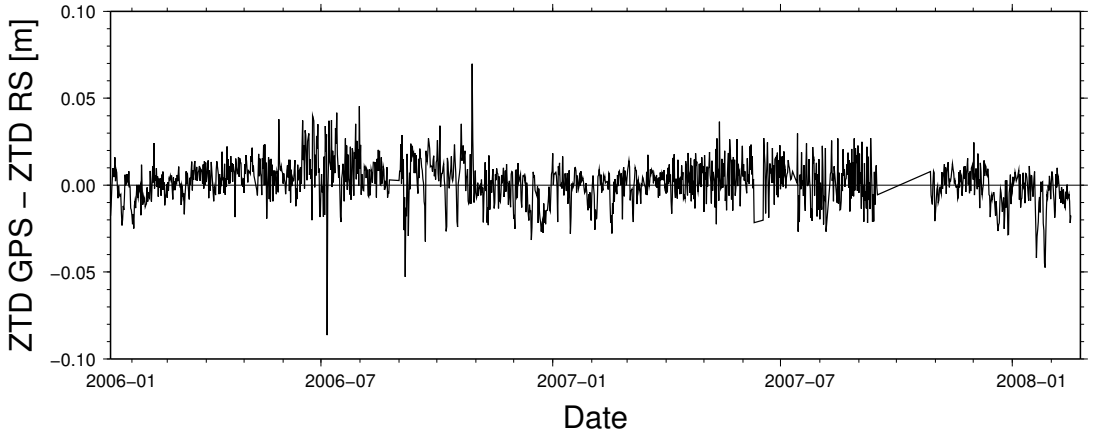

Figure 6.6: Difference between zenith total delays derived from radio soundings and GPS (ZTD GPS minus ZTD radio soundings) at the station in Payerne.

In Figure 6.7, the histograms for the time series of zenith total delays derived a) from balloon sounding and b) from GPS are shown. The observations from the two series are similar distributed. Both histograms have a positive skewness which indicates that they are not normally distributed.

The parameters of the model described by Equation 6.12 are estimated for the two time series of the zenith total delay (see Table 6.3). For zenith total delays derived from balloon soundings and from GPS phase observations, the seasonal amplitudes for day and night values also differ significantly. The same is true for the seasonal phase shift between day and night. The mean values at noon and at night differ significantly for zenith total delays computed from radio soundings whereas they do not for GPS-derived zenith total delays. Obviously, solar effects influence the two measurement sources differently. Assuming no difference between the zenith path delays at night and at noon would mean that the observed systematic difference between the zenith total delays derived from balloon soundings at day and night is related to measurement errors. As seen

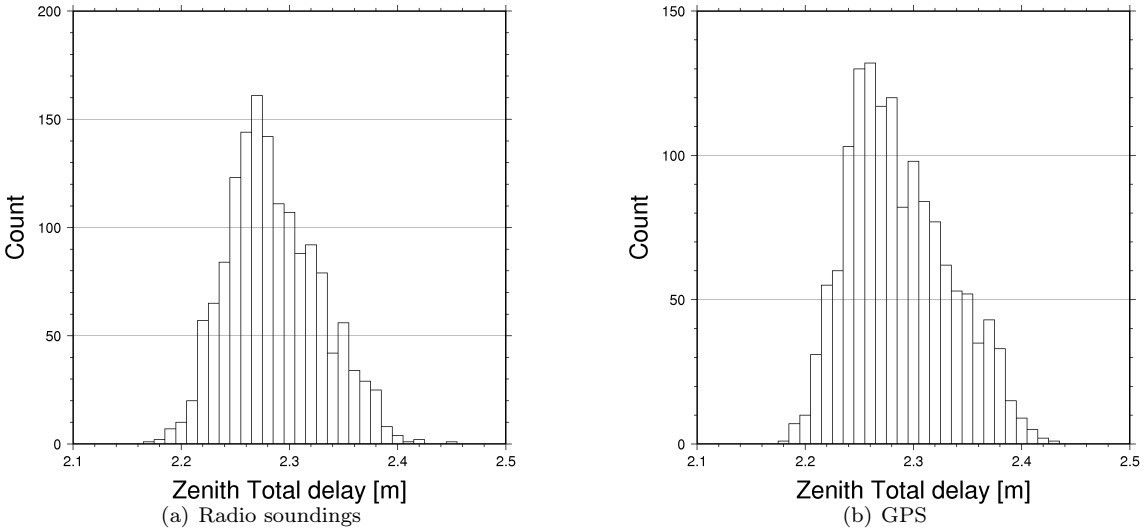

(a) Radio soundings (b) GPS

Figure 6.7: Histogram of zenith total delays computed a) from radio sound launches at Payerne, and b) from GPS measurements. The data sets include data from January 2006 to December 2007 with a sample rate of 12 hours.

in the previous section, differences between temperatures measured by sensors mounted on radio soundings at day and night can be related to heating by solar radiation. At daytime, heating by solar radiation leads to too high temperature measurements and, accordingly, to zenith total delays which are smaller than the truth. This large difference can, however, not fully explained by the measurement error in the temperature sensor (see Figures 6.3) as the measured temperatures would need to be biased by a several Kelvin. This would suggest that the humidity measurements are also biased. On the other hand, zenith path delays computed from GPS phase observations may be influenced by a higher density of electrons in the ionosphere during daytime. Although the ionospheric delays are reduced to a large extent by the combination of the two frequencies emitted by GPS satellites and by the building of double differences, the remaining part may affect the estimated zenith path delays. Investigations have shown that the remaining part can reach 2 mm path delay at low elevations in quiet ionosphere condition (Lutz et al. 2010). The years 2006-2008 are years with low solar activity. We can, therefore, conclude that the observed day-night difference in the zenith total delays cannot be explained by ionospheric effects.

Figure 6.8 shows the difference between the postfit residuals of the zenith total delays (GPS minus radio sounding). The standard deviation of the series is 1.08 cm. Computing the power spectrum of the series shows no dominating frequencies. In Figure 6.9, the monthly mean and standard deviation are plotted. The biases show no seasonal cycles whereas the standard deviations tend to be larger during summer.

6.2.2 Zenith dry delays

Zenith dry delays can be computed from meteorological observations on the Earth's surface using the dry Saastamoinen model (see Equation 2.16). Such delays are subtracted from zenith total delays, which are estimated by the GPS processing software, to get zenith wet delays. As a consequence of this, measurement and modeling errors of the dry delay have a direct impact on the wet delays and, accordingly, on the tomographic results. Therefore, an accurate modeling of zenith dry delays is essential for the accuracy of ground-based GNSS tomography.

The mean value for the time series from the dry Saastamoinen model and from radio soundings are 2.1858 m and 2.1831 m, respectively. They show a significant bias of 0.26 cm. The standard deviations do not significantly differ (1.62 cm and 1.69 cm, respectively). The two series are very

Table 6.3: Fitted values and their standard deviations for the parameters of Equation 6.12. They are estimated from zenith total delays derived from radio soundings and from GPS phase observations.

Measurement source	Parameter	Fitted value	Standard deviation
Radio soundings			
	μ_{day}	2.2832 m	0.0011 m
	$\delta\mu$	0.0113 m	0.0015 m
	a_{day}	0.0395 m	0.0015 m
	a_{night}	0.0466 m	0.0015 m
	ϕ_{day}	52.8284 d	2.2025 d
	ϕ_{night}	54.8141 d	1.9217 d
GPS phase observations			
	μ_{day}	2.2893 m	0.0012 m
	$\delta\mu$	0.0036 m	0.0017 m
	a_{day}	0.0477 m	0.0017 m
	a_{night}	0.0483 m	0.0016 m
	ϕ_{day}	56.8350 d	2.0502 d
	ϕ_{night}	55.6297 d	2.0110 d

highly correlated (0.995) and, thus, the difference of the two series has a small standard deviation (0.16 cm), which is one order of magnitude smaller than those of the time series of zenith dry delays. No seasonal cycle is recognizable in the two time series. Figure 6.10 shows the time series of zenith dry delays estimated from ground-based measurements using the dry Saastamoinen model.

According to the model described by Equation 6.12, a parameter set is estimated for the time series of zenith dry delays from ground-based measurements and from radio soundings. Both time series have a sample rate of 12 h with observations at noon and midnight. Ground-based measurements at times that differ from midnight and noon are not considered. Table 6.4 lists the fitted parameters for both time series. For both series, there is no significant difference between the delays at noon and at night.

Zenith dry delays are mainly influenced by pressure variations and less by temperature variations (see Equation 2.16). Therefore, zenith dry delays computed by the dry Saastamoinen model are rather insensitive to biased temperature and humidity measurements (see also Figures 6.3 and 6.4). Consequently, we can assume that no systematic day-night difference in the zenith dry delay exists.

In the previous subsection, we have observed a systematic difference of about 1 cm in the zenith total delay computed from balloon soundings. The fact that no systematic day-night difference is present in the zenith dry delay relativizes the supposition that the day-night difference in the zenith total delay of balloon sounding measurements is mainly based on systematic measurement errors. The possibility that systematic errors of balloon soundings cancel mutually out is small as we would then expect differences in the seasonal cycles of the zenith dry delay derived from balloon soundings and from dry Saastamoinen model. But, no significant differences are observed in the parameters describing seasonal variability.

6.2.3 Zenith wet delays

Ground-based GNSS tomography is based on wet path delays. As GPS processing software provides zenith total delays, the dry part has to be eliminated before the tomographic processing. In our setup, the Saastamoinen model is used to estimate the dry part (see Equation 2.16). In this subsection, the resulting zenith wet delays are compared to zenith wet delays computed from data provided by balloon soundings. As in the previous subsections, data of the meteorological station in Payerne is considered.

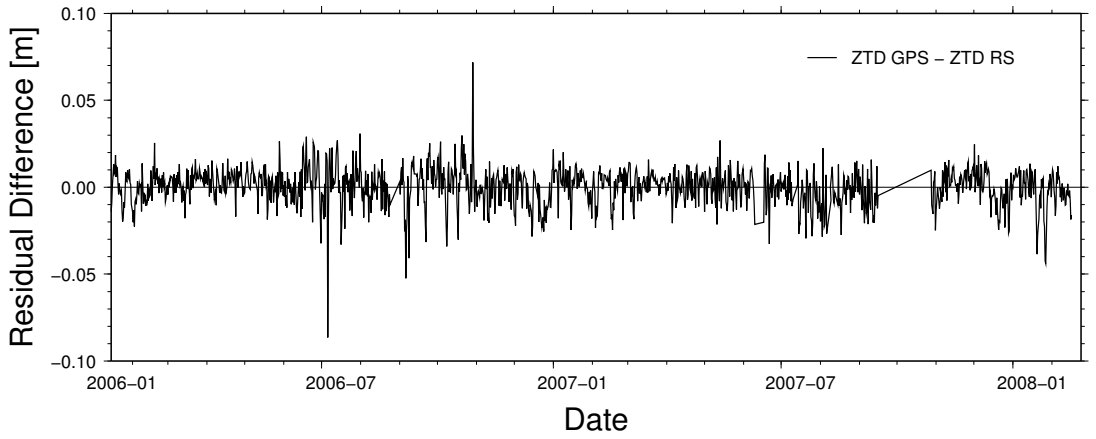

Figure 6.8: Time series of the postfit residual difference. The model parameters of Equation 6.12 are fitted for zenith total delays computed from GPS phase observations and for zenith total delays calculated from balloon soundings. The difference is calculated by subtracting the balloon sounding residuals from those of GPS phase observations.

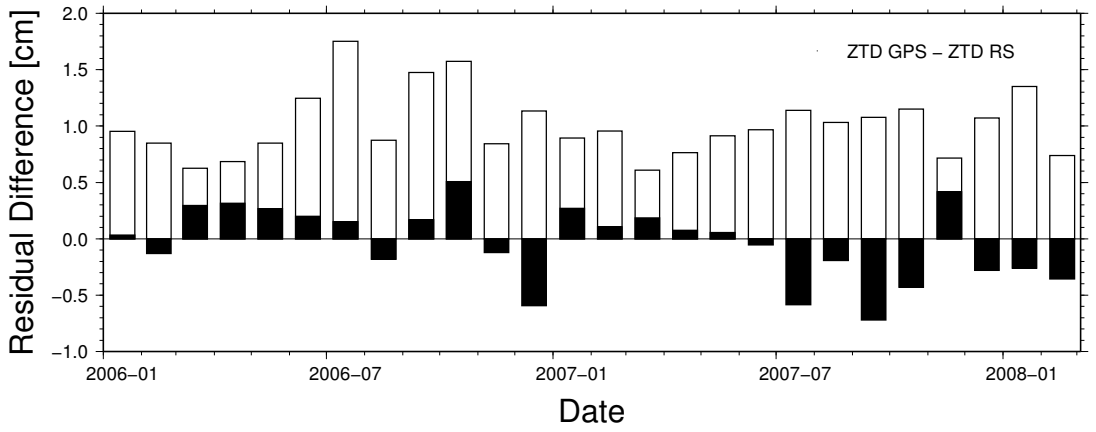

Figure 6.9: Monthly biases (GPS minus radio soundings) and standard errors of the residuals according to the model described by Equation 6.12. The black bars refer to the bias and the white bars to the standard error.

The time series of zenith wet delays shows a seasonal cycle (see Figure 6.11). This can also be seen in the fitted parameters (see Equation 6.12 and Table 6.5). The amplitude of the seasonal cycle is about 4.4-5.1 cm for zenith wet delays derived from balloon sounding data and about 5.1 cm for those derived from GPS phase observations. These amplitudes are similar to those estimated for zenith total delays. This implies that the seasonal cycle of zenith total delays is mainly caused by the wet part of the zenith path delays. Looking at the seasonal phase shifts, they are also similar to those of the zenith total delays.

The mean values are 10 cm and 10.4 cm for zenith wet delays at noon derived from balloon sounding and from GPS phase observations, respectively. The difference between the mean values of zenith wet delays from the different measurement sources is about 2 mm smaller than the difference of mean values of zenith total delays. The zenith wet delays at midnight are 1.2 cm larger than those at noon for delays computed from balloon sounding data. This is a significant difference. On the other hand, the difference between midnight and noon for zenith wet delays computed from GPS phase observations is not significant. The day-night differences are of the same magnitude as for zenith total delays.

The postfit residuals of the two time series are highly correlated with 0.943. This is even larger

Table 6.4: Fitted parameters and their standard deviations for the parameters of Equation 6.12. The two time series of zenith dry delays are computed from radio soundings and from ground-based measurements in Payerne.

Measurement source	**Parameter**	**Fitted value**	**Standard deviation**
Radio soundings			
	μ_{day}	2.1829 m	0.0006 m
	$\delta\mu$	0.0002 m	0.0008 m
	a_{day}	0.0074 m	0.0008 m
	a_{night}	0.0067 m	0.0008 m
	ϕ_{day}	295.3 d	7.8 d
	ϕ_{night}	294.2 d	10.4 d
Ground-based measurements			
	μ_{day}	2.1854 m	0.0006 m
	$\delta\mu$	0.0009 m	0.0008 m
	a_{day}	0.0071 m	0.0008 m
	a_{night}	0.0067 m	0.0008 m
	ϕ_{day}	302.6 d	6.8 d
	ϕ_{night}	303.3 d	7.3 d

Table 6.5: Fitted parameters and their standard deviations for zenith wet delays computed from radio soundings and from GPS phase observations at Payerne using the model described by Equation 6.12. The dry part of the zenith total delays derived from GPS phase observations are modeled from ground-based measurments using the dry Saastamoinen model.

Measurement source	**Parameter**	**Fitted value**	**Standard deviation**
Radio soundings			
	μ_{day}	0.1003 m	0.0011 m
	$\delta\mu$	0.0115 m	0.0015 m
	a_{day}	0.0439 m	0.0015 m
	a_{night}	0.0507 m	0.0015 m
	ϕ_{day}	61.1 d	2.0 d
	ϕ_{night}	61.2 d	1.8 d
GPS phase observations			
	μ_{day}	0.1038 m	0.0012 m
	$\delta\mu$	0.0029 m	0.0017 m
	a_{day}	0.0514 m	0.0018 m
	a_{night}	0.0518 m	0.0017 m
	ϕ_{day}	62.6 d	2.1 d
	ϕ_{night}	61.8 d	2.0 d

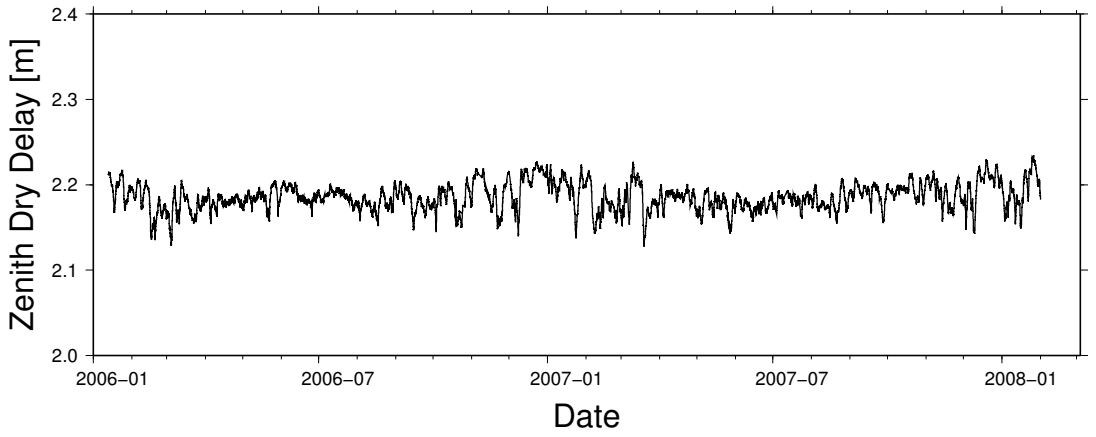

Figure 6.10: Time series of zenith dry delays computed from ground-based meteorological measurements at Payerne using the dry Saastamoinen model.

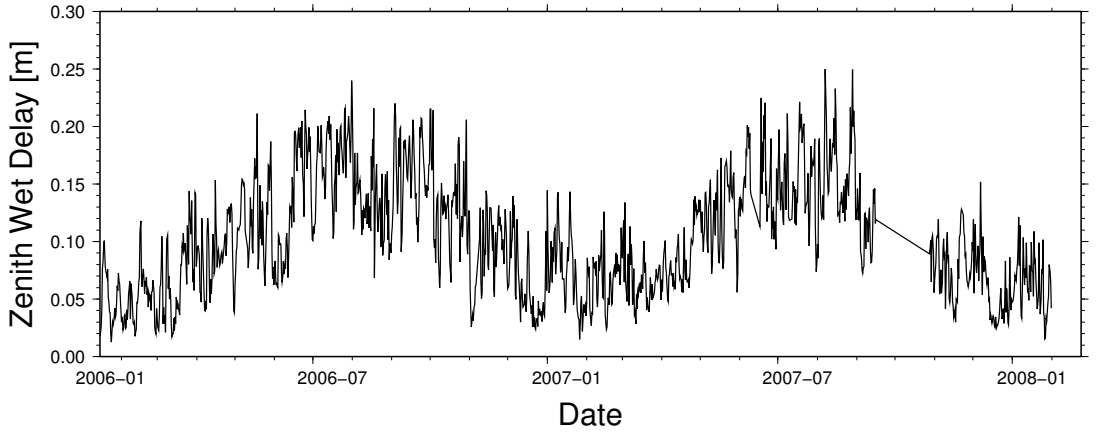

Figure 6.11: Time series of zenith wet delays (ZWD). They are computed from zenith total minus zenith dry delay. The former are estimated from GPS phase observations and the latter by the Saastamoinen model from ground-based measurements.

than for zenith total delay. Out of these two time series, the difference can be computed (GPS minus balloon soundings). The resulting time series has a standard deviation of 1.08 cm and is plotted in Figure 6.12.

6.3 Conclusions

Time series of zenith path delays derived from different sensors are compared among each other. Precision and systematic errors of these sensors have been investigated and their impact on the wet refractivity and the tropospheric path delays has been considered. Sensors attached to balloon sounding devices and sensors installed at synoptic stations are included in these investigations.

For meteorological conditions found in mid-latitudes, the precision of the wet refractivity derived from balloon soundings and from synoptic stations is less than 4 ppm and 2 ppm standard deviation (0.6 $\mathrm{g\,m^{-3}}$ and 0.3 $\mathrm{g\,m^{-3}}$ in absolute humidity), respectively. The precision quickly improves with lower temperatures and is smaller than 0.5 ppm (0.07 $\mathrm{g\,m^{-3}}$) for temperatures smaller than 0° C. Thus, the precision is sufficient small in the upper part of the troposphere for evaluating tomographic algorithms.

Meteorological sensors suffer from different error sources which mainly cause measurement

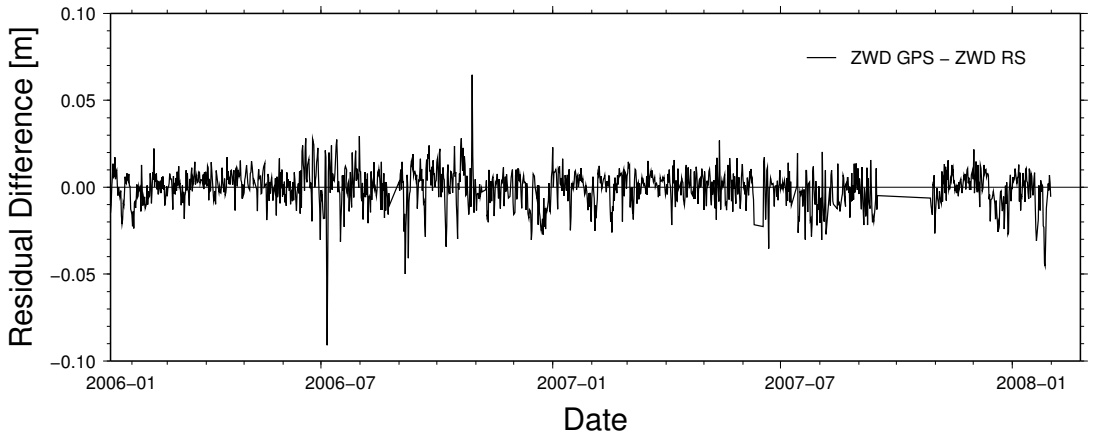

Figure 6.12: Time series of the postfit residual differences. Parameters according to Equation 6.12 are fitted to the zenith wet delays derived from GPS phase observations and for zenith wet delays computed from balloon soundings in Payerne. The difference is computed by subtracting the postfit residuals of balloon soundings from those of GPS.

biases. The investigations have shown that most important error sources in view of validating GNSS tomography are

- solar-related effects, such as heating by solar radiation. In wet refractivity units, heating of the temperature sensor by solar radiation causes a systematic error up to 1 ppm (0.15 $\mathrm{g\,m^{-3}}$). Due to its decrease with height, it has to be taken into account predominantly in the lower part of the troposphere.
- the deposition of ice or water on the sensors is another significant source of systematic errors. This effect can lead to large errors up to a few tens of ppm wet refractivity in the lower part of the troposphere and is needed to be considered in the interpretation of the tomographic results.

Comparing the uncertainty in balloon sounding measurements to the discretitazion errors in the tomographic reconstruction process, they are both of the same order of magnitude and have to be taken into account by assessing tomographic algorithms with balloon sounding data. Another error source in the evaluation is the departure of the true balloon track from an instantaneous vertical climb.

Differences between wet path delays used as input data to the tomography and the delays derived from balloon soundings introduce uncertainties in the evaluation of the tomographic algorithms. During the day, zenith wet delays from GPS are 3.5 mm larger than those from balloon soundings. During the night, the opposite is observed: Zenith wet delays from balloon sounding are about 5 mm larger than those from GPS. Comparing the two time series, we see a high correlation of 0.943. These discrepancies have to be considered in the evaluation of the tomographic algorithms.

An error source in the zenith wet delays derived from GPS data stems from the modeling of the dry part of the path delay. Although the dry part of the Saastamoinen model (see Equation 2.16) is relatively insensitive to errors in temperature measurements (less than 0.25 ppm for a temperature error of 1 K), comparisons between time series of zenith dry delays modeled by Saastamoinen's model and delays computed from balloon sounding data show a bias of 2.5 mm. Apart from this bias, the time series are highly consistent: The correlation between them is 0.995. Compared with the uncertainty in the zenith total delays, the uncertainty in the dry part is about one order of magnitude smaller. Therefore, the elimination of the dry part by Saastamoinen's model is accurate enough for tomographic reconstruction.

Chapter 7

Potential of new GNSSs and dense networks in view of GNSS tomography

In recent years, many advances have been made in GNSS technology and in the processing of GNSS signals. For instance, the newest generation of GPS satellites provides a third frequency which improves the modeling of the ionospheric effects and offers new possibilities in ambiguity resolution. Additionally, the number of GNSS satellites have been steadily increased. GLONASS will achieve full constellation in 2011 and two more GNSSs are in development, such as the European Galileo and the Chinese COMPASS. The receiver technology has been improved, too. This development leads to multi-GNSS capable receivers that are available at relatively low costs making dense networks affordable and GNSS even more attractive for surveying and meteorology. Finally, cutoff angles for GNSS signals are considerably lowered due to advances in the GNSS processing. Low-elevation signals are important in GNSS tomography. What do all these developments mean in view of GNSS tomography and what is the impact of them on the precision of the refractivity estimated with GNSS tomography? These questions will be discussed in this chapter. In particular, the following points will be investigated with the help of an error analysis:

- The potential of additional GNSSs to improve the precision of GNSS tomography will be estimated.
- The impact of denser GNSS networks on the precision of GNSS tomography will be analyzed and a practical extension of a GNSS network in Switzerland will be evaluated.
- Recommendations for the selection of receiver locations will be devised. Properties such as satellite visibility and station height distribution of the network will be considered.

7.1 Configurations

The error analyses are carried out with the help of the tomography software AWATOS. The software has been evaluated in several studies in recent years (e.g. Troller 2004; Troller et al. 2006; Lutz 2009 and Lutz et al. 2010). In Troller et al. 2007, AWATOS has been investigated for a study period of one year. The evaluations have shown a good agreement between the tomographic solutions and the refractivity distribution derived from radio soundings and the numerical weather prediction (NWP) model COSMO-7.

Since our focus is on Switzerland, a similar configuration to that given by Troller et al. 2006 is used as base configuration. Some of the configuration options have been modified in this chapter to investigate their impact on the formal accuracy of the unknown refractivities. The base configuration and derivations from it are listed in Table 7.1.

Table 7.1: Configuration options used for the error analyses.

Parameter	**Base configuration**	**Variations**
Horizontal resolution	3×6 cells	2×4, 6×12
Vertical resolution	15 levels	5, 10, 20 and 30 levels
Cutoff elevation angle	10°	0°, 3°, 5°
Satellite system	GPS only	GPS and Galileo
Number of receivers	31 stations (AGNES)	92 stations (AGNES and SwissMetNet)
Observations	GNSS double difference delays	
Pseudo-observations	A priori values and neighborhood averaging constraints	

The investigations presented in this chapter represent the measurement configuration of 20$^{\text{th}}$ November 2006 (24 hours) in Switzerland. As input data, the geometry of the rays between satellites and receiver stations, and the accuracy of double difference delays, a priori values, and intervoxel constraints are considered. With this information, AWATOS is capable to compute the formal error of the unknowns. On the basis of the formal errors, configurations are compared with each other.

Horizontal and vertical resolution

The area between 46.0°-47.5° latitude and 6.5°-9.5° longitude is horizontally subdivided into 2×4, in 3×6 or in 6×12 grid cells. Each of these cells has dimension 0.75°×0.75°, 0.5°×0.5°, and 0.25°×0.25°, respectively. The 0.5°×0.5° grid is shown in Figure 7.1.

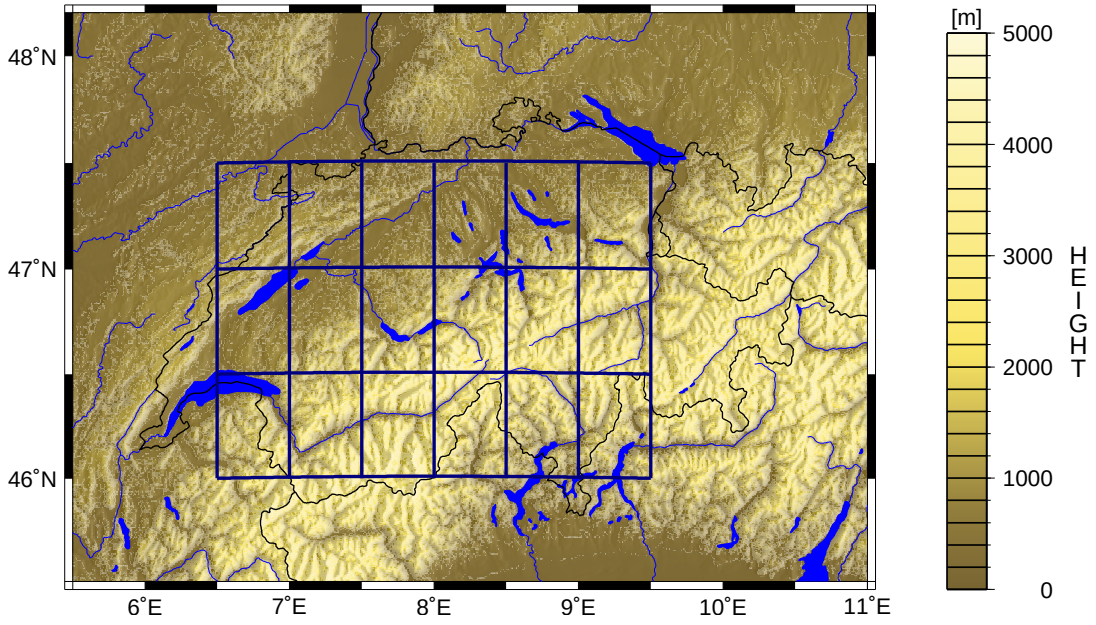

Figure 7.1: Model domain and the horizontal floor plan of the model grid with 0.5° grid spacing (blue lines).

In contrast to the horizontal dimensions, the vertical grid resolution varies with height. The vertical extent of the model grid is subdivided into n layers by

$$\Delta h_i \;=\; \Delta h_0\, q^i, \qquad \text{for } i = 1 \ldots n-1 \tag{7.1}$$

where Δh_i is the thickness of the i-th layer, Δh_0 the thickness of the lowest layer and q the so-called growth factor. A factor of 1.3 is chosen for the configurations with 5, 10 and 15 layers, 1.23 for that with 20 layers and 1.13 for that with 30 layers. The vertical extent of the grid ranges from 200 to 15000 m above mean sea level for all configurations. Figure 7.2 shows the vertical grid resolutions for the 4 different configurations.

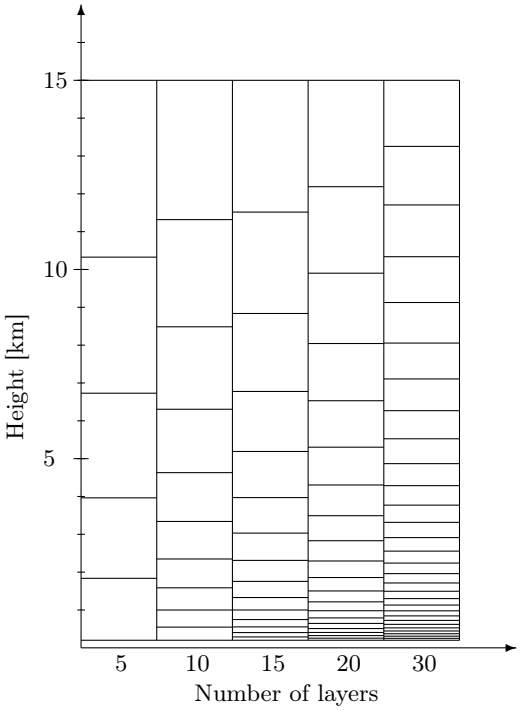

Figure 7.2: Vertical grid resolutions used in the tomographic processing.

Cutoff elevation angle

A major challenge in ground-based GNSS tomography is the fact, that there are no rays traversing the model domain tangentially to the Earth's surface. The lack of this information has a negative impact on the vertical resolvability of the water vapor distribution. Figure 7.3 shows that only signals from stations located $<$ 25 km away from the next lateral column boundary and with elevation angles lower than 30° traverse the lateral column boundaries below the model top at 15 km. Rays with a low elevation angle contribute most to the vertical resolution and are, therefore, important in GNSS tomography. In this study, different cutoff angles of 10°, 5°, 3° and 0° are investigated. Due to the mountainous topography in Switzerland, the topography has to be taken into account. Accordingly, the visibility has been computed for each receiver station using the digital elevation model DEM25 (Swisstopo 2004).

At lower elevation angles, effects, such as multipath, have an increasing impact on the accuracy of slant path delays. This impact is considered by modeling the accuracy (variance) of slant path delays proportional to $1/\cos^2(\vartheta)$ where the ϑ denotes the zenith angle.

Global navigation satellite systems

Currently, most GNSS applications process GPS observations, only. The use of other GNSSs, such as GLONASS and Galileo, will considerably increase the amount of measurements and have the potential to significantly improve the accuracy of the parameters estimated by GNSS processing

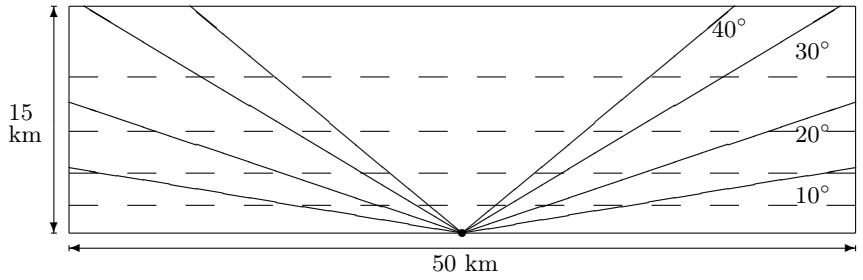

Figure 7.3: A vertical column of the model grid (5 layers) is shown. The layer boundaries are indicated by dashed lines. The size of the cells corresponds to the grid resolution used in the investigations. In the middle of the lowest cell, a receiver is placed (black dot) which tracks signals at various elevation angles (solid lines).

software. The satellite constellation of Galileo and, especially, that of GLONASS show larger nominal inclinations compared to that of GPS. This will increase the coverage at high latitudes.

In this experiment, the impact of observations from the additional GNSS Galileo together with GPS on the formal error of the unknown refractivities is investigated. GPS ephemeris of GPS week 1402 from the International GNSS Service (IGS) are used and for Galileo, the ephemeris are computed assuming a full constellation. For observations of the two systems, the same accuracy is assumed.

Receiver network

In Switzerland, a dense GNSS permanent network called AGNES is available (see Section 4.1). It comprises 31 GNSS stations well-distributed over the whole country (see Figure 7.4). SwissMetNet is the meteorological network operated by the Swiss Federal Office of Meteorology and Climatology (see Section 4.3). If we equip the SwissMetNet with GNSS receivers, this would increase the number of GNSS stations to 92. The costs of this extension are considerably smaller than setting up a separate network from scratch as infrastructure, such as communication and power supply, is already available and the administrational efforts are smaller. Investigations of the impact of this network extension on the formal error of the estimated refractivities will show if this update is recommendable in view of GNSS tomography.

Beside the investigations on the practical network extension, experiments with synthetically generated networks are carried out. The stations are placed at the nodes of a regular mesh. Meshes with different mesh widths and different number of nodes are used to vary the number of stations (see Table 7.2). The height of the stations are randomly set. For each network configuration, the probability density function

$$p(x) = \lambda e^{-\lambda x} \tag{7.2}$$

with a dedicated value for the coefficient λ is applied (see Table 7.2). Figure 7.5 shows histograms of the height distribution for networks of 200 stations for various distribution coefficients λ. The same realizations of the distribution functions are used in the experiments. The impact of the station density and distribution of the station height on the formal error will also be investigated (see Section 7.3.3).

7.2 Methods

In the error analysis, a modified version of the software package AWATOS is used (Troller 2004). Double difference delay observations and pseudo-observations, such as a priori values and intervoxel constraints, are combined in a least squares adjustment. Observations are processed in hourly batches and for each batch, a single adjustment is carried out. Observation errors are assumed

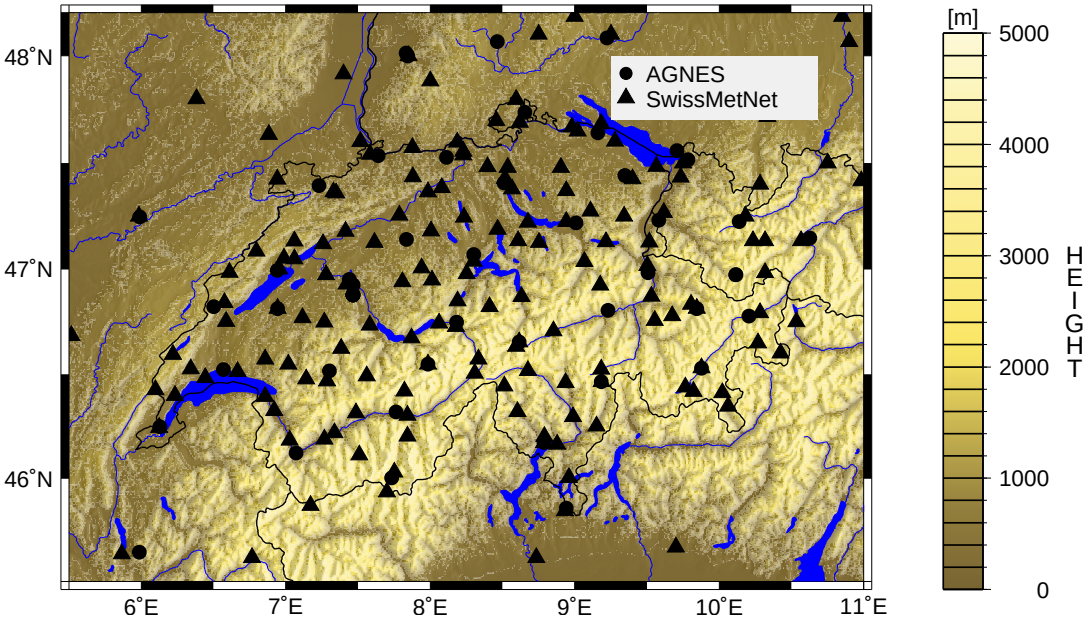

Figure 7.4: Map displaying the GNSS permanent network AGNES (black circles) and the meteorological network SwissMetNet (back triangles).

Table 7.2: Configuration options for the synthetically generated networks

Option	**Values**
Height distribution	Exponentially distributed station heights with various values for the distribution parameter $\lambda = \{0.0006, 0.0008, 0.001, 0.0015, 0.002, 0.003\}$ or the same height of 200 m for all stations
Mesh/#Stations	4×8/32, 6×12/72, 8×16/128, 10×20/200, 12×24/288, 14×28/392

to be normally distributed and the observation equations are linear. This allows a proper error propagation.

Least squares adjustment

The linear observation equation written in matrix notation is

$$\mathbf{b} = \mathbf{A}\,\mathbf{x} + \boldsymbol{\eta} \tag{7.3}$$

where $\mathbf{b}$ is the observation vector, $\mathbf{A}$ the observation matrix, $\mathbf{x}$ the unknown parameters (refractivity values), and $\boldsymbol{\eta}$ the normally distributed measurement errors. The most probable solution is obtained by a least squares adjustment. The least squares problem is stated as

$$\min_{\mathbf{x}} \left\| \mathbf{B}^{-1} \left(\mathbf{A}\,\mathbf{x} - \mathbf{b} \right) \right\|_2. \tag{7.4}$$

where $\mathbf{B}$ denotes the Cholesky factorization of the measurement error covariance matrix $\mathbf{C}_{bb}$. The least squares problem can be solved with the *method of normal equations* which formulates the problem as a linear system.

$$\mathbf{A}^T\,\mathbf{C}_{bb}^{-1}\,\mathbf{A}\,\mathbf{x} = \mathbf{A}^T\,\mathbf{C}_{bb}^{-1}\,\mathbf{b} \tag{7.5}$$

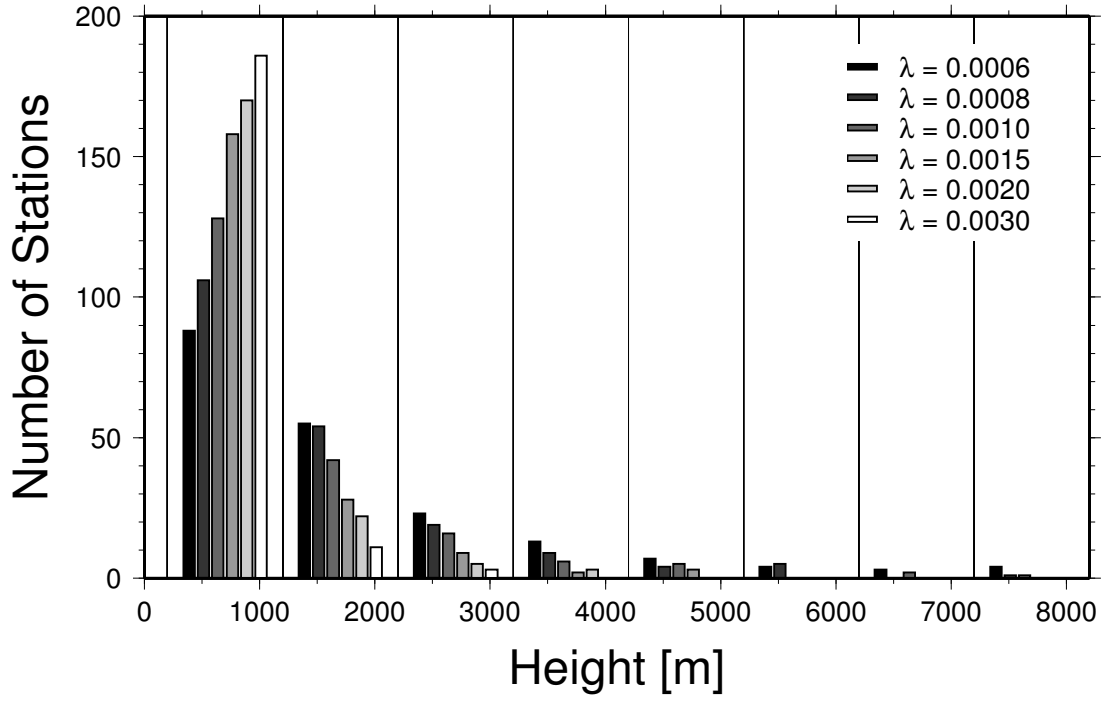

Figure 7.5: Histogram of station heights for 6 networks with different height distributions. Each network consists of 200 GNSS stations. The heights are exponentially distributed (see Equation 7.2) with parameters $\lambda = 0.0006, 0.0008, 0.001, 0.0015, 0.002$ and 0.003.

The covariance matrix of the unknown parameters $\mathbf{C}_{xx}$ can be easily derived from the normal equation.

$$\mathbf{C}_{xx} \;=\; \left(\mathbf{A}^T\,\mathbf{C}_{bb}^{-1}\,\mathbf{A}\right)^{-1} \tag{7.6}$$

This shows that no observation vector is needed to compute the covariance matrix of the unknown parameters. The knowledge of the measurement constellation described by the observation matrix $\mathbf{A}$ and of the measurement error covariance matrix $\mathbf{C}_{bb}$ is sufficient.

In least squares adjustment, one often likes to change the influence of certain observations relative to others. A reason for a different weighting of the observations can be different measurement errors. However, the accuracy of an observation is often known only relative to the accuracy of another one. As the least squares solution is not affected by multiplying the covariance matrix of the measurement errors with a constant, the use of relative accuracies is often preferred. The covariance matrix of the measurement error is replaced by the matrix containing the relative accuracies. This matrix is called cofactor matrix of the observations and is denoted by $\mathbf{Q}_{bb}$. The following formula relates the covariance matrix $\mathbf{C}_{bb}$ with the cofactor matrix $\mathbf{Q}_{bb}$

$$\mathbf{C}_{bb} \;=\; \sigma_0^2\,\mathbf{Q}_{bb} \tag{7.7}$$

where σ_0 is the unit-weight standard error. The cofactor matrix of the unknown parameters $\mathbf{Q}_{xx}$ is computed the same way as the covariance matrix of the unknown parameters:

$$\mathbf{Q}_{xx} \;=\; \left(\mathbf{A}^T\,\mathbf{Q}_{bb}^{-1}\,\mathbf{A}\right)^{-1} \tag{7.8}$$

The least squares adjustment implemented in AWATOS works with cofactor matrices. In order to compute the covariance matrix of the known parameters, the unit-weight standard error σ_0 is needed. This standard error is estimated from a real GPS least squares adjustment from 20th November 2006 by

$$\hat{\sigma}_0^2 \;=\; \frac{1}{n-r}\,\mathbf{v}^T\,\mathbf{Q}_{bb}^{-1}\,\mathbf{v} \tag{7.9}$$

where $\hat{\sigma}_0$ is the estimated unit-weight standard error, n the number of observations, r the number of unknowns and $\mathbf{v} = \mathbf{A}\hat{\mathbf{x}} - \mathbf{b}$ the postfit residuals.

Error measures

The formal error of a tomographic solution ε is computed from the cofactor matrix of the unknown parameters

$$\varepsilon = \sqrt{\frac{\hat{\sigma}_0^2}{r} \sum_{i=1}^{r} q_{i,i}} \tag{7.10}$$

where r is the number of unknown parameters, $q_{i,i}$ the i-th diagonal element of the cofactor matrix $\mathbf{Q}_{xx}$ and $\hat{\sigma_0}$ the estimated unit-weight standard error. The formal error of the tomographic solution is also evaluated for different layers. The formal error in the l-th layer is computed by

$$\varepsilon_l = \sqrt{\frac{\hat{\sigma}_0^2}{|\mathcal{H}_l|} \sum_{i \in \mathcal{H}_l} q_{i,i}} \tag{7.11}$$

where $\mathcal{H}_l$ is the set of all voxel indices of the voxels located in the l-th layer.

As a least squares adjustment is computed for each hour, one gets a time series of formal errors. Several statistical measures are computed from such time series. These are

- the *mean formal error* (MFE)

$$\bar{\varepsilon} = \sqrt{\frac{1}{|\mathcal{T}|} \sum_{t \in \mathcal{T}} \varepsilon_t^2} \tag{7.12}$$

  where ε_t is the formal error of the tomographic solution at time t and $\mathcal{T}$ the set of all time points for which solutions are available,

- the *absolute temporal variability* of the formal error (ATV)

$$\nu_a = \sqrt{\sqrt{\frac{1}{|\mathcal{T}|} \sum_{t \in \mathcal{T}} \left(\varepsilon_t^2 - \bar{\varepsilon}^2\right)^2}}, \text{ and} \tag{7.13}$$

- the *relative temporal variability* of the formal error (RTV)

$$\nu_r = \sqrt{\sqrt{\frac{1}{|\mathcal{T}|} \sum_{t \in \mathcal{T}} \left(\frac{\varepsilon_t^2 - \bar{\varepsilon}^2}{\bar{\varepsilon}^2}\right)^2}}. \tag{7.14}$$

7.3 Results and discussion

7.3.1 Geometry of the satellite constellation

Dilution of precision (DOP) is a simple precision measure in satellite navigation based on the geometric constellation of the visible satellites (Geiger 1987; Seeber 2003). In view of assimilation of GNSS observations into numerical weather prediction models, a simple monitoring of the tomographic solution in terms of quality is desirable. In this subsection, the use of DOP to monitor the formal error of the tomographic solution is investigated.

The squared formal error of the tomographic solution ε^2 is computed using the base configuration and a cutoff elevation angle of 5°. The resulting time series are compared to geometric DOPs (GDOP) calculated at a virtual station located at 47° N, 7° E, and 400 m height.

The two time series are plotted in Figure 7.6. The GDOP values are most of the time lower than 3 m^2 which indicates excellent geometric satellite constellations. In addition, the two time

series are highly correlated. The correlation coefficient of the hourly maximum values is 0.801. This shows that temporal changes in the formal error are mainly related to the geometry of the satellite constellation. The investigation has also revealed that GDOP can be used as a simple precision measure for monitoring the tomographic solution.

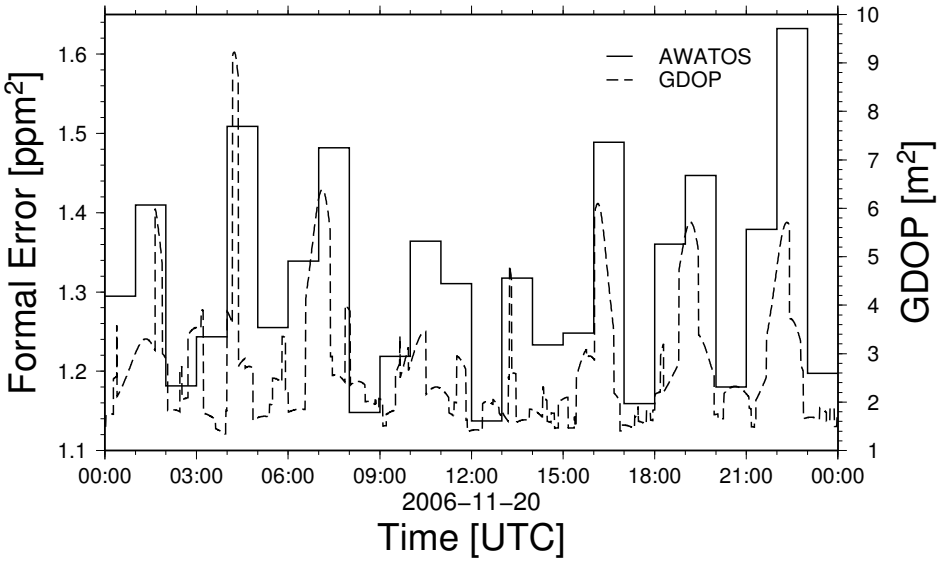

Figure 7.6: Time series of the geometric dilution of precision (GDOP) for a virtual station located at 47°N, 7°E, and 400 m height (dashed line) and of the formal error computed from the tomographic solution (solid line).

7.3.2 Cutoff angles and satellite visibility

The change of the cutoff elevation angle for satellite observations in GNSS processing has a significant effect on the formal error of the tomographic solution. Lowering the cutoff angle decreases the mean formal error by about 20% (see Table 7.3). This shows the importance of low-elevation rays in GNSS tomography. Rays visible at low elevations contain valuable information for the resolution of vertical structures in the atmosphere and, thus, significantly contribute to precise results in GNSS tomography. Their importance in GNSS tomography shows the need for accurate models in GNSS processing as they increase the precision of low-elevation delays and allows to actually include low-elevation rays in the processing. The strong impact of low-elevation rays in GNSS tomography affects the selection of receiver stations. A good satellite visibility for receiver stations is essential for precise results in GNSS tomography.

In Figure 7.7a), time series of the formal errors are plotted for configurations with different cutoff elevation angles. The temporal variability of the formal errors is only weakly affected by changing the cutoff angle. A small increase of the relative temporal variability can be observed at lower cutoff elevation angles (see Table 7.3). The appearance and disappearance of satellites have a large impact on the measurement geometry and are, therefore, a major contributor of the temporal variability observed in the formal error. If the cutoff elevation angle is lowered, the impact of these events on the formal error increases as low-elevation rays contribute disproportionally high to the precision of the tomographic solution.

Figure 7.8a) shows the impact on the formal error with changing the cutoff elevation angles in different layers. The strongest effect is visible in layers between 4 and 8 km height. At these heights, the angle between crossing rays are on average closer to 90° than in layers below and above this height range. In contrast to that, the influence of changing the cutoff elevation angle on the formal error in lower layers is relatively small. In these layers, only rays with low elevations cross each other. Hence, crossing rays show rather acute intersecting angles which results is lower

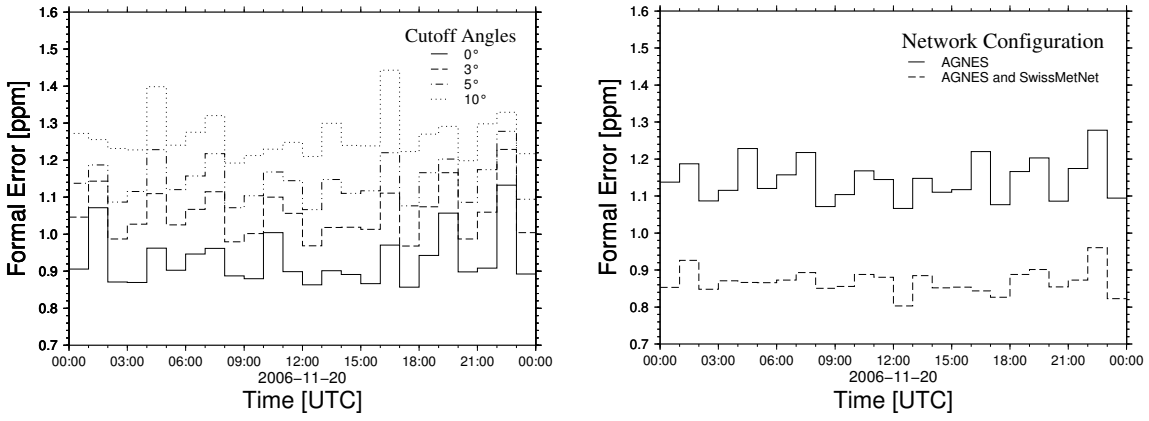

(a) Cutoff angle

(b) Network

Figure 7.7: Time series of the formal errors of the tomographic solutions computed a) with different cutoff elevation angles and b) using networks with different numbers of receiver stations.

resolution capabilities. This similarly holds for layers above 8 km except in the top layer where the formal errors are considerably improved by a lower cutoff angle. The reason for this improvement in the top layer is not clear, but, might be related to the combination of the special intervoxel constraints in the boundary layer and the low-elevation observations.

Table 7.3: Statistics of the formal errors of the tomographic solutions. The correlation coefficients between the time series for different cutoff elevation angles are listed. In addition, the mean formal error (MFE), absolute temporal variability (ATV) and relative temporal variability (RTV) are computed from each of the time series.

	0°	**3°**	**5°**	**10°**	**MFE [ppm]**	**ATV [ppm]**	**RTV [-]**
0°	1.000	0.945	0.834	0.480	0.933	0.141	0.151
3°	0.945	1.000	0.949	0.646	1.055	0.145	0.138
5°	0.834	0.949	1.000	0.819	1.146	0.131	0.114
10°	0.480	0.646	0.819	1.000	1.266	0.159	0.126

7.3.3 Network density

Three studies are carried out to investigate the impact of network properties on the formal accuracy of the tomographic solutions. Namely, the station density and the distribution of the station heights in the network are investigated. In the first study, the practical extension of the AGNES network by equipping the SwissMetNet with GNSS receivers is evaluated. In the other two studies, synthetically generated networks with different numbers of stations and station height distributions are analyzed.

The extension of the AGNES network by the SwissMetNet decreases the formal error of the tomographic solution by about 20% (see Table 7.4). The formal errors in the layers are not equally affected by this extension. Formal errors are mainly improved in the lower part of the troposphere (see Figure 7.8b)). There are 2 effects unequally influencing the formal errors at different layers:

1. Vertical atmospheric structures can be precisely resolved by GNSS observations even with large elevation angles in that part of the troposphere which is well populated with receiver stations. For the extended network, these are the lowest 3 km of the troposphere.

2. A ray traverses only voxels located at the same height as the receiver station or above that station. Thus, voxels located at lower heights are less frequently traversed than those at higher

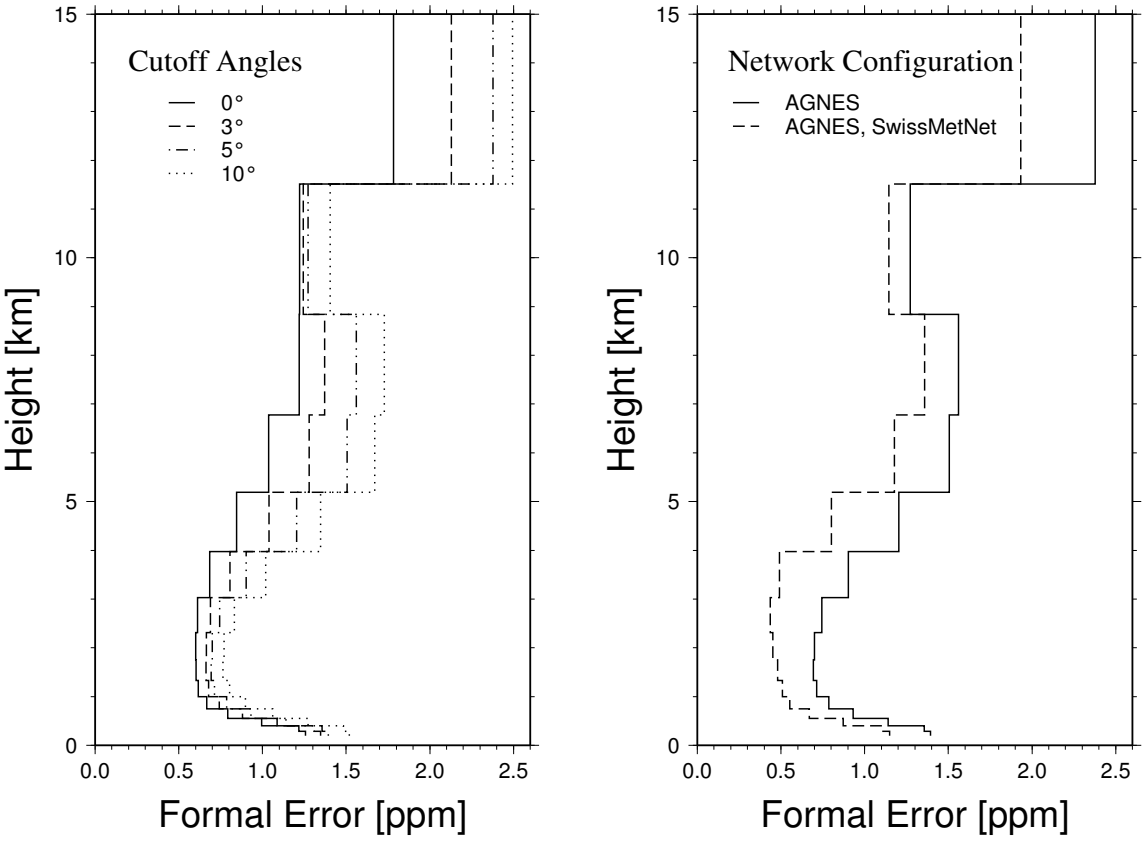

(a) Cutoff angle

(b) Network

Figure 7.8: Formal errors of tomographic solutions in dependence of the height are computed a) with different cutoff elevation angles and b) with different network configurations.

altitudes. As a result of this, the improvement of the formal error increases with height and the maximal improvement is reached at the height of the top station of the network. Above this height, the improvement remains constant with height.

In Figure 7.8b), one can see that the formal error is already considerably improved in the lowest part of the troposphere. This indicates that this improvement is at least partially caused by the first effect. In addition, the improvement of the formal error steadily increases with height and reaches its maximum at approximately 3500 m altitude. Similar improvements are achieved between 3500 m and 6000 m. This coincides with the second effect and with the height of the top station (3630 m altitude) in the extended network. The reason for the smaller increase of the formal error with height between 6000 m and 11500 m and large improvement of the formal error in the top layer is not clear and needs further investigations.

We can expect smaller temporal variations of the formal error by the particular extension of the AGNES network (see Figure 7.7b)). The absolute and relative temporal variability have been decreased by a factor of 2 (see Table 7.4). It seems that denser networks are less sensitive to the satellite constellation. Beside the significant decrease of the mean formal error, this is another important improvement and shows the potential of this particular network extension.

In the second study, two experiments are carried out. In both experiments, network configurations with different numbers of receiver stations are used. The configurations of the two experiments differ in the distribution of the station heights. In the first one, all stations are located at 200 m altitude. In the other one, station heights are exponentially distributed with distribution parameter λ=0.001 (see Equation 7.2).

Table 7.4: Statistics of the formal errors of the tomographic solutions. The correlation between the time series using different receiver networks are listed. The AGNES network includes 31 stations and the extended network (AGNES in combination with SwissMetNet) 92 stations. In addition to the corrections, the mean formal error (MFE), the absolute temporal variability (ATV), and relative temporal variability (RTV) of the time series are listed.

	AGNES	**Ext. network**	**MFE [ppm]**	**ATV [ppm]**	**RTV [-]**
AGNES	1.000	0.759	1.146	0.131	0.114
Ext. network	0.759	1.000	0.869	0.058	0.067

In both experiments, the mean formal error is decreased by increasing the network density (see Figure 7.9a)). The improvements are significantly larger for the configurations with well distributed station heights than for those with all stations located at the same height. With the help of the $1/\sqrt{n}$-rule, one can assess the improvement of the formal error by increasing the number of observations. This rule assumes that all observations contain equally valuable information. As each station contributes on average a similar number of observations to the tomographic inversion, one can apply the rule to the number of stations instead of to the number of observations. For the experiment with all stations located at the same height, the decrease of the formal error is much smaller than estimated by the $1/\sqrt{n}$-rule. On the other hand, similar improvements as expected from the $1/\sqrt{n}$-rule are achieved with the configurations including well distributed station heights. This is remarkable with respect to the use of pseudo-observations. Pseudo-observations can be understood as a Tikhonov regularization. If the number of observations are increased in a Tikhonov-regularized least squares problem, the formal error decreases less than proposed by the $1/\sqrt{n}$-rule given that the Tikhonov factor is kept constant.

Looking at Figure 7.9b), the mean formal error decreases with the number of stations and the decrease becomes smaller with larger numbers of stations. The following model mirrors these considerations.

$$\varepsilon(n) = \varepsilon_a + \varepsilon_m \exp\left(-\frac{n}{n_s}\right) \tag{7.15}$$

where ε_a is the value of the horizontal asymptote, ε_m the maximal decrease of the formal error due to the observations, n the number of observations, and n_s the scaling factor.This model is fitted for the two experiments. The estimated parameters are listed in Table 7.5. For both experiments, the horizontal asymptote is larger than zero. A horizontal asymptote at values $\varepsilon_a > 0$ indicates that the least squares problem is ill-conditioned or even ill-posed and needs additional information which can be provided by pseudo-observations. The value ε_a can be regarded as the part of the formal error which is exclusively controlled by pseudo-observations. In our study, the experiment using a network with well distributed station heights shows a significantly smaller value for this parameter than the other experiment. This suggests a) that considerably lower formal errors can be achieved with networks showing well distributed station heights and b) that the solutions computed with such networks are much less sensitive to pseudo-observations. The estimated value for the parameter ε_m is significantly larger for the experiment using a network with well distributed station heights than for the other one. This indicates that a larger gain in formal accuracy can be achieved by increasing the network density in a network with well distributed station heights than in an network with stations located all at the same height.

In the third study, configurations with differently distributed station heights are used. For all configurations, the network includes the same number of stations (200 stations). The station heights are exponentially distributed with different distribution parameter λ (see Equation 7.2). Histograms for the different network configurations are plotted in Figure 7.5. For each network configuration, the formal error of the tomographic solution is computed. The mean formal error for each λ is shown in Figure 7.10. The results of this study confirm the positive impact of well distributed station heights on the formal error seen in the previous study. These results show that the distribution of the station heights is a key property of a network used for GNSS tomography.

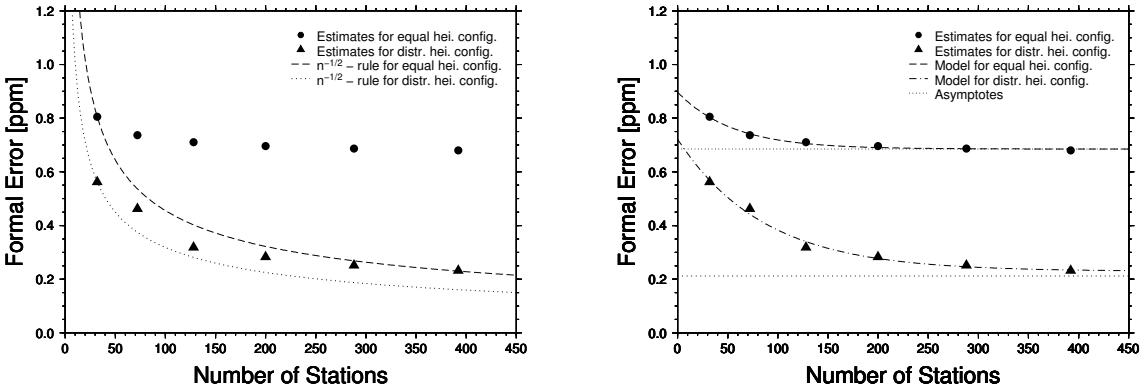

(a) $1/\sqrt{n}$-rule (b) Model according to Equation 7.15

Figure 7.9: Mean formal error of the tomographic results versus the number of receiver stations for configurations with stations located all at the same height (black circles) and for configurations with exponentially distributed station heights (black triangles). a) The dashed lines indicate the expected improvement of the formal error according to the $1/\sqrt{n}$-rule. b) The model described by Equation 7.15 has been fitted to the mean formal errors of the two experiments. The model's solutions are represented by the dashed lines. The model approaches to an asymptote if the number of stations tends to infinity. This asymptotes are indicated by the dotted lines.

From these 3 studies about the impact of the denser receiver networks on the formal error in GNSS tomography, one can conclude the following:

- The formal error can be significantly decreased with denser receiver networks.
- The distribution of the station height in the network is a key property of a GNSS network and has a large impact on the formal accuracy of tomographic solutions.
- The decrease of the formal error is limited. The limit can be decreased by a network configuration with well distributed station heights. Other types of observations are, however, needed to further improve the formal accuracy.
- The improvements by increasing the number of receiver stations is similar to the $1/\sqrt{n}$-rule if the station heights are well distributed in the network.
- The vertical resolution capability is the limiting factor in ground-based GNSS tomography. Observations providing information on the vertical wet refractivity distribution are the observations which ideally complement ground-based GNSS observations.

Table 7.5: Estimated parameters of the model described by Equation 7.15 for the experiments using a network with stations located all at the same height and using a network with exponentially distributed station heights. The residual standard error of the fitted models is 0.006 ppm and 0.018 ppm, respectively.

	Equal height			**Exponentially distributed heights**		
Parameter	**Estimate**	**Std. Error**	**t value**	**Estimate**	**Std. Error**	**t value**
ε_a [ppm]	0.685	0.004	168.00	0.229	0.017	13.72
ε_m [ppm]	0.212	0.022	9.71	0.493	0.039	12.65
n_s [-]	54.622	8.166	6.69	85.885	14.707	5.84

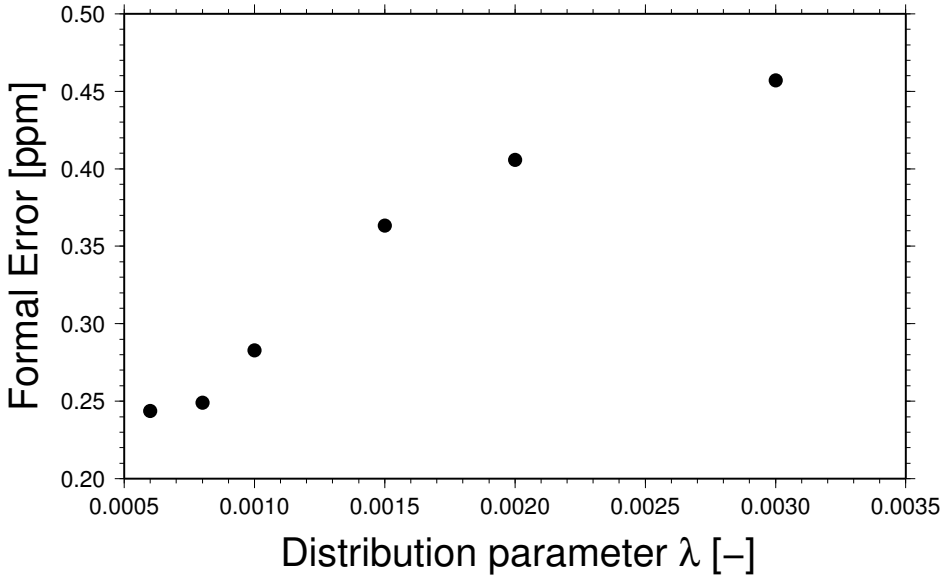

Figure 7.10: Plot of mean formal error of the tomographic solutions for different station height distributions. The exponential distribution with parameter λ is used (see Equation 7.2). An increasing parameter λ is equivalent to a narrower station height distribution.

7.3.4 Additional global navigation satellite systems

The use of the additional GNSS Galileo decreases the mean formal error by about 10% (see Table 7.6). This is much less compared to the impact of lowering the cutoff elevation angle and to increase the station density. Figure 7.11 shows the time series of the formal error for the two configurations. The time series computed with the configuration including Galileo varies much less in time than that using GPS only. Including Galileo in GNSS tomography decreases the absolute and the relative temporal variability by a factor of 2 (see Table 7.6). The mean formal error in different layers is shown for the two configurations in Figure 7.12. The investigations have revealed that the mean formal error in the layers are equally affected by the use of the additional GNSS. Galileo shows similar constellation features as GPS which leads to a similar measurement geometry for Galileo observations as for GPS ones. This might be a reason why the mean formal error in the layers is equally affected. Even though the impact of other GNSSs on the formal accuracy is not investigated in this chapter, one can expect similar improvements with the GNSSs GLONASS and COMPASS.

Table 7.6: Formal error statistics of the tomographic solution using different GNSSs. The correlation between the two time series is listed. In addition, the mean formal error (MFE), the absolute temporal variability (ATV) of the formal error and the relative temporal variability (RTV) of the formal error is computed.

	Correlation	**MFE [ppm]**	**ATV [ppm]**	**RTV [-]**
GPS	0.730	1.146	0.131	0.114
GPS+Gal.	0.730	1.049	0.064	0.061

7.3.5 Horizontal and vertical grid resolution

Increasing the resolution of the model leads to more unknown parameters. Consequently, there are less observations per unknown which results in larger values on the diagonal of the cofactor matrix

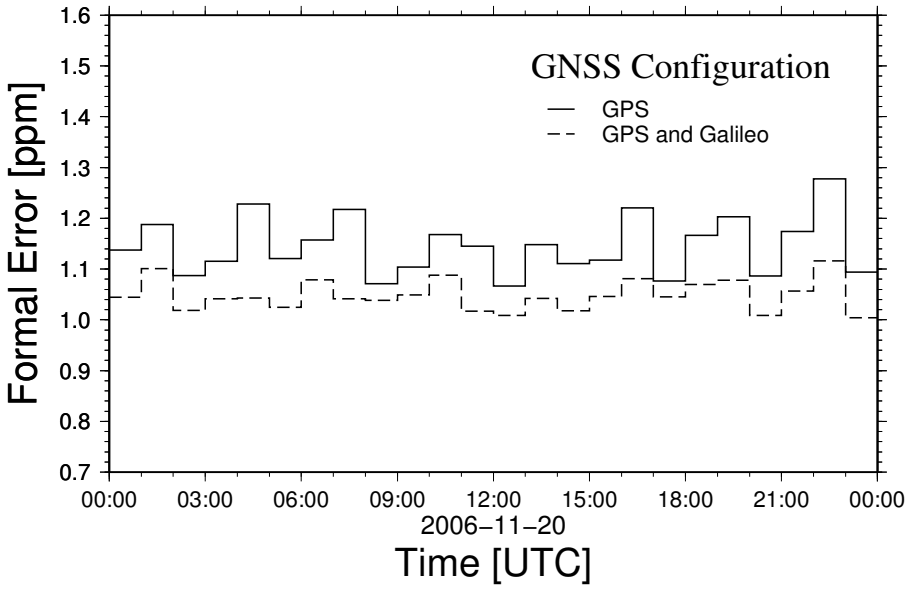

Figure 7.11: Time series of the formal accuracy using configurations with different GNSSs.

of the unknown parameters. Contrary, the a posteriori unit-weight standard error σ_0 becomes smaller because the finer grid resolution allows a more accurate representation of the reality. The tradeoff between these two effects determines the optimal grid resolution. In the experiments carried out in this section, the effect of more accurate representations of the truth is disregarded and, accordingly, the same unit-weight standard error is assumed for all grid configurations.

The mean formal error is computed for each layer and for each grid configuration used in the tomographic processing. The investigations have shown that the mean formal error averaged over all layers tends to be larger for fine grids than for coarse grids if the unit-weight standard error is not accordingly adjusted. Changing the horizontal grid resolution affects more the mean formal error in layers at high altitude than in the layers at low altitude (see Figure 7.13a)). In contrast to that, refining the vertical grid resolution increases the formal errors in the layers below 1500 m altitude (see Figure 7.13b)). The dissimilar effects with respect to horizontal and vertical grid refinements might be related to different resolvability capabilities of GNSS tomography in the vertical and horizontal dimensions. The resolution capabilities of vertical structures are especially limited above the top receiver station in GNSS tomography. In this part of the atmosphere, the parameters are mainly influenced by pseudo-observations. As the number of pseudo-observations increases proportionally to the grid refinement and GNSS observations make only a limited contribution to the vertical resolvability, the unknown parameters are similarly good determined as before the grid refinement. In the lowest 1500 m of the troposphere, GNSS observations considerably contribute to the vertical resolvability due to the good height distribution of the stations within this layer. As a result of this, the decrease of the number of GNSS observations per layer affects the formal error in these layers. This is exactly what can be observed in Figure 7.13b).

7.3.6 Combination of the improvements and their joint potential

Lowering the cutoff elevation angle, the use of an additional GNSS and a larger number of receiver stations are configuration options which show considerable improvements of the formal accuracy. In this section, the joint potential of these options is investigated and in particular if the single improvements are cumulative with respect to the formal accuracy.

In Figure 7.14, time series of 5 different configurations are shown. Setting the cutoff elevation angle to 0° and using additional receiver stations are the configuration options with the largest impact on the formal error. For both, the mean formal error is decreased by about 25%. The

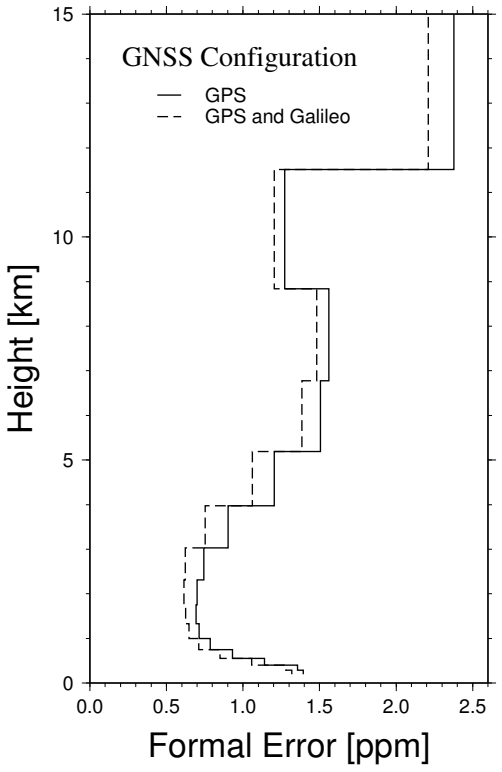

Figure 7.12: Formal error in different layers. The tomographic model is evaluated with configurations using different GNSSs.

use of the additional GNSS Galileo improves the mean formal error by only 10%. Combining the use of Galileo with lowering the cutoff angle or with the use of SwissMetNet leads to similarly accurate results and their joint improvements are mostly cumulative. Hence, the mean formal error is decreased by about 30% (see Table 7.7).

Table 7.7: Statistics on the formal error achieved by modifying multiple configuration options. The mean formal error (MFE), the absolute temporal variation (ATV) and the relative temporal variation (RTV) are listed in the table.

	MFE [ppm]	**ATV [ppm]**	**RTV [-]**
5°, -Galileo, -SwissMetNet	1.146	0.131	0.114
5°, +Galileo, +SwissMetNet	0.803	0.035	0.044
0°, +Galileo, -SwissMetNet	0.810	0.064	0.079
0°, -Galileo, +SwissMetNet	0.484	0.040	0.084
0°, +Galileo, +SwissMetNet	0.419	0.014	0.035

Lower formal errors can be achieved if the cutoff elevation angle is lowered and additional stations from the SwissMetNet are used. This decreases the mean formal error by about 60% compared to the base configuration. Even lower formal errors are obtained by combining all three improvements. They decrease the formal error from 1.146 ppm to 0.419 ppm which corresponds to a relative decrease of 65%.

Concerning the temporal variability, the use of the additional GNSS Galileo and the network extension have shown the largest decrease of the temporal variability. Combining these two modifications results in the cumulation of the single improvements in terms of the relative temporal variability (see Table 7.7).

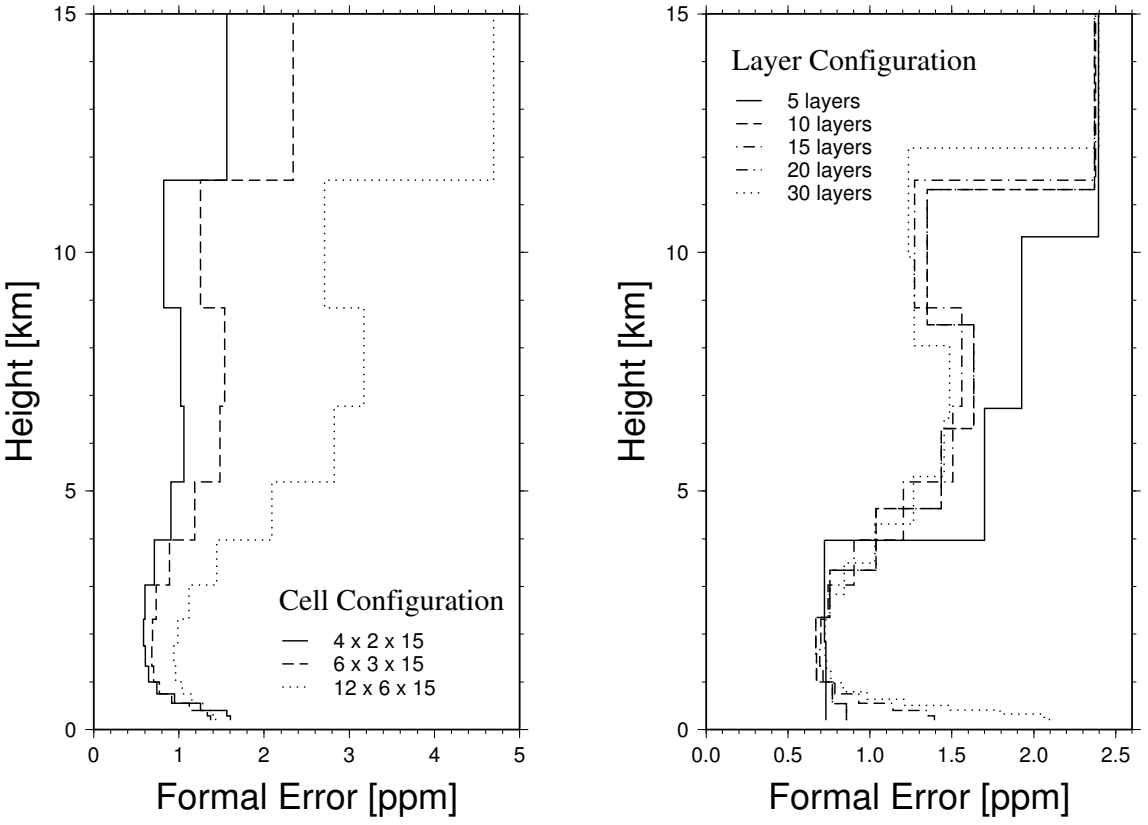

(a) Horizontal resolution

(b) Vertical resolution

Figure 7.13: Mean formal error in different layers for horizontal and vertical grid refinements. The tomographic model is evaluated with configurations using a) different horizontal grid resolutions and b) different vertical grid resolutions.

Figure 7.15 shows how much the formal error in the individual layers are affected. For all layers, an improvement of the formal error can be observed. The layers between 4 km and 8 km show the largest decrease of the formal error, especially if the cutoff angle is lowered.

7.4 Conclusions

The investigations presented in this chapter have clearly shown that certain configurations significantly decrease the formal error of the tomographic solution. Lowering the cutoff elevation angle and increasing the number of ground stations cause major improvements. However, the increase is not the same in all layers. Taking signals at low elevations into account mainly affects layers between 4 to 8 km altitude whereas increasing the number of stations influences the meteorologically more relevant layers below 4 km altitude.

Compared to the first two modifications, the use of the additional global navigation system Galileo increases the formal accuracy less. The main effect of the use of Galileo is the lower temporal variability of the formal accuracy. This decrease is preserved even if multiple configuration options are combined and their effects are cumulative. This is also true for the improvements of the formal error.

The extension of the AGNES network with the locations of the SwissMetNet has been investigated in this chapter. The investigations revealed that equipping the SwissMetNet with GNSS receivers would ideally complement the AGNES network. This practical network extension de-

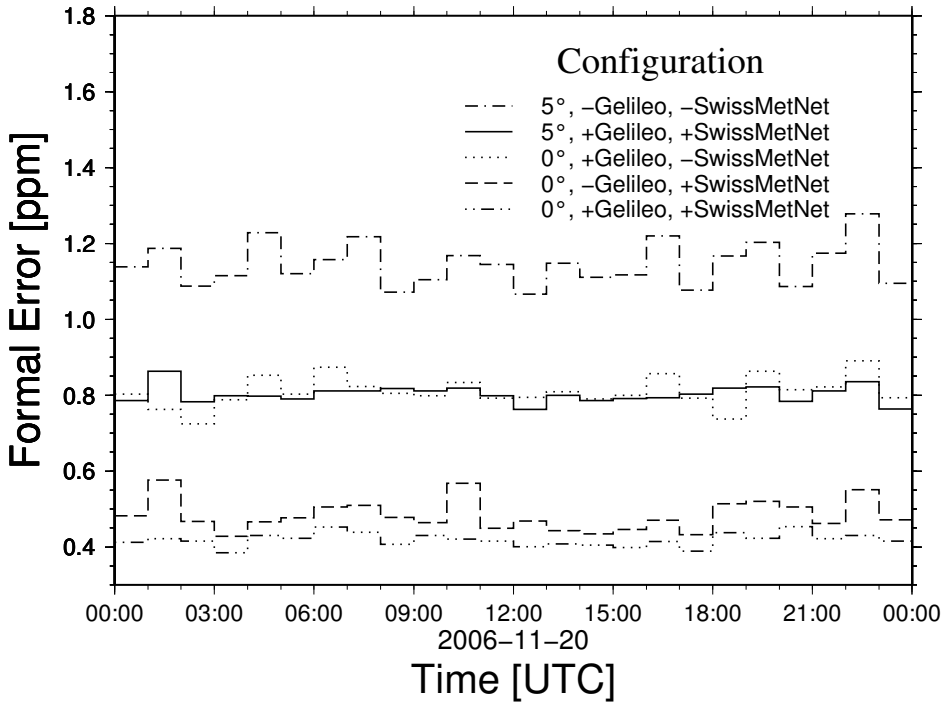

Figure 7.14: Time series of the formal errors computed with several improved configuration options.

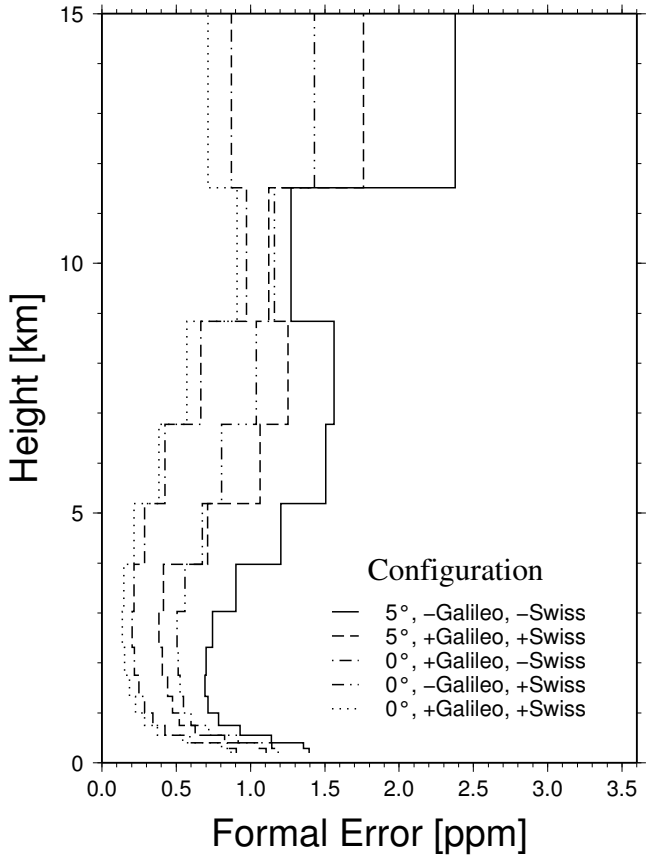

Figure 7.15: Formal error of tomographic solutions at different heights. Configurations with multiple improved parameter options are used.

creases the formal error by about 20%. The expected cost for such an extension would be roughly 1-2 million Euros and is recommended in view to provide accurate GNSS observations for meteorological applications.

A poor height distribution of the stations is a limiting factor for the formal accuracy and cannot completely be compensated by increasing the number of receiver stations. Therefore, it is highly recommended to take the station height into account when setting up a receiver network. The investigations have also revealed that a good satellite visibility at the receiver stations is essential for precise tomographic results.

Chapter 8

Simulation-based evaluation of the new tomographic algorithms

What are the capabilities of GNSS tomography to reconstruct atmospheric structures? This question is regularly debated in the GNSS tomography community (see Bastin et al. 2007; Bender and Raabe 2007; Bender et al. 2011). Especially, the capability to reconstruct vertical structures is of interest and will be considered in this chapter. In addition, the convergence properties of the tomographic algorithm will be investigated and the impact of the network design on the vertical resolution will be discussed. This chapter is divided into two parts. In a first part, theoretical aspects of the capabilities to reconstruct vertical structures will be investigated. In a second part, experiments with simulated GPS data are carried out investigating if and how fast the tomographic solutions converge and how well vertically varying patterns are resolved.

8.1 Theoretical considerations of the resolvability of vertical structures

The measurement geometry of GNSS tomography is characterized by rays which enter the model grid at the top and end at the receiver located on Earth's surface. Though this measurement configuration enables to accurately resolve horizontal structures, it is not obvious if vertical structures can be resolved. The capability to resolve vertical structures will be investigated with the help of two layer-models.

The refractivity in the layers can be estimated by solving a linear inversion problem where the observation matrix is denoted by $\mathbf{H}$, the refractivities within the layers by $\mathbf{n}$ and the GPS slant path observations by $\mathbf{\Delta}$.

$$10^{-6}\,\mathbf{H}\,\mathbf{n} \;=\; \mathbf{\Delta} \tag{8.1}$$

Assuming constant refractivity within the layers, the observation matrix $\mathbf{H}$ contains geometrical path lengths of the rays within the respective layers (see also Section 3). The inverse problem is solved using the least squares technique. Therefore, the normal equation is build.

$$\underbrace{10^{-12}\,\mathbf{H}^T\,\mathbf{H}}_{\mathbf{N}}\,\mathbf{n} \;=\; 10^{-6}\,\mathbf{H}^T\,\mathbf{\Delta} \tag{8.2}$$

To solve this equation system, the normal equation matrix $\mathbf{N}$ have to be invertable. In this subsection, the structure of the matrix $\mathbf{N}$ is analyzed with respect to its invertability. This should help us to better understand how well vertical structures in the atmosphere can be reconstructed with GNSS tomography.

Two layer-models are considered, a) in plane (Cartesian) geometry and b) in spherical geometry. The first model is illustrated in Figure 8.1a). A ray hits the Earth's surface with a zenith angle ϑ_0. On its way, it crosses a layer (gray shaded) with thickness δr. The distance between the lower

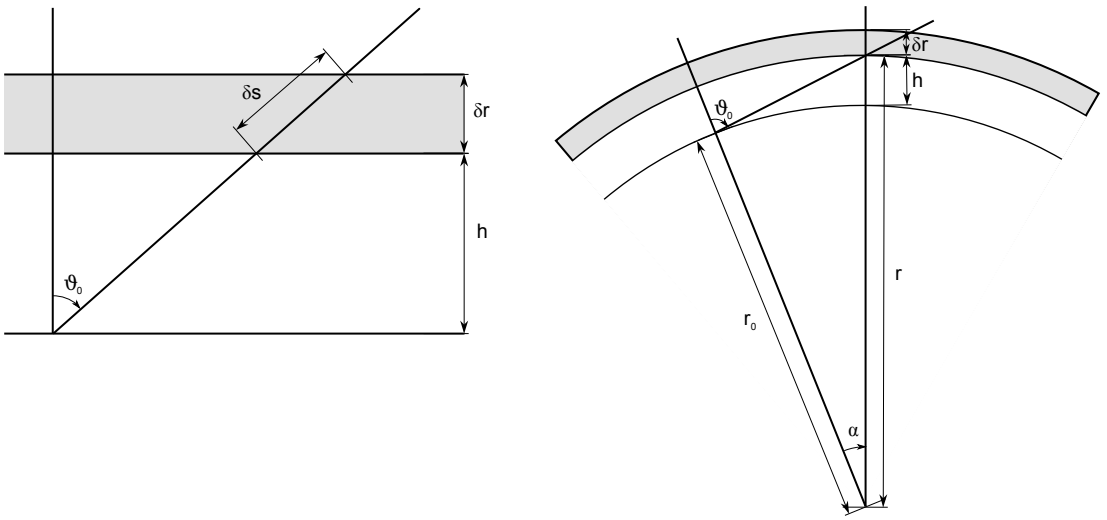

(a) Plane geometry (b) Spherical geometry

Figure 8.1: Path length of a ray within a layer (gray shaded) in a) plane (Cartesian) geometry and in b) spherical geometry. The height of the layer above the Earth's surface is denoted by h, the layer thickness by δr and the path length within the layer by δs.

boundary of the layer and the Earth's surface is denoted by h and the path length of the ray within the layer by δs. The path length δs in the planar case can be computed by

$$\delta s \;=\; \frac{1}{\cos(\vartheta_0)}\,\delta r. \tag{8.3}$$

Figure 8.1b) shows the spherical layer-model. The spherical model has an additional parameter r_0 describing the radius of the Earth's surface. The radius of the lower boundary of the layer is denoted by $r = r_0 + h$, where h is the distance between the lower layer boundary and the Earth's surface. As in the planar model, the variables ϑ_0, δr, and δs describe the zenith angle of the ray hitting the Earth's surface, the thickness of the layer, and the path length of the ray within the layer, respectively. In the spherical model, the path length δs is

$$\delta s \;=\; \frac{\mathrm{d}s}{\mathrm{dr}}\,\delta r \;=\; \frac{r}{\sqrt{r^2 \;-\; r_0^2\,\sin^2(\vartheta_0)}}\,\delta r \tag{8.4}$$

and can be written as Taylor series

$$\delta s \;=\; \frac{1}{\cos(\vartheta_0)}\,\delta r \;\underbrace{-\,\frac{1}{r_0}\,\frac{\sin^2(\vartheta_0)}{\cos^3(\vartheta_0)}\,h\,\delta r + \mathrm{R}_1(h)}_{\mathrm{R}_0(h)}\,. \tag{8.5}$$

where $\mathrm{R}_l(h)$ is the remainder of the l-th order spherical approximation. For a complete derivation see Appendix E.

In Equation 8.3, the distance δs within the layer depends only on the layer thickness δr and the zenith angle ϑ_0. The height h of the layer above Earth's surface has no influence on the path length and, thus, varying the parameter h in the observation equation has no influence on the delay. As no information about the location of the layer is contained in Equation 8.3, no vertical structures can be resolved in the planar case.

In the first order approximation of the spherical model, the distance δs is determined by two terms. The first term (zeroth order spherical approximation) is equal to the planar model. The

second one is related to the spherical effect. This term will be referred to as *first spherical term*. In contrast to the planar model, the first spherical term includes the distance h between Earth's surface and the lower layer boundary. This is a necessary condition to resolve vertical structures.

What are the conditions influencing the first spherical term? The first spherical term vanishes in certain circumstances. In the case where the Earth's radius r_0 tends to infinity, the first spherical term becomes zero. From a geometrical point of view, the smaller the curvature is the larger the radius. In the limit case, the Earth's surface becomes flat and this corresponds to the planar case. The first spherical term also vanishes if the zenith angle ϑ_0 or the height h of the layer are zero. In the case where $\vartheta_0 = 0$ the path lengths are equal to the layer thicknesses. Consequently, no correction for the curvature is necessary. In another case where $h = 0$, the first spherical term vanishes due to the linearization used in the derivation of Equation 8.5 (see Appendix E).

The remainder $\mathrm{R}_0(h)$ in Equation 8.5 describes the spherical effect. To evaluate the impact of the spherical effect on the path length, we write the ratio between the remainder and the path length as

$$\xi_{\delta s} \;=\; \frac{\mathrm{R}_0(h)}{\delta s} \;=\; \frac{\delta s \;-\; \frac{\delta r}{\cos(\vartheta_0)}}{\delta s}. \tag{8.6}$$

In Figure 8.2, the ratio is displayed with respect to the zenith angle ϑ_0 for given layer heights h and using a radius $r_0 = 6370$ km. If the zenith angle ϑ_0 is zero, the ratio is also zero as the planar approximation perfectly fits the spherical model. On the other hand, if the zenith angle ϑ_0 tends to 90°, the ratio tends to infinity. This illustrates that the planar approximation strongly differs from the spherical model in this case. Table 8.1 lists at which zenith angle certain ratios are achieved for different layer heights. For path lengths in layers located in the lower troposphere (500-2000 m), the ratio is larger than 1% for rays with zenith angle ϑ_0 larger than 85°. In the middle troposphere (2000-8000 m), the ratio is larger than 1% for rays with zenith angle larger than 80°. This shows that rays with larger zenith angles become more important if the spherical effect is of interest.

Table 8.1: Zenith angles for ratio $\xi_{\delta s} = 0.1\%$, 1%, 10%, and 100% and for $h = 500$ m, 1000 m, 2000 m, 4000 m, and 8000 m. The ratio describes the spherical effect on the path length normalized by the path length (see Equation 8.6 and Figure 8.2).

layer height	**0.1%**	**1%**	**10%**	**100%**
500 m	74.353°	84.950°	88.434°	89.586°
1000 m	68.393°	82.877°	87.786°	89.414°
2000 m	60.749°	79.979°	86.871°	89.171°
4000 m	51.626°	75.972°	85.580°	88.828°
8000 m	41.777°	70.548°	83.764°	88.344°

How do the elements of the normal matrix $\mathbf{N} = \mathbf{H}^T\mathbf{H}$ look like? Using Equation 8.4, the elements in $\mathbf{H}$ can be written as

$$\delta s_{i,j} \;=\; \frac{r_0 \;+\; h_j}{\sqrt{(r_0 \;+\; h_j)^2 \;-\; r_0^2\, sin^2(\vartheta_{0\,i})}}\, \delta r_j \tag{8.7}$$

or using its first order approximation stated in Equation 8.5

$$\delta s_{i,j} \;\approx\; \frac{1}{\cos(\vartheta_{0\,i})}\, \delta r_j \;-\; \frac{1}{r_0}\frac{\sin^2(\vartheta_{0\,i})}{\cos^3(\vartheta_{0\,i})}\, h_j\, \delta r_j \tag{8.8}$$

where δr_j is the thickness of the j-th layer, h_j is the height of the j-th layer and $\vartheta_{0\,i}$ is the zenith angle of the i-th observation. The normal matrix $\mathbf{N} = \mathbf{H}^T\mathbf{H}$ can be formed assuming an infinite number of observations distributed uniformly between zenith angles 0° and $\vartheta_{0,\,\mathrm{max}}$. The diagonal elements of $\mathbf{N}$ become (see Appendix E)

$$N_{j,j} \;=\; \frac{10^{-12}\,(r_0 \;+\; h_j)}{\vartheta_{0,\,\mathrm{max}}\,\sqrt{(r_0 \;+\; h_j)^2 \;-\; r_0^2}}\, \arctan\left(\frac{\sqrt{(r_0 \;+\; h_j)^2 \;-\; r_0^2}\, \tan(\vartheta_{0,\,\mathrm{max}})}{r_0 \;+\; h_j}\right) \delta r_j^2 \tag{8.9}$$

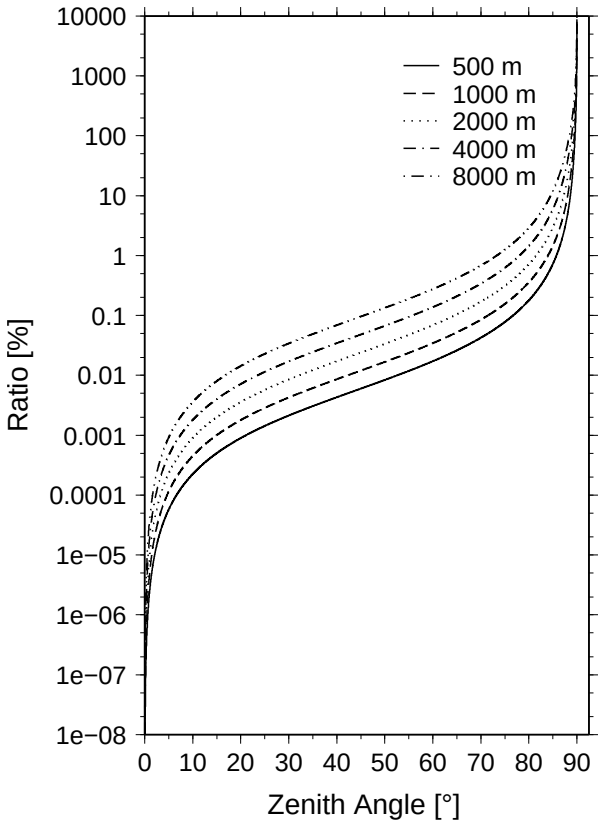

Figure 8.2: Ratio $\xi_{\delta s}$ between the remainder of the zeroth order spherical approximation $\mathrm{R}_0(h)$ and the exact spherical path length with respect to the zenith angle ϑ_0 and layer height h.

and as a Taylor series expansion

$$N_{j,j} = \underbrace{\frac{10^{-12}}{\vartheta_{0,\max}} \tan(\vartheta_{0,\max})\, \delta r_j^2}_{\tilde{N}_{l\,j,j}} + \underbrace{\frac{10^{-12}}{\vartheta_{0,\max}} \frac{\tan^3(\vartheta_{0,\max})}{r_0} \left(\frac{h_j^2}{5\, r_0} \tan^2(\vartheta_{0,\max}) - \frac{2\, h_j}{3} \right) \delta r_j^2 + M_{1\,j,j}(h)}_{M_{0\,j,j}(h)} \quad (8.10)$$

where h_j is the height of the j-th layer and δr_j the j-th layer thicknesses (for details, see Appendix E). Equation 8.10 consists of two parts: a) $\tilde{N}_{0\,j,j}$ related to the l-th order approximation (see Equation 8.5) and b) $M_{l\,j,j}$ related to the remainder of l-th order.

The following list shows the convergence behavior for the parameters h and r_0:

- In the case where h tends to 0 or r_0 to infinity, the diagonal elements of the normal matrix become equal to the zeroth order approximation $\tilde{N}_{0\,j,j}$ (see Equation 8.10).

$$\lim_{h \to 0} N_{j,j} = \frac{10^{-12}}{\vartheta_{0,\max}} \tan(\vartheta_{0,\max})\, \delta r_j^2 \quad (8.11)$$

$$\lim_{r_0 \to \infty} N_{j,j} = \frac{10^{-12}}{\vartheta_{0,\max}} \tan(\vartheta_{0,\max})\, \delta r_j^2 \quad (8.12)$$

  This means that the spherical effect vanishes and that the diagonal elements become independent of the layer height h.

- In the cases where h tends to minus or plus infinity or r_0 to 0, the diagonal elements only depend on the layer thickness δr.

$$\lim_{h \to \pm\infty} N_{j,j} \;=\; 10^{-12}\,\delta r_j^2 \tag{8.13}$$

$$N_{j,j}\Big|_{r_0=0} \;=\; 10^{-12}\,\delta r_j^2 \tag{8.14}$$

In GNSS tomography, the layers are usually subdivided into voxels and only a limited area is investigated. This restricts the possible zenith angles at a certain station for rays traversing this voxel requiring that all rays have to traverse the top layer within the area of interest. In Figure 8.1b), the angle α can also be interpreted as a measure of the horizontal extent of the investigated area. The angle α can be computed from the horizontal extent l by

$$\alpha \;=\; \frac{l}{r_0} \tag{8.15}$$

where α is in radian and r_0 the radius of the sphere. According to this measure α, the considered zenith angles of the rays range from $\vartheta_0 = 0$ to $\vartheta_{0,\,\max}$, with the latter given as a function of the horizontal extent of the area of interest α in radian and the layer height h.

$$\vartheta_{0,\,\max} \;=\; \pi \;-\; \arccos\left(\frac{r_0 \;-\; (r_0+h)\,\cos(\alpha)}{\sqrt{r_0^2 \;+\; (r_0+h)^2 \;-\; 2\,r_0(r_0+h)\,\cos(\alpha)}}\right) \tag{8.16}$$

where r_0 is the radius of the sphere (see Appendix E).

Assuming a single-layer model with layer thickness δr, layer height h, and with a restricted layer width α, how accurate can the refractivity be estimated within this layer? In a LSQ adjustment with a single unknown, the normal matrix becomes a scalar. This scalar value can be computed from Equation 8.9 using Equation 8.16 to determine $\vartheta_{0,\,\max}$. From the scalar value, the square root of the cofactors normalized by the layer thickness is computed and plotted with respect to the layer height for finite layer widths (l=3.47, 6.95, 13.9, 27.8, and 55.6 km) in Figure 8.3. The cofactors are measures indicating how accurate the single unknowns can be computed. The larger the cofactor, the less accurate the refractivity within the layer can be estimated. For all layer widths, the accuracy monotonically decreases with height. The wider the layers are, the more accurate the estimated refractivities become. The most accurate estimates can be expected from the heights where the rays span the largest zenith angle range. This is at the height where the lowest observed ray is at a zenith angle of 90°. In the case where the height tends to infinity, the uncertainty approaches 1 meaning that the uncertainty is bounded.

The contribution of the spherical effect to the diagonal elements of the normal matrix (see Equation 8.10) is computed the following way for limited zenith angle ranges:

$$\begin{aligned}\xi_N(h_j) \;&=\; \frac{|M_{0\,j,j}|}{N_{j,j}} \;=\; \frac{|\tilde{N}_{0\,j,j} \;-\; N_{j,j}|}{N_{j,j}} \\ &=\; \left|1 \;-\; \left(\frac{\sqrt{(r_0+h)^2 \;-\; r_0^2}}{r_0 \;+\; h}\;\frac{\tan(\vartheta_{0,\,\max})}{\arctan\left(\frac{\sqrt{(r_0+h)^2 \;-\; r_0^2}\,\tan(\vartheta_{0,\,\max})}{r_0+h}\right)}\right)\right|\end{aligned} \tag{8.17}$$

where $\vartheta_{0,\,\max}$ is given in Equation 8.16. Figure 8.4 shows the spherical contribution with respect to the layer height for different horizontal resolutions. The spherical effect on the diagonal elements disproportionately decreases with height. The decrease is monotone. At the height where rays down to $\vartheta_{0,\,\max} = 90°$ are observed the contribution of the spherical effect tends to infinity. As $N_{j,j}$ is bounded by a finite value, the spherical contribution must compensate the planar contribution which tends to infinity. Thus, the spherical contribution approaches 0 if the height h tends to infinity. It can be concluded that two effects are responsible for the disproportionate decrease of the spherical effect:

- On the one hand, the diagonal elements of the normal matrix using the zeroth order approximation is independent of the layer height. On the other hand, the diagonal elements $N_{j,j}$ decrease with height. This difference must be compensated by the remainder $M_{0\,j,j}$ of the zeroth order approximation, hence, by the terms related to the spherical effect.
- The restriction of the visibility of rays by considering layers with finite width enforces the disproportionate decrease. The contribution of the spherical effect increases with the zenith angle. As the maximal zenith angle of the observed rays decreases with height, the contribution of the spherical effect also decreases.

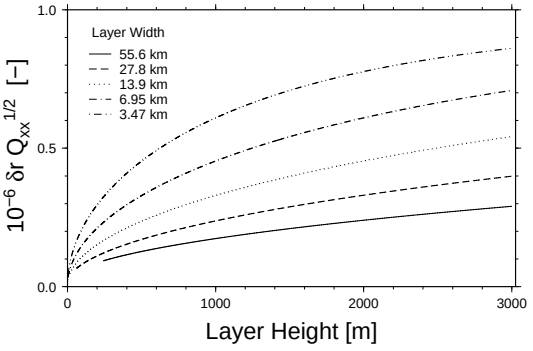

Figure 8.3: Cofactors of a spherical single-layer model depending on the layer height, computed for a layer whose width is restricted to the values 3.47 km, 6.95 km, 13.9 km, 27.8 km, and 55.6 km.

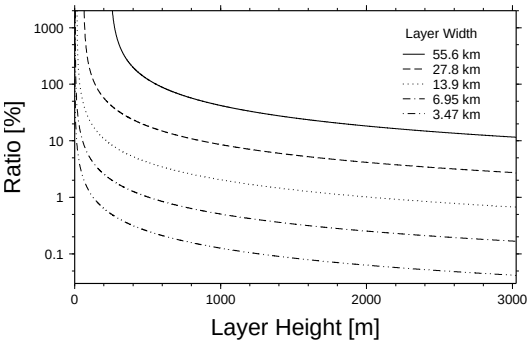

Figure 8.4: Spherical contribution $\xi_N(h)$ to the diagonal elements of the normal matrix vs. layer height for a layer whose horizontal extent is restricted to the values 3.47 km, 6.95 km, 13.9 km, 27.8 km, and 55.6 km.

What does this mean in terms of network design? The formulation used within this section can be used to investigate how the network design influences the impact of the spherical effect. Moving the receiver station in Figure 8.1b) to the right decreases the zenith angle of the ray crossing the layer at the same point. As soon as the stations is below the crossing point, the minimal zenith angle of 0° is reached. Moving the station further to the right increases the zenith angle again. Equation 8.16 can also be interpreted in the way that the maximal observable zenith angle of a ray crossing a layer at the border of the area covered by the network is restricted by the horizontal extent α of the network area. Combining Equations 8.10 and Equation 8.16 then reveals that the spherical effect disproportionately increases with the maximal zenith angle of the considered rays and, hence, the spatial extent of the area of investigation. However, the increase is limited by the fact that a single crossing point is only visible from a bounded area on the sphere. This shows that the impact of the spherical effect on the diagonal elements of the normal matrix is related to the horizontal extent of the area of interest and, hence, on the spatial extent of the receiver network.

8.2 Experiments with simulated data

Investigations on how well the three parametrizations (see Section 3.3) approximate two synthetic atmospheric patterns are carried out. The synthetic patterns are refractivity fields varying along the vertical. The first pattern is an average refractivity profile computed from data of weather balloons launched at Payerne. The motivation for this experiment is to investigate the convergence behavior of the algorithms and possible systematic errors. The second experiment is a spike layer test. The proper reconstruction of sharp vertical refractivity changes is of importance, since they can occur during inversions. Inversions are an atmospheric pattern commonly observed in the Swiss Plateau during winter (Wanner 1979). By varying the height and the thickness of the spike layers, the vertical resolution capabilities of the tomographic algorithms are investigated and compared to the theoretical considerations of the preceding section.

8.2.1 Setup and method

The starting point of the experiments is a refractivity field, also referred to as *original field* in this section (see Figure 8.5). Based on this field, a *forward model* simulates measurements. At this stage, measurement errors may be added to the simulated data. A refractivity field is then estimated with the tomographic approach (also called *backward model*) using the simulated observations from the preceding step. Finally, the estimated field is compared to the original one. This procedure enables us to investigate the properties of the backward model such as the convergence behavior, the vertical resolvability, and the impact of measurement errors on the reconstructed field.

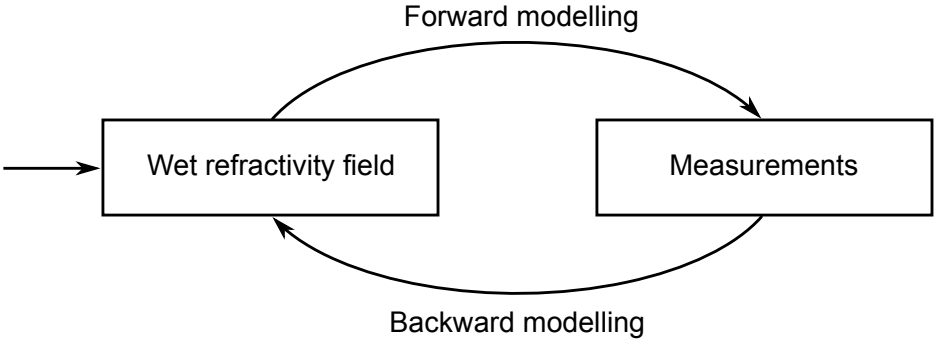

Figure 8.5: Schematic layout of the simulations.

Forward modeling

GPS double difference delays are simulated with the forward model using a sampling rate of 30 s. The duration of the simulation period is 24 h and the GPS satellite constellation of 26$^{\text{th}}$ November 2006 is used. The simulation period approximately corresponds to a ground-track repetition period of GPS. Figure 8.6 shows the receiver network. The network consists of 31 stations and the locations of its stations coincide with the AGNES stations (see Section 4.1). Figure 8.7 shows the height distribution of these stations. The station heights range from 310 m up to 3584 m above the reference ellipsoid. Most stations in the Swiss Plateau are located below 1000 m altitude whereas large parts of the stations in the Alps are at altitudes between 1000-2000 m.

The measurements are computed using a raytracer (see Appendix A). The raytracer considers the wet refractivity field up to 15'000 m and only includes rays to satellites with zenith angles $\vartheta_0 \leq 85°$. Additive Gaussian noise is added to each slant delay. The noise mapped to the zenith shows a standard deviation of 5 mm. The standard deviation of the noise increases with the zenith angle ϑ_0 by $1/\cos(\vartheta_0)$. Double difference delays are computed from these slant delays using the minimum distance strategy to determine the baselines. All the configurations of the forward model are summarized in Table 8.2.

Backward modeling

The backward model solves the stochastic differential equation (SDE) stated in Equation 3.35, which corresponds to a random walk on the wet refractivity field. The Kalman filter approach is used to combine the time evolving solution of the SDE with the measurements simulated by the forward model (see Section 3).

The wet refractivity field is discretized along the 3D ellipsoidal coordinates. The core area ranges from 6.5-9.5E° in longitude, 46-47.5N° in latitude, and 0-15'000 m in WGS84 ellipsoidal height. Additionally, the core area is surrounded by a fringe of 10° to ensure that no ray path crosses the lateral boundaries of the model area. The horizontal discretization is 0.5°, which corresponds to a horizontal resolution of about 37 km (see Figure 8.6). The thickness of the layers increases with height (see Figure 8.7).

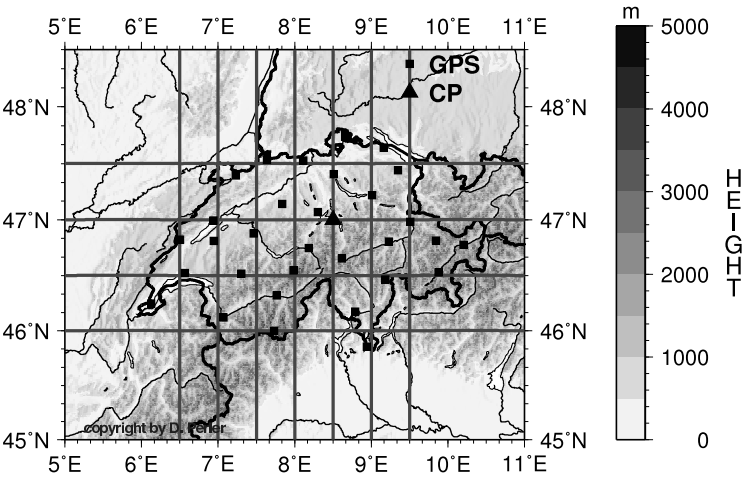

Figure 8.6: Map covering the core area of investigation with GPS stations (black squares) and the vertical comparison profile (black triangle). The gray lines indicate the floor plan of the grid used in the tomographic processing.

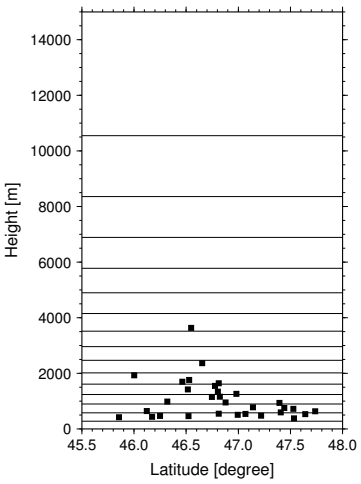

Figure 8.7: Height distribution of the GPS stations (black squares) and the levels of the ellipsoidal voxel model used in the tomographic processing.

The initial values of the SDE are given by a vector representing the initial refractivity field and a matrix describing the covariances within this field. In both experiments, the initial vector is set to zero and represents the state 30 seconds before the first GPS double difference observation is available, i.e. 25$^{\text{th}}$ November 2006 at 23:59:30 UTC. The covariances are based on investigations using balloon sounding measurements. The parameters of the backward model are listed in Table 8.3.

The propagation step size of 30 seconds is chosen equal to the sampling rate of the GPS double difference observations. The model used in the stochastic term (also referred to as prediction error) of the SDE contains a matrix $\tilde{\mathbf{Q}}\,\delta$ describing the spatial correlation and a scaling matrix $\tilde{\mathbf{G}}$ (see Section 3). The correlation matrix $\tilde{\mathbf{Q}}\,\delta$ is assumed to be equal to the correlation of the initial value. The scaling matrix is a diagonal matrix containing values exponentially decreasing with height. These values are considered with observations made at synoptic stations in Switzerland (see Section 5.4).

In the experiments, GPS double difference observations down to an elevation of 5° are used and they are regarded to be correlated with each other if they comprise a common slant delay. No

Table 8.2: Parameter settings for the forward model.

Parameter	**Value**
Simulation period	24 hours
Simulated observations	GNSS double difference path delays
Number of GPS stations	31 stations
Satellite systems	GPS
Sampling rate of the measurements	30 seconds
Cutoff angle	5°
Integration height	15'000 meter above reference ellipsoid
Type of measurement noise	Additive Gaussian
Measurement noise	5 mm std. dev. in zenith direction
Baseline strategy	Minimum distance

Table 8.3: Parameter settings of the initial state used in the backward model (tomography algorithm).

Parameter	**Value**
Initial state	0 ppm
Initial variance at reference level (0 m above ref. ellipsoid)	121 ppm^2
Scaling height of the variance model	2178 m
Vertical scaling length of the correlation model	1000 m
Horizontal scaling length of the correlation model	400 km

pseudo-observations are added. The measurement error of a slant delay is assumed to be additive Gaussian and two slant delays are regarded to be uncorrelated. The standard deviation of a slant delay is set to 5 mm in zenith direction and it increases with $1/\cos(\vartheta_0)$ with increasing zenith angle ϑ_0. The parameters of the prediction and the observation models are listed in Table 8.4.

Evaluation methods

The evaluation of the algorithms is based on comparisons between the field estimated by the backward model and the original field. At specific points in space and time, the difference of the two fields is computed (estimated field minus original). Three different strategies are applied to specify comparison points:

Evolutionary strategy: In the evolutionary strategy, the two evolving fields are compared every 5 minutes at 1441 points distributed uniformly along the vertical profile located at 47.0°N and 8.5°E (see Figure 8.6). The profile ranges from 600 m (approximately Earth's surface) to 15'000 m above the reference ellipsoid and is situated in the core area of investigation, but not in the high mountains. This allows to analyze the troposphere in the lower altitudes, too. Note that, for the constantly parametrized approach, the refractivities need to be evaluated in the voxel column ranging from 8.0-8.5°E and 46.5-47°N.

Spatial strategy: In the spatial strategy, the estimated field at the end of the simulation period is compared to the original field at 1 million points uniformly distributed over the space ranging from 6.5-9.5°E longitude, from 46.0-47.5°N latitude, and from 200-12'500 m height. This covers the core of the investigation area (see Figure 8.6).

Table 8.4: Parameter settings of the backward model.

Parameter	**Value**
Prediction model	
Prediction model	Random walk on wet refractivity
Prediction step size	30 seconds
Prediction error	Multi variant additive Gaussian
Prediction error on the reference level	110 $\text{ppm}^2\,\text{day}^{-1}$
Scaling height of the prediction error	2178 m
Vertical scaling length of the correlation	1000 m
Horizontal scaling length of the correlation	400 km
Observation model	
Observations	GPS double difference path delays
Pseudo-observations	None
Cutoff angle of GPS observations	5°
Covariance model of the observations	Full covariance model

Combined strategy: In this strategy, the evolving estimated field is compared to the original field every 5 minutes at 1 million points uniformly distributed over the space ranging from 6.5-9.5°E longitude, from 46.0-47.5°N latitude, and from 200-12'500 m height.

8.2.2 Results and discussion

Convergence tests with exponential refractivity distribution with height

The results presented in this section are based on a simulation using a field with refractivities decreasing exponentially with height. The field shows no variation in latitude, longitude and time. The vertical variation is described by the function

$$\mathrm{N}(h) = N_0 \exp\left(-\frac{h}{h_s}\right) \tag{8.18}$$

where the refractivity [ppm] at height h [m] is denoted by $\mathrm{N}(h)$, the refractivity at the reference level by N_0=77.5 ppm, and the scale height by h_s=2178 m. The values for the parameters N_0 and h_s are estimated from balloon sounding data at Payerne spanning a period of 2 years.

Figures 8.8 a)-c) show solutions along the vertical profile for different parametrizations using the evolutionary evaluation strategy. Solutions are plotted every 5 minutes with different gray shades beginning with light gray. The solutions computed with the trilinear and with the spline/bilinear parametrizations are smooth whereas the solutions calculated with the constant parametrization show staircase-shaped patterns. These patterns correspond to the grid layers.

Figures 8.8 d)-e) show the deviation of the solutions from the model profile. The deviations are plotted every 5 minutes with the same gray scale as in the previous subplots. The solutions of all three parametrizations approximate well the model profile already after a short simulation time. However, the limitation of the constantly parametrized approximation can be clearly seen in Figure 8.8 d). The errors become as large as 3.8 ppm in the lower troposphere. The maximum errors are obviously smaller for the other two parametrized solutions, 1.1 ppm and 0.7 ppm for the trilinear and the spline/bilinear case, respectively (see Figure 8.8 e)-f)). Considering the entire profile, the standard error is again significantly smaller for the trilinearly parametrized and spline-based solutions than for that with a constant parametrization (see Table 8.5).

Table 8.5: Statistical comparison of the three parametrizations based on synthetic tests. Double difference observations were generated from an atmosphere where the refractivity decreases exponentially with height. The simulated data served as input for the tomographic software. The statistics is based on 1441 points distributed uniformly along the vertical profile in the center of the area of investigation after one simulation day. All values are given in [ppm] refractivity units.

Parameterization	**Mean**	**Standard error**	**Maximum error**
constant	0.010	0.871	3.832
trilinear	0.008	0.176	1.060
spline/bilinear	0.004	0.209	0.716

The solutions computed with the spline-based parametrization show a small positive bias around 12 km altitude. This bias is located in between two nodes and can lead to negative refractivities. The choice of another spline condition at the top of the model grid may reduce the bias. The natural spline conditions requiring no curvature at the boundary nodes can be replaced by a condition fixing the slope.

The combined evaluation strategy is applied to generate the plots in Figure 8.9. The plots show the median and the quartiles computed from the differences between estimated refractivities and model at 1 million points vs. simulation time. All three plots show fast convergence of the median error towards near-zero values within the first 15 minutes of the simulation. After this time, the convergence rate becomes slow for all parametrizations. This is especially true for the constant parametrization. The median errors after 24 h simulation time are 0.032 ppm, 0.020 ppm, and

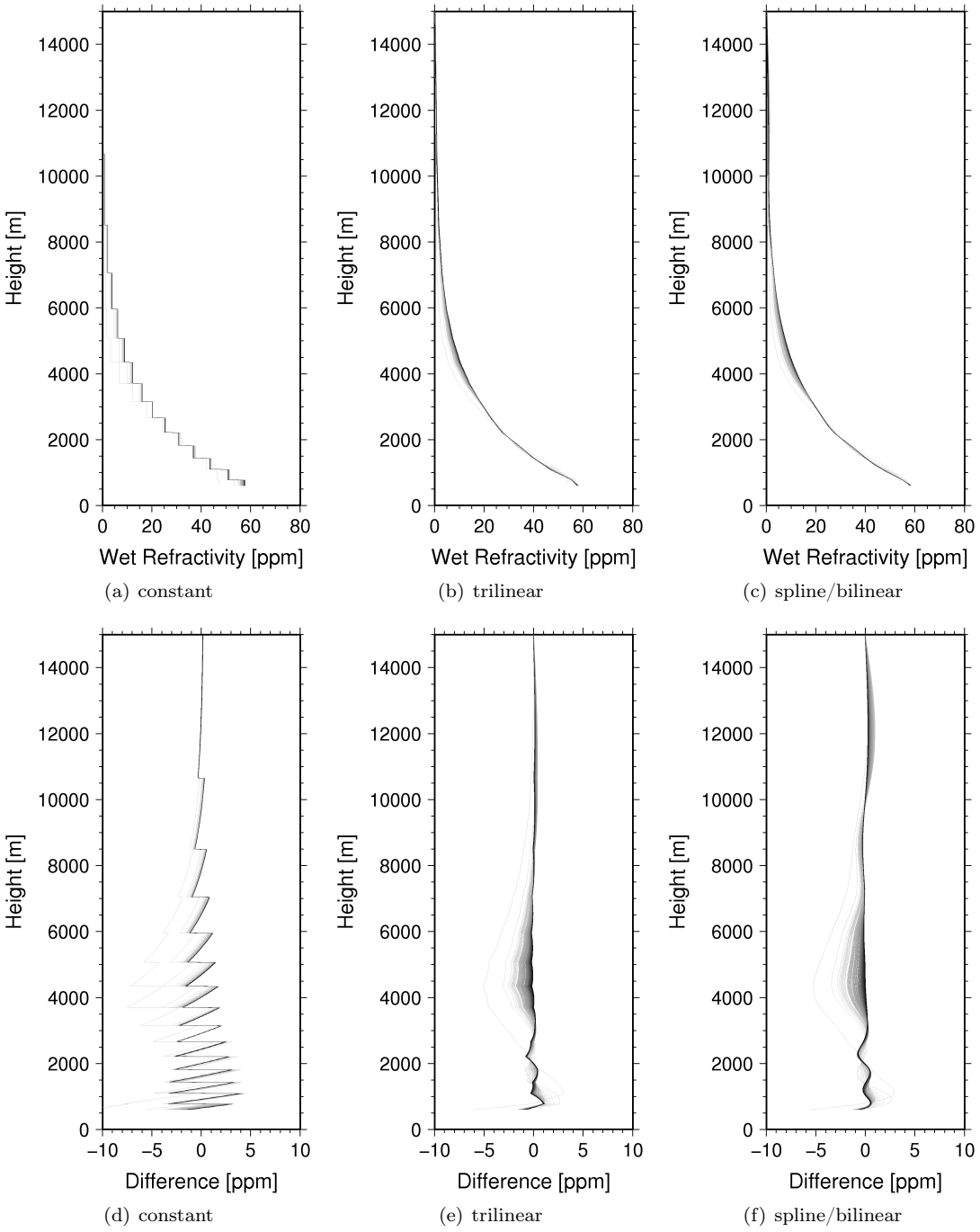

(a) constant (b) trilinear (c) spline/bilinear

(d) constant (e) trilinear (f) spline/bilinear

Figure 8.8: Tomographic results using simulated double difference observations with different parametrizations along the vertical profile at 47.0°N/8.5°E in refractivity units. a) b) c) Refractivity profiles. d) e) f) Differences between retrieved profiles and the synthetic model profiles (computed minus model). Observations are generated from an atmosphere with refractivities decreasing exponentially with height. Every 5 minutes, a profile is plotted starting from light gray shade at the beginning to black at the end of one simulation day. Figures a) and d) represent the result with constant parametrization, b) and e) with trilinear, and c) and f) with bilinear/spline parametrization.

0.005 ppm for the constant, trilinear, and spline/bilinear parametrizations, respectively. Summing up these systematic differences leads to a bias in the zenith path delay of less than 0.5 mm for all parametrizations. This is one order of magnitude smaller than the accuracy of zenith path delays estimated by GPS processing software and shows that the tomographic reconstruction process does not produce or annihilate artificial refractivity. Looking at the time-dependent behavior, the median of the errors is larger than zero at the beginning. For the constant and trilinear parametrizations, it becomes positive after 40 and 5 minutes, respectively. For the spline/bilinear parametrization it remains negative.

The inter quartile ranges (IQR) quickly decrease for all three parametrizations at the beginning of the simulation period. After 15 minutes, they are between 0.778 ppm for the constant and 1.388 ppm for the spline/bilinear parametrization (see Table 8.6). This shows that atmospheric changes can be quickly resolved by the tomographic algorithm. After 1.5 h simulation time, only little changes are observed for the IQRs for the constant parametrization. They considerably decrease for the trilinear and for the spline/bilinear parametrizations during the last 22.5 hours of the simulation. After the 24 h simulation period, the IQRs for the trilinear and spline/bilinear parametrizations are significantly smaller than the IQR for the constant parametrization. This is in agreement with the results presented in Table 8.5.

Table 8.6: Inter quartile range (IQR) in [ppm] of the difference between the original field and the estimated field after different simulation times.

Parametrization	**15′**	**30′**	**45′**	**60′**	**90′**	**24 h**
Constant	0.778	0.705	0.667	0.638	0.619	0.595
Trilinear	1.102	0.993	0.913	0.758	0.749	0.153
Spline/bilinear	1.388	1.277	1.177	1.066	1.034	0.304

Layer tests

For the spike layer experiment, refractivity fields with a common property are used: The fields are 0 ppm everywhere except within one layer where the refractivity is 3.5 ppm. This value corresponds to the accuracy achieved by in-situ measurements (see Flores et al. 2000). The refractivity fields differ in the height and thickness of this layer. Spike layer thicknesses of 200 m, 400 m, and 800 m located at different heights are investigated. Using a spike layer thickness of 800 m, the vertical perturbations cause a change in the measured tropospheric delays of the same order as the noise level of the path delay observations. The bottom of the layers are located at 500 m up to 4000 m in 500 m steps and, additionally, one at 5000 m and one at 6000 m above the reference ellipsoid.

Figure 8.10 shows the refractivity along the vertical profile located at 47.0°N/8.5°E for the original field and the fields computed with the different parametrizations after 24 h simulation time. The thickness of the spike layer is 400 m and approximately corresponds to the height resolution of the grid at this altitude. The discontinuities of the spike layer function cannot be exactly resolved by the trilinearly parametrized and spline-based voxel modeling. In contrast, the constantly parametrized representation is capable to reproduce them exactly as long as the discontinuities are at the borders of a voxel. If the voxel boundaries are not coinciding with the spike layer, the constantly parametrized approach smooths out the spike layer much more than the trilinearly parametrized and the spline-based ones. The trilinearly parametrized and the spline-based approaches show much clearer negative refractivity values below and above the layer than in the constantly parametrized case. The maximum peak is aligned with voxels in the solutions of the constantly parametrized approach and is shifted to voxel boundaries in the trilinear parametrization. However, the peak is well centered in the spline/bilinear case.

A more quantitative view of the accuracies is achieved using the spatial evaluation strategy applied to simulation runs with different original fields. There are 30 runs per parametrization (3 layer thicknesses times 10 layer heights). The accuracy is assessed by computing the IQR from the difference between the original and the estimated field at the comparison points for

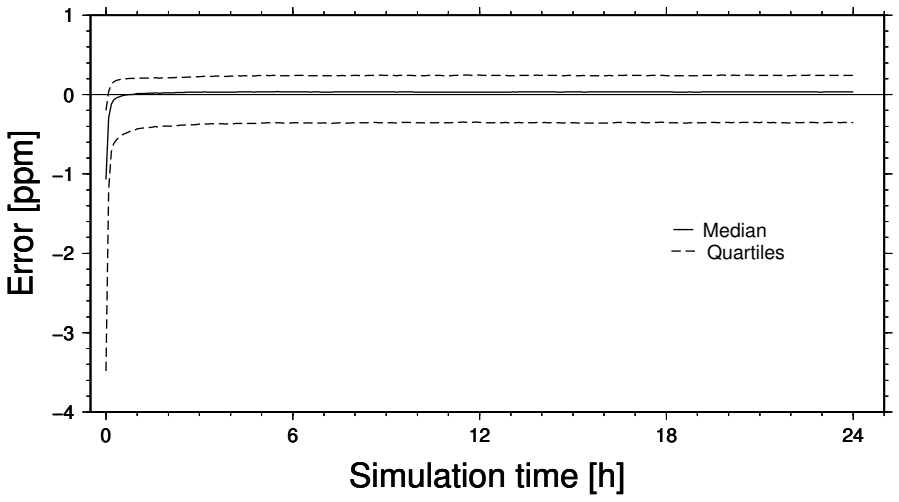

(a) const

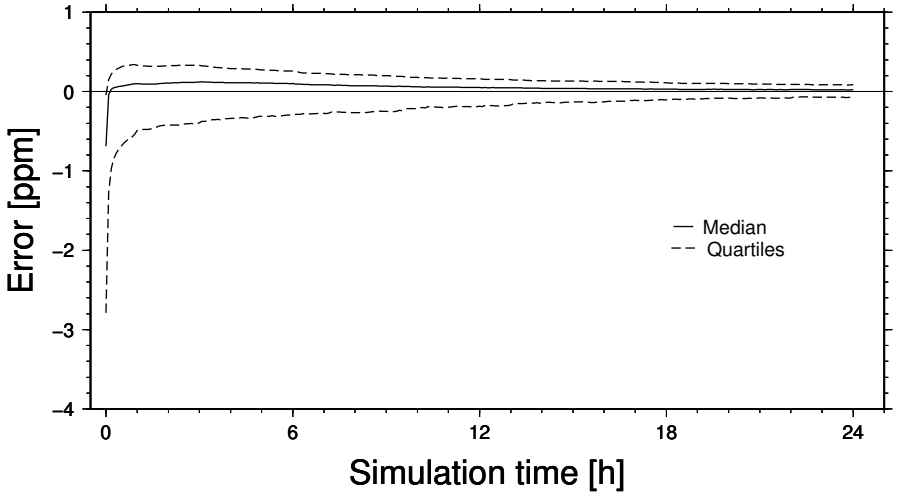

(b) trilinear

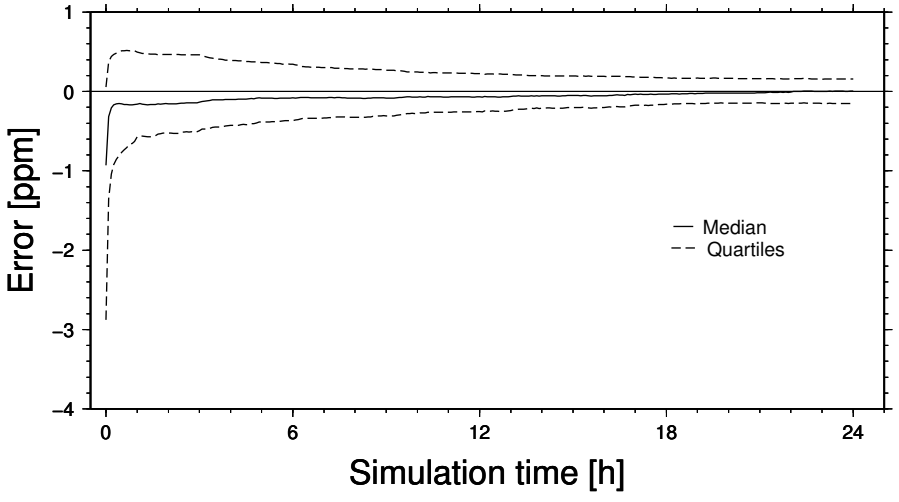

(c) spline/bilinear

Figure 8.9: Time evolution of the median and quartiles of the computed minus modeled refractivities from 1 million uniformly distributed points for a) constant, b) trilinear, and c) spline/bilinear parametrization.

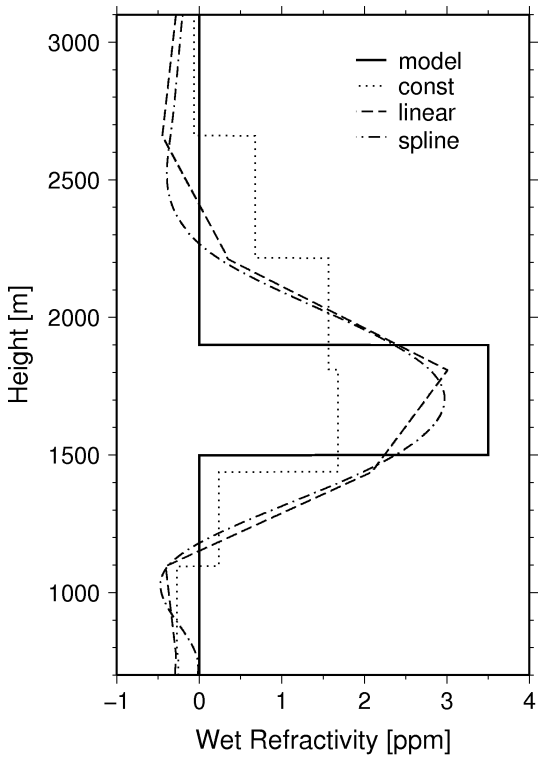

Figure 8.10: Refractivity values along a profile. The solid line represents the given model atmosphere from which GPS double difference observations are generated. The spike has the lower bound at 1500 m altitude and a thickness of 400 m. The refractivity within the spike layer is 3.5 ppm and 0 ppm elsewhere. Using the simulated observations, the dotted line is the solution of the constantly parametrized approach, the dashed one the solution of the trilinear approach and the dash-dotted the solution of the spline/bilinear approach. Note that neither vertical nor horizontal constraints are used.

each simulation run. A smaller IQR reflects a better accuracy. Hypothesis testing is used to decide whether the IQRs among the parametrizations significantly differ from each other. As the sample size is rather small (30 different spike layer profiles for each parametrization) and normal distribution cannot be assured, we used the Wilcoxon signed-rank test (Rice 1995) with a significance level of 0.05. The IQRs of the spline/bilinear parametrized solutions are significantly smaller than those from the trilinear parametrized and the constantly parametrized solutions. The accuracy of the trilinear parametrized solutions is better than that of the constantly parametrized solutions, however, not as obvious as in the previous comparisons.

Figures 8.11a) and b) show box-whisker diagrams depicting the differences between original and computed fields using the spatial evaluation strategy. Each box represents one simulation run. There are 10 boxes per plot and their ordinates are equal to the center heights of the layers. The layer thicknesses are 800 m and 200 m in Figures 8.11a) and b), respectively. For both plots, the same grid is used in the backward model employing the linear parameterization (see Figure 8.7). This grid will be referred to as *default grid*.

How well a spike layer is resolved depends mainly on its height and its thickness. Spike layers with a thickness of 800 m are well reproduced below 4500 m (see Figure 8.11a)). Thinner spike layers are not as well resolved as the 800 m spike layers. As shown by Figure 8.11b), thinner ones are only well represented below 3500 m.

The investigations show that an insufficient grid spacing is not a major cause for the poor retrieval of high altitude spike layers. Figures 8.11c) and d) are computed using an equidistant grid of 200 m vertical resolution in the backward model. The solutions show the same characteristics

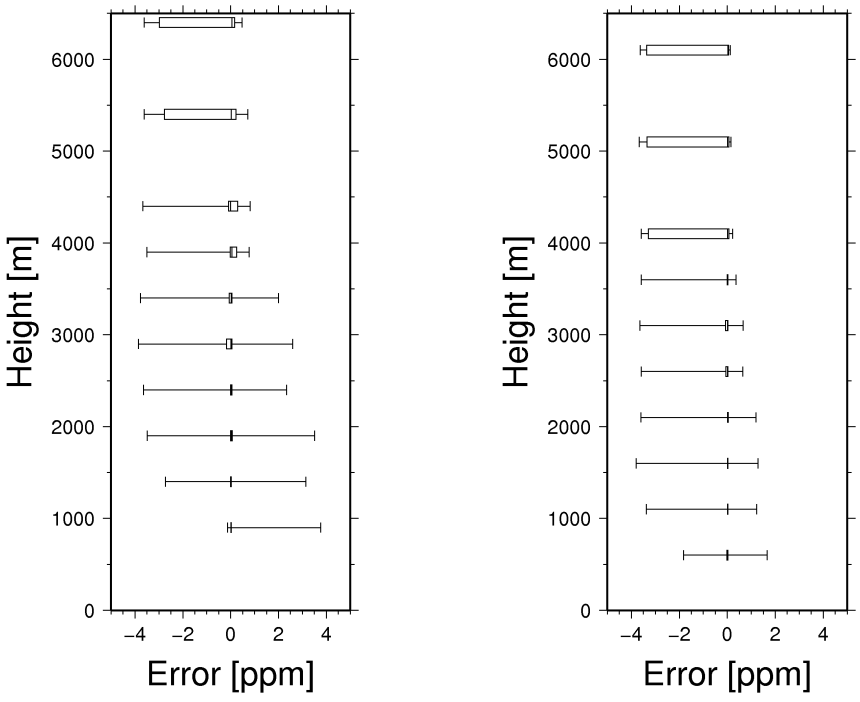

(a) spike layer thickness of 800 m, exponential grid

(b) spike layer thickness of 200 m, exponential grid

(c) spike layer thickness of 800 m, equidistant grid

(d) spike layer thickness of 200 m, equidistant grid

Figure 8.11: Box-whisker plots of the difference between computed and modeled refractivities with different spike layer heights using the spline/bilinear parametrization. In the first column, a spike layer thickness of 800 m is given and in the second a thickness of 200 m. Two different grids are used. The grid used in the first row has exponentially decreasing height resolution ranging from 280 m up to 4320 m and the grid used in the second row has a constant height resolution of 200 m.

as the solutions calculated with the default grid. The IQRs shown in Figure 8.11a) do not differ remarkably from those in Figure 8.11c) although the finer grids have a much smaller grid resolution than the thickness of the spike layers. Even for a thinner spike layer of 200 m, no obvious difference in accuracy is observed between the two grid configurations (see Figures 8.11b) and d)).

The results plotted in Figure 8.11a) show that the layers below the top station at 3584 m altitude (see Figure 8.7) are well resolved. This is due to the good height distribution of the stations in the network. Furthermore, Figure 8.11a) shows 2 well resolved spike layers located above the top station between 3500 m and 4500 m altitude. This indicates that also above the top station information about the vertical refractivity distribution can still be gained.

What does this mean in view of Equation 8.5? In the layer experiment, the layer heights h_j and layer thickness δr_j are known. The radius r_0 corresponds to the Earth's radius. The experiment revealed that some of the unknown refractivities within the voxels above the top station can be accurately computed. This is only possible if the normal matrix $\mathbf{N}$ is invertible. In the case where only the zeroth order approximation (planar part) is considered, the normal matrix is singular. This suggests that the normal matrix becomes invertible due to the spherical effect and that this effect allows vertical resolution above the top station.

The results in Figures 8.11a)-d) strongly suggest that the vertical resolvability quickly decreases with height above the top station. This is in agreement with the theoretical considerations. Compared to the diagonal elements in the normal matrix, the spherical effect disproportionately decreases with height in the spherical layer-model. As shown in Figure 8.4, the contribution of the spherical effect super-exponentially decreases within the first 1000 m above the top station. The agreement between the observations in the experiments and the theoretical considerations indicates the importance of a large zenith angle range of the rays traversing the corresponding voxels and the impact of the spherical effect on the vertical resolvability (see Section 8.1).

Regarding the network design, a good vertical distribution of the receiver station is recommended as the vertical resolvability quickly decreases above the top station. According to the theoretical considerations in the previous section, the horizontal extent generally increases the impact of the spherical effect. It is, therefore, expected that this will positively influence the vertical resolvability.

8.3 Conclusions

In this chapter, the vertical resolvability was investigated with theoretical considerations and simulations. The convergence behavior was analyzed with simulated data. In a first part, the observation matrix was investigated with the help of a spherical layer-model. In the second part, simulations were carried out. The tomographic algorithm parametrizing the voxels in different ways were assessed using simulated data generated from different model atmospheres.

The simulations have shown that AWATOS 2 has a quick convergence rate. The tomographic solution converges within 30 minutes simulation time to a solution with an IQR smaller than 1 ppm (0.15 $\mathrm{g\,m^{-3}}$ absolute humidity) for the trilinear and constant parametrizations. This shows the capability of the tomographic software to quickly reproduce changes in the atmosphere in its solution. The investigations also revealed that the discretization error is one of the main error sources for constantly parametrized voxels. The discretization error significantly decreases with the use of more sophisticated voxel parametrizations such as trilinear or spline/bilinear voxel parametrization. The standard deviation after 24 h simulation time in the convergence test was reduced by 80%, the maximal error by 72% and the bias by 20% if the trilinear voxel parametrization was used instead of the constant one.

In a second experiment, the vertical resolvability was investigated. Spike layers at different heights and with different thicknesses had to be estimated by the tomographic software AWATOS 2. The experiment revealed that layers below the top station could be accurately reconstructed by the tomographic approach. Layers above the top station are also correctly resolved. However, the vertical resolvability quickly decreases with height. Layers located 1000 m above the top station are poorly reproduced. Nevertheless, this indicates that the tomographic approach in the way it is

used in this work is capable of resolving vertical structures above the top station. The agreement with the theoretical considerations suggests that the Earth's curvature allows to resolve vertical structures.

The experiments confirmed the recommendations on network design made in Chapter 7. To achieve good vertical resolvability, the stations should be well distributed across the possible topographic altitudes. As the wet refractivity field features small-scale variations, a sufficiently dense network is needed. Based on the investigations about the wet refractivity field in Chapter 5, we recommend GNSS networks with a mean inter-station distance smaller 15 km in alpine regions. Theoretical considerations also suggested that a larger horizontal extent of the network has a positive impact on the vertical resolvability.

Chapter 9

Evaluation of the GPS tomography with a long-term study

In this chapter, the three parameterizations (constant, trilinear, and spline/bilinear) of the tomography software AWATOS 2 are evaluated with real data. The data have been collected in the GPS permanent network in Switzerland AGNES and from receivers located in adjoining regions. A long-term study is carried out using one year of data from these stations. The data are processed for each of the three parameterizations and compared to measurements from different sources, such as balloon soundings and analyses of a numerical weather prediction model. The results computed with the different voxel parameterizations are discussed in terms of accuracy and are compared to the results achieved with simulated data. Furthermore, a regional and seasonal assessment is carried out. Based on this assessment, a bias correction model is implemented and evaluated.

9.1 Configuration and evaluation methods

In the experiments presented in this chapter, GPS path delay observations from the Swiss permanent network AGNES and from stations located in the adjoining countries are used. The processed data comprises observations between 15$^{\text{th}}$ January 2006 and 28$^{\text{th}}$ January 2007. The wet part of GPS double difference delays is used as input into the tomographic processing. No other observations are taken into account. Tropospheric path delays have been derived from raw GPS phase observations using the GPS processing software Bernese 5.0. To separate the wet part from the total tropospheric path delay, the partial pressure of dry air is needed at the GPS receiver stations. At stations where no sensors provide the needed meteorological data, the meteorological quantities are interpolated using the collocation software COMEDIE (see Section 3.2.2).

GPS processing with Bernese 5.0

Tropospheric path delays are computed as part of the operational processing at the Swiss Federal Office of Topography. The GPS data processing uses data collected by the Swiss GPS permanent network AGNES and by other stations located in Europe (see Section 4.1). Table 9.1 lists the main parameters of the configuration used in this operational processing. GPS phase observations with a sampling rate of 30 seconds are processed in double difference mode using the ionosphere-free linear combination. Daily solutions are computed which are then stacked together to weekly solutions. The IGS satellite orbit product *rapid orbits* are used (Dow et al. 2009). Observations down to a cutoff angle of 10° are considered and the baseline strategy maximizing the number of observations is used (Dach et al. 2007). Tropospheric path delays are computed using Niell's mapping functions (Niell 1996). A priori values are calculated with the dry part of Saastamoinen'smodel

(Saastamoinen 1973a) and using dry Niell mapping function. These a priori values are corrected by a piecewise linear function with a step size of 1 hour. Niell's wet mapping function is used for estimating these corrections.

Table 9.1: Main parameters of the configuration used in the GPS processing with Bernese 5.0.

Parameter	**Value**
Processing mode	Double difference processing estimating weekly solutions using the ionosphere-free L_3 combination
Orbit product	IGS rapid orbits
Sampling rate	30 s
Cutoff angle	10°
Baseline strategy	Maximum number of observations
Troposphere model	
A priori model	Dry delay: Saastamoinen model using dry Niell mapping function, Wet delay: zero
Correction model	Estimation of piecewise linear path delays using the wet Niell mapping function

Tomographic processing with AWATOS 2

Tomographic solutions have been computed with three different configurations for a period of one year. The basic configuration is the same for all 3 configurations and differs only in the voxel parameterization used. The constant, trilinear, and spline/bilinear voxel parameterizations are considered. The tropospheric double difference delays prepared with Bernese 5.0 are processed by AWATOS 2 in weekly batches. Successive batches have an overlap of 6 hours. The choice of the overlap duration is based on the investigations of the convergence rate (see Section 8.2). The simulations have shown that the error of the tomographic solution is less than 1 ppm after 30 minutes accumulation time. With an overlap of 6 hours between two consecutive batches, initialization effects can be neglected.

The state vector in the Kalman filter is initialized with refractivities, which exponentially decrease with height (see Equation 8.18). The exponential model has been fitted to data of balloon soundings launched in Payerne in the years 2006 and 2007. The remaining parameters for the initial state are based on investigation using NWP model data and observations from the SwissMetNet (see Section 5). The parameters are listed in Table 9.2.

Table 9.2: Parameter setting of the initial state used in the tomographic processing.

Parameter	**Value**
Initial value at reference height	77.5 ppm
Scaling height of the initial value model	2178 m
Initial variance at reference level	10'000 ppm^2
Vertical scaling length of the correlation model	1216 m
Horizontal scaling length of the correlation model	86 km

The prediction model is the same as that used in the synthetic tests (see Table 9.3). The parameters of the prediction error model are based on the investigations presented in Section 5. The prediction model is implemented as a random walk on the wet refractivities and the prediction error is modeled as additive Gaussian (see Section 3.4). In the update step, several observations and pseudo-observations are considered as follows:

GPS double difference observations: GPS double difference path delay observations down to an elevation of 10° are used. This cutoff angle is equal to that used in GPS raw data processing. Two double difference observations are regarded as being correlated if they comprise a common slant path delay. Otherwise, double difference delays are considered as independent from each other. The standard deviation of the measurement error is assumed to be 5 mm in zenith direction for a slant path delay (e.g. Troller 2004). The standard deviation increases with $1/\cos(\vartheta)$ where ϑ is the zenith angle.

Vertical gradient constraints: In the long-term study, vertical gradient constraints are used (see Equation 3.49c)). Their weights are chosen in order to minimize the error between balloon sounding data and the outcome of the tomographic processing. Data from 4 weeks at different seasons have been considered for this weighting task. The vertical gradient constraints are based on the same average profile as used for determining the initial state vector (see Equation 8.18).

Boundary layer constraints: Grid point observations are introduced at the lateral boundaries of the grid. The values at the grid points are modeled with the average profile described by Equation 8.18. The weight of such pseudo-observations is equal to the reciprocal of the prediction error at the particular point. In that way, the formal accuracy of the refractivity at the boundaries remains constant over time if no further information is provided by other measurements.

Table 9.3: Parameter settings of the tomographic processing.

Parameter	**Value**
Prediction model	
Prediction model	Random walk on wet refractivity
Prediction step size	30 seconds
Prediction error	Multi-variate additive Gaussian
Prediction error on the reference level	346 ppm^2 day^{-1}
Scaling height of the prediction error	1216 m
Vertical scaling length of the correlation	1216 m
Horizontal scaling length of the correlation	86 km
Observation model	
Observations	GPS double difference path delays
Pseudo-observations	Vertical smoothing constraints
Cutoff angle of GPS observations	10°
Covariance model of the observations	Full covariance model

Figure 9.1 shows the floor plan of the grid used in the tomographic processing (solid blue lines). The spacing of the grid is 0.5° in latitudinal and 1/3° in longitudinal direction. This corresponds to a resolution of about 37 km. The core area covers large parts of Switzerland and ranges from 6.5-10° E in longitude, and 46-47.$\bar{6}$° N in latitude. Additionally, the core area is surrounded by a fringe of 10° to ensure that no ray path crosses the lateral boundaries of the model area (not shown in Figure 9.1). Vertically, the atmosphere is subdivided into 17 levels ranging between 0 and 15'000 m WGS84 ellipsoidal height. The distance between two adjoining levels is increasing with height (see Figure 8.7).

Tropospheric delays from 46 GPS stations are taken into account (black squares in Figure 9.1). The stations are located in or near the core area. Receivers located farther away are not considered as no rays between them and the GPS satellites cross voxels in the core area.

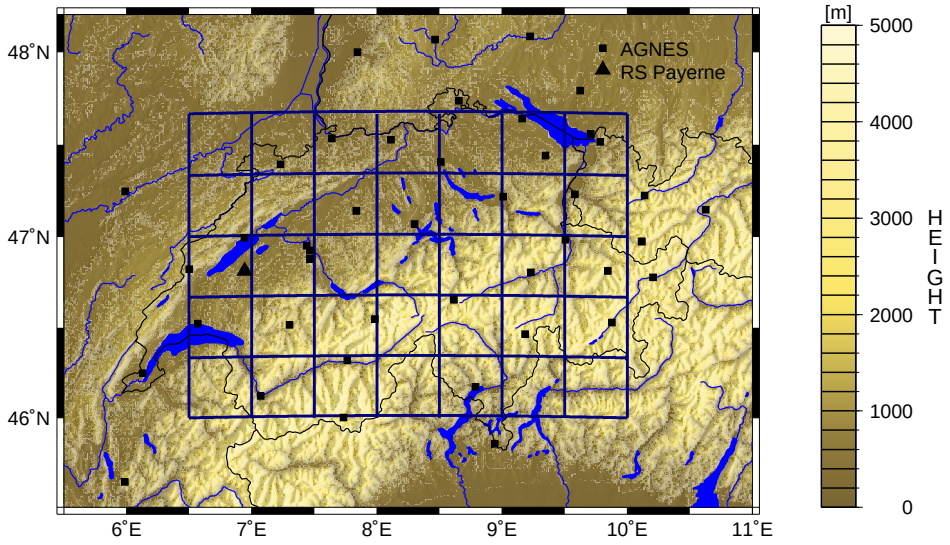

Figure 9.1: View of the investigation area. The tomographic grid covers large parts of Switzerland. The grid has a horizontal spacing of about 37 km. The black squares represent the GNSS receiver stations. The black triangle denotes the balloon sounding station at Payerne.

Evaluation methods

The estimated fields are compared to measurements from balloon soundings and to the analyses of the NWP model COSMO-7.

Balloon soundings: Balloon sounding data from the station in Payerne are considered (black triangle in Figure 9.1). The data set consists of in-situ measurements irregularly recorded by the radiosonde during the ascents. Each time, when a temperature and humidity measurement is available, a wet refractivity value is computed. An instantaneous and vertical climb is assumed for the balloon tracks. Each value computed from a balloon sounding is then compared to the wet refractivity estimated by the tomographic technique at the same location and time. The statistical evaluations are based on the difference of these values (estimated minus measured). All differences are equally weighted in the statistical evaluations and are considered as independent from each other.

At midnight and at noon, balloon soundings are launched. Comparing the zenith delays computed from balloon soundings in Payerne with GPS derived delays have shown different biases for midnight and noon (see Section 6). Due to this different biases, data from midnight and noon are treated separately in the investigations.

NWP COSMO-7: The hourly analyses of the NWP COSMO-7 are considered (see Section 4.4). At each grid point of the NWP, the wet refractivity is computed and compared to the wet refractivity estimated by the tomographic software (estimated minus model). Only grid points located in the core area of the tomographic processing and grid points below 15'000 m altitude are considered. Based on the wet refractivity differences at these grid points, a weighted RMS error is computed. The weights are proportional to the volume a NWP grid point represents. The comparison with NWP model data provides the possibility to evaluate the solutions of the tomographic processing in different regions.

9.2 Results and discussion

Figure 9.2a) and 9.2b) show the difference between the wet refractivity derived from balloon soundings launched at noon in Payerne (490 m altitude) and those computed with constant and with trilinear parameterization along the vertical profile above the balloon sounding station, respectively. The right subplots illustrate the mean difference (continuous line) and the 68.26% quantiles assuming normal distribution (dashed lines) for the entire time span of the investigation. The top subplots display the expected difference and the 68.26% quantiles over the entire height domain.

In Figure 9.2a), staircase-shaped patterns are visible. They exactly correspond to the voxel boundaries. If the trilinear or spline parameterization is used, no such patterns are visible (see Figures 9.2b) and 9.3). This shows that more complex parameterizations, such as the trilinear one, prevent discontinuities at voxel boundaries and reduce biases at the top and bottom boundaries of the voxels.

Both plots show a dry bias for the GPS measurements (refractivities of the GPS solution are smaller in average than those from balloon soundings). Especially below 2000 m altitude for the constant parameterization and 3000 m for the trilinear one, distinct dry biases are visible. For both parameterizations, biases are maximal at an altitude of about 1000-1300 m during summer. During this season, the standard deviation is about 2 ppm larger than during winter (see top subplot in Figures 9.2a) and b)). No seasonal variability is visible in the bias. Contrary to that, the comparison with balloon soundings launched at midnight shows a seasonal variation of the bias of 0.5-1 ppm (see Figure 9.4a)). Comparing them to the variations on the synoptic time scale, synoptic-scale effects cause variations which are one order of magnitude larger than those from diurnal variations. This shows that synoptic-scale effects are dominant on the scale of our setup.

Figure 9.4 shows the difference along the vertical profile above Payerne between wet refractivity derived from GPS data and from balloon soundings launched a) at midnight and b) at noon for the trilinear parameterization, respectively. At midnight, the GPS-derived solutions show a larger dry bias than at noon. This difference agrees with the investigations about the systematic errors between GPS derived zenith wet delays and delays computed from balloon soundings (see Section 6). They revealed that the zenith wet delays derived from GPS are smaller (indicating a more dry atmosphere) than those computed from balloon soundings at midnight. The opposite is observed at noon: GPS-derived zenith wet delays are larger than those from balloon soundings. From this we can conclude that the day-night difference observed in the evaluation of the tomography is related to the differences between GPS-derived path delays and those from balloon soundings.

In Table 9.4, the standard deviations are listed for several parameterizations and layers. The standard deviation decreases with height. The new parameterizations (trilinear and spline) show a significantly lower standard error in the lower troposphere (below 3 km altitude). Above this level, the constant parameterization shows a lower standard deviation than the other two parameterizations. Above 6 km altitude, that is, however, mainly related to the a priori values at the top of the grid. In the case of constant parameterization, refractivity within a voxel is represented by a single parameter. In contrast to that, the refractivity within a voxel is determined by the parameters at the grid nodes in the non-constantly parameterized field. This means that a priori values introduced at the top of the grid have a much stronger influence on the top layer in the constantly parameterized case than in the non-constantly parameterized cases. Since the gradients in this layer are small and the wet refractivity is small compared to low-altitude layers, the introduced a priori values for constant parameterization are a suitable approximation. Furthermore, these a priori values decrease the impact of observations or modeling errors from GPS measurements on the top layer. Comparing the different parameterizations over all layers, the trilinear and the spline parameterizations show a significantly lower standard deviation than the classical constant one. With respect to the measured wet refractivities, the tabulated precisions correspond to a relative error of about 15%.

Figures 9.5a)-9.5c) show the weighted RMS error of the estimated wet refractivity field with respect to data from COSMO-7. The data set spans a period of 1 year and the statistics is computed for each vertical column of the NWP model. The most accurate results are achieved in the Alps where the RMS error is 2-4 ppm. On the Swiss Plateau, slightly larger RMS errors are observed

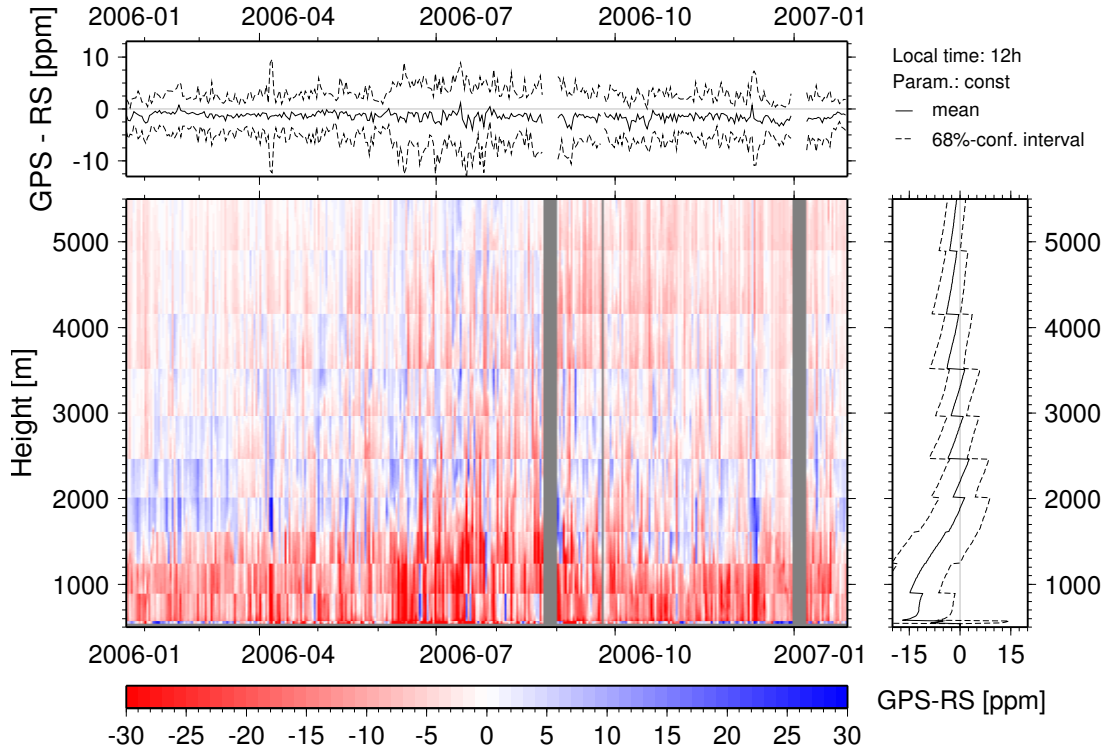

(a) constant

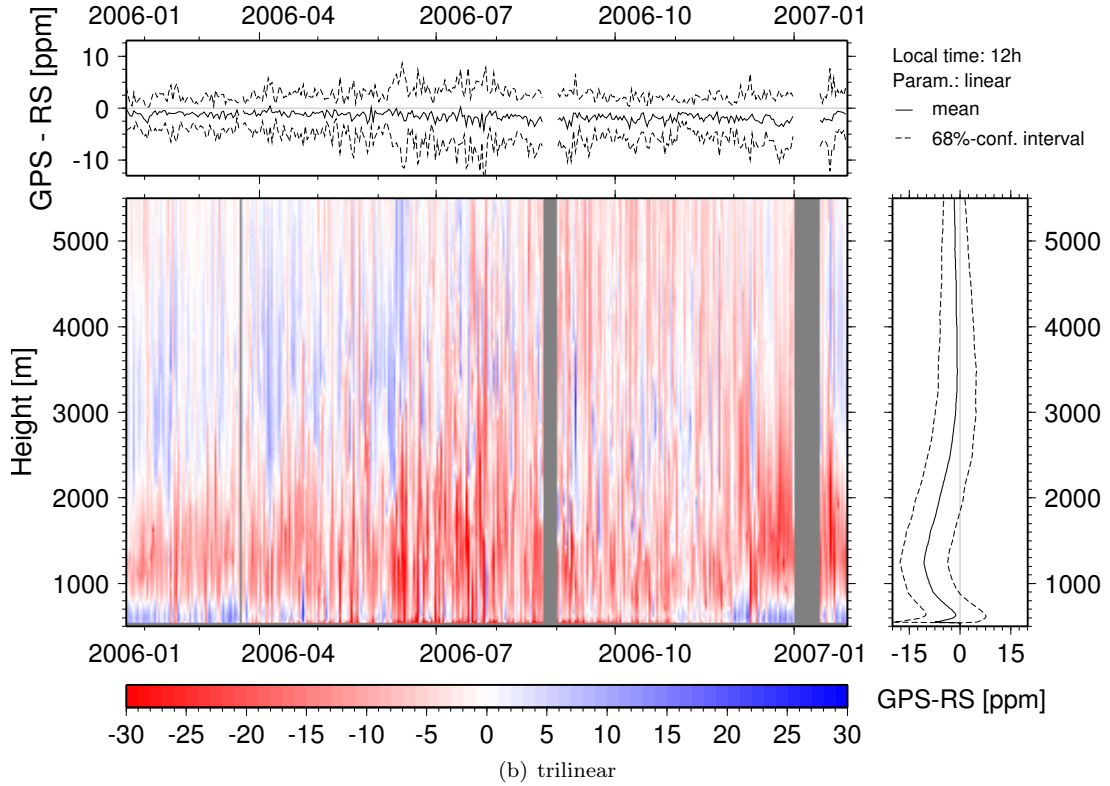

(b) trilinear

Figure 9.2: Wet refractivity difference between tomographic solutions and observations computed from balloon soundings launched at Payerne at noon for a) constant and b) trilinear parameterization.

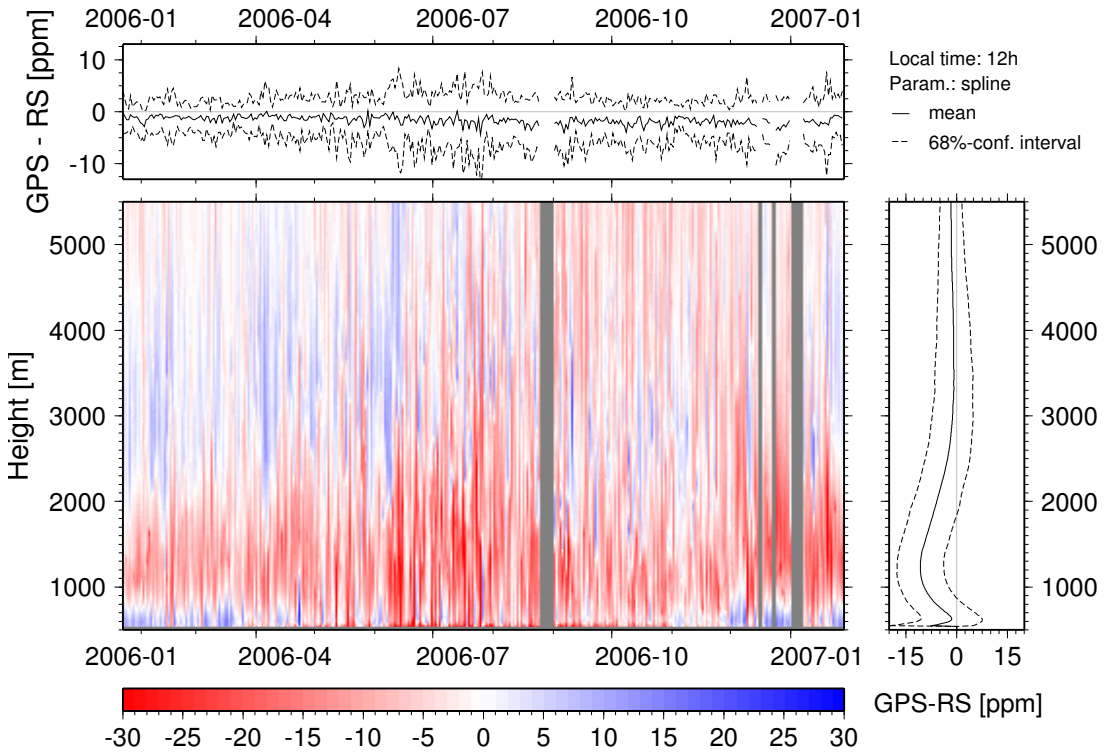

Figure 9.3: Wet refractivity difference between tomographic solutions and observations computed from balloon soundings launched at Payerne at noon for the spline parameterization.

(6-8 ppm). Outside the core area, the RMS errors are significantly larger and range up to an RMS error of 16 ppm. The latter is related to the coarse grid resolution and sparse observations in these areas.

Comparing the results from the different parameterizations, the constant parameterization shows slightly better results than the trilinear and spline parameterizations (see Table 9.5). Looking for common patterns in Figures 9.5a)-9.5c), we find tile-shaped patterns for the constant parameterization. Their largest spatial gradients coincide with the lateral voxel boundaries. This indicates that this kind of pattern is related to how a voxel is parameterized. As a single parameter describes the refractivity field within a voxel in the constant parameterization. A continuously changing property of the refractivity field over the area cannot be accurately represented by this parameterization and leads to discontinuities at the voxel boundaries. This is exactly what we observe in this plot.

Table 9.4: Standard deviation of wet refractivity differences between the balloon sounding observations and the tomographic solutions. The balloon sounding measurements are grouped according to the given height layers.

Height	**Constant**	**Trilinear**	**Spline**
0-1500 m	13.353 ppm	9.670 ppm	9.722 ppm
1500-3000 m	8.800 ppm	8.152 ppm	8.258 ppm
3000-4500 m	5.197 ppm	6.085 ppm	6.086 ppm
4500-6000 m	3.097 ppm	3.759 ppm	3.730 ppm
6000-15'000 m	1.365 ppm	2.267 ppm	2.521 ppm
0-15'000 m	**7.587 ppm**	**6.443 ppm**	**6.517 ppm**

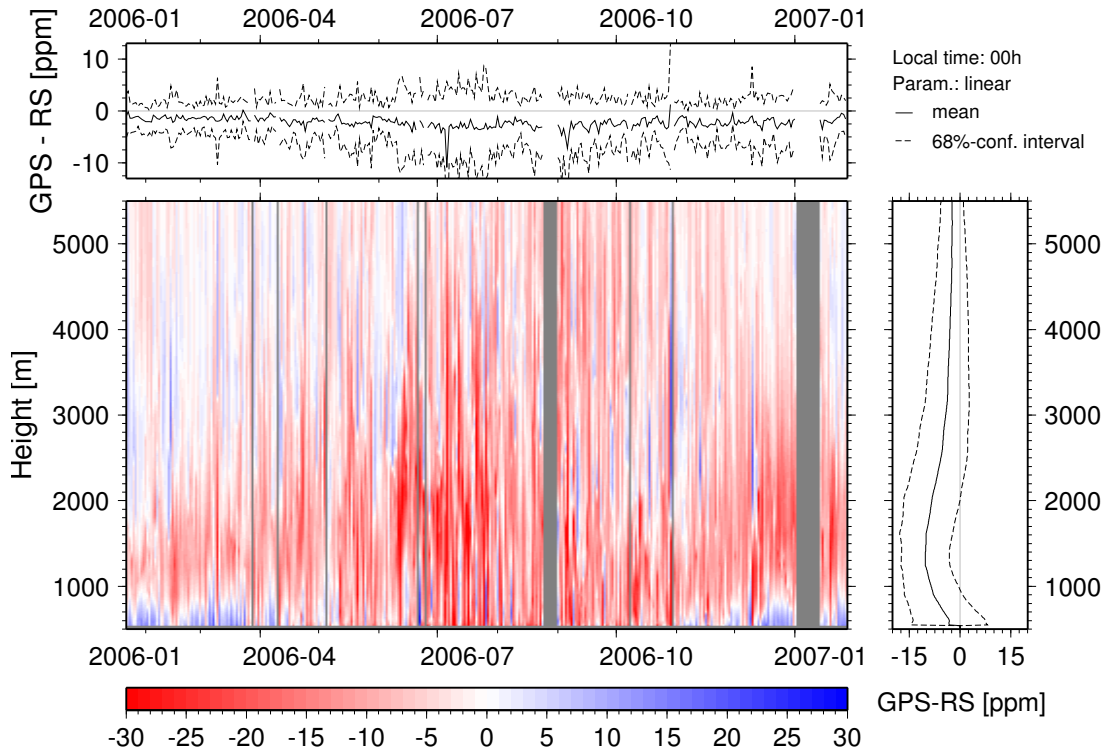

(a) 0 h UTC

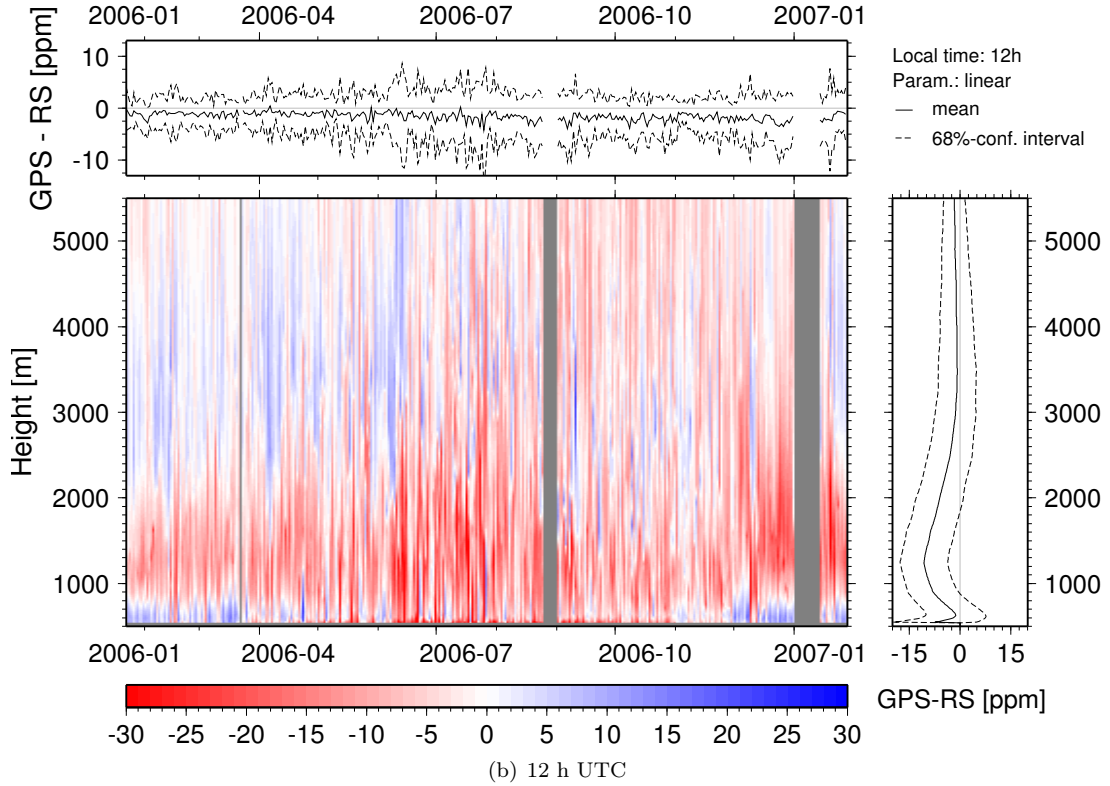

(b) 12 h UTC

Figure 9.4: Wet refractivity difference between tomographic solutions and observations computed from balloon soundings launched at Payerne for the trilinear parameterization at a) 0 and b) 12 h UTC.

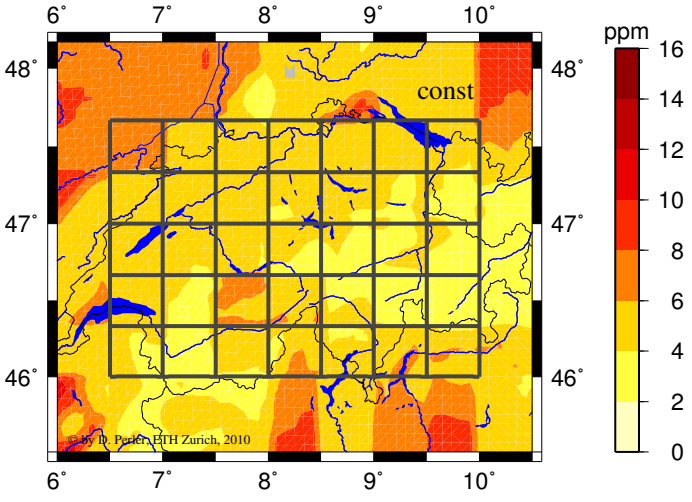

(a) constant

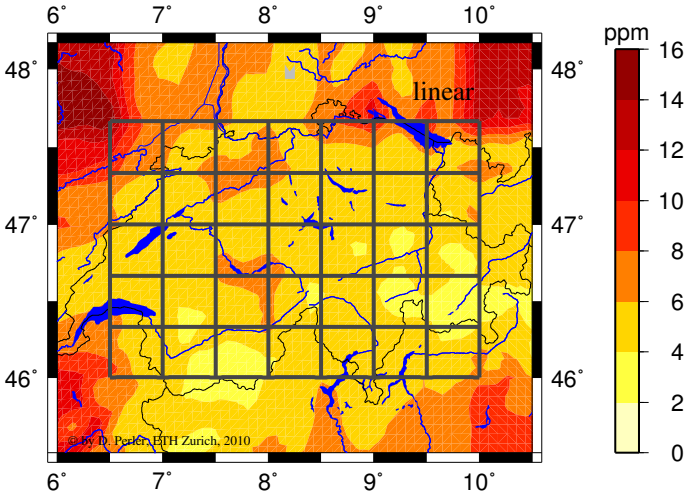

(b) trilinear

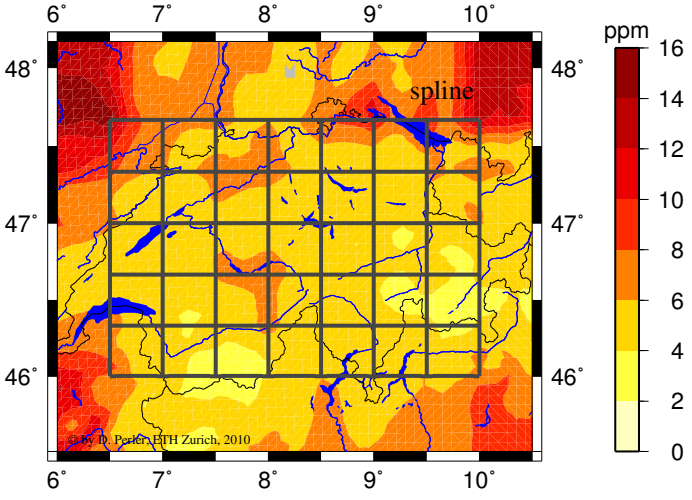

(c) spline

Figure 9.5: Weighted RMS errors computed from the wet refractivity difference between COSMO-7 and the tomographic solution using a) constant, b) trilinear, and c) spline parameterization. One year of data is considered between Earth's surface and 15'000 m altitude.

Table 9.5: RMS error in ppm wet refractivity units of the tomographic solution with respect to the analysis of COSMO-7. Tomographic solutions based on constant, trilinear and spline parameterizations are considered. Columns entitled *Uncorr.* describes the RMS error without any bias correction. For the values in the columns headed by *Corr.*, a bias correction is applied to the tomographic solutions (see also Section 9.3).

	Constant [ppm]		**Linear [ppm]**		**Spline [ppm]**	
	Uncorr.	**Corr.**	**Uncorr.**	**Corr.**	**Uncorr.**	**Corr.**
500 m	19.162	9.881	14.010	11.846	14.021	11.731
1000 m	17.068	11.310	14.237	11.994	14.332	12.003
1500 m	13.200	9.852	13.252	10.479	13.239	10.331
2000 m	11.555	9.328	11.109	8.936	11.122	8.618
3000 m	8.975	8.463	8.437	7.441	8.497	7.545
4000 m	7.750	7.575	7.688	7.253	7.943	6.865
5000 m	4.946	4.778	5.904	4.094	5.950	4.271
6000 m	2.990	2.898	3.853	3.779	3.665	3.098
0-15000 m	**4.673**	**3.150**	**4.802**	**3.092**	**4.887**	**3.034**

As expected, the trilinear and the spline parameterizations show a different common pattern from that observed by the constant parameterization. Larger RMS values are often found along voxel boundaries and around grid nodes. This can be explained by the different voxel parameterization. In contrast to the constant parameterization, the refractivity within a voxel is determined by the refractivities at the corners of the voxel. Trilinear as well as spline parameterization use bilinear interpolation in the horizontal. Thereby, the estimated field tends to be more accurate in the center of the voxel than towards the boundaries or the corners of the voxel. This is even strengthened by the fact that no horizontal smoothing constraints are used.

Comparing the accuracies achieved with respect to the balloon soundings in Payerne (see Table 9.4) and to the NWP COSMO-7 (see Table 9.5), large differences can be observed between them. To a large extent, they are related to the different evaluation method: All balloon sounding measurements are equally weighted, but they are not uniformly distributed over the height (see Figure 4.4). The density of the available measurements generally decreases with height and, therefore, errors at low altitudes have a larger impact on the global accuracy than those at high altitudes. In contrast to that, the data from the NWP COSMO-7 is weighted proportional to the volume which a grid node represents. This corresponds to equally weighted balloon sounding measurements if they were uniformly distributed along the vertical.

Figures 9.6-9.8 show the RMS of the tomographic solution with respect to the analysis of COSMO-7 at different height levels. Largest RMS errors are found at levels at low altitudes and a strong decrease of the RMS error with height is visible. This explains why better absolute accuracies are achieved over the alpine regions than over the Swiss Plateau incorporating the whole atmosphere (see Figures 9.5a)-9.5c)). In the highly elevated alpine regions, the low-elevated levels responsible for large parts of the errors are not present whereas they are over the Swiss Plateau.

In Figure 9.6, tile-shaped patterns are again clearly visible. Especially in Figure 9.6e) and f) around the location 46.5° N and 7.8° E, such a pattern can be found. The large RMS error within the voxels at this location is related to the GPS receiver station on Jungfraujoch, which is located in this voxel at an altitude of about 3500 m. The rather large RMS error indicates that the information provided by this station differs from the properties of the NWP field in the vicinity of Jungfraujoch. Although the station is located at 3500 m, large RMS errors are observed in altitudes below the station height. In Figures 9.7 and 9.8, large RMS errors can also be observed in this voxel. However, the pattern shows the characteristics typical for the non-constant parameterizations. The maximal uncertainties are centered along the eastern boundary of the voxel. This coincides well with the location of the receiver station at Jungfraujoch (46°33' N 7°59' E). Contrary to the solution of the constant parameterization, layers at lower altitudes than the height of that station are not

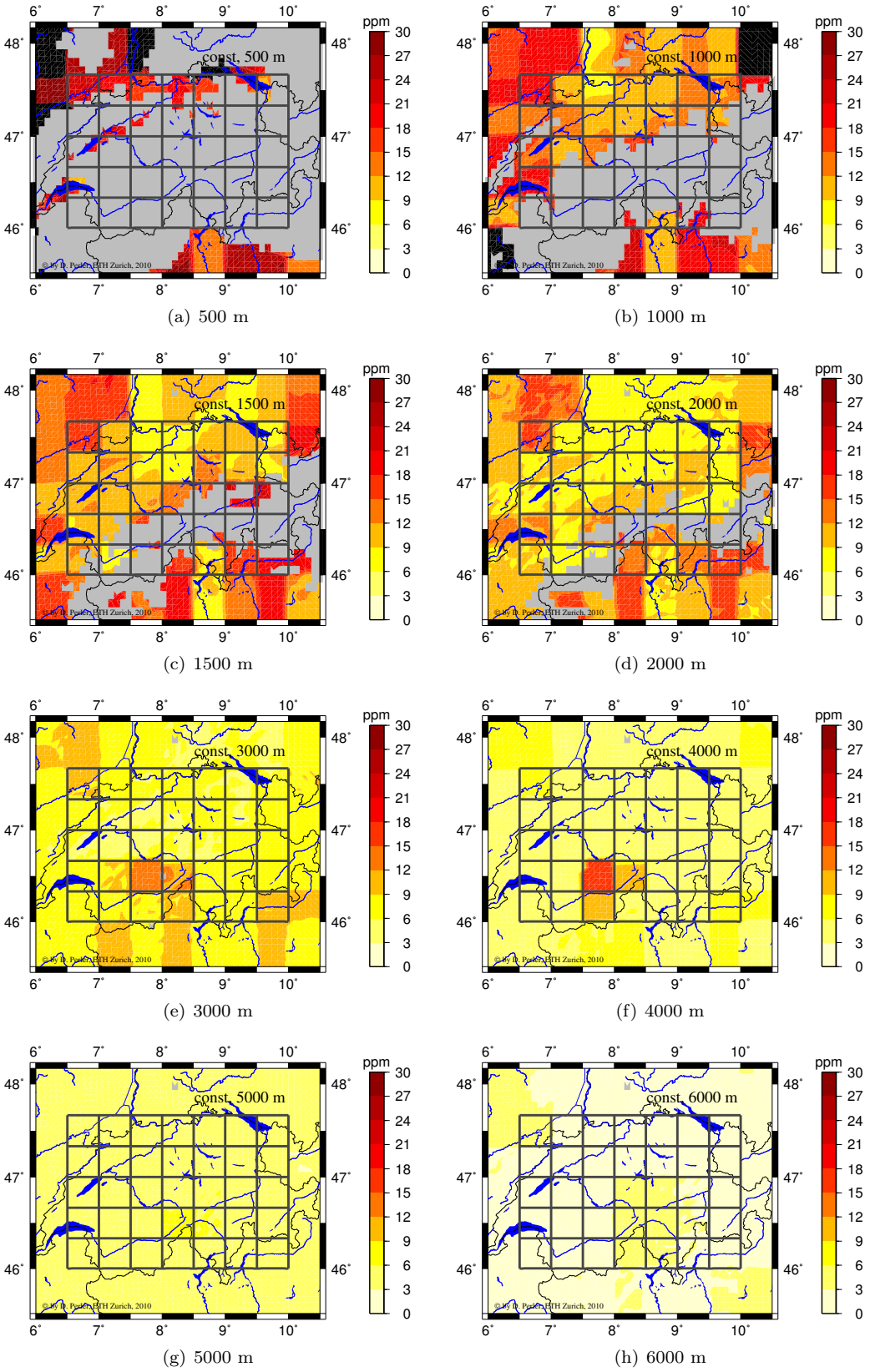

(a) 500 m (b) 1000 m

(c) 1500 m (d) 2000 m

(e) 3000 m (f) 4000 m

(g) 5000 m (h) 6000 m

Figure 9.6: RMS error of the GPS tomography using constant parameterization with respect to the analysis of COSMO-7 interpolated to different height levels. Black areas indicate regions with an RMS error larger than 30 ppm and gray areas regions in which the Earth's surface is above the considered level.

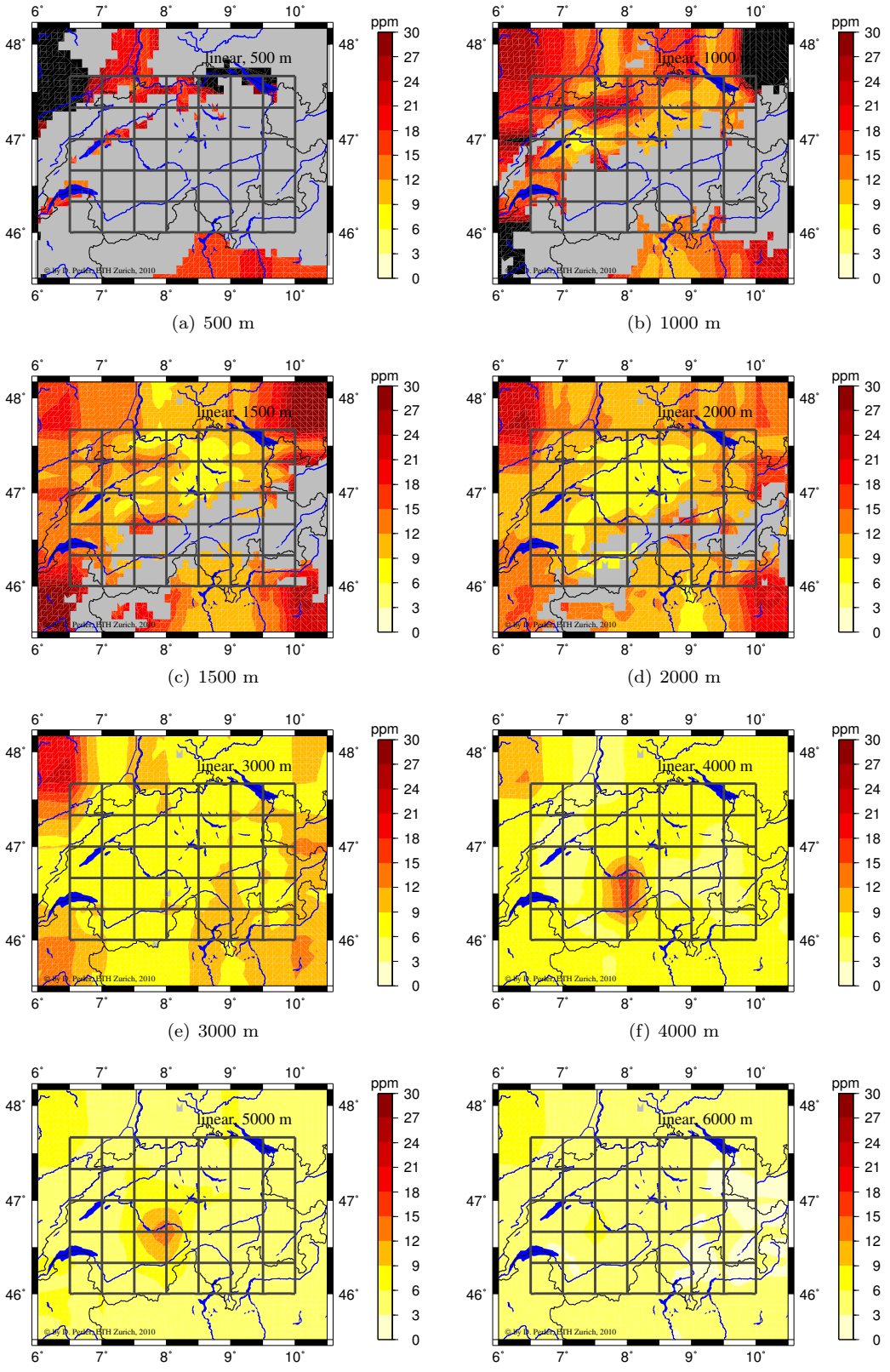

(a) 500 m (b) 1000 m

(c) 1500 m (d) 2000 m

(e) 3000 m (f) 4000 m

(g) 5000 m (h) 6000 m

Figure 9.7: RMS error of the GPS tomography using trilinear parameterization with respect to the analysis of COSMO-7 interpolated to different height levels. Black areas indicate regions with an RMS error larger than 30 ppm and gray areas regions in which the Earth's surface is above the considered level.

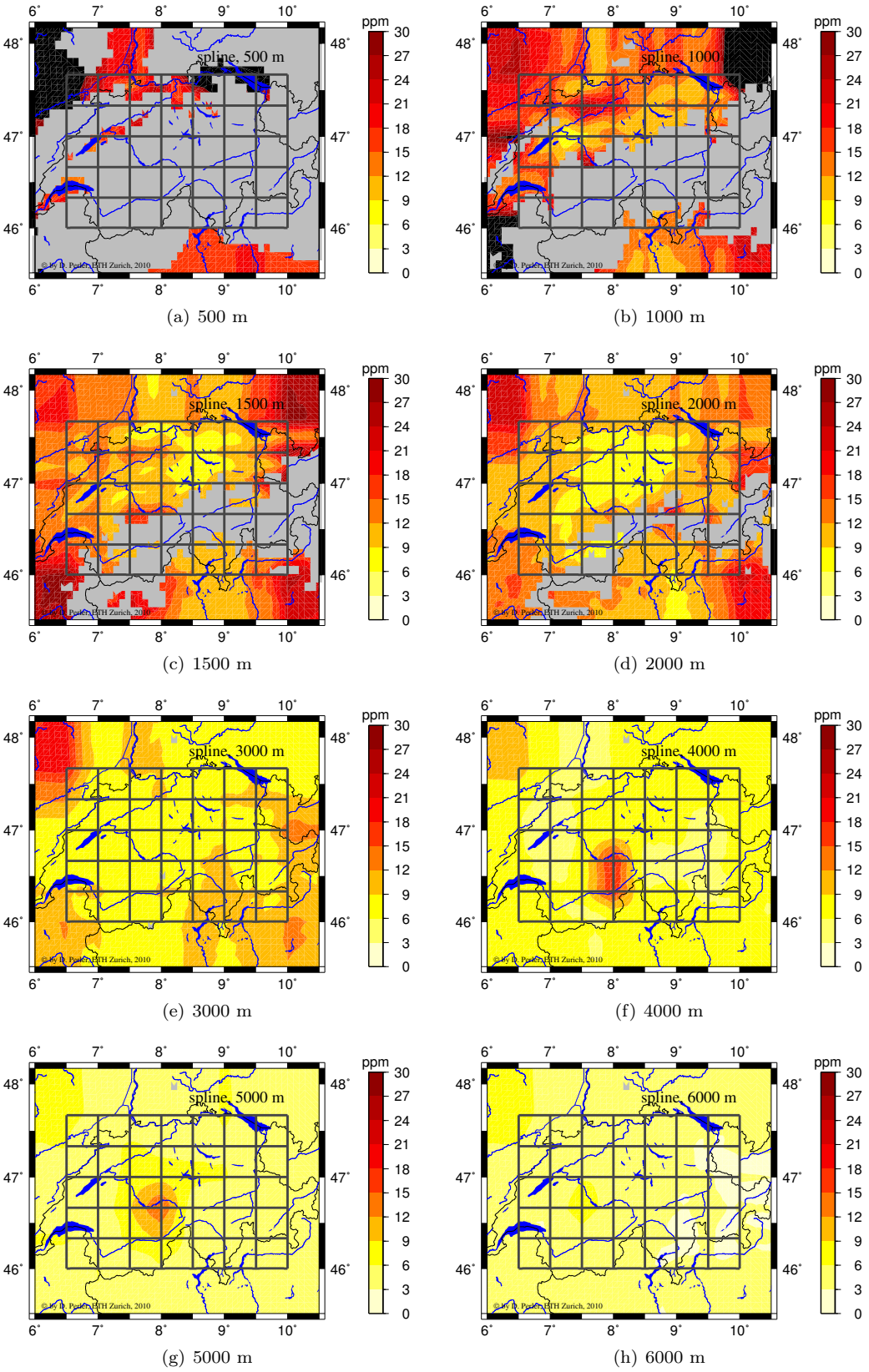

(a) 500 m (b) 1000 m

(c) 1500 m (d) 2000 m

(e) 3000 m (f) 4000 m

(g) 5000 m (h) 6000 m

Figure 9.8: RMS error of the GPS tomography using spline parameterization with respect to the analysis of COSMO-7 interpolated to different height levels. Black areas indicate regions with an RMS error larger than 30 ppm and gray areas regions in which the Earth's surface is above the considered level.

affected. On the other hand, the 5000 m level shows a larger RMS error compared to the results of the constant parameterization. We can conclude that non-constant parameterization can more accurately localize such effects and that the impact is spatially more restricted compared to the solution computed with constant parameterization. These findings also indicate that high-elevated receiver stations, such as Jungfraujoch, may introduce artefacts. Therefore, the impact of such stations should be carefully investigated before they are processed in an operational setup.

Figure 9.9 shows the seasonal RMS errors of the tomographic solution computed with constant parameterization with respect to COSMO-7. During winter (December-February) and spring (March-May), the RMS errors are significantly smaller than during the other seasons (see Table 9.6). This agrees well with the investigations about the seasonal variability of the wet refractivity in Sections 5.1 and 5.2. They revealed that during summer, largest wet refractivity values and spatial variability are observed. The investigations have also shown a larger spatial variability in autumn than in spring. This suggests that the accuracy of the reconstructed field is strongly related to the spatial variability of the wet refractivity field and, thus, to the discretization error.

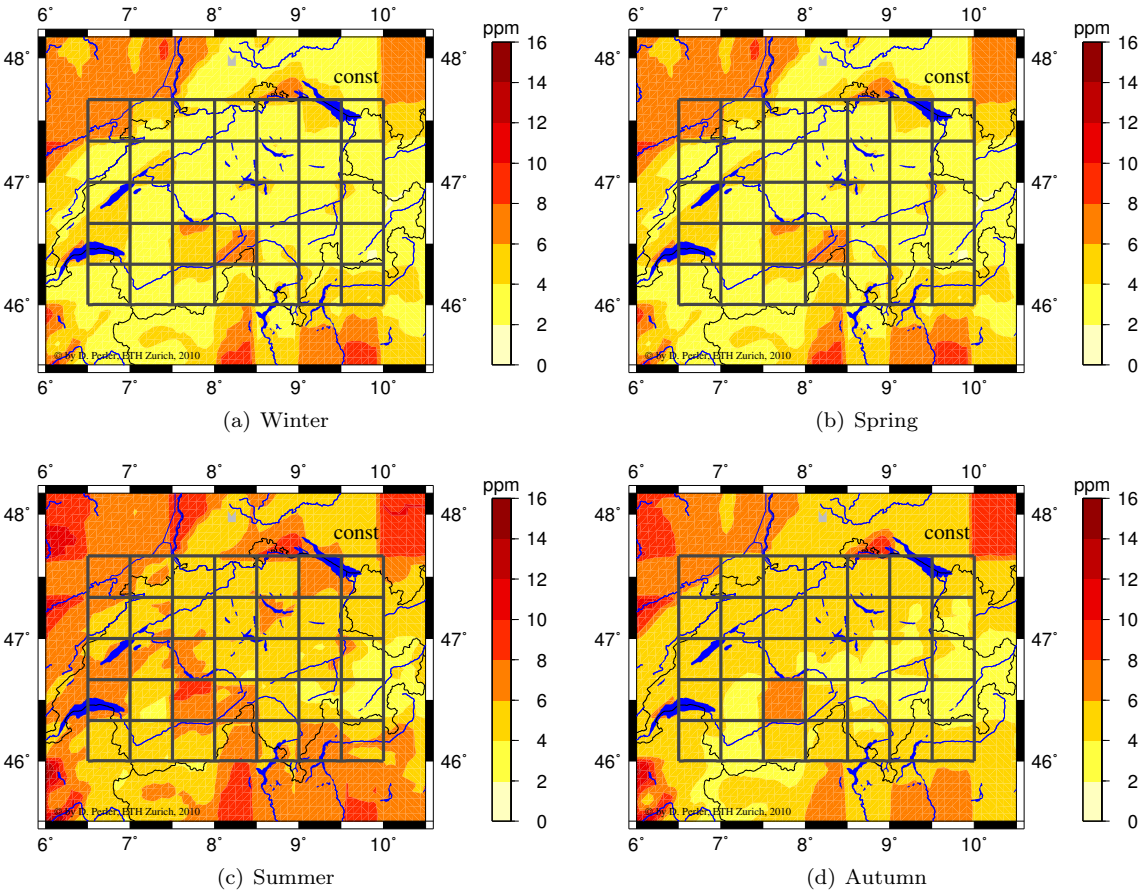

(a) Winter (b) Spring

(c) Summer (d) Autumn

Figure 9.9: Weighted RMS error of the tomographic solution using constant parameterization with respect to COSMO-7 evaluated for different seasons. The RMS error is in ppm wet refractivity units.

The diurnal cycle of the RMS error of the tomographic solution with respect to COSMO-7 is shown in Figure 9.10. The minimal RMS error is reached during the morning. At noon, the RMS error increases by about 2-3 ppm and reaches the diurnal maximum in the late afternoon. Afterwards, it monotonically decreases until it reaches again the diurnal minimum in the morning. Larger RMS errors during the afternoon are expected as solar radiation causes thermal convection in the atmosphere. The resulting small-scale perturbations cannot be resolved by the grid used in

Table 9.6: Weighted RMS error of tomographic solutions with respect to COSMO-7 evaluated for different seasons and parameterizations. Each season comprises 3 months.

	Constant	**Linear**	**Spline**
Winter (December-February)	4.004 ppm	4.083 ppm	4.063 ppm
Spring (March-May)	3.973 ppm	4.591 ppm	4.674 ppm
Summer (June-August)	5.678 ppm	6.633 ppm	6.749 ppm
Autumn (September-November)	4.535 ppm	5.465 ppm	5.554 ppm

our setup (see Section 5.2). This is reproduced in the diurnal cycle of the RMS error. As the data set used to computed these RMS errors considers all 4 seasons and thermal convection is mainly observed during summer in mid-latitudes on the northern hemisphere, a more distinct diurnal cycle of the RMS error is expected during summer (see Section 5.1).

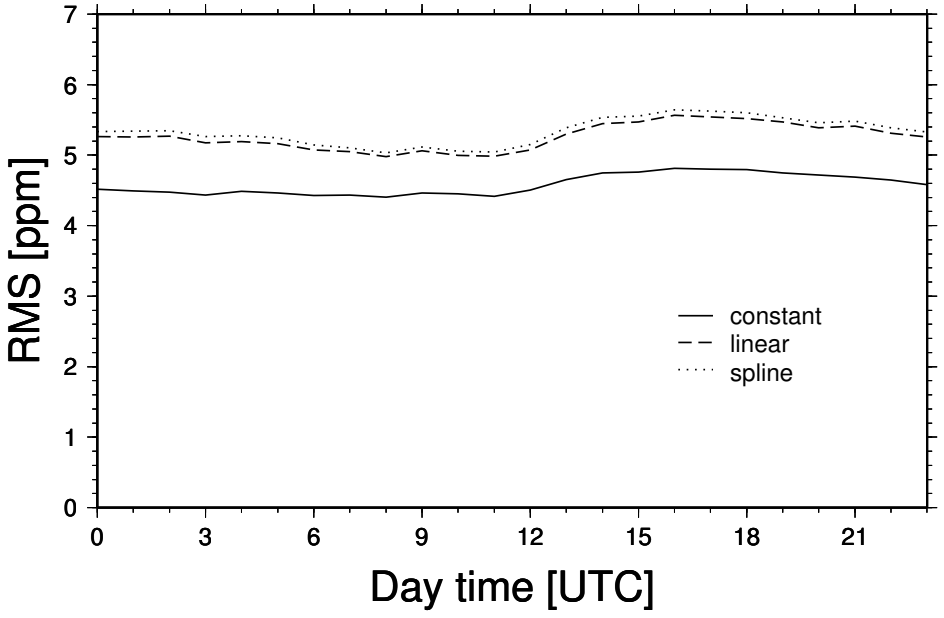

Figure 9.10: Weighted RMS error of different parameterized tomographic solutions with respect to COSMO-7 at different day times. The values are in ppm wet refractivity units.

Looking at Figure 9.11, the largest diurnal changes of the RMS error are observed in alpine areas. This supports the hypothesis that diurnal variations in the RMS error are mainly driven by convective processes because such processes are usually stronger in alpine regions. However, comparing the mean diurnal variability of the RMS error with the total variability, the diurnal one is about one order of magnitude smaller than the total one. This relativizes the importance of the diurnal variability compared to other factors, such as variations caused by synoptic scale effects.

The statistics about the accuracy of the tomography presented so far give only an average view over time and space. Particular cases are not addressed. Table 9.7 is a first try to list effects which have an impact on the precision which are not due to the tomographic processing. The error ranges caused by particular effects at certain times and locations are estimated. These ranges are coarse guesses and should be treated with care. The ranges are mainly estimated from the outcome of the investigations presented in Section 6 and observations from this section. Balloon sounding measurements are a main source of errors and can considerably vary between sensors of different manufacturers. Heating by solar radiation causes a rather small error compared to others, but it occurs more frequently. An error source with a large impact is icing or wetting of the sensors. This effect can be occasionally observed if a balloon traverses a cloud or an area with relative humidity

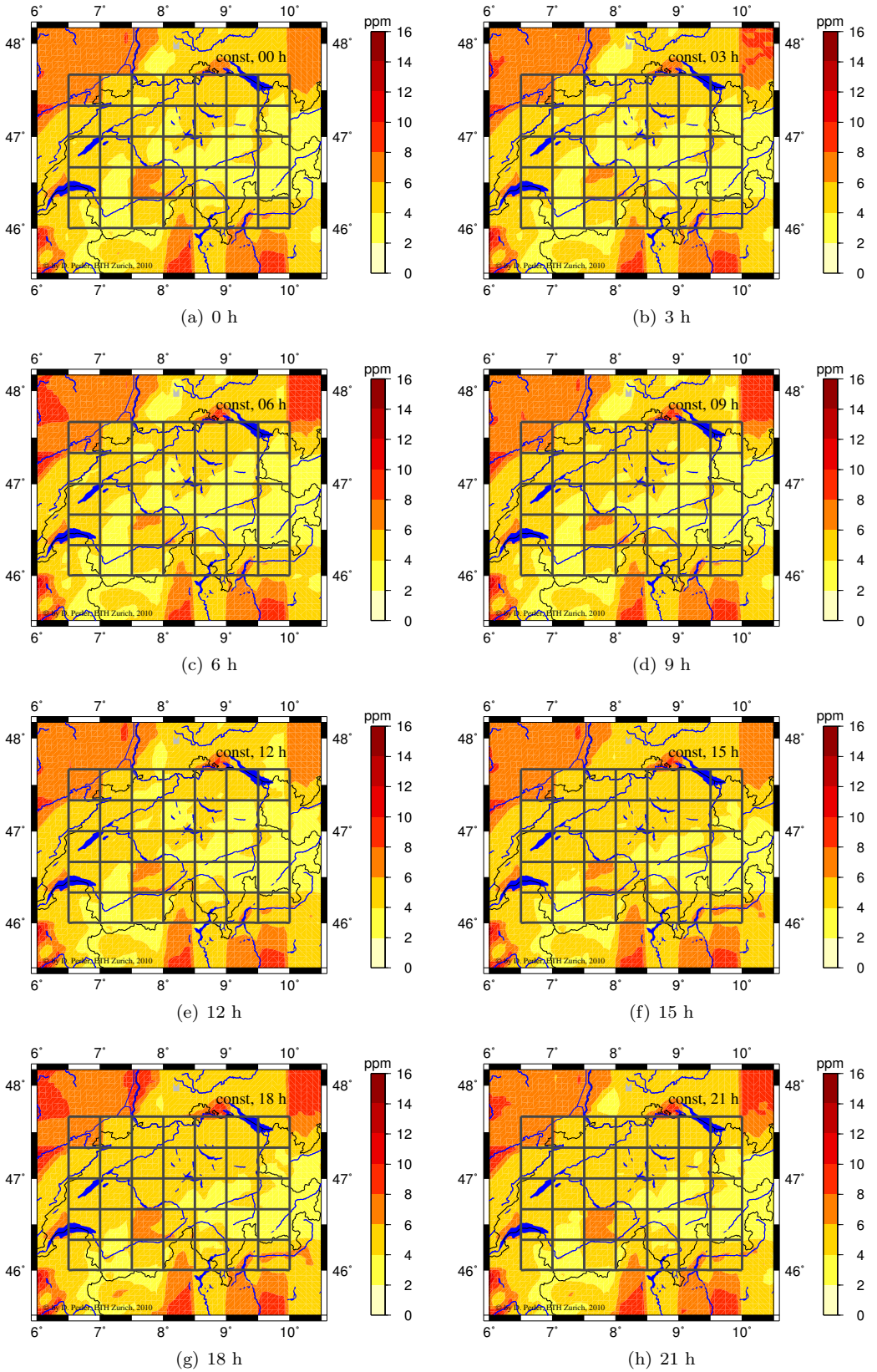

(a) 0 h (b) 3 h

(c) 6 h (d) 9 h

(e) 12 h (f) 15 h

(g) 18 h (h) 21 h

Figure 9.11: Weighted RMS error of tomographic solution using constant parameterization with respect to COSMO-7 at selected day times. The values are in ppm wet refractivity units.

near the saturation level. Errors with a similarly large impact are related to the tempo-spatial variability of the wet refractivity field. On the one hand, the balloon track can depart from the assumed instantaneous and vertical climb of the balloon due to advection of the balloon by wind. In that case, the refractivities are compared at different locations and this can introduce errors. On the other hand, the finite parameter set used in tomographic reconstruction may not have the necessary degrees of freedom to reproduce the true atmosphere. These discretization errors can be quite large in particular cases. Another error source is the GNSS processing. There are several unmodeled or incomplete modeled effects such as higher-oder ionospheric effects, multipath and phase center variations of the antenna which can be found in the postfit residuals. Postfit residuals are important for GNSS tomography as they are expected to contain information on the anisotropic water vapor distribution in the troposphere.

Table 9.7: Error budget for the tomographic evaluation. The error level reflects the error range a certain effect can cause.

Error source	**Uncorrected error level**
Heating by solar radiation	0-1 ppm
Icing/wetting of sensors	0-30 ppm
Departure true/assumed of balloon track	0-30 ppm
Discretization error	0-30 ppm
Higher-order ionospheric terms	0-2 cm *
Multipath	0-5 cm *
Antenna phase center variation	0-1 cm *

* personal communication with A. Geiger

9.3 Bias correction model and its evaluation

In the previous section, some systematic errors with respect to data from balloon soundings have been observed, such as a dry bias in the lower layers. In this section, a simple model will be presented to reduce such systematic errors. With the help of this model, these errors should be better quantized and, finally, should lead to a better understanding of the tomographic technique and its limitations. In addition, this should allow us to better formulate strategies to further improve GNSS tomography.

Figure 9.12 shows a time series of the difference between the tomographic solution and COSMO-7 at the grid point located at 46.905° N, 7.482° E and 1198 m altitude (gray dots). The time series clearly shows a seasonal cycle. This is also rendered in the bias correction model:

$$\hat{\mu}(t) = a_0 + a \cos\left(2\,\pi\,\frac{t}{\tau} - \phi\right) \tag{9.1a}$$

$$= a_0 + a_1 \sin\left(2\,\pi\,\frac{t}{\tau}\right) + a_2 \cos\left(2\,\pi\,\frac{t}{\tau}\right) \tag{9.1b}$$

with the time t, the seasonal period $\tau = 365.25$ days, and the parameters a_0, $a = \sqrt{a_1^2 + a_2^2}$, and $\phi = \arctan(a_1/a_2)$. Equation 9.1a) can be reformulated into the linear Equation 9.1b). The parameters a_0, a_1 and a_2 are fitted by a linear LSQ adjustment at each grid node of the NWP COSMO-7. Performing the bias correction at each NWP grid node allows us to eliminate a) local effects and artifacts of the NWP model, and b) artefacts caused by the parameterization and the measurement constellation. bias

For the time series shown in Figure 9.12, the model parameters are fitted. The solid line in the figure represents the solution of the fitted model parameters. The correction is largest in February and reaches the minimum in summer. Therefore, we can expect that the bias correction decreases the RMS error during winter more than during summer. This will further increase the seasonal variability of the accuracy. Considering the whole year, the bias correction decreases the RMS error

from 9.962 ppm to 8.213 ppm at this grid point. Testing the single parameters of the model for their relevance reveals that all 3 parameters are significantly different from zero. Detailed statistics about the parameters are listed in Table 9.8.

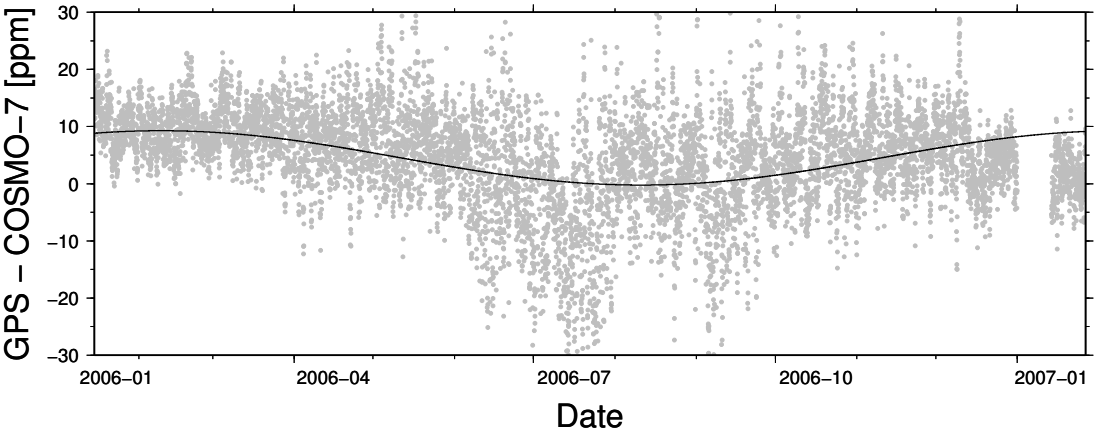

Figure 9.12: Difference between the tomographic solution and COSMO-7 at the location 46.905° N, 7.482° E and 1198 m height indicated by gray dots. The black line represents the solution of the fitted model (see Equation 9.1a)).

Figure 9.13 shows the parameter a_0 on different height levels for the case using constant parameterization. Largest biases are found in the layers close to the Earth's surface where the tomographic solution tends to be too wet (indicated by the blue color). At higher elevations, the opposite can be observed: the tomographic solution is too dry. The parameter a_0 is shown for the trilinear and the spline parameterization in Figures 9.14 and 9.15, respectively. The fitted parameter values for these two parameterizations are similar to each other, but are considerably different from those of the constant parameterization. Namely, they show horizontal gradients within the voxels in layers below 2000 m altitude. As generally only a single station resides in a voxel column and bilinear parameterization is used in the horizontal, local systematic gradients in the GPS observations seem a reasonable explanation for these gradients. These local gradients might not be representative for the whole voxel and, thus, cause these systematic differences.

In the vicinity of Jungfraujoch (46°33' N 7°59' E), strong biases of the order of 10 ppm are detected below 4000 m altitude in the solutions based on constantly parameterized voxels. Contrary, the solutions using non-constant parameterizations show no such distinct correction values. This indicates that more complex parameterizations can better handle conditions similar to that found in the Jungfraujoch area. Whether this will improve the accuracy of the bias corrected solution will be discussed later in this section. Nonetheless, this confirms that data from such stations should be handled with care.

Considering the whole troposphere, we have seen dry biases of the tomographic solution compared to the balloon soundings launched in Payerne (e.g. Figures 9.4a) and b)). Are such dry biases also present in other regions? Figures 9.16a)-9.16c) show the integrated biases along the zenith direction with respect to COSMO-7. The integrated bias is also referred to as *zenith wet path delay*

Table 9.8: Parameters of the bias correction model for the grid point located at 46.905° N, 7.482° E, and 1198 m height (see Equation 9.1b)).

Parameter	**Estimate**	**Std. Error**	**t value**
a_0	4.518 ppm	0.088 ppm	51.37
a_1	2.007 ppm	0.124 ppm	16.12
a_2	4.309 ppm	0.124 ppm	34.66

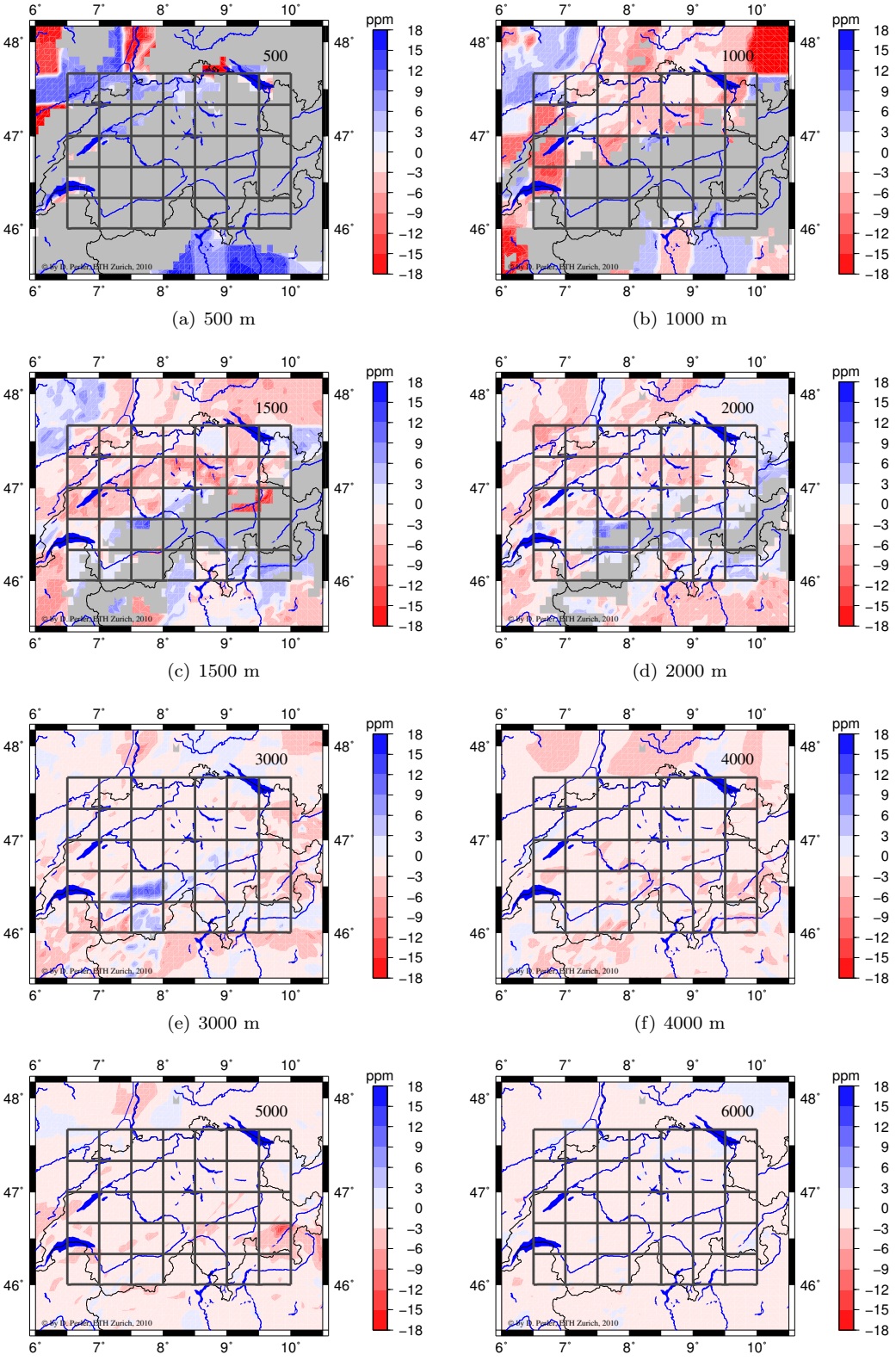

(a) 500 m (b) 1000 m

(c) 1500 m (d) 2000 m

(e) 3000 m (f) 4000 m

(g) 5000 m (h) 6000 m

Figure 9.13: Estimated biases of the constantly parameterized solution with respect to COSMO-7 on different height levels. The displayed values correspond to the parameter a_0 in Equation 9.1b).

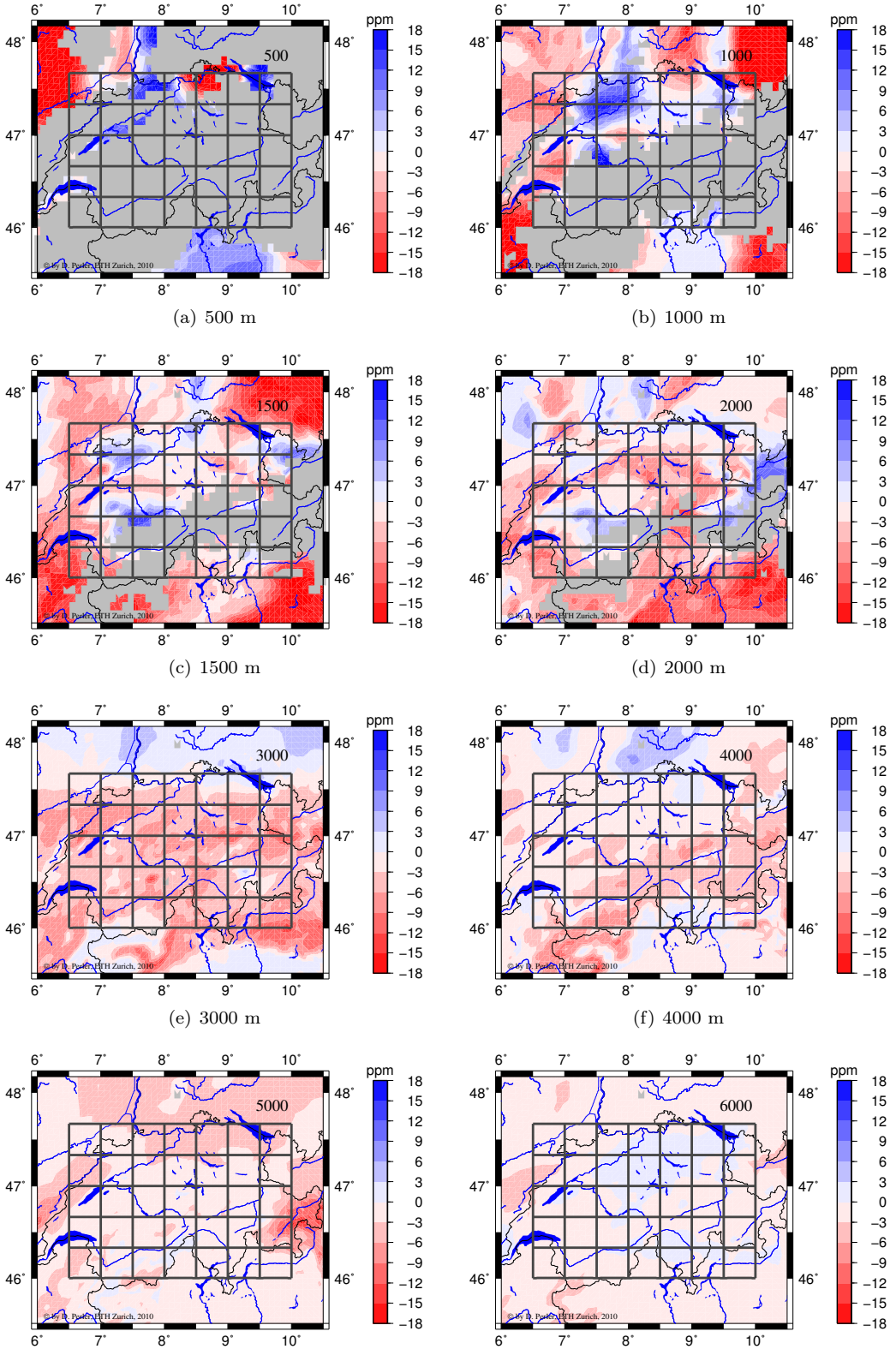

(a) 500 m (b) 1000 m

(c) 1500 m (d) 2000 m

(e) 3000 m (f) 4000 m

(g) 5000 m (h) 6000 m

Figure 9.14: Estimated biases of the trilinear parameterized solution with respect to COSMO-7 on different height levels. The displayed values correspond to the parameter a_0 in Equation 9.1b).

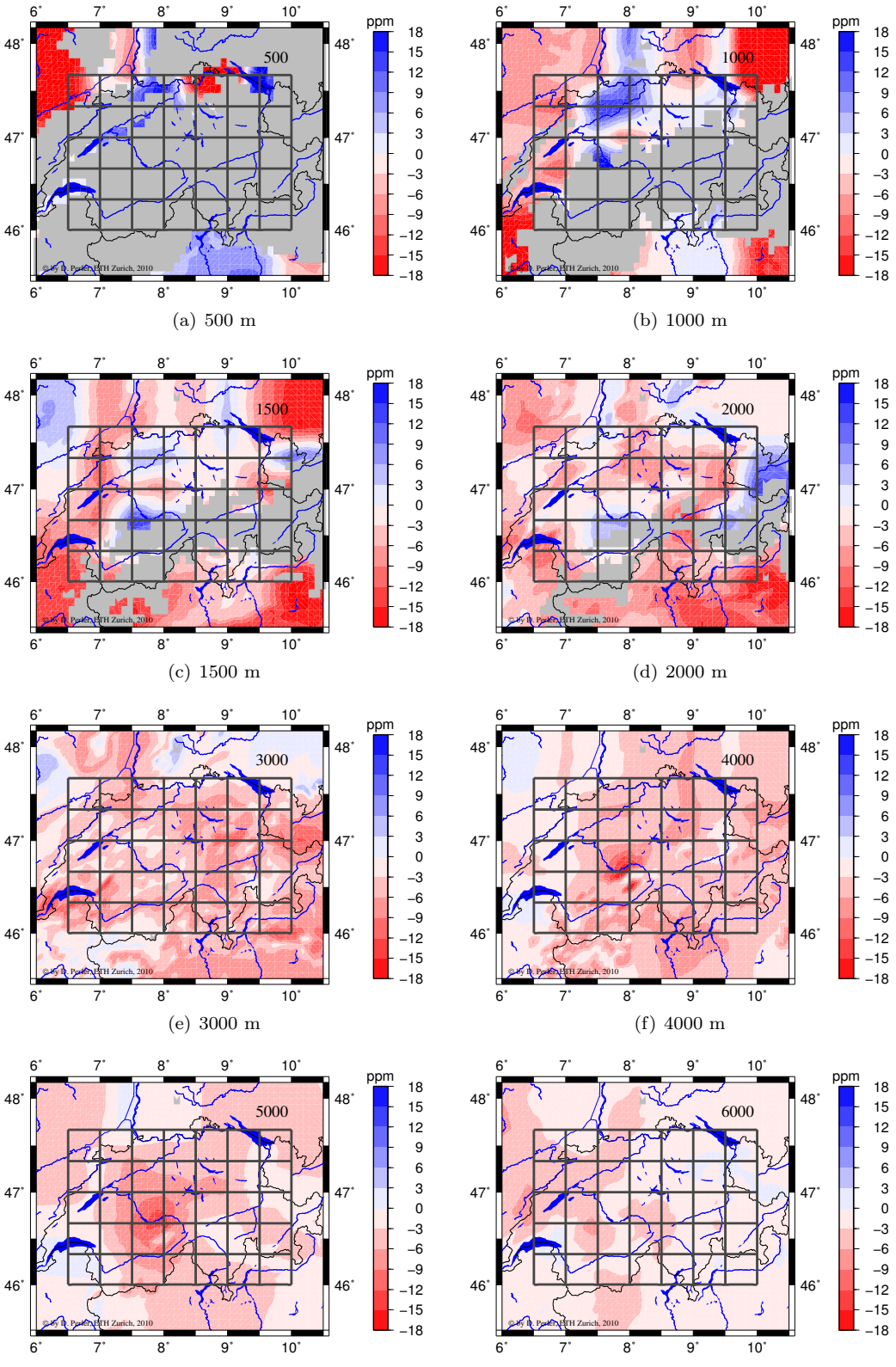

(a) 500 m (b) 1000 m

(c) 1500 m (d) 2000 m

(e) 3000 m (f) 4000 m

(g) 5000 m (h) 6000 m

Figure 9.15: Estimated biases of the spline parameterized solution with respect to COSMO-7 on different height levels. The displayed values correspond to the parameter a_0 in Equation 9.1b).

bias. The delays are computed by integrating the parameter a_0 of the bias correction model along the vertical. In the case with constantly parameterized voxels, the tomographic solutions show a dry bias of about 3-10 mm. Small dry and even wet biases are observed in alpine regions. Towards the boundaries of the core area and outside the core area, the bias tends to be larger and more dry.

For the trilinearly parameterized voxels, the zenith path delay biases tend to be smaller compared to those of the constantly parameterized voxels. There are regions showing a wet bias up to 5 mm delay. Outside the core area, rather large dry biases are visible. The latter are related to a priori values introduced at the lateral boundaries of the grid which are significantly smaller than those of COSMO-7. Adapting these pseudo-observations should reduce the dry bias outside the core area.

For the solutions computed with the spline parameterization, large dry biases of about 5-15 mm are visible. This type of parameterization clearly shows the largest dry biases of all 3 parameterizations and, nowhere, wet biases are observed. Investigations have shown that a large parts of the dry biases are produced in the top grid layer. This indicates that the combination of the pseudo-observation at the top level in combination with the boundary condition of the natural cubic splines is problematic and one should consider to use other boundary conditions, such as fixing the first derivative of the spline function. Another possibility would be to modifying intervoxel constraints in the way to rather affect the first derivative at the grid points than the wet refractivity difference between two adjoining grid points.

Figures 9.16a)-9.16c) show a larger dry bias in Payerne compared to most other regions for all 3 parameterizations. This means that biases shown by the comparison with balloon sounding data are generally larger and more dry than those observed in the other regions. We can, therefore, conclude that the comparisons with balloon soundings in Payerne (Table 9.4) are too pessimistic. Nevertheless, the tomographic solutions tend to be too dry compared to the NWP COSMO-7 in most regions.

The distinct differences in the integrated biases between the parameterizations show that the tomographic solutions are sensitive to the voxel parameterization with respect to zenith wet delays. This suggests that the setup and especially the choice of the parameterization and intervoxel constraints are crucial for accurate tomographic results. On the other hand, this also indicates that GNSS tomography with double difference observations has a limited robustness regarding integrated quantities. From this point of view, it is debatable to prefer slant path delays over double difference delays. Due to the differencing, a single double difference observations contains no information about the absolute path delay. Therefore, the use of slant path delays may have a positive impact on the accuracy regarding integrated quantities.

Figure 9.17 shows the seasonal amplitude of the bias correction for the constantly parameterized solution with respect to COSMO-7. Large amplitudes are mainly found below 4000 m altitude and tile-shaped patterns similar to those observed in Figure 9.5a) are present in these layers. The shape of these patterns changes at heights between 4000-5000 m: Largest values are found along mountain ridges. This suggests that seasonal variations are related to the voxel parameterization and to local effects. Comparing the amplitudes to the mean biases (parameter a_0), they are of the same order of magnitude. In several regions and below 3000 m altitude, the seasonal variation even tends to be larger than the mean bias. This means that dry and wet biases can be observed at a single point at different seasons. The other two parameterizations show much smaller seasonal variations (see Figures 9.18 and 9.19). Thus, the ratio between the seasonal variation and the mean bias is also smaller. This is an indicator that the solutions of more complex parameterized voxels are more consistent over time which is an important property regarding the assimilation into NWP models.

The seasonal maxima are reached between late autumn and winter at low altitudes. Above 3000 m altitude, the maxima are shifted towards spring and summer (see Figures 9.20-9.22). This corresponds to a phase shift of about half a year between low- and high-elevated layers and can be interpreted in the way that the systematic seasonal variation is largely a variation in the vertical distribution. During winter, the tomographic solution has a more wet bias in low-elevated layers and a more dry bias in high-elevated layers with respect to the mean bias. The opposite is then observed during summer. As the vertical resolvability in GNSS tomography is limited, vertical

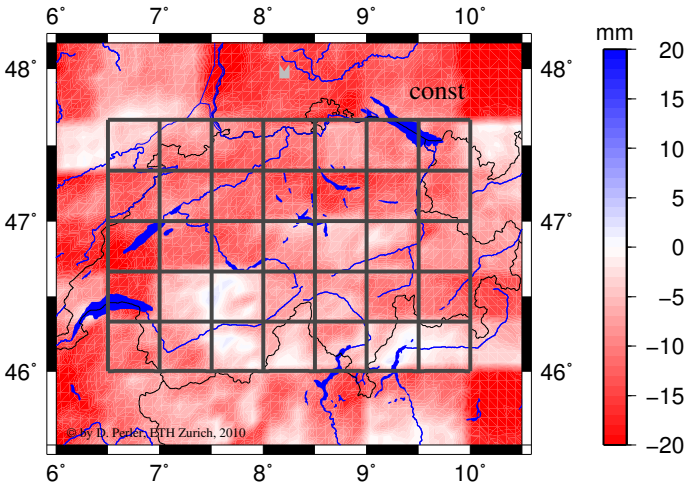

(a) constant

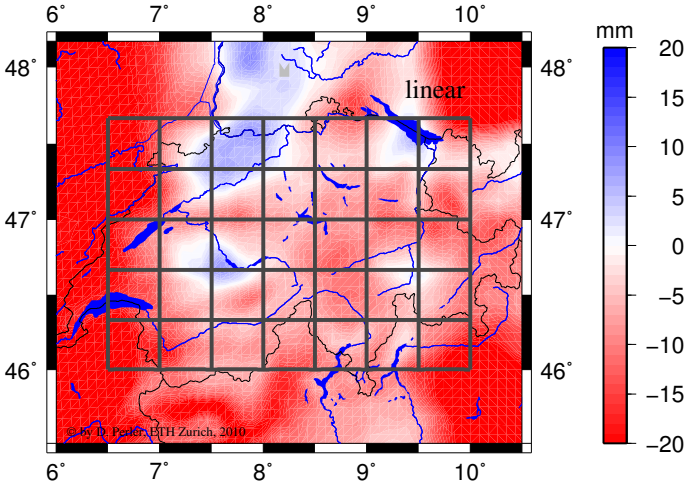

(b) trilinear

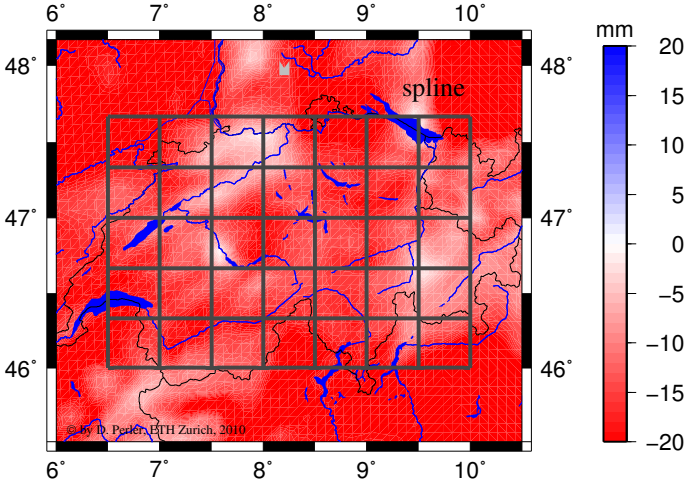

(c) spline

Figure 9.16: Integrated biases along the zenith direction computed from a) the constant, b) the trilinear, and c) the spline-parameterized solutions with respect to COSMO-7.

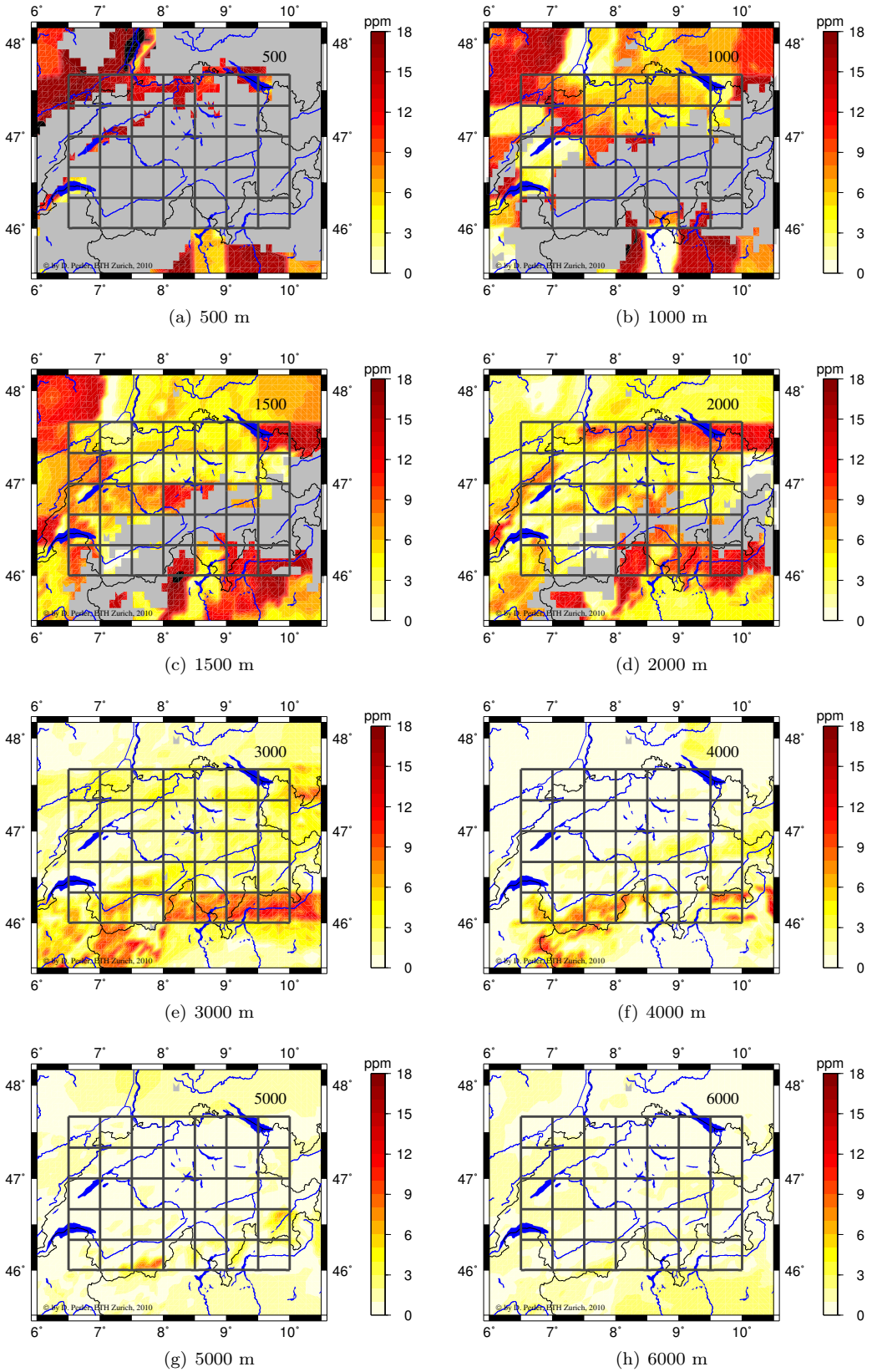

(a) 500 m (b) 1000 m

(c) 1500 m (d) 2000 m

(e) 3000 m (f) 4000 m

(g) 5000 m (h) 6000 m

Figure 9.17: Seasonal amplitude variation of the bias with respect to COSMO-7 using constantly parameterized voxels. Gray shaded areas indicate regions in which the Earth's surface is above the considered level.

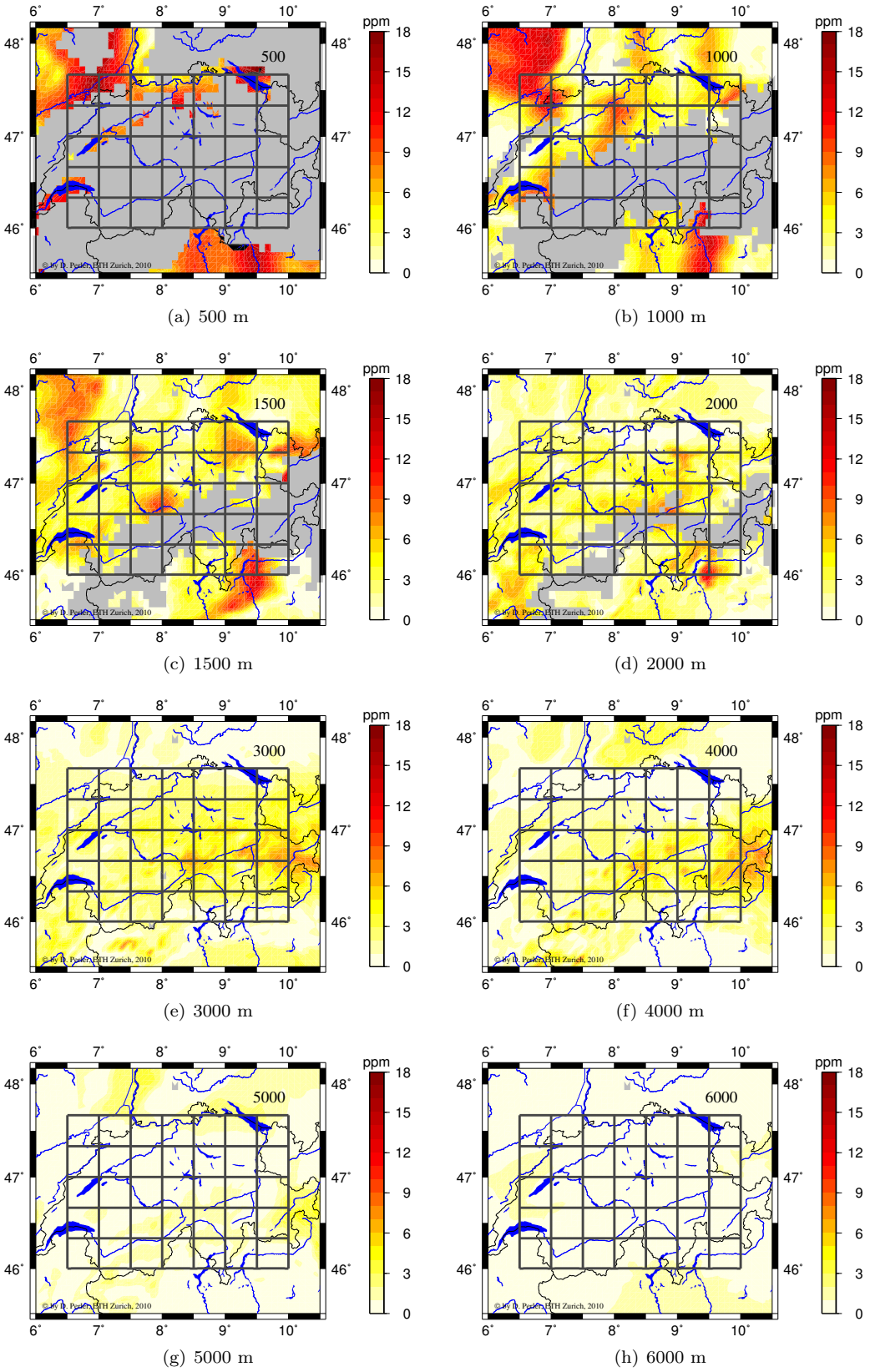

(a) 500 m (b) 1000 m

(c) 1500 m (d) 2000 m

(e) 3000 m (f) 4000 m

(g) 5000 m (h) 6000 m

Figure 9.18: Seasonal amplitude variation of the bias with respect to COSMO-7 using trilinearly parameterized voxels. Gray shaded areas indicate regions in which the Earth's surface is above the considered level.

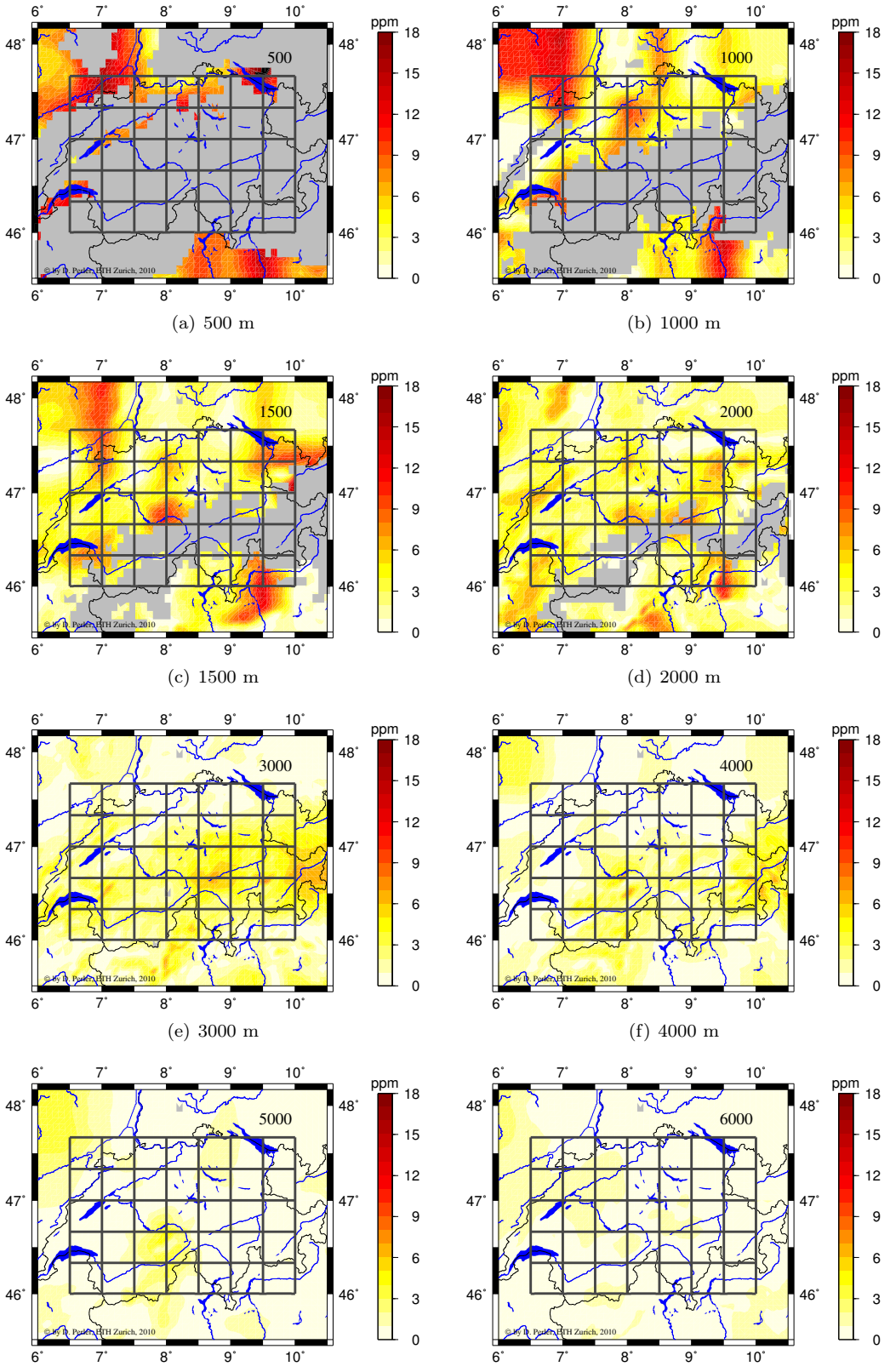

(a) 500 m (b) 1000 m

(c) 1500 m (d) 2000 m

(e) 3000 m (f) 4000 m

(g) 5000 m (h) 6000 m

Figure 9.19: Seasonal amplitude variation of the bias with respect to COSMO-7 using spline parameterization. Gray shaded areas indicate regions in which the Earth's surface is above the considered level.

intervoxel constraints play a crucial role concerning the vertical distribution of the wet refractivity. This suggests that a departure of the wet refractivity vertical distribution on which the intervoxel constraints are based from the truth leads to systematic errors in the vertical distribution in the tomographic results. Although the vertical distribution varies with time, the same vertical distribution is assumed for the whole year in our setup. This might be the reason for the systematic errors in the vertical distribution of the wet refractivity. Adaptive vertical intervoxel constraints might reduce these errors.

Figures 9.23-9.25 show the RMS error with respect to COSMO-7 for different parameterizations on selected height levels after applying the bias correction model on the tomographic solutions. They still show the same typical pattern as seen in the RMS error plots without bias correction. The RMS values are, however, significantly decreased (see Table 9.5), at least at low altitudes.

Below 1500 m altitude, the bias correction model has a large impact on the accuracy of solutions based on constantly parameterized voxels and leads to even more accurate results than with the more complex parameterizations. An explanation of this could be that local gradients induced by a single GPS station are not representative for the gradients on the grid scale. As the station density is rather low compared to the grid resolution (less than one station per voxel column in average) and no ray crossings occur below several hundred meters above the Earth's surface, the field is not well determined. Thus, the local gradients are visible in the solutions and increase the RMS error along the voxel boundaries.

Above 1500 m altitude, the solutions of the more complex parameterizations become more accurate than those computed with the constant parameterization. This is an indicator that the more entangled rays better determine the field and, therefore, can better suppress the effects of non-representative local gradients. Investigations using horizontal intervoxel constraints in the layers below 1500 m altitude may clarify this hypothesis.

Comparing the results of the different parameterizations, the estimated refractivities based on the complex parameterizations are more accurate on heights between 1500-5000 m than those based on the constant parameterization. The same holds if the whole atmosphere is considered. The results based on the more complex parameterizations are improved by 2% and 4% compared with that based on the constant parameterization (see Table 9.5).

Concerning the accuracy in the vicinity of Jungfraujoch (46°33' N 7°59' E), the complex parameterizations show significantly more accurate results than the constant parameterization. Large RMS errors are limited to a radius of a few kilometers around the Jungfraujoch whereas several voxels around Jungfraujoch are affected in the case of the constant parameterization. This confirms the better resolvability of the complex parameterizations compared to that of constant parameterization and agrees with the results of the synthetic tests presented in Section 8.2.

9.4 Conclusions

The investigations in this chapter revealed a good performance in terms of accuracy for the new tomography software AWATOS 2. An RMS error of 3.0 ppm (0.4 $\mathrm{g\,m^{-3}}$ absolute humidity) is achieved with respect to the NWP COSMO-7 including 1 year of data. This demonstrates the high potential of GNSS tomography to improve the initial state of numerical weather prediction models. Compared to the predecessor AWATOS, the new algorithms in AWATOS 2 show significantly more accurate results (Troller 2004; Troller et al. 2006). This shows the positive impact of the enhancements such as the Kalman filter, the improved statistical model, the new intervoxel constraints and the voxel parameterizations on the accuracy of the results.

The investigations revealed that tomographic solutions show significant systematic errors. Sources of these errors are effects due to the discretization of the space by the voxel parameterization, and systematic differences between the input data and data used for the validation. These errors can be considerably reduced by a bias correction model. The RMS error with respect to the NWP COSMO-7 decreases from 4.9 ppm (0.7 $\mathrm{g\,m^{-3}}$) to 3.0 ppm (0.4 $\mathrm{g\,m^{-3}}$) for the solution usingspline

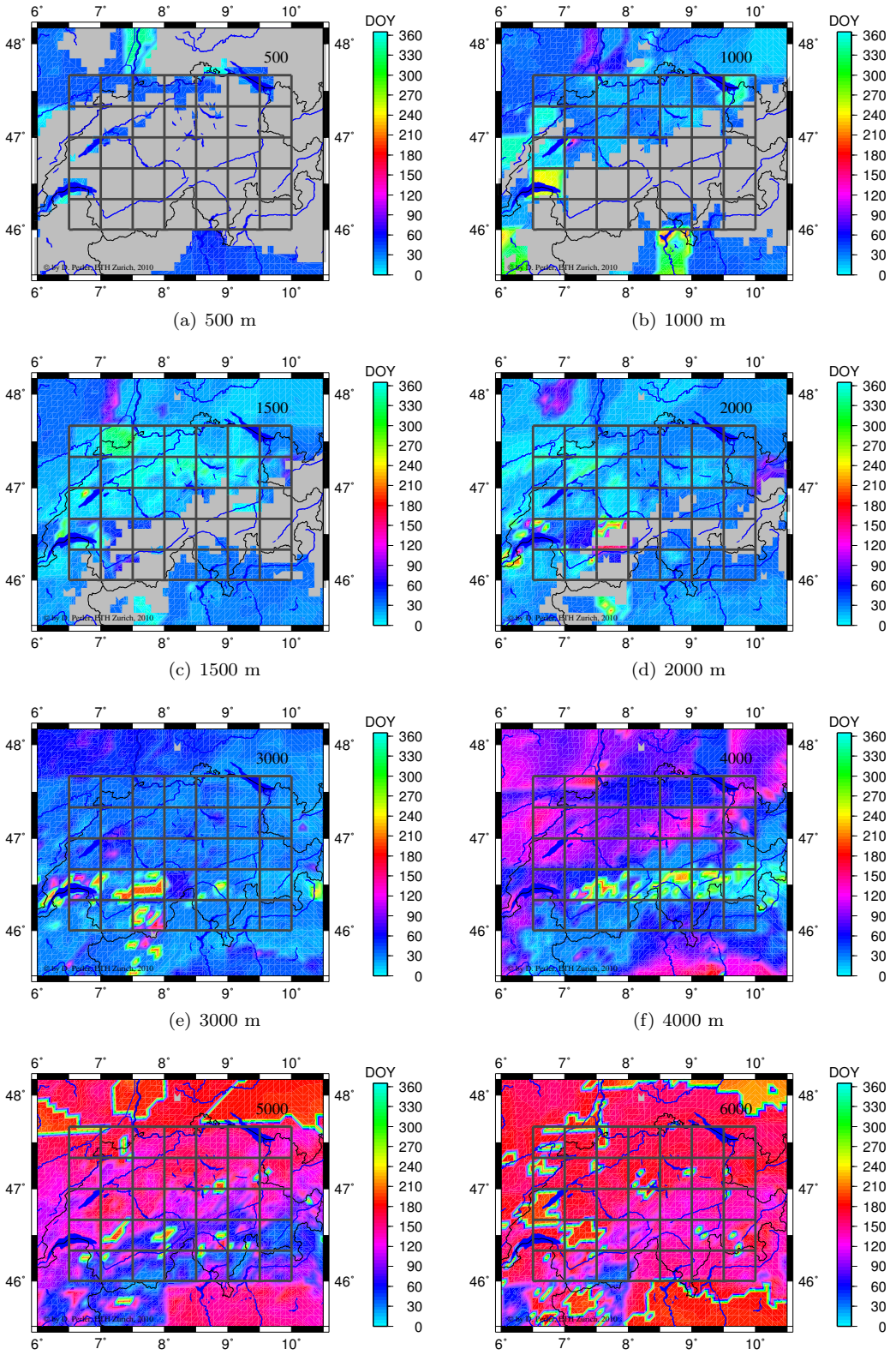

(a) 500 m (b) 1000 m

(c) 1500 m (d) 2000 m

(e) 3000 m (f) 4000 m

(g) 5000 m (h) 6000 m

Figure 9.20: Phase shift of the seasonal maximal bias with respect to COSMO-7 for constant parameterization. The shifts are given in day of year. Gray shaded areas indicate regions in which the Earth's surface is above the considered level.

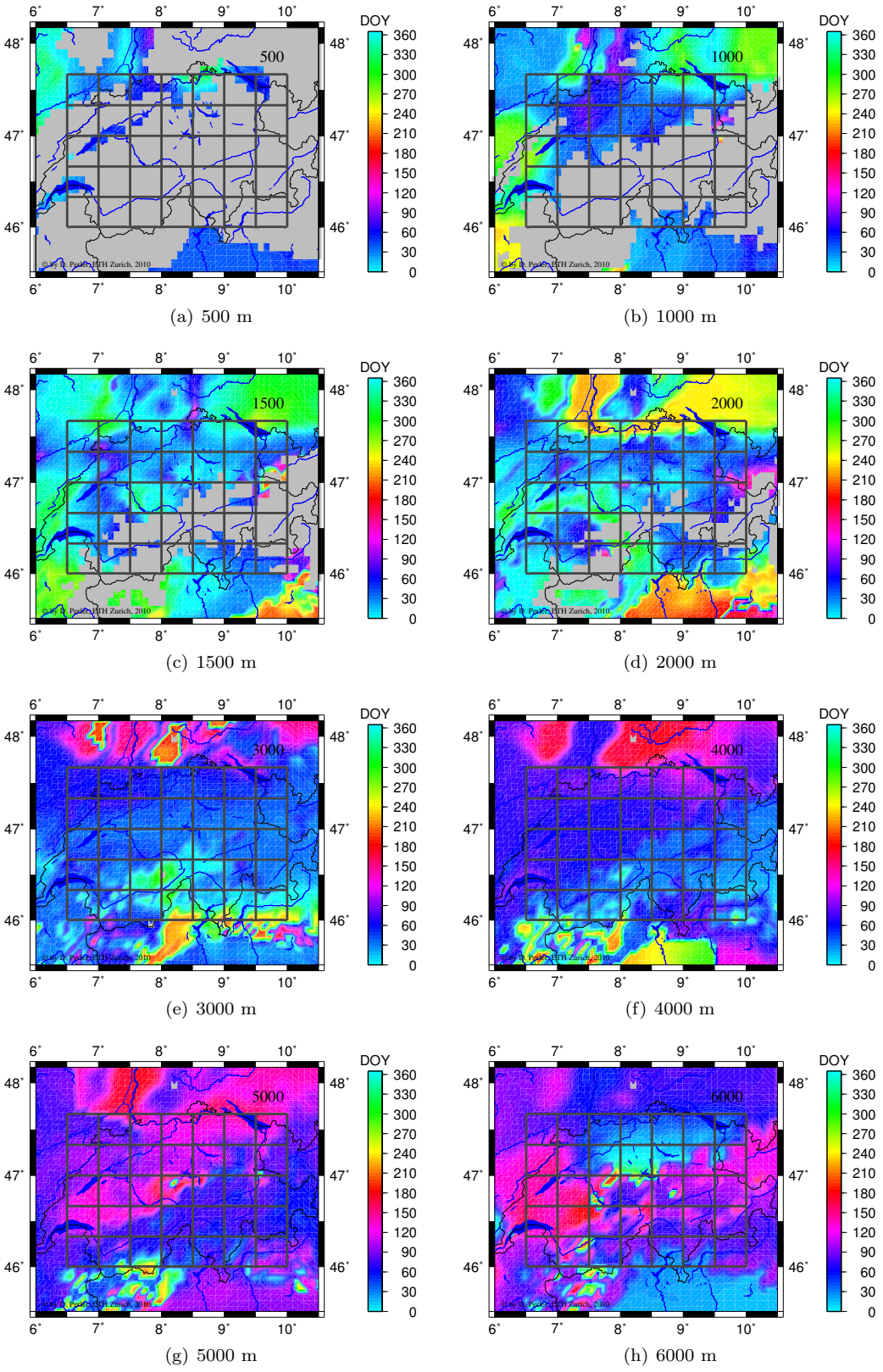

(a) 500 m (b) 1000 m

(c) 1500 m (d) 2000 m

(e) 3000 m (f) 4000 m

(g) 5000 m (h) 6000 m

Figure 9.21: Phase shift of the seasonal maximal bias with respect to COSMO-7 for the trilinear parameterization. The shifts are given in day of year. Gray shaded areas indicate regions in which the Earth's surface is above the considered level.

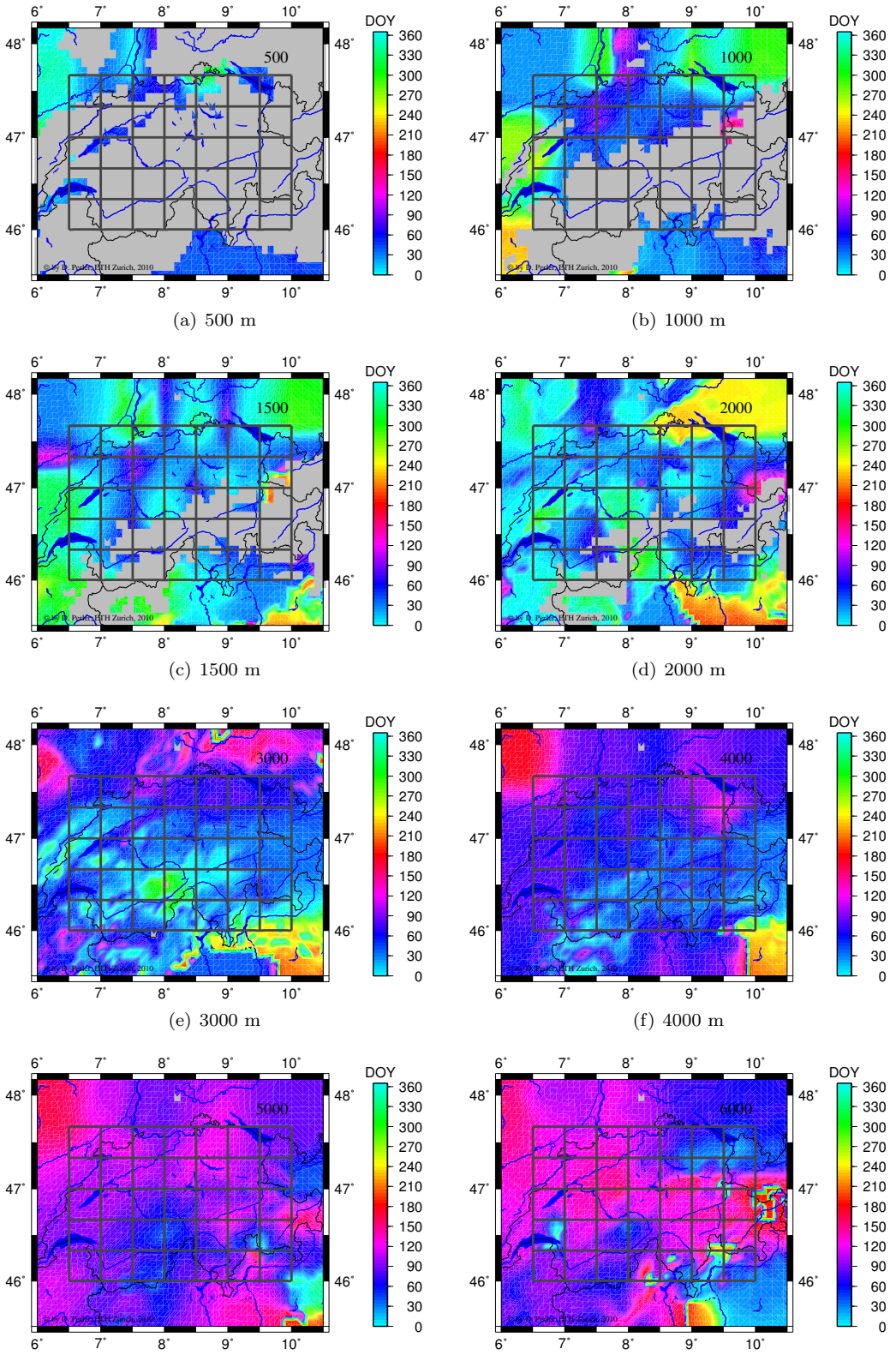

(a) 500 m (b) 1000 m

(c) 1500 m (d) 2000 m

(e) 3000 m (f) 4000 m

(g) 5000 m (h) 6000 m

Figure 9.22: Phase shift of the seasonal maximal bias with respect to COSMO-7 for the spline parameterization. The shifts are given in day of year. Gray shaded areas indicate regions in which the Earth's surface is above the considered level.

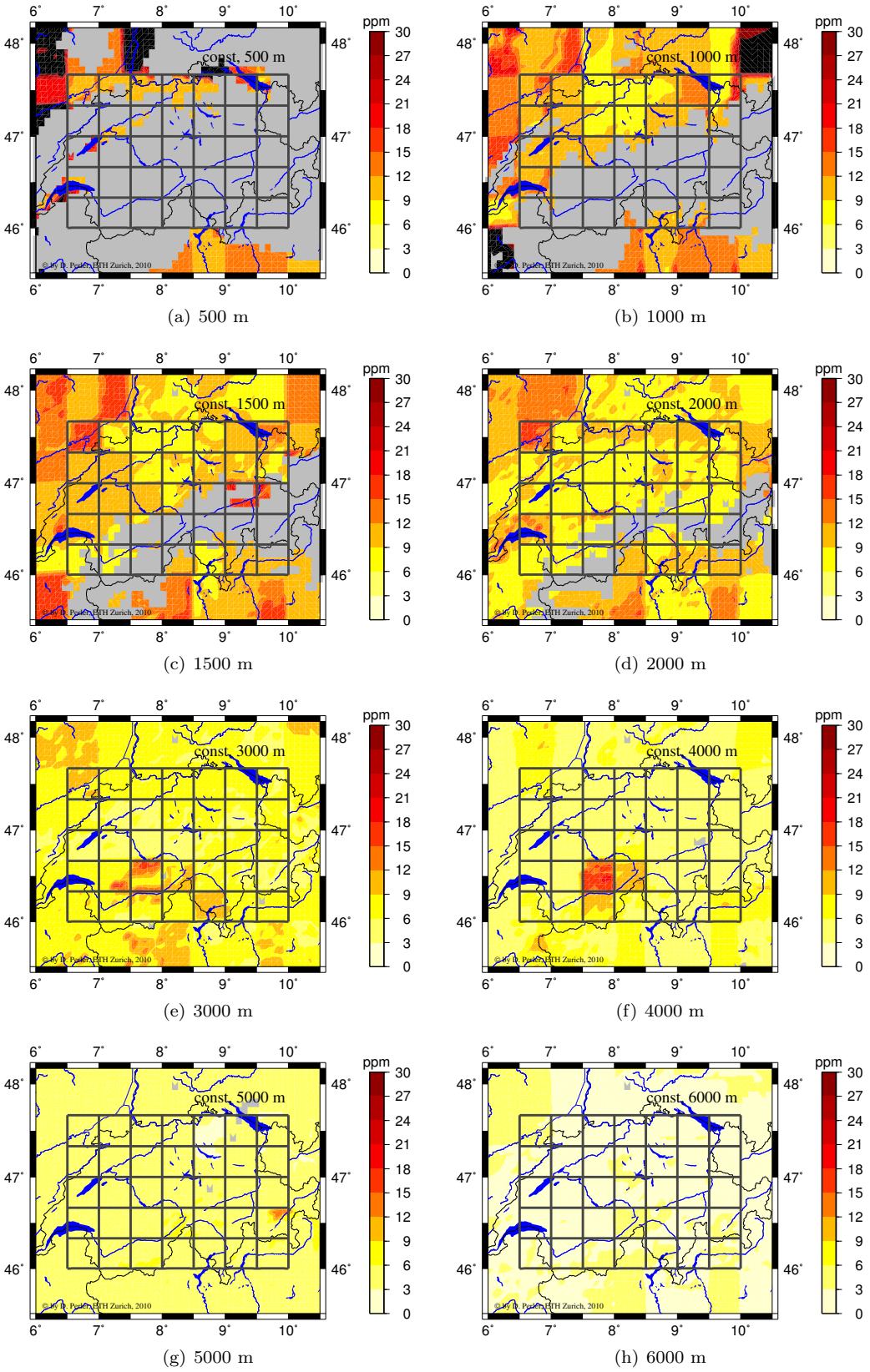

(a) 500 m (b) 1000 m

(c) 1500 m (d) 2000 m

(e) 3000 m (f) 4000 m

(g) 5000 m (h) 6000 m

Figure 9.23: RMS error of the tomographic solutions computed with constant parameterization with respect to COSMO-7 on selected height level using the bias correction model. Gray shaded areas indicate regions in which the Earth's surface is above the considered level.

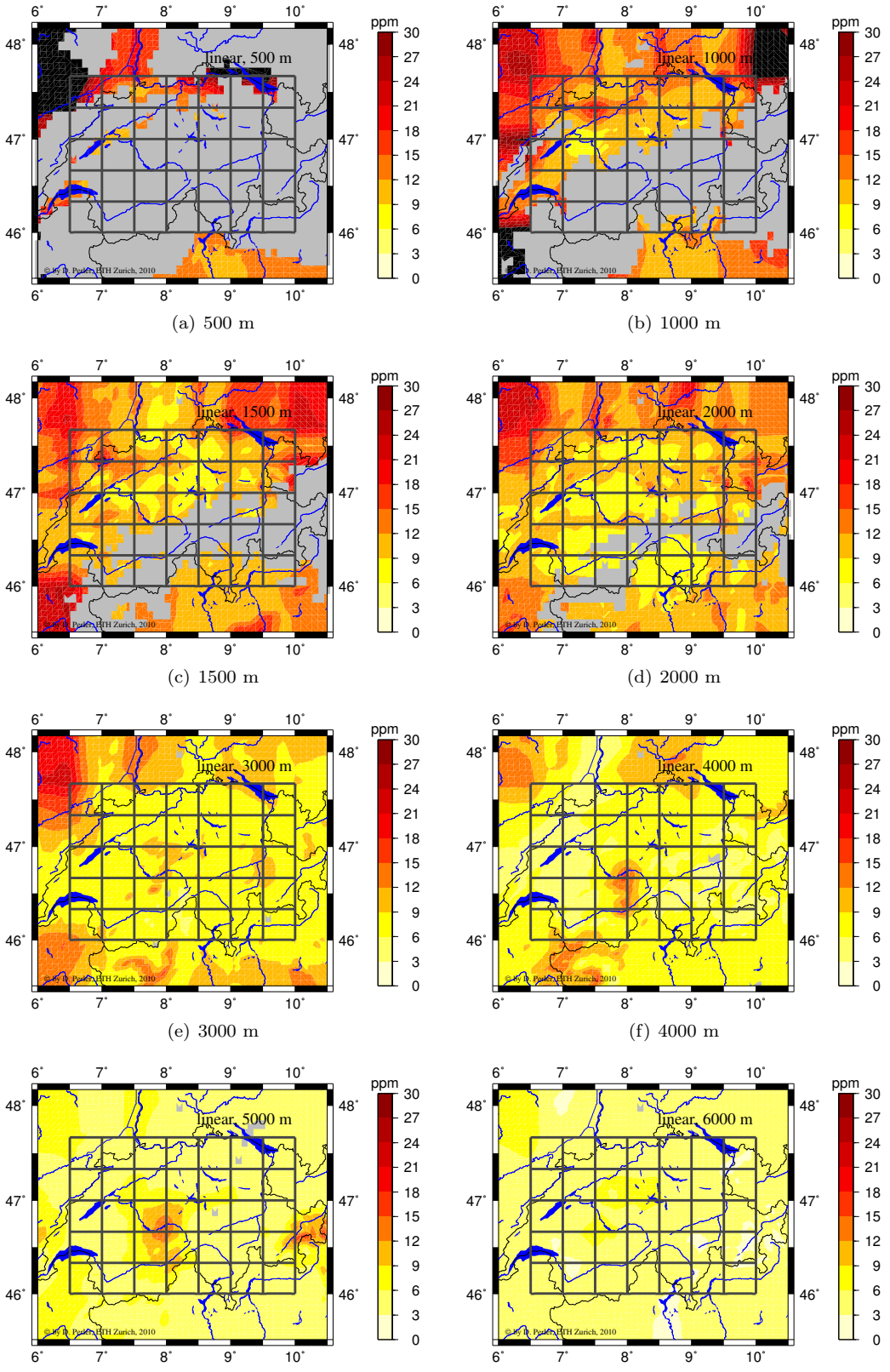

(a) 500 m (b) 1000 m

(c) 1500 m (d) 2000 m

(e) 3000 m (f) 4000 m

(g) 5000 m (h) 6000 m

Figure 9.24: RMS error of the tomographic solutions computed with trilinear parameterization with respect to COSMO-7 on selected height level using the bias correction model. Gray shaded areas indicate regions in which the Earth's surface is above the considered level.

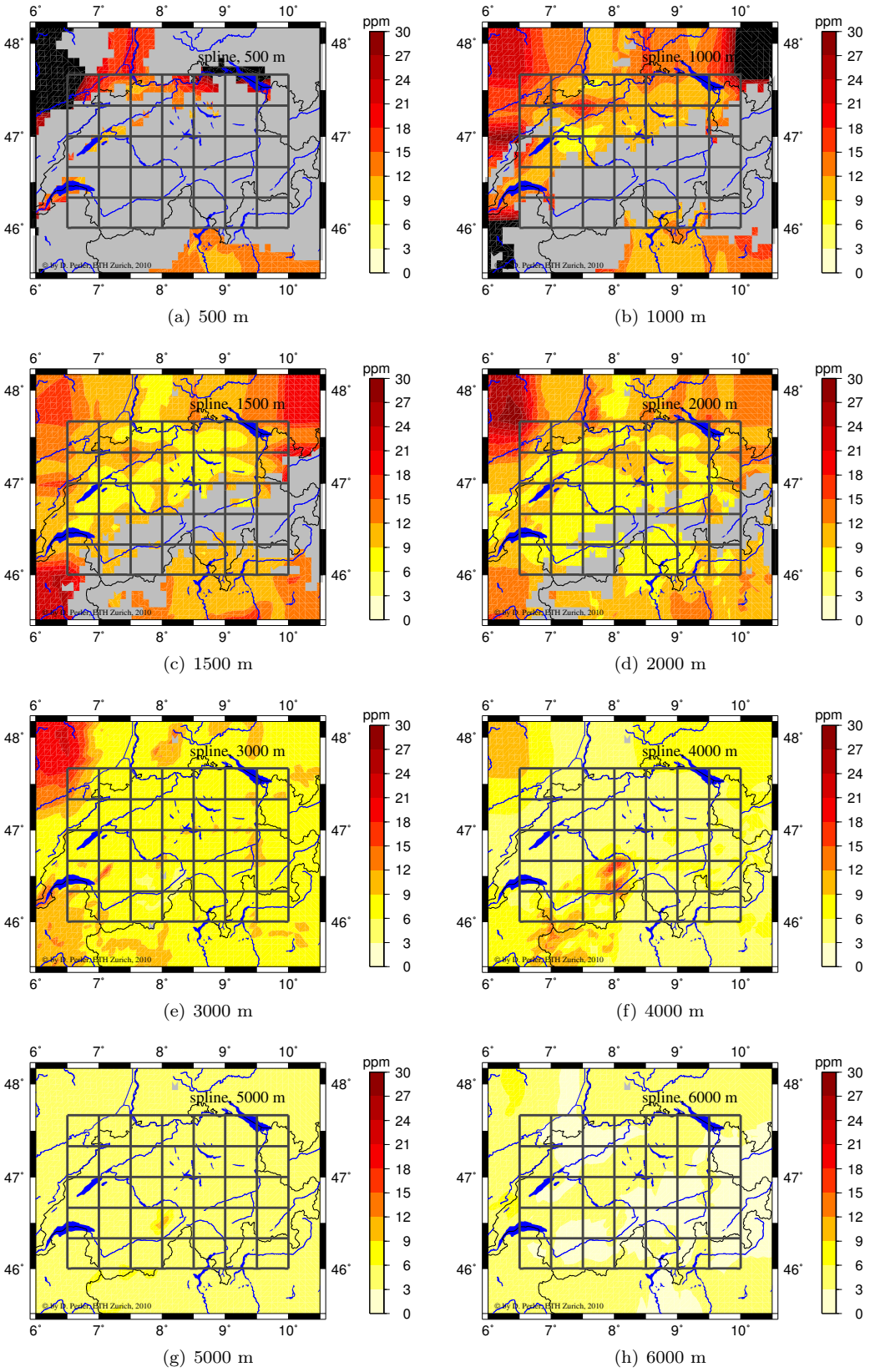

(a) 500 m (b) 1000 m

(c) 1500 m (d) 2000 m

(e) 3000 m (f) 4000 m

(g) 5000 m (h) 6000 m

Figure 9.25: RMS error of the tomographic solutions computed with spline parameterization with respect to COSMO-7 on selected height level using the bias correction model. Gray shaded areas indicate regions in which the Earth's surface is above the considered level.

parameterization. Besides the algorithmic improvements, the bias correction considerably decreases the RMS error of the tomographic solution with respect to COSMO-7 and is, therefore, highly recommended.

Comparisons with balloon sounding measurements and data from the NWP COSMO-7 showed that the accuracy is improved by more complex voxel parameterizations such as the trilinear or spline parameterization. With the spline parameterization, the standard error decreases by about 15% with respect to the data of balloon soundings launched at Payerne. Compared to the NWP COSMO-7, the improvement is much smaller and is of the order of 5% (including the application of the bias correction model). The case study addressing the local conditions in the vicinity of the highly elevated GNSS station Jungfraujoch revealed that the special local conditions near Jungfraujoch are significantly better reproduced by the non-constant parameterizations. Large biases and RMS errors are limited to the vicinity of this receiver station whereas the whole voxel and to a certain extent adjoining voxels are affected in the case where the constant parameterization is used. We can, therefore, recommend the use of the trilinear or spline parameterization. As the results of these two parameterizations are very similar, they are rated as equal in terms of accuracy.

Different parameterizations lead to a different vertical distribution of the systematic errors and to different integrated biases along the zenith direction. This sensitivity indicates a limited vertical resolvability and confirms the results of the synthetic tests in Section 8.2. Undifferenced observations such as zenith wet delays or slant path delays may improve the accuracy with respect to integrated quantities. Further investigations will reveal if the use of slant path delays instead of double difference delays will improve the accuracy.

The limited capability of GNSS tomography to resolve vertical structures is also supported by the observation that the vertical distribution of the systematic errors varies throughout the year. The departure of the vertical water vapor distribution, on which the intervoxel constraints are based, from the true distribution introduces systematic errors. These systematic departures are reduced by the bias correction. Adaptive intervoxel constraints should be considered to further decrease the impact of this effect.

Chapter 10

Conclusions

Within this thesis, the tomography system AWATOS 2 for estimating the 4D distribution of tropospheric refractivity has been implemented. The system is able to process integral measurements, such as GNSS double difference and slant path delays, and point measurements (e.g. from synoptic networks, balloon soundings and aircrafts). Tests with simulated and with real data have demonstrated the good performance of the assimilation system and the positive impact of the new models on the accuracy of the results. The simulation capabilities of AWATOS 2 have turned out to be useful for investigating the theoretical possibilities and limitations of the tomographic reconstruction based on GNSS double difference path delays.

In AWATOS 2, a trilinear and spline-based parametrization of the refractivity field are implemented. Investigations including simulated data and GPS double difference observations collected from 46 receiver stations over one year have shown superior performance of the new parametrizations compared to the classical constant one. The errors with respect to balloon soundings have been decreased by 15% using the new parametrizations instead of the constant one. As both new parametrizations achieve similarly accurate results, but the spline-based operates at higher computational costs, trilinear parametrization should be favored.

The long-term study revealed that there exist systematic differences between the tomographic solutions and the analysis of the NWP model. The bias correction model presented in this study reduces the RMS error with respect to the NWP model by 35% to 3.0 ppm (0.4 $\mathrm{g\,m^{-3}}$ abolute humidity). The bias can be explained to some extent by systematic differences between the input and the validation data and by discretization errors. In view of assimilation into a NWP model, a high-resolution bias correction model is strongly recommended. It is suggested that a similar grid resolution should be chosen for the bias correction model as for the NWP model. This allows to reduce the discretization errors and local effects which are related to differences between the true topography and that of the NWP model. For further applications, the possibility to reduce systematic differences at the observation-level should be considered.

Synthetic tests have indicated that vertical structures above the top station of the receiver network can be reconstructed by GNSS tomography. Thin refractivity layers above the top station are, however, weakly resolved compared to layers below the top station. In addition, the vertical resolvability of such layers quickly decreases with increasing layer height. Theoretical considerations suggest that the resolution of such structures are possible due to the spherically layered atmosphere.

The limited capability to resolve vertical structures is also visible in the results of the long-term study. Systematic differences between the tomographic solutions and the analyses of the NWP model are present. The analysis of these differences indicates the problematic influence of the intervoxel constraints. The investigations have shown that the distribution of the wet refractivity can considerably depart from the horizontal layering, especially in mountainous regions. Therefore, the horizontally smoothing intervoxel constraints should be used with care. The use of vertical smoothing constraints is, however, also challenging as the weak vertical resolvability of

GNSS tomography makes the solution sensitive to intervoxel constraints. It is suggested to use adaptive intervoxel constraints or, better, supplementary observations which provide more accurate information on the vertical distribution of the wet refractivity.

The investigations based on the 2 km grid NWP model data have shown small-scale structures of the wet refractivity field. Representing these data on a coarser grid of 37 km resolution revealed a discretization error of about 8 ppm (1.2 $\mathrm{g\,m^{-3}}$) RMS error at the 2000 m level in Switzerland. Thus, the difference in resolution between NWP model data and tomographic solutions is definitely a non-negligible error source. The impact of this error source can be reduced by high-resolution tomography and dense GNSS receiver networks.

Most of the investigations presented in this thesis are based on the existing operational measurement setup using GPS measurements from the AGNES receiver network. With the help of an error analysis, the impact of technical improvements, such as additional receiver stations, their specific locations and additional GNSSs, on the formal accuracy have been investigated. The study revealed that receiver stations should be placed at different altitudes whenever possible and at locations where satellites are visible down to low elevations. The accuracy is mainly improved in the lower 4 km of the troposphere. A practical extension of the AGNES network with additional receiver stations at the locations of the SwissMetNet (SMN) revealed an improvement of about 20% in formal accuracy. This extension would increase the number of receiver stations from 31 to 91. The use of the additional GNSS Galileo improves the formal accuracy by about 10-15%. The main effect is, however, a more constant accuracy over time. These analyses have revealed the potential of the new GNSSs to improve the accuracy of the tomography and the strong positive impact of dense receiver networks.

Chapter 11

Outlook

In this thesis, the investigations focus on the accurate reconstruction of the wet refractivity field. The step from wet refractivity to humidity has not been considered. To successfully assimilate humidity data derived from GNSS, this step has to be addressed in further investigations. Another issue is how to cope with the departure of the true topography from that of the NWP model orography, especially pronounced in alpine regions. In these regions, the RMS remains large even after applying the previously presented bias correction.

The theoretical investigations and the long-term study have shown the limited capability of GNSS tomography to resolve vertical structures. Complementary observations such as radio occultations, meteorological measurements from aircrafts and satellite imagery have large potential to improve the accuracy of GNSS tomography. AWATOS 2 already provides the possibility to assimilate such observations. Case studies are suggested to show the impact of such observations on the accuracy of the tomographic solutions.

A debatable point is whether to use zero difference delays or double difference delays as input data in GNSS tomography. Double difference processing has the advantage that ambiguities can be better resolved as with precise point positioning. This may result in more precise tropospheric path delays, which is crucial for GNSS tomography. On the other hand, the differencing complicates the tomographic processing, the investigations of the postfit residuals and a bias correction on the GNSS delays.

Independent of the processing strategy of GNSS raw observations, the accuracy of the tropospheric delays rely on the adequacy of the mapping functions. The investigations with the NWP model and balloon sounding data have revealed that the wet refractivity field can show significant perturbations from layered atmosphere. The impact of such departures from the usual structure of the wet refractivity distribution on the wet path delays is not clear and needs further investigations.

GNSS tomography is one of the few water vapor remote sensing techniques operating at all weather conditions. Assimilating the tomographic results into NWP models will have a large impact on forecasting extreme weather situations, as many observations from other remote sensing techniques are missing in these cases. It is, therefore, essential to better understand the accuracy and reliability of the tomographic solutions in extreme weather situations.

References

Anaman, K. A., J. J. Thampapillai, A. Henderson-Sellers, P. F. Noar, and P. J. Sullivan (1995). Methods of assessing the benefits of meteorological services in Australia. *Meteorological Applications 2*(1), 17–29.

Baldauf, M., A. Seifert, F. J., D. Majewski, M. Raschendorfer, and T. Reinhardt (2011). Operational convective-scale numerical weather prediction with COSMO model: description and sensitivities. *Monthly Weather Review*. accepted.

Bastin, S., C. Champollion, O. Bock, P. Drobinski, and F. Masson (2007). Diurnal Cycle of Water Vapor as Documented by a Dense GPS Network in a Coastal Area during ESCOMPTE IOP2. *Bull. Am. Meteorol. Soc. 46*, 167–182.

Bender, M., G. Dick, M. Ge, Z. Deng, J. Wickert, H.-G. Kahle, A. Raabe, and G. Tetzlaff (2011). Development of a GNSS water vapour tomography system using algebraic reconstruction techniques. *Advances in Space Research 47*, 1704–1720.

Bender, M., G. Dick, M. Ramatschi, M. Ge, G. Gendt, M. Rothacher, A. Raabe, and T. G. (2009). Estimates of the information provided by GPS slant data observed in Germany regarding tomographic applications. *Journal of Geophysical Research 114*, D06303.

Bender, M. and A. Raabe (2007). Preconditions to ground based GPS water vapour tomography. *Ann. Geophys. 25*, 1727–1734.

Bender, M., R. Stosius, F. Zus, G. Dick, J. Wickert, and A. Raabe (2011). GNSS water vapour tomography? Expected improvements by combining GPS, GLONASS and Galileo observations. *Advances in Space Research 47*, 886–897.

Bevis, M., S. Businger, S. Chiswell, T. A. Herring, R. A. Anthes, C. Rocken, and R. H. Ware (1994, March). GPS Meteorology: Mapping Zenith Wet Delays onto Precipitable Water. *J. Appl. Meteor. 33*, 379–386.

Bevis, M., S. Businger, T. A. Herring, C. Rocken, R. A. Anthes, and R. H. Ware (1992). GPS Meteorology: Remote Sensing of Atmospheric Water Vapor Using the Global Positioning System. *J. Geophys. Res. 97*(D14), 15787–15801.

Bian, J., H. Chen, H. Vömel, Y. Duan, Y. Xuan, and D. Lü (2011). Intercomparison of humidity and temperature sensors: GTS1, Vaisala RS80, and CFH. *Adv. Atmos. Sci. 28*(1), 139–146.

Bizouard, C. and L. Seoane (2010). Atmospheric and oceanic forcing of the rapid polar motion. *J. Geod. 84*, 19–30.

Brockmann, E., S. Grünig, D. Ineichen, and S. Schaer (2006). Monitoring the Automated GPS Network of Switzerland, AGNES. In *EUREF Publication No. 16, Mitteilungen des Bundesamtes für Kartographie und Geodäsie, Band 40*. Riga, June 15-17, 2006.

Brockmann, E., M. Kistler, U. Marti, S. A., B. Vogel, W. A., and U. Wild (2007). New developments in Swiss National Geodetic Surveying. Technical report, Swiss Federal Office of Topography swisstopo.

Bruyninx, C. and F. Roosbeek (2009). EPN status and new developments. In *EUREF Publication No. 17, Mitteilungen des Bundesamtes für Kartographie und Geodäsie, Band 42*, pp. 71–81. London, United Kingdom, June 06-09 2007.

Buzzi, M. (2008). *Challenges in Operational Numerical Weather Prediction at High Resolution in Complex Terrain*. Ph. D. thesis, ETH Zurich, Switzerland. Diss No. 17714.

Champollion, C., F. Masson, M.-N. Bouin, A. Walpersdorf, E. Doerflinger, O. Bock, and J. van Baelen (2005). GPS water vapour tomography: preliminary results from the ESCOMPTE field experiment. *Atmos. Res. 74*, 253–274.

Chapman, S. and R. S. Lindzen (1970). *Atmospheric Tides: Thermal and Gravitational*. D. Reidel publishing company.

Ciotti, P., E. R. Westwater, M. T. Decker, A. J. Bedard, and B. B. Stankov (1987). Ground-based microwave radiometric observations of the temporal vanation of atmospheric geopotential height and thickness. *IEEE Transactions on Geoscience and Remote Sensing 25*, 600–615.

Clark, K. M. (2002). The Use of Computer Modeling in Estimating and Managing Future Catastrophe Losses. *The Geneva Papers on Risk and Insurance 27*, 181–195.

Clark, P. (2009). Issues with high-resolution NWP. MOSAC-14 14.6, UK MetOffice. 12-13 November.

Collaud Coen, M., E. Weingartner, M. Furger, S. Nyeki, A. S. H. Prévôt, M. Steinbacher, and U. Baltensperger (2011). Planetary boundary influence at the Jungfraujoch analyzed by aerosol cycles and synoptic weather types. *Atmos. Chem. Phys. Discuss. 11*, 985–1024.

Dach, R., U. Hugentobler, P. Fridez, and M. Meindl (2007). *Bernese GPS Software Version 5.0*. Astronomical Institute, University of Bern.

Dankers, R., L. Feyen, and O. B. Chrstensen (2009). On the benefit of high-resolution climate simulations in impact studies of hydrological extremes. *Hydrology and Earth System Sciences Discussions 6*, 2573–2597.

de Argandoña, J., D., A. Ezcurra, J. Sáenz, B. Campistron, G. Ibarra-Berastegi, and F. Saïd (2010). Atmospheric tides over the Pyrenees: Observational study and numerical simulation. *Q. J. R. Meteorol. Soc. 136*, 1263–1274.

Doms, G. and U. Schättler (2002). *A Description of the Nonhydrostatic Regional Model LM. Part I: Dynamics and Numerics*. COSMO.

Dow, J. M., R. E. Neilan, and C. Rizos (2009). The International GNSS Service in a changing landscape of Global Navigation Satellite Systems. *J. Geod. 83*, 191–198.

Duan, J., M. Bevis, P. Fang, Y. Bock, S. Chiswell, S. Businger, C. Rocken, F. Solheim, T. van Hove, R. Ware, S. McClusky, T. A. Herring, and R. W. King (1996). GPS Meteorology: Direct Estimation of the Absolute Value of Precipitable Water. *J. Appl. Meteor. 35*, 830–838.

Eckert, V., M. Cocard, and A. Geiger (1992a). COMEDIE (Collocation of Meteorological Data for Interpretation and Estimation of Tropospheric Pathdelays, Teil I: Konzepte, Teil II: Resultate. Technical Report 194, ETH Zürich. Grauer Bericht.

Eckert, V., M. Cocard, and A. Geiger (1992b). COMEDIE (Collocation of Meteorological Data for Interpretation and Estimation of Tropospheric Pathdelays, Teil III: Software. Technical Report 195, ETH Zürich. Grauer Bericht.

Ecoplan/Sigmaplan (2007). Auswirkung der Klimaänderung auf die Schweizer Volkswirtschaft. Technical report, Federal Office of the Environment, Bern, Switzerland.

Elgered, G., J. M. Johansson, B. O. Rönnäng, and J. L. Davis (1997). Measuring regional atmospheric water vapor using the Swedish permanent GPS network. *Geophys. Res. Lett. 24*(21), 2663–2666.

Emardson, T. R., G. Elgered, and J. M. Johansson (1998). Three months of continuous monitoring of atmospheric water vapor with a network of Global Positioning System receivers. *J. Geophys. Res. 103*(D2), 1807–1820.

Essen, L. and K. D. Froome (1951). The Refractive Indices and Dielectric Constants of Air and its Principal Constituents at 24,000 Mc/s. In *Proceedings of the Physical Society, Section B*, Volume 64/10, pp. 862–875.

Falconer, R. H., D. Cobby, P. Smyth, G. Astle, J. Dent, and B. Golding (2009). Pluvial flooding: new approaches in flood warning, mapping and risk management. *J. of Flood Risk Management 2*, 198–208.

Flores, A., J. V.-G. de Arellano, L. P. Gradinarsky, and A. Rius (2001, February). Tomography of the Lower Troposphere Using a Small Dense Network of GPS Receivers. *IEEE Transactions on Geoscience and Remote Sensing 39*(2), 439–447.

Flores, A., G. Ruffini, and A. Rius (2000). 4D tropospheric tomography using GPS slant wet delays. *Ann. Geophys. 18*, 223–234.

Frei, C. and C. Davies, H. (1993). Anomaly in the Alpine diurnal pressure signal: Observations and theory. *Q. J. R. Meteorol. Soc. 119*, 1269–1289.

Frei, T. (2010). Economic and social benefits of meteorology and climatology in Switzerland. *Meteorological Applications 17*, 39–44.

Fujiwara, M., M. Shiotani, F. Hasebe, H. Voemel, S. J. Oltmans, P. W. Ruppert, T. Horinouchi, and T. Tsuda (2003). Performance of the Meteolabor "Snow White" chilled-mirror hygrometer in the tropical troposphere: Comparisons with the Vaisala RS80 A/H-Humicap sensors. *Journal of Atmospheric and Oceanic Technology 20*, 1534–1542.

Geiger, A. (1987). Einfluss richtungsabhängiger Fehler bei Satellitenmessungen. Technical Report 130, Institute of Geodesy and Photogrammetry, ETH Zurich.

Geiger, A. and M. Cocard (1992). Collocational methods in atmospheric ray tracing. In J. C. de Munck and T. A. T. Spoelstra (Eds.), *Refraction of transatmospheric signals in geodesy*, pp. 191–195. Netherlands Geodetic Commission.

Gelb, A. (1974). *Applied Optimal Estimation*. MIT Press.

Gradinarsky, L. P. (2002). *Sensing Atmospheric Water Vapor Using Radio Waves*. Ph. D. thesis, Chalmers University of Technology, Göteborg, Sweden.

Gradinarsky, L. P. and P. Jarlemark (2004). Ground-Based GPS Tomography of Water Vapor: Analysis of Simulated and Real Data. *J. Meteor. Soc. Japan 82*(1B), 551–560.

Guerova, G., E. Brockmann, J. Quiby, F. Schubiger, and C. Matzler (2003). Validation of NWP Mesoscale Models with Swiss GPS Network AGNES. *J. Appl. Meteor. 42*, 141–150.

Haase, J., M. Ge, H. Vedel, and E. Calais (2003). Accuracy and Variability of GPS Tropospheric Delay Measurements of Water Vapor in the Western Mediterranean. *J. Appl. Meteor. 42*, 1547–1568.

Hamilton, K. (1981). Latent heat release as a possible forcing mechanism for atmospheric tides. *Monthly Weather Review 109*(1), 3–17.

Hann, J. and R. Süring (1957). *Lehrbuch der Meteorologie* (5th ed.). C. H. Tauchnitz, Leibzig.

Hartmann, G. K. and R. Leitinger (1984). Range errors due to ionospheric and tropospheric effects for signal frequencies above 100 MHz. *Bull. Géod. 58*, 109–136.

Hartmann, T. and H.-G. Wenzel (1995). The HW95 tidal potential catalogue. *Geophys. Res. Lett. 22*(24), 3553–3556.

Haurwitz, B. and D. Cowley, A. (1975). The barometric tides at Zürich and on the summit of Säntis. *Pageoph 113*, 354–364.

Hill, R. J., R. S. Lawrence, and J. T. Priestley (1982). Theoretical and calculational aspects of the radio refractive index of water vapor. *Radio Science 17*(5), 1251–1257.

Hirahara, K. (2000). Local GPS tropospheric tomography. *Earth Planets Space 52*, 935–939.

Hirter, H. (1998). Mehrdimensionale Interpolation von Meteorologischen Feldern zur Berechnung der Brechungsbedingungen in der Geodäsie. Mitteilung 64, Inst. of Geodesy and Photogrammetry, ETH Zurich.

Hofmann-Wellenhof, B., H. Lichtenegger, and J. Collins (2001). *GPS Theory and Practice*. Springer, Wien, New York.

Hogg, D. C., F. O. Guiraud, and W. B. Sweezy (1981). The short-term temporal spectrum of precipitable water vapor. *Science 213*, 1112–1113.

Ifadis, I. M. (2000). A new approach to mapping the atmospheric effect for GPS observations. *Earth Planets Space 52*(10), 703–708.

Ineichen, D., E. Brockmann, and S. Schaer (2009). Enhancing the Swiss Permanent GPS Network (AGNES). In *EUREF Publication No. 17, Mitteilungen des Bundesamtes für Kartographie und Geodäsie, Band 42*, pp. 139–144. London, United Kingdom, June 06-09 2007.

ISO 2533:1975 (1975). *Standard Atmosphere*. International Organization for Standardization, Geneva, Switzerland.

Jacob, D., L. Bärring, O. Christensen, J. Christensen, M. de Castro, M. Déqué, F. Giorgi, S. Hagemann, M. Hirschi, R. Jones, E. Kjellström, G. Lenderink, B. Rockel, E. Sánchez, C. Schär, S. Seneviratne, S. Somot, A. van Ulden, and B. van den Hurk (2007). An inter-comparison of regional climate models for Europe: model performance in present-day climate. *Climatic Change 81*, 31–52. 10.1007/s10584-006-9213-4.

Jacobson, M., Z. (2005). *Fundamentals of atmospheric modeling* (2 ed.). Cambridge Uni. Press.

Kraus, H. (2004). *Die Atmosphäre der Erde* (3 ed.). Springer.

Kruse, L. P. (2001). *Spatial and Temporal Distribution of Atmospheric Water Vapor using Space Geodetic Techniques*, Volume 61 of *Geodätisch-geophysikalische Arbeiten in der Schweiz*. Swiss Geodetic Commission.

Lazo, J. K. and L. G. Chestnut (2002). Economic value of current and improved weather forecasts in the U.S. household sector. US-NOAA.

Lazo, J. K., E. Morss, and J. L. Demuth (2009). 300 Billion Served. *Bull. Amer. Meteor. Soc. 90*(6), 785–798.

Leick, A. (1989). *GPS satellite surveying* (1st ed.). Weley.

Leiviäkangas, P., R. Hautala, J. Räsänen, R. Öörni, S. Sonninen, M. Hekkanen, M. Ohlström, A. Venäläinen, and S. Saku (2008). Benefits of Meteorological Services in Croatia. Technical report, Finnish Meterological Institute, Helsinki.

Lindzen, R. S. (1978). Effect of daily variations of cumulonimbus activity on the atmospheric semidiurnal tide. *Monthly Weather Review 106*, 526–533.

Livingstone, D. M. (1997). Break-up dates of alpine lakes as proxy data for local and regional mean surface air temperatures. *Climate Change 37*(2), 407–439.

Lutz, S. (2009). *High-resolution GPS tomography in view of hydrological hazard assessment*, Volume 76 of *Geodätisch-geophysikalische Arbeiten in der Schweiz*. Swiss Geodetic Commission.

Lutz, S., S. Schär, M. Meindl, R. Dach, and P. Steigenberger (2010). Higher-order ionospheric modeling for CODE's next reprocessing activities. IGS Workshop, Newcastle upon Tyne, England.

Lutz, S., M. Troller, D. Perler, A. Geiger, and H. G. Kahle (2010). Better Weather Prediction Using GPS. *GPS World 21*(7), 40–47.

Matoušek, J. and J. Nešetřil (1998). *Invitation to Descrete Mathematics*. Oxford University Press.

Melbourne, W., R. Anderle, M. Feissel, R. King, D. McCarthy, D. Smith, B. Tapley, and R. Vicente (1983). Project MERIT standards. *U.S. Naval Observatory Circulars 167*, 96 pp.

Mendes, V. B. (1999, April). Modeling the neutral-atmospheric propagation delay in radiometric space techniqes. Ph.D. dissertation 199, University of New Brunswick, Canada.

Meteolabor (2002). Thermometer vt36. http://www.meteolabor.ch/vt36_e.pdf.

Meteolabor (2008). Thermo-hygrometer vtp37. http://www.meteolabor.ch/vtp37_e.pdf.

Miloshevich, L. M., H. Vömel, A. Paukkunen, W. J. Heymsfield, and S. S. J. Oltmans (2001). Characterization and correction of relative humidity measurements from Vaisala RS80-A radiosondes at cold temperatures. *Journal of Atmospheric and Oceanic Technology 18*, 135–156.

Moritz, H. (1973). *Least-Squares Collocation*. Number 75 in Reihe A: Theoretische Geodäsie. München: Deutsche Geodätische Kommission.

Nash, J., J. B. Elms, and T. J. Oakley (1995). Relative humidity sensor performance observed in recent international radiosonde comparisons. In *Ninth AMS Symposium on Meteorological Observations and Instrumentation*, pp. 43–48. Charlotte, North Carolina.

Niell, A. E. (1996). Global mapping functions for the atmosphere dely at radio wavelengths. *J. Geophys. Res. 101*, 3227–3246.

Nilsson, T. and L. Gradinarsky (2005). Correlations Between Slant Wet Delays Measured by Microwave Radiometry. *IEEE Transactions on Geoscience and Remote Sensing 43*(5), 1028–1035.

Nilsson, T. and L. Gradinarsky (2006). Water Vapor Tomography Using GPS Phase Observations: Simulation Results. *IEEE Transactions on Geoscience and Remote Sensing 44*(10), 2927–2941.

Obukhov, A. M. (1960). Statistically orthogonal extensions of empirical functions. *Izv. Akad. Nauk SSSR, Ser. Geofiz 3*, 432–439.

Øksendal, B. (2010). *Stochastic Differential Equations: An Introduction with Applications* (6 ed.). Springer.

Palumbo, A. (1975). Lunar tides in meteorological data. *Q. J. R. Meteorol. Soc. 101*, 995–1001.

Palumbo, A. (1998). Atmospheric tides. *Journal of Atmospheric and Solar-Terrestrial Physics 60*(3), 279–287.

Perler, D., A. Geiger, and F. Hurter (2011). 4D GPS water vapor tomography: new parameterized approaches. *J. Geod. 85*(8), 539–550.

Perler, D., F. Hurter, E. Brockmann, D. Leuenberger, D. Ruffieux, A. Geiger, and M. Rothacher (2010). GNSS meteorology: Activities in Switzerland. In *Proceedings of the 7th Management Committee (MC7) and Working Group (WG) Meeting, Colone (Germany)*.

Petit, G. and B. Luzum (2010). IERS technical note no 36. Technical report, IERS Convention Centre.

Pilon, P. J. (2005). *Guidelines for reducing flood losses*. United Nations.

Rice, John, A. (1995). *Mathematical Statistics and Data Analysis* (Second ed.). International Thomson Publishing.

Richner, H. (1999). Grundlagen aerologischer Messungen speziell mittels der Schweizer Sonde SRS 400. Technical Report 61, Swiss Federal Office of Meteorology and Climatology.

Rockel, B. and K. Woth (2007). Extremes of near-surface wind speed over Europe and their future changes as estimated from an ensemble of RCM simulations. *Climatic Change 81*, 267–280.

Rocken, C., R. Ware, T. van Hove, F. Solheim, C. Alber, J. Johnson, M. Bevis, and S. Businger (1993). Sensing atmospheric water vapor with the Global Positioning System. *Geophys. Res. Lett. 20*(23), 2631–2634.

Rüeger, J. M. (2002). Refractive Index Formulae for Radio Waves. In *Integration of Techniques and Corrections to Achieve Accurate Engineering*.

Ruffieux, D. and J. Joss (2003). Influence of radiation on the temperature sensor mounted on the Swiss Radiosonde. *J. Atmos. Ocean. Technol. 20*, 1576–1582.

Saastamoinen, J. (1972). Atmospheric Correction for Troposphere and Stratosphere in Radio Ranging of Satellites. In S. W. Henriksen, A. Macini, and B. H. Chovitz (Eds.), *The Use of Artificial Satellites for Geodesy*, Volume 15 of *Geophysics Monograph*, pp. 247–251. Washington, D.C.: American Geophysical Union.

Saastamoinen, J. (1973a). Contributions to the theory of atmospheric refraction. *Bull. Géod. 105*, 279–298.

Saastamoinen, J. (1973b). Contributions to the theory of atmospheric refraction: Introduction to practical computation of astronomical refraction. *Bull. Géod. 107*, 383–397.

Saastamoinen, J. (1973c, March). Contributions to the theory of atmospheric refraction: Part II. Refraction corrections in satellite geodesy. *J. Geod. 47*(1), 13–34.

Schönwiese, C. D. (2000). *Praktische Statistik für Meteorologen und Geowissenschaftler* (3 ed.). Gebrüder Borntraeger.

Schwarz, H. R. (1997). *Numerische Mathematik* (4 ed.). Teubner.

Seeber, G. (2003). *Satellite Geodesy* (2 ed.). Berlin, New York: Walter de Gruyter.

Sidorenkov, N. (2003). Influence of the atmospheric tides on the earth rotation. *Celestrial Mechanics and Dynamical Astronomy 87*, 27–38.

Sidorenkov, N. (2009). *The Interaction Between Earth's Rotation and Geophysical Processes*. Wiley.

Siebert, M. (1961). Atmospheric tides. *Advances in Geosciences 7*, 105–183.

Smith, Jr, E. K. and S. Weintraub (1953). The Constants in the Equation for Atmospheric Refractive Index at Radio Frequencies. In *Proceedings of the Institute of Radio Engineers*, Volume 41/8, pp. 1035–1037.

Stoer, J. and R. Bulirsch (1980). *Introduction to Numerical Analysis*. New York: Springer-Verlag.

Stull, R. B. (1999). *An Introduction to Boundary Layer Meteorology*. Dordrecht: Kluwer Academic Publishers. Reprint.

Suter, S., T. Konzelmann, C. Mühlhäuser, M. Begert, and A. Heimo (2006). SwissMetNet – The new automatic meteorological network of Switzerland: Transition from old to new network, data management and first results. In *Proceedings of the 4th International Conference on Experience with Automatic Weather Stations (4th ICEAWS)*. Altis Park Hotel, Lisbon, Portugal, 24-26 May 2006.

Swisstopo (2004). DHM25-the digital height model of Switzerland. Technical report, Swiss Federal Office of Topography.

Tatarskii, V. I. (1971). *The effects of the turbulent atmosphere on wave propagation*. Israel Program for Scientific Translations Ltd. translated from russian by IPST Staff.

Thayer, G. D. (1974). An improved equation for the radio refractive index of air. *Radio Science 9*, 803–807.

Torge, W. (2003). *Geodäsie* (2 ed.). Walter de Gruyter.

Tregoning, P., R. Boers, D. O'Brien, and M. Hendy (1998, November). Accuracy of absolute precipitable water vapor estimates from GPS observations. *J. Geophys. Res. 103*(D22), 28,701–28,710.

Treuhaft, R. N. and G. E. Lanyi (1987). The effect of the dynamic wet troposphere on radio interferometric measurements. *Radio Science 22*(2), 251–265.

Troller, M. (2004). *GPS based Determination of the Integrated and Spatially Distributed Water Vapor in the Troposphere*, Volume 67 of *Geodätisch-geophysikalische Arbeiten in der Schweiz*. Swiss Geodetic Commission.

Troller, M., B. Bürki, M. Cocard, A. Geiger, and H.-G. Kahle (2002). 3-D refractivtiy field from GPS double difference tomography. *Geophys. Res. Lett. 29*(24), 2149.

Troller, M., M. Cocard, and A. Geiger (2002). *Softwarepackage Comedie: Collocation of Meteorological Data for Interpolation and Estimation of Tropospheric Pathdelays. User documentation*. Geoedesy and Geodynamics Lab, ETH Zurich. Version 1.1.

Troller, M., A. Geiger, E. Brockmann, and H.-G. Kahle (2006). Determination of the spatial and temporal variation of tropospheric water vapour using CGPS networks. *Geophys. J. Int. 167*(2), 509–520.

Troller, M., D. Leuenberger, E. Brockmann, A. Geiger, and H.-G. Kahle (2007). GPS-Tomography: Results and Analyses of the Operational Determination of Humidity Profiles over Switzerland. *Geophys. Res. Abstr. 9*.

Troller, M., S. Lutz, A. Walpersdorf, A. Geiger, B. Bürki, O. Bock, E. Doerflinger, and H. G. Kahle (2005). Determination of Continuous 3D Water Vapor Distribution Using the High-Density GPS Network of the ESCOMPTE Campaign. 6th ESCOMPTE workshop, Marseille.

Vömel, H., M. Fujiwara, M. Shiotani, F. Hasebe, S. J. Oltmans, and J. E. a. Barnes (2003). The behavior of the snow white chilled-mirror hygrometer in extremely dry conditions. *Journal Of Atmospheric And Oceanic Technology 20*, 1560–1567.

Wang, J., H. L. Cole, D. J. Carlson, E. R. Miller, K. Beierle, and T. K. Laine (2002). Corrections of humidity measurement errors from the Vaisala RS80 radiosonde – application to TOGA COARE data. *Journal of Atmospheric and Oceanic Technology 19*, 981–1002.

Wanner, H. (1979). Zur Bildung, Verteilung und Vorhersage winterlicher Nebel im Querschnitt Jura–Alpen. *Geogr. Bernensia G7*, 240 p.

Wehrli, J. (1986). Räumliche Interpolation des Druckfeldes aus Messungen des ANETZ unter Verwendung vereinfachten Krigings. Master's thesis, Diplomarbeit, LAPETH, ETH Zürich.

WMO (2008). *Guide to Meteorological Instruments and Methods of Observation* (7 ed.). 8. World Meteorological Organization, Geneva.

Zappa, M., M. W. Rotach, M. Arpagaus, M. Dorninger, C. Hegg, A. Montani, R. Ranzi, F. Ament, U. German, G. Grossi, S. Jaun, A. Rossa, S. Vogt, A. Walser, J. Wehrhan, and C. Wunram (2008). MAP D-PHASE: real-time demonstration of hydrological ensemble prediction systems. *Atmos. Sci. Lett. 9*, 80–87.

Appendix A

Ray-tracing in ellipsoidal coordinate systems

In GNSS tomography, the atmosphere is discretized in so-called voxels. They are laterally limited by faces of constant longitude and latitude. Two faces parallel to the reference ellipsoid limit the voxel along the vertical. Signals are emitted by satellites and received at stations usually located on the Earth's surface. The ray path between satellite and receiver is modeled by a straight line. Some of these rays cross voxels of our model. To determine, which voxels are traversed is the work of the ray-tracing algorithm.

There are 3 cases of intersections: intersection with a) longitudinal, b) latitudinal, and c) horizontal boundary faces. An intersection between a longitudinal voxel boundary and a straight line is the simplest case. The boundary face is an unbent plane and the intercept point can be easily computed, therefore. The ray line is described by

$$\mathbf{g}(r) \;=\; \mathbf{x}_0 \;+\; r\,\mathbf{dx} \;=\; \begin{bmatrix} x_0 \\ y_0 \\ z_0 \end{bmatrix} \;+\; r \begin{bmatrix} dx \\ dy \\ dz \end{bmatrix} \tag{A.1}$$

and the limiting plane by

$$\mathbf{f}_\lambda(s,t) \;=\; s \begin{bmatrix} \cos(\lambda) \\ \sin(\lambda) \\ 0 \end{bmatrix} \;+\; t \begin{bmatrix} 0 \\ 0 \\ 1 \end{bmatrix}, \tag{A.2}$$

where $\mathbf{x_0}$ is a coordinate on the ray path (e.g. the coordinates of the receiver station), $\mathbf{dx}$ the direction of the ray with $\|\mathbf{dx}\|_2 = 1$, λ is the longitude of the face, and r, s and t the free parameters describing the ray path and the face, respectively. Setting $\mathbf{g}(r) = \mathbf{f}_\lambda(s,t)$ and solve this equation for r leads to

$$\hat{r} \;=\; \frac{x_0 \sin(\lambda) \;-\; y_0 \cos(\lambda)}{dy \cos(\lambda) \;-\; dx \sin(\lambda)}. \tag{A.3}$$

The estimated parameter r is equal to the distance between the point $\mathbf{x}_0$ and the intersection of the ray path $\mathbf{g}(s)$ with the plane $\mathbf{f}_\lambda(s,t)$. Thus, the intercept point is $\mathbf{x} = \mathbf{x}_0 + r\,\mathbf{dx}$.

A bit more complicated is the latitudinal case. This case can be attributed to an intersection between a straight line and a cone. The ray is again described as in Equation A.1. The cone can be constructed by rotating the normal vector on the Earth's surface around the Earth's rotation axis (z-axis). This leads to the quadratic equation $a\,r^2 + b\,r + c = 0$ with

$$\begin{aligned} a &= \cos^2(\phi)\,dz^2 - \sin^2(\phi)\,(dx^2 + dy^2) \\ b &= \cos^2(\phi)\,\tilde{z}\,dz - \sin^2(\phi)\,(x\,dx + y\,dy) \\ c &= \cos^2(\phi)\,\tilde{z}^2 - \sin^2(\phi)\,(x^2 + y^2) \\ \tilde{z} &= z + \frac{a_e e^2 \sin(\phi)}{\sqrt{1-e^2\sin^2(\phi)}}, \end{aligned}$$

where a_e the Earth's major axis, e the excentricity of the Earth's ellipsoid, and ϕ the latitude of the face.

The intercept point between the top and bottom of a voxel cannot be described in closed form. The root finding algorithm *Newton-Raphson* was used to find the intersection point (Schwarz 1997). The following system of equations must be solved:

$$\left|\begin{aligned} (R_n + h)\cos(\phi)\cos(\lambda) - x_0 - r\,dx = 0 \\ (R_n + h)\cos(\phi)\sin(\lambda) - y_0 - r\,dy = 0 \end{aligned}\right|, \tag{A.4}$$

where ϕ denotes the latitude, λ the longitude, h the height above the Earth's ellipsoid, d the Earth's semi-major axis, e the excentricity, $R_n = d/\sqrt{1 - e^2\sin^2(\phi)}$, and $r = ((R_n(1-e^2) + h)\sin(\phi) - z_0)/dz$.

Appendix B

Newton-Cotes quadrature

Newton-Cotes quadrature is a numerical method to estimate a definite integral. The Newton-Cotes quadrature formulas approximate the integrand by Lagrange polynomials (Schwarz 1997; Stoer and Bulirsch 1980). In our setup, Lagrange polynomials of order 4 are used. An integral of the function $\mathrm{f}(x)$ in the interval $[a, b]$ is then approximated by

$$\int_a^b \mathrm{f}(x)\mathrm{d}x = \frac{2h}{45}\Big(7\big(\mathrm{f}(a)+\mathrm{f}(b)\big) + 32\big(\mathrm{f}(x_1)+\mathrm{f}(x_3)\big) + 12\mathrm{f}(x_2) + \sum_{k=1}^{N-1}\Big(14\mathrm{f}(x_{4k}) + 32\big(\mathrm{f}(x_{4k+1})+\mathrm{f}(x_{4k+3})\big) + 12\mathrm{f}_{4k+2}\Big)\Big)$$

with

$$h = \frac{b-a}{4N}, \qquad x_j = a + jh, (j = 1, 2, \ldots, 4N-1).$$

Appendix C

Empirical Orthogonal Functions

The method of Empirical Orthogonal Functions (EOF) is a technique for analyzing the variability of a scalar field (Obukhov 1960). It is widely used in meteorology and is closely related to Principle Component Analysis (PCA). The method can be used to identify patterns of scalar fields and their variation in time. Further, a quantity is indicating how important the single patterns are. In this way, principle patterns or components are extracted. However, the principle patterns are not necessarily related to a physical process, but they can help to characterize the data.

Another application of EOF is the removal of noise from data. Thereby, patterns with low importance are interpreted as noise and are truncated. The data is then reconstructed by using the principle components.

The method works on a discretized field. Let us assume that we have measurements at the points $p_j (j = 1, \ldots, m)$. For each of these points, we have a measurement at time $t_i (i = 1, \ldots, n)$. All these observations are collected in a $n \times m$ matrix $\mathbf{D}$. As a first step, the mean values and, if desired, trends and seasonal effects are removed from each of the time series (e.g. from each of the columns in $\mathbf{D}$). Let us call the resulting matrix $\mathbf{F}$.

The goal of the method is to find m patterns v_k which maximize

$$\sum_{i=1}^{n} (v_k^T f_i)^2 \tag{C.1}$$

subjected to the orthogonal constraint

$$v_k^T v_k = 0, \tag{C.2}$$

where f_i is the i-th row vector of $\mathbf{F}$. Applying the methods of Lagrange multipliers leads to the eigenvalue problem

$$\mathbf{F}^T \mathbf{F} v = \lambda v \tag{C.3}$$

with the eigenvalues λ. Thereby, the eigenvalues indicate the importance of the corresponding pattern, and the eigenvectors or patterns are uncorrelated in the space of the field. Since $\mathbf{F}$ contains the detrended data of the scalar field, $\mathbf{F}^T \mathbf{F}$ is the covariance matrix of the field.

Appendix D

Atmospheric tides in times series of wet refractivity

Further investigations of the spectra shown in Figures 5.3 a) and b) revealed additional peaks at periods around 8 h, 12 h, and 24 h. To get more distinct spectra, a much longer period is evaluated. The data set consists of pressure, temperature and humidity measurements with a sampling rate of 10 minutes at the synoptic station in Payerne and Mount Säntis. Each time series spans a period beginning in January 1984 and ending in September 2010 (see Figure D.1a) and b)).

Figures D.1a) and b) show the spectra of the wet refractivity computed from temperature and humidity measurements at the synoptic stations in Payerne and Mount Säntis, respectively. In the spectrum belonging to Payerne, 3 peaks on both sides of the peak corresponding to the 24 h cycle are visible. These 6 peaks are even more distinct than the 24 h peak. In the spectrum belonging to Mount Säntis, only 2 peaks are visible besides the 24 hour peak. In contrast to the spectrum from Payerne, the 24 h peak is the most pronounced one. The amplitudes are at about 1 ppm and are of the same magnitude on both sites. The exact amplitudes of the most distinct peaks are listed in Table D.1.

The observed frequencies correspond to the main solar tidal frequencies published in Petit and Luzum 2010. The peaks at periods of 24.066 h and 23.934 h are identified with the main solar tide P_1 and the lunisolar declinational tide K_1, respectively. The periods of 23.869 and 24.132 h correspond to solar elliptical components π_1 and ψ_1, respectively. The outermost peak at a period of 23.804 h refers to solar declination component φ_1. The peak at period of 24.199 h has no name but corresponds to a tidal component related to the Sun (Hartmann and Wenzel 1995).

Sidorenkov 2003, Sidorenkov 2009 and Bizouard and Seoane 2010 have investigated the influence of diurnal atmospheric tides on Earth rotation. Sidorenkov analyzed the relative atmospheric angular momentum vectors computed from NCEP/NCAR reanalysis. The significant diurnal frequencies listed in Table D.1 are also found in his spectral analysis. Beside these frequencies, he observed significant frequencies around 28.235 h. No significant peaks are found in this band in our spectra of the wet refractivity time series.

Comparing Figures D.1a) and b) shows that the tidal effects π_1, ψ_1, φ_1 and that with period 24.199 h are only visible in the spectrum at Payerne but not on Mount Säntis. The reason for that is not clear and needs further investigations.

The main semi-diurnal peaks visible in Figures D.1a) and b) are listed in Table D.1. They coincide with tidal frequencies published in Sidorenkov 2009. The period of 11.967 h is indicated as K_2, that of 11.984 h as R_2, 12.016 h as T_2, and 12.033 h as $2T_2$. There are two additional peaks with periods of 11.951 h and 12.049 h. Both of them are unnamed in the tide catalog published by Hartmann and Wenzel 1995. All the visible semi-diurnal frequencies are related to solar induced tidal components. Their amplitudes are of the same size as the amplitudes of the diurnal cycles.

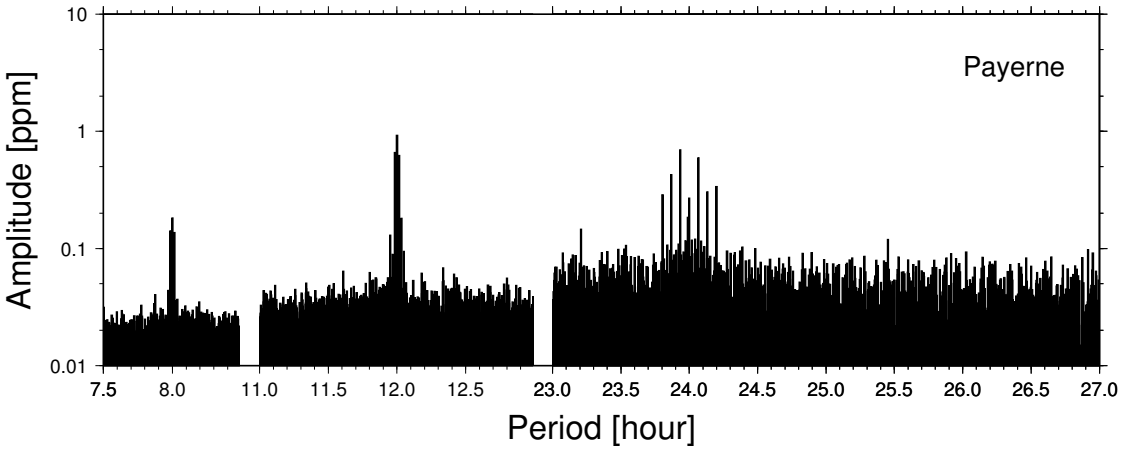

(a) Payerne

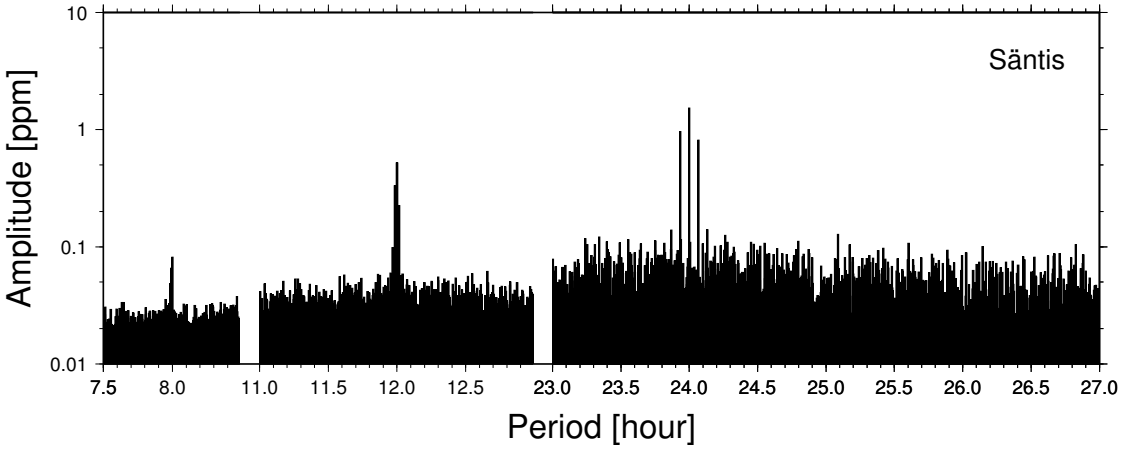

(b) Säntis

Figure D.1: Amplitude spectra of wet refractivity computed from the time series spanning more than 26 years of data measured at the synoptic stations a) Payerne and b) Mount Säntis.

Ter-diurnal frequencies are also found. In contrast to the diurnal and semi-diurnal ones, they coincide with lunar-induced tidal components and their amplitude is about one magnitude smaller than the one from diurnal and semi-diurnal cycles.

In Table D.2, the amplitudes of main gravimetric tides at mid-latitudes are listed. Comparing them to the observed ones in Table D.1, the tides which influence the gravitational acceleration strongest are not the ones with the most pronounced amplitude in the spectra of the wet refractivity time series. The partial tides Q_1, O_1, N_2, M_2 and M_3 are not distinguishable from noise in the spectra. This indicates that the atmospheric tides are not mainly driven by the change of the gravitational acceleration. By looking at which of the tides are absent in the spectra, one sees that only lunar tides are missing. Siebert 1961, Chapman and Lindzen 1970 and Lindzen 1978 state that recurring variations in insolation and the resulting thermal effects are mainly responsible for atmospheric tides. This confirms the suppositions that the atmospheric tides are not mainly driven by changes in gravitational acceleration. In the following, the time series of pressure, temperature and specific humidity will be considered.

In the last decades, pressure time series from synoptic stations have been investigated in Switzerland by Haurwitz and Cowley 1975 and by Palumbo 1975. They mainly focused on the solar partial tides S_1 and S_2 and on the lunar tides M_1 and M_2. Haurwitz and Cowley 1975 investigated the differences in amplitude observed on Mount Säntis and in Zurich and estimated the mean temper-

Table D.1: Main cycles with periods equal or shorter than 1 day computed from temperature and humidity measurements at the synoptic stations in Payerne and Mount Säntis. The time series is sampled with 10 minutes and spans 26 years. For diurnal, semi-dirunal, and ter-dirunal cycles, the sampling period dt of the spectra and threshold amplitude (*limit*) is given.

Payerne		**Säntis**	
Period [h]	**Amplitude [ppm]**	**Period [h]**	**Amplitude [ppm]**
Diurnal cycles		*dt ≈ 11 s*	*limit = 0.2 ppm*
24.199	0.340		
24.132	0.304		
24.066	0.597	24.066	0.815
24.000	0.270	24.000	1.533
23.934	0.694	23.934	0.965
23.869	0.427		
23.804	0.287		
Semi-diurnal cycles		*dt ≈ 2.5 s*	*limit = 0.08 ppm*
12.049	0.095		
12.033	0.182		
12.016	0.622	12.016	0.224
12.000	0.929	12.000	0.519
11.984	0.661	11.984	0.332
11.967	0.089	11.967	0.098
11.951	0.130		
Ter-diurnal cycles		*dt ≈ 1 s*	*limit = 0.08 ppm*
8.015	0.137		
8.007	0.104		
8.000	0.182	8.000	0.082
7.985	0.142		

ature difference between these two sites assuming hydrostatic equilibrium. Palumbo 1975 has also analyzed time series of temperature and estimated the influence of the tidal temperature change on the pressure time series to explain the unexpected large tidal amplitudes in the pressure time series. In addition, Palumbo 1998 has investigated time series of humidity measurements to better explain the larger pressure amplitude for S_2 than for S_1. Frei and Davies 1993 and de Argandoña et al. 2010 have studied diurnal atmospheric tides over the European Alps and over the Pyrenees, respectively. To our knowledge, no other partial tides are considered in meteorological data, yet. The high sampling rate of 10 minutes and the length of the time series (26 years) allows a high spectral resolution which is sufficient to resolve additional diurnal and semi-diurnal partial tides.

If solar insolation is the main driving effect of solar tides, this should be visible in the spectra of pressure, temperature and humidity on which the computation of the (wet) refractivity is based. The diurnal partial tides P_1, S_1 and K_1 are visible in the spectrum of pressure measurements (see Figure D.2a)). The side peaks have an amplitude of 0.1 hPa and the main peak at S_1 0.34 hPa. Haurwitz and Cowley 1975 estimated an amplitude for S_1 of 0.2735 hPa in Zurich. This is of the same order of magnitude as observed in Payerne, but, it is not clear if the difference of 0.063 hPa can be explained by different local conditions. It is also debatable if the peaks generally explained with solar tides are not biased by measurment errors such as effects from solar radiation on the sensor.

The semi-diurnal partial tides M_2, $2T_2$, R_2, S_2 and K_2 are visible. The amplitude of S_2 is, with 0.42 hPa, larger than that of the S_1 partial tide. This corresponds to the findings stated in Haurwitz and Cowley 1975. There are also ter-diurnal partial tides visible which correspond to those seen in the spectrum of the wet refractivity.

Whereas only solar partial tides are visible in the spectrum computed from the wet refractivity

Table D.2: Main gravimetric partial tides at latitude 45° and height 0 m. (Source: Torge 2003)

Symbol	**Period [h]**	**Amplitude [nms^{-2}]**
Diurnal cycles		
Q1	26.87	59.5
O1	25.82	310.6
P1	24.07	144.6
K1	23.93	436.9
Semi-diurnal cycles		
N2	12.66	71.9
M2	12.42	375.6
S2	12.00	174.8
K2	11.97	47.5
Ter-diurnal cycles		
M3	8.28	5.2

time series, there are also lunar tides recognizable in the pressure spectrum. The identifiable lunar tides are the M_2 partial tide, the synodic moon period (29.322 days) and its second and third harmonics.

In Figure D.2b), the spectrum computed from the temperature time series is plotted. It shows the same characteristic frequencies as the spectrum of the wet refractivity time series. The largest amplitudes are observed at the diurnal tides with a maximum of about 5 K in S_1. The semi-diurnal partial tides are between half and one order of magnitude smaller than the diurnal ones. The ter-diurnal tides are also smaller than those in the semi-diurnal band and have an amplitude of about 0.1 K.

The supposition that variations in insolation are the main driving effect for atmospheric tides fits in with the observations made in the spectra of the pressure and the temperature time series. Although the variation of gravitational acceleration caused by lunar tides are stronger than those caused by solar tides, the solar tidal components observed in the spectra of pressure and temperature are significantly more distinct than those of the Moon. This indicates that the variations of gravitational acceleration cannot be the main driving effect. The fact that the spectrum of the temperature shows only solar tides and that a change in temperature is strongly related to changes in insolation indicates that variations in insolation is the main tidal driving effect in the troposphere. These observations fit in with the findings made by Hamilton 1981.

Figure D.2c) shows the spectrum of the specific humidity. It looks similar to that derived from the wet refractivity and from the temperature time series. The existence of the tidal signal in the time series confirms the strong influence of variations in insolation on atmospheric tides, as changes in the specific humidity near the Earth's surface are strongly related to variations in insolation and the resulting evapotranspiration. Further investigations have shown that the tidal signal observed in the wet refractivity time series is mainly related to tidal variation in humidity.

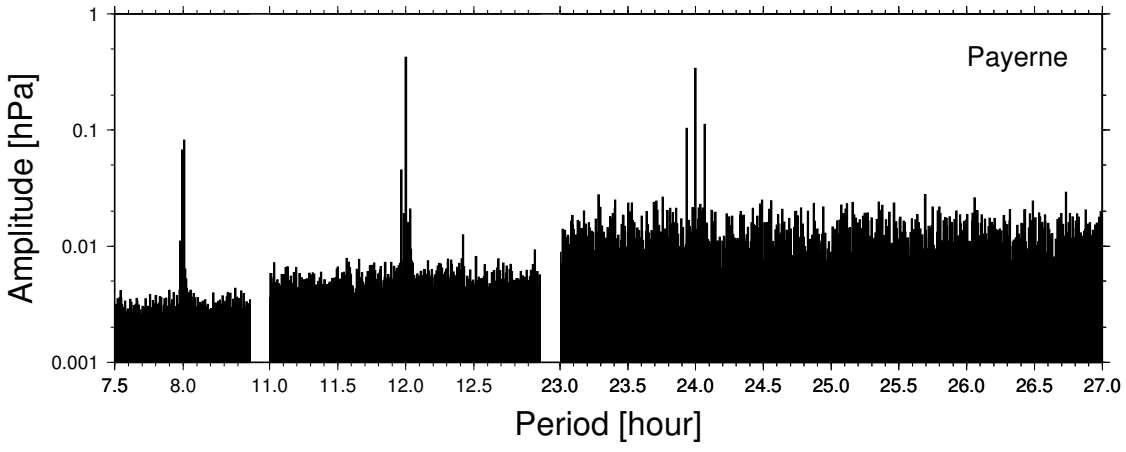

(a) Pressure

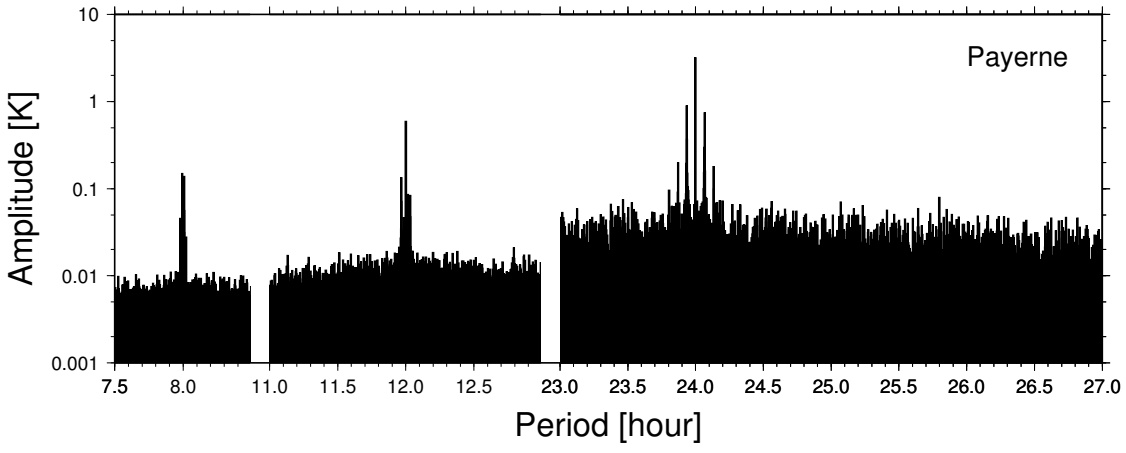

(b) Temperature

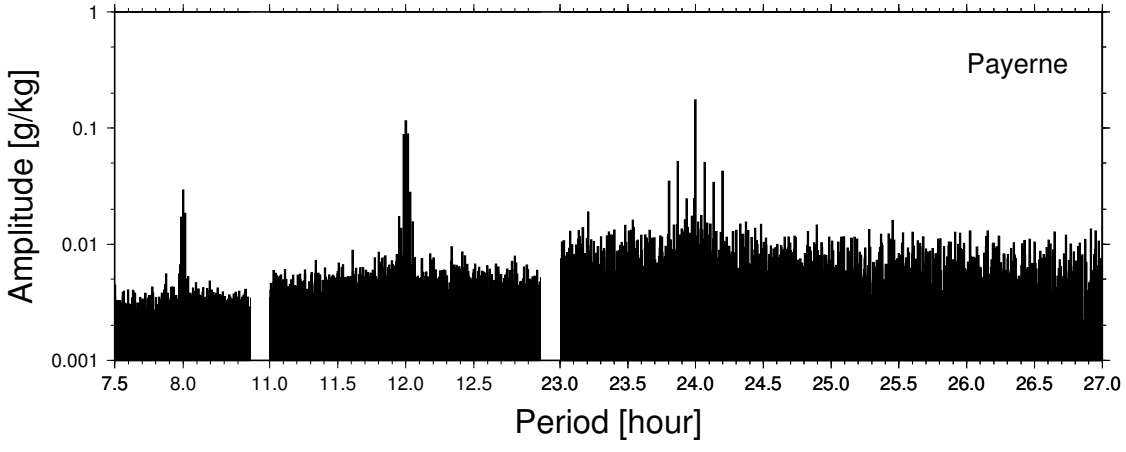

(c) Specific humidity

Figure D.2: Amplitude spectra of a) pressure, b) temperature and c) specific humidity computed from the time series spanning more than 26 years of data measured at the synoptic station in Payerne.

Appendix E

Geometrical path length in spherical geometry

Geometrical path length within a layer in spherical geometry

In the following, a formula will be derived to approximate the geometrical path length δs of a ray within a layer. The ray hits a sphere with radius r_0 with a zenith angle ϑ_0. The distance between the center of this sphere and the lower boundary of the layer is $r = r_0 + h$, where h is the height of the lower layer boundary above the sphere. The thickness of the layer is denoted by δr. Figure E.1 illustrates the situation.

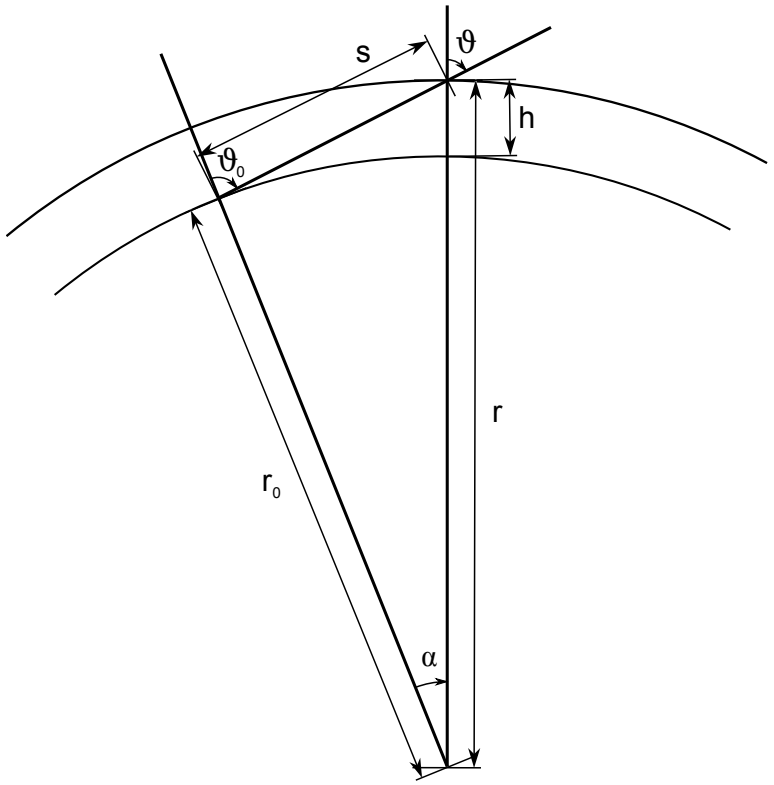

Figure E.1: Illustration of the spherical model. A ray hits the surface of the sphere with radius r_0 with zenith angle ϑ_0. The geometrical path length of the ray between the spheres with radius r_0 and r is denoted by s.

The geometrical path length s between the sphere and the lower boundary of the layer can be computed with the help of the Law of Sines (Equation E.1a), Pythagorean identity (Equation E.1b) and the Law of Projection (Equation E.1c).

$$\frac{r_0}{\sin(\vartheta)} = \frac{r}{\sin(\pi - \vartheta_0)} \tag{E.1a}$$

$$\sin^2(\vartheta) + \cos^2(\vartheta) = 1 \tag{E.1b}$$

$$s = r_0 \cos(\pi - \vartheta_0) + r \cos(\vartheta) \tag{E.1c}$$

The geometrical path length s is then

$$s = \sqrt{r^2 - r_0^2 \sin^2(\vartheta_0)} - r_0 \cos(\vartheta_0) \tag{E.2}$$

Assuming that the layer thickness δr is small compared to the distance r, the geometrical path length δs can be approximated by

$$\delta s = \frac{\mathrm{d}s}{\mathrm{d}r}\delta r = \frac{r}{\sqrt{r^2 - r_0^2 \sin^2(\vartheta_0)}}\delta r. \tag{E.3}$$

Finally, the geometrical path length δs is linearized at $r = r_0$.

$$\begin{aligned} \delta s &\approx \delta s\Big|_{r=r_0} + \frac{\mathrm{d}\,\delta s}{\mathrm{d}r}\Big|_{r=r_0} (r - r_0) \\ &\approx \frac{1}{\cos(\vartheta_0)}\delta r - \frac{1}{r_0}\frac{\sin^2(\vartheta_0)}{\cos^3(\vartheta_0)}\, h\, \delta r \end{aligned} \tag{E.4}$$

The linearized form will be referred to as *first order spherical approximation.*

Normal matrix in spherical geometry

Assuming constant refractivity within the layers and using the spherical model presented in the previous section, the observation equation is written in Einstein's summation notation as

$$10^{-6}\, \delta s_{i,j}\, n_j \;=\; \Delta_i \tag{E.5}$$

where $\delta s_{i,j}$ is the path length of the i-th ray in the j-th layer, Δ_i the path delay in metrical units of the i-th ray and n_j the refractivity within the j-th layer. According to Equation E.3, the geometrical path length for the i-th ray in the j-th layer can be written as

$$\delta s_{i,j} \;=\; \frac{r_0 + h_j}{\sqrt{(r_0 + h_j)^2 - r_0^2 \sin^2(\vartheta_{0\,i})}}\delta r_j. \tag{E.6}$$

and the geometrical path length of the first spherical approximation as

$$\delta s_{i,j} \;\approx\; \underbrace{\frac{1}{\cos(\vartheta_{0\,i})}}_{c_i}\, \delta r_j \;-\; \underbrace{\frac{1}{r_0}\frac{\sin^2(\vartheta_{0\,i})}{\cos^3(\vartheta_{0\,i})}}_{b_i}\, h_j\, \delta r_j \tag{E.7}$$

The elements of the normal matrix are then defined by

$$\begin{aligned} N_{j,k} &= 10^{-12}\, \delta s_{i,j}\, \delta s_{i,k} \\ &= \frac{r_0 + h_j}{\sqrt{(r_0 + h_j)^2 - r_0^2 \sin^2(\vartheta_{0\,i})}} \frac{r_0 + h_k}{\sqrt{(r_0 + h_k)^2 - r_0^2 \sin^2(\vartheta_{0\,i})}}\, \delta r_j\, \delta r_k \end{aligned} \tag{E.8}$$

and the elements of the normal matrix using the first spherical approximation

$$\begin{aligned} N_{j,k}^{(1)} &= 10^{-12}\,\delta s_{i,j}\,\delta s_{i,k} \\ &= 10^{-12}\,(c_i\ -\ b_i\,h_j)\,(c_i\ -\ b_i\,h_k)\,\delta r_j\,\delta r_k \\ &= 10^{-12}\left(\left[c_i^2\right]\ -\ \left[b_i\,c_i\right](h_j\ +\ h_k)\ +\ \left[b_i^2\right]h_j\,h_k\right)\delta r_j\,\delta r_k \end{aligned} \tag{E.9}$$

where the 1 in the superscript in N denotes the first spherical approximation. Assuming observations uniformly distributed between zenith angles $\vartheta_{0\,a}$ and $\vartheta_{0\,b}$, leads to

$$\begin{aligned} N_{j,k} = \frac{10^{-12}}{\vartheta_{0\,b}-\vartheta_{0\,a}}\int_{\vartheta_{0\,a}}^{\vartheta_{0\,b}} & \frac{r_0+h_j}{\sqrt{(r_0+h_j)^2-r_0^2\sin^2(\vartheta_{0\,i})}} \\ & \frac{r_0+h_k}{\sqrt{(r_0+h_k)^2-r_0^2\sin^2(\vartheta_{0\,i})}}\,\mathrm{d}\vartheta_0\,\delta r_j\,\delta r_k \end{aligned} \tag{E.10}$$

and for the first spherical approximation

$$\begin{aligned} N_{j,k}^{(1)} = \frac{10^{-12}}{\vartheta_{0\,b}-\vartheta_{0\,a}}\Bigg(&\int_{\vartheta_{0\,a}}^{\vartheta_{0\,b}}\frac{1}{\cos^2(\vartheta_0)}\,\mathrm{d}\vartheta_0 \\ &-\frac{1}{r_0}\int_{\vartheta_{0\,a}}^{\vartheta_{0\,b}}\frac{\sin^2(\vartheta_0)}{\cos^4(\vartheta_0)}\,\mathrm{d}\vartheta_0\,(h_j\ +\ h_k) \\ &+\ \frac{1}{r_0^2}\int_{\vartheta_{0\,a}}^{\vartheta_{0\,b}}\frac{\sin^4(\vartheta_0)}{\cos^6(\vartheta_0)}\,\mathrm{d}\vartheta_0\,h_j\,h_k\Bigg)\,\delta r_j\,\delta r_k. \end{aligned} \tag{E.11}$$

As no analytical solution for the integral in Equation E.10 for $j \neq k$ is found, the solution is only given for the case where $j = k$:

$$N_{j,j} = \frac{(r_0+h_j)\,\arctan\left(\frac{\sqrt{(r_0+h_j)^2-r_0^2}\,\tan(\vartheta_0)}{r_0\,h_j}\right)}{10^{12}\,(\vartheta_{0\,b}-\vartheta_{0\,a})\,\sqrt{(r_0+h_j)^2\ -r_0^2}}\Bigg|_{\vartheta_{0\,a}}^{\vartheta_{0\,b}}\delta r_j^2. \tag{E.12}$$

In contrast to that, the integrals in Equation E.11, can also be analytically solved for $j \neq k$:

$$\begin{aligned} N_{j,k}^{(1)} = \frac{10^{-12}}{\vartheta_{0\,b}-\vartheta_{0\,a}}\Bigg(&\tan(\vartheta_0)\Big|_{\vartheta_{0\,a}}^{\vartheta_{0\,b}}-\frac{h_j\ +\ h_k}{3\,r_0}\tan^3(\vartheta_0)\Big|_{\vartheta_{0\,a}}^{\vartheta_{0\,b}} \\ &+\ \frac{h_j\,h_k}{5\,r_0^2}\tan^5(\vartheta_0)\Big|_{\vartheta_{0\,a}}^{\vartheta_{0\,b}}\Bigg)\,\delta r_j\,\delta r_k \end{aligned} \tag{E.13}$$

Maximal observed zenith angle in spherical geometry

Dividing the layer in segments restricts the observable zenith angles at a given receiver location on the sphere for a given segment. In the following, a formula will be given that describes the maximal zenith angle of a ray traversing a layer segment of infinitesimal thickness with radian measure α and with the lower horizontal boundary at the same angular coordinate as the location of the receiver (see Figure E.1). The maximal observable zenith angle can be computed with the help of the Law of Cosine (Equation E.14) and the Law of Projection (Equation E.1c).

$$s^2 = r_0^2\ +\ r^2\ -\ 2\,r_0\,r\,\cos(\alpha) \tag{E.14}$$

The maximal observable zenith $\vartheta_{0,\,\max}$ angle is then

$$\vartheta_{0,\,\max} = \pi\ -\ \arccos\left(\frac{r_0\ -\ (r_0+h)\cos(\alpha)}{\sqrt{r_0^2\ +\ (r_0+h)^2\ -\ 2r_0(r_0+h)\cos(\alpha)}}\right) \tag{E.15}$$

using $r = r_0 + h$.

Appendix F

Supplementary plots of the long-term study

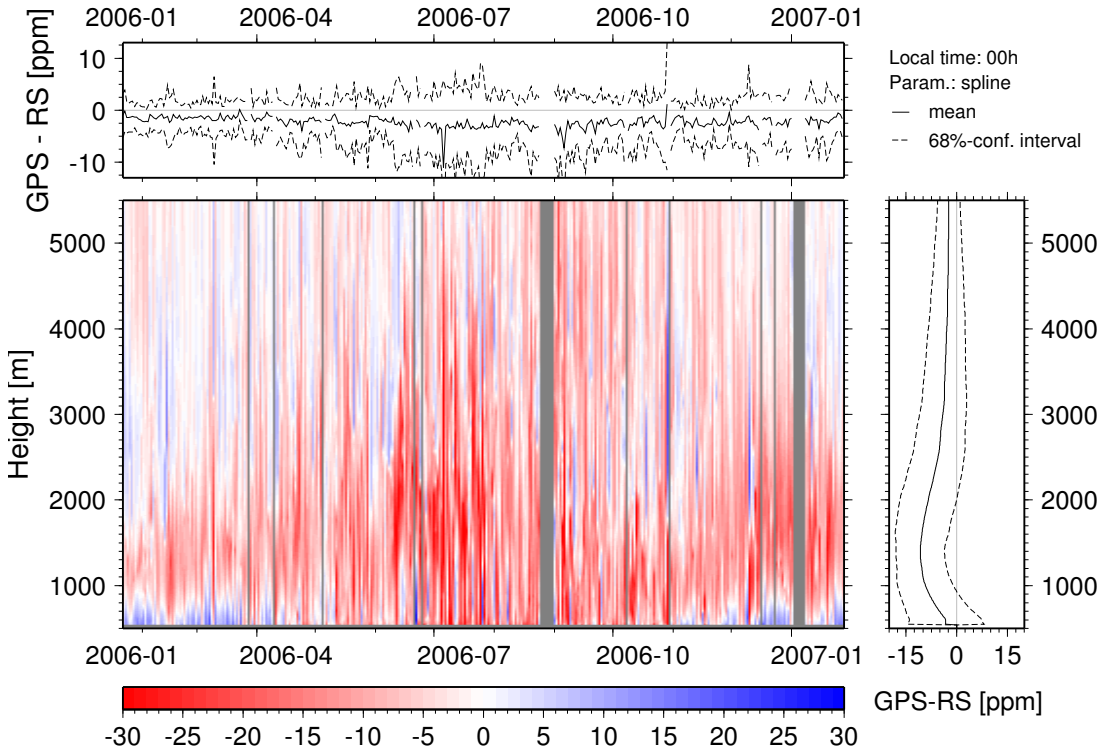

Figure F.1: Wet refractivity difference between tomographic solutions and observations computed from balloon soundings launched at Payerne for spline parameterization at 0 h UTC.

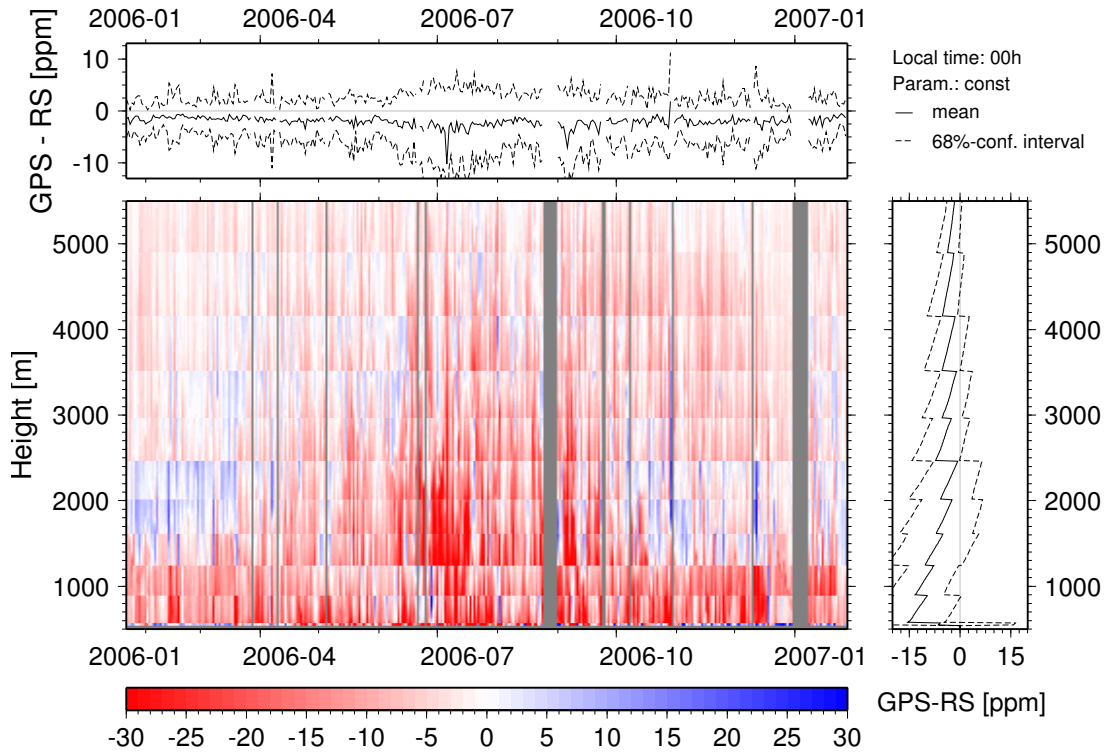

(a) 0 h UTC

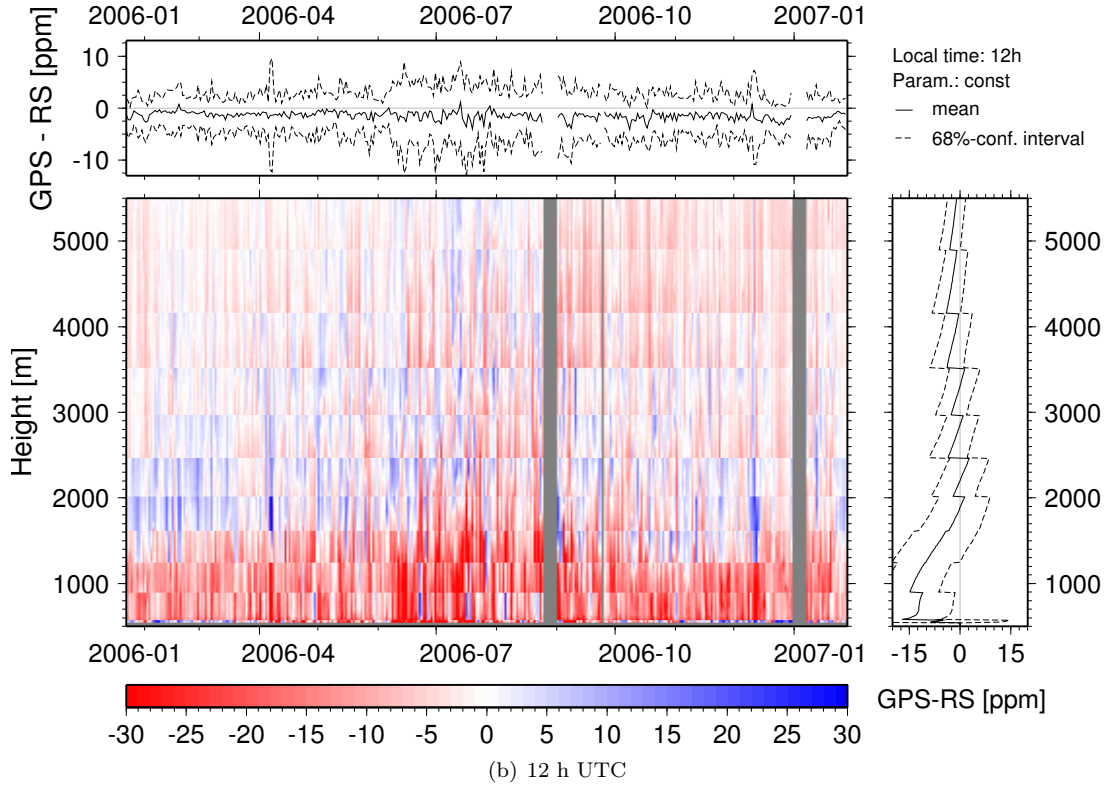

(b) 12 h UTC

Figure F.2: Wet refractivity difference between tomographic solutions and observations computed from balloon soundings launched at Payerne for constant parameterization at (a) 0 and (b) 12 h UTC.

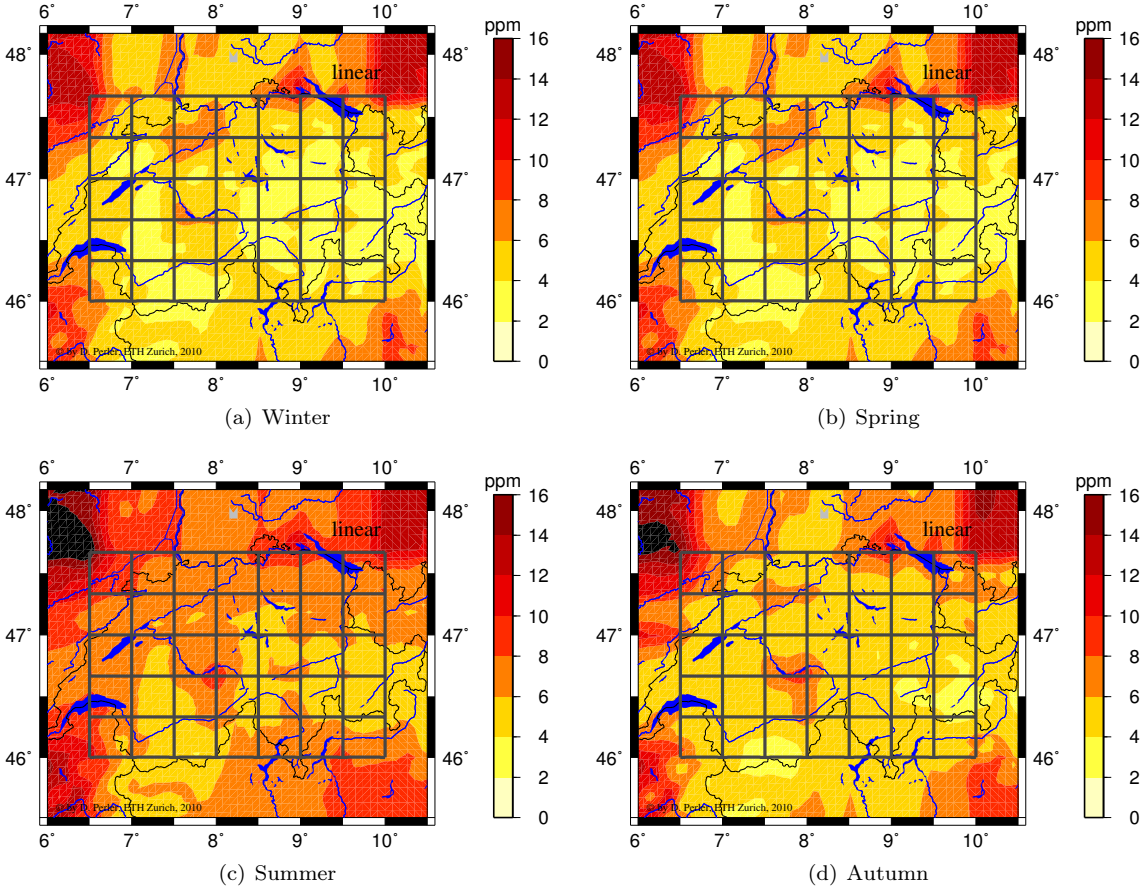

(a) Winter (b) Spring

(c) Summer (d) Autumn

Figure F.3: Weighted RMS of the tomographic solution using linear parameterization with respect to COSMO-7 evaluated for different seasons. The RMS is ppm wet refractivity units.

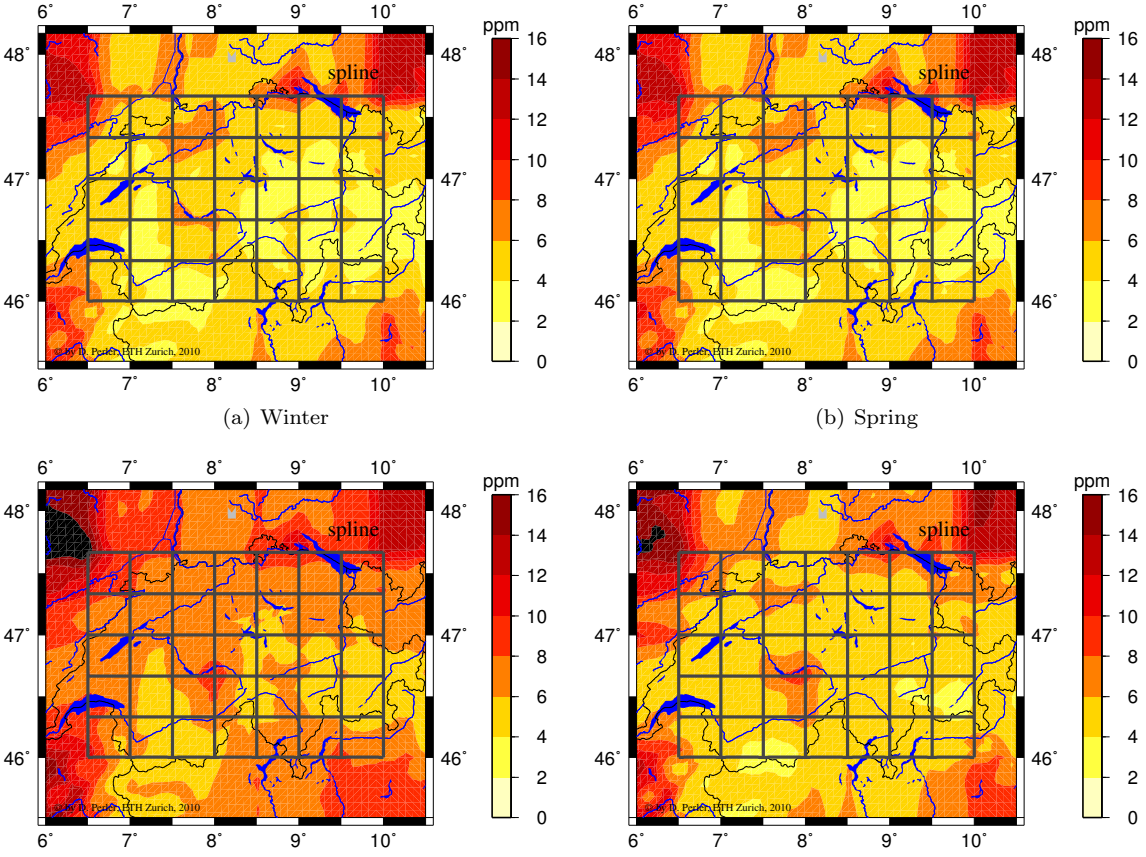

Figure F.4: Weighted RMS of the tomographic solution using spline parameterization with respect to COSMO-7 evaluated for different seasons. The RMS is ppm wet refractivity units.

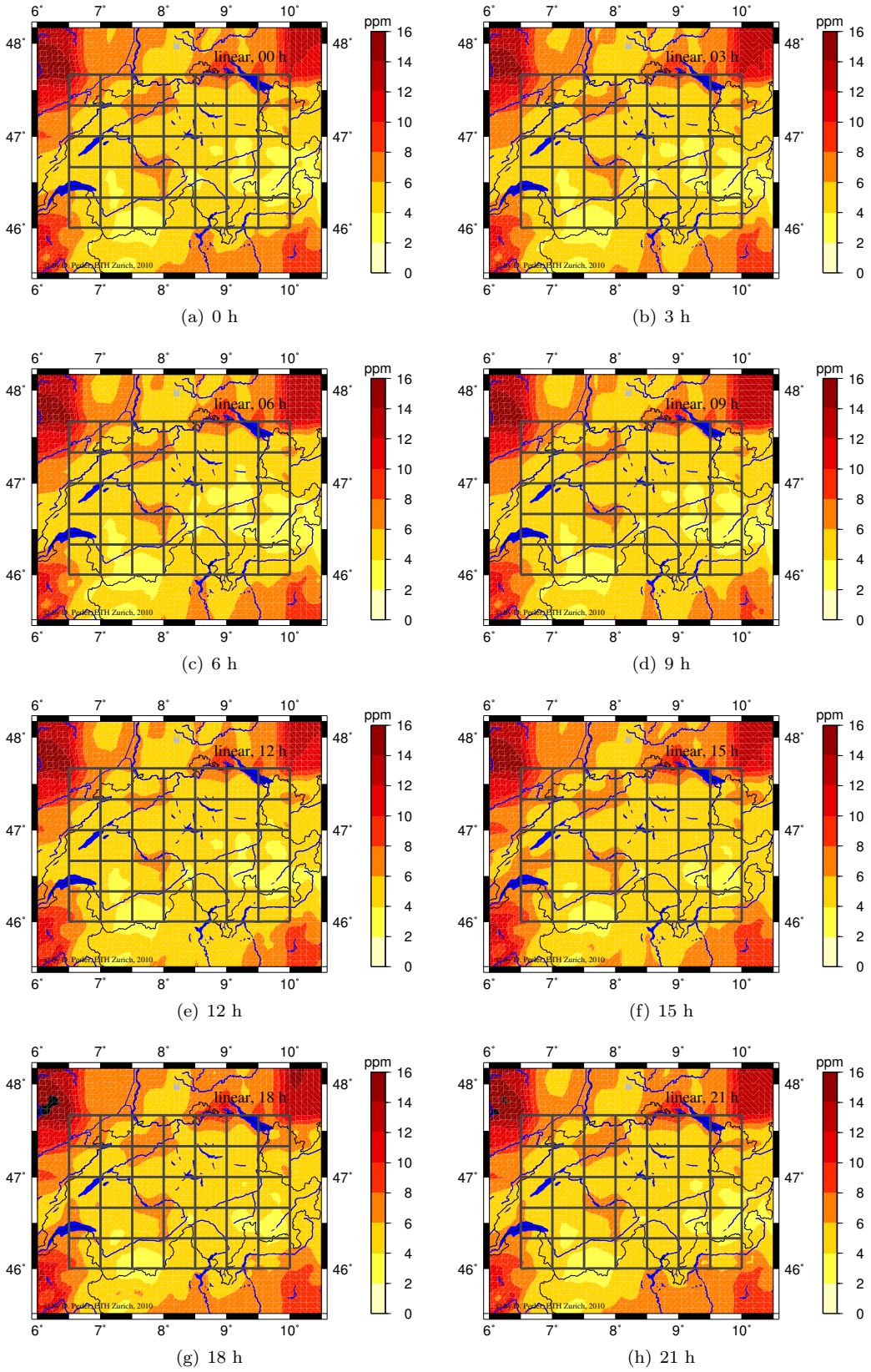

(a) 0 h (b) 3 h

(c) 6 h (d) 9 h

(e) 12 h (f) 15 h

(g) 18 h (h) 21 h

Figure F.5: Weighted RMS of tomographic solution using linear parameterization with respect to COSMO-7 at selected day times. The values are in ppm wet refractivity units.

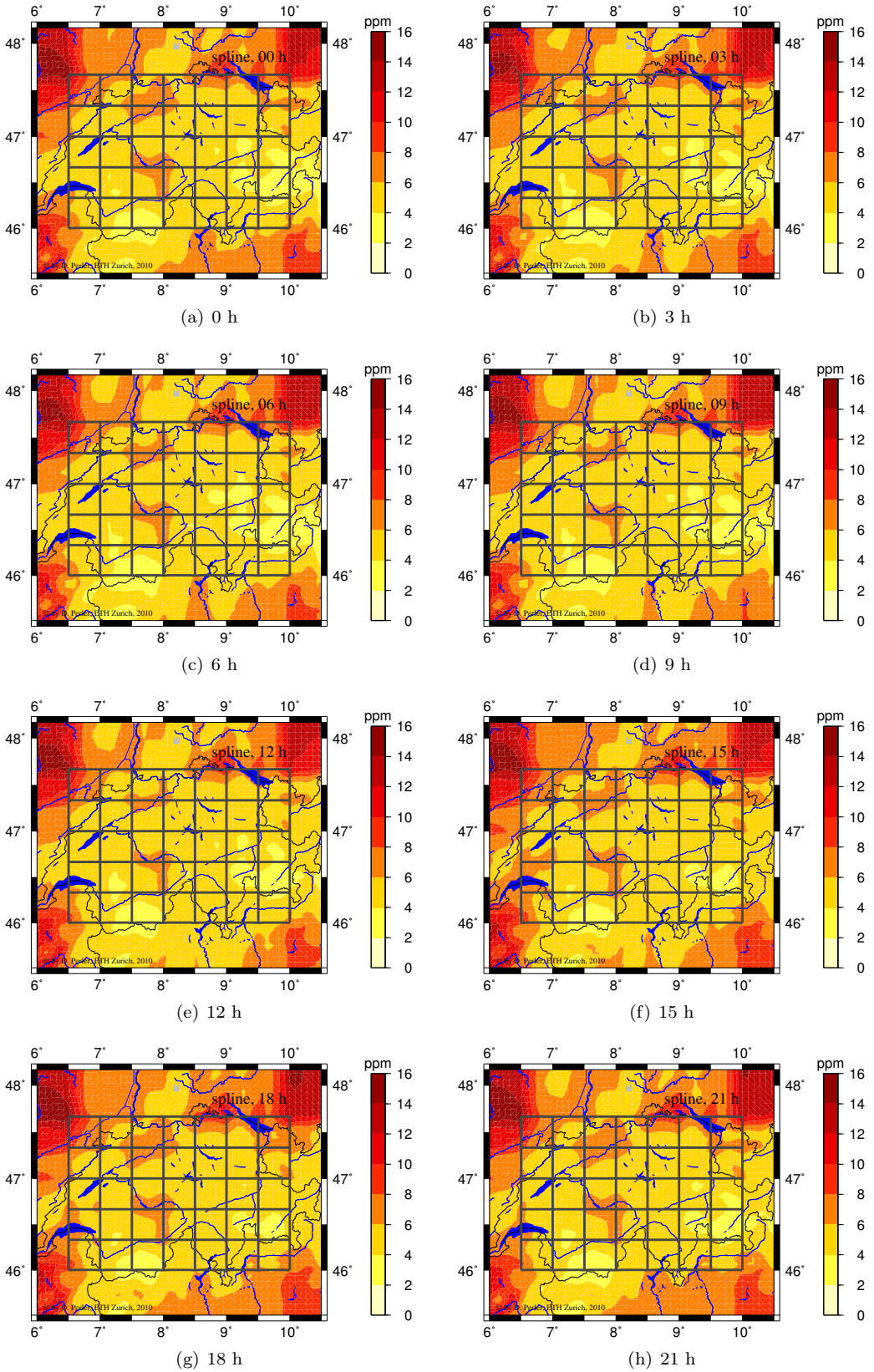

(a) 0 h (b) 3 h

(c) 6 h (d) 9 h

(e) 12 h (f) 15 h

(g) 18 h (h) 21 h

Figure F.6: Weighted RMS of tomographic solution using spline parameterization with respect to COSMO-7 at selected day times. The values are in ppm wet refractivity units.

“Geodätisch-geophysikalische Arbeiten in der Schweiz”

(Fortsetzung der Publikationsreihe ”Astronomisch-geodätische Arbeiten in der Schweiz”) der Schweizerischen Geodätischen Kommission (www.sgc.ethz.ch)

62 2001 Solar Spectrometry for Determination of Tropospheric Water Vapor. Bernd Sierk, 212 Seiten.

63 2001 Analysis of refraction influences in geodesy using image processing and turbulence models. Philipp Flach, 175 Seiten.

64 2003 INS/GPS Integration for Pedestrian Navigation. V. Gabaglio, 161 Seiten.

65 2003 Efficient Methods for Determining Precise Orbits of Low Earth Orbiters Using the Global Positioning System. Heike Bock, 214 Seiten.

66 2003 Capteurs et Algorithmes pour la Localisation Autonome en Mode Pédestre. Quentin Ladetto, 121 Seiten.

67 2004 GPS based Determination of the Integrated and Spatially Distributed Water Vapor in the Troposphere. Marc Troller, 172 Seiten.

68 2005 Geodetic Mobile Solar Spectrometer. Alexander Somieski, 205 Seiten.

69 2005 Absolute Airborne Gravimetry. Henri Baumann, 142 Seiten.

70 2006 The *Swiss Trolley* – A Modular System for Track Surveying. Ralph Glaus, 184 Seiten.

71 2006 Development of a Robotic Mobile Mapping System by Vision-Aided Inertial Navigation: A Geomatics Approach. Fadi Atef Bayoud, 157 Seiten.

72 2007 Das neue Landeshöhennetz der Schweiz LHN95. Andreas Schlatter, 373 Seiten.

73 2007 Pseudo-Stochastic Orbit Modeling of Low Earth Satellites Using the Global Positioning System. Adrian Jäggi, 214 Seiten.

74 2008 Cartographie Mobile en Temps Réel. Hervé Gontran, 162 Seiten.

75 2008 Mutual Validation of Satellite-Volume 75 Geodetic Techniques and its Impact on GNSS Orbit Modeling. Claudia Flohrer, 198 Seiten.

76 2009 High-resolution GPS tomography in view of hydrological hazard assessment. Simon Lutz, 202 Seiten.

77 2009 Trajectory Determination and Analysis in Sports by Satellite and Inertial Navigation. Adrian Wägli, 175 Seiten.

78 2009 GPS Based Dynamic Monitoring of Air Pollutants in the City of Zurich. Philippe Kehl, 156 Seiten.

79 2010 In-flight Quality Assessment and Data Processing for Airborne Laser Scanning. Philipp Schaer, 166 Seiten.

80 2010 Sea Surface Topography and Marine Geoid by Airborne Laser Altimetry and Shipborne Ultrasound Altimetry. Philippe Limpach, 207 Seiten.

81 2010 Global Gravity Field Determination Using the GPS Measurements Made Onboard the Low Earth Orbiting Satellite CHAMP. Lars Prange, 213 Seiten.

82 2011 Analysis of long-term GPS observations in Greece (1993-2009) and geodynamic implications for the Eastern Mediterranean. Michael D. Müller, 186 Seiten.

83 2011 Combined Analysis of Observations from Different Global Navigation Satellite Systems. Michael Meindl, 150 Seiten.

84 2012 Water Vapor Tomography using Global Navigation Satellite Systems. Donat Perler, 198 Seiten.